ISSN 0912-1803

PHOTON FACTORY ACTIVITY REPORT

1995

#13

NATIONAL LABORATORY FOR HIGH ENERGY PHYSICS, KEK

Photon Factory Activity Report 1995

Staff members and visitors of the Photon Factory gathered in front of the PF building.

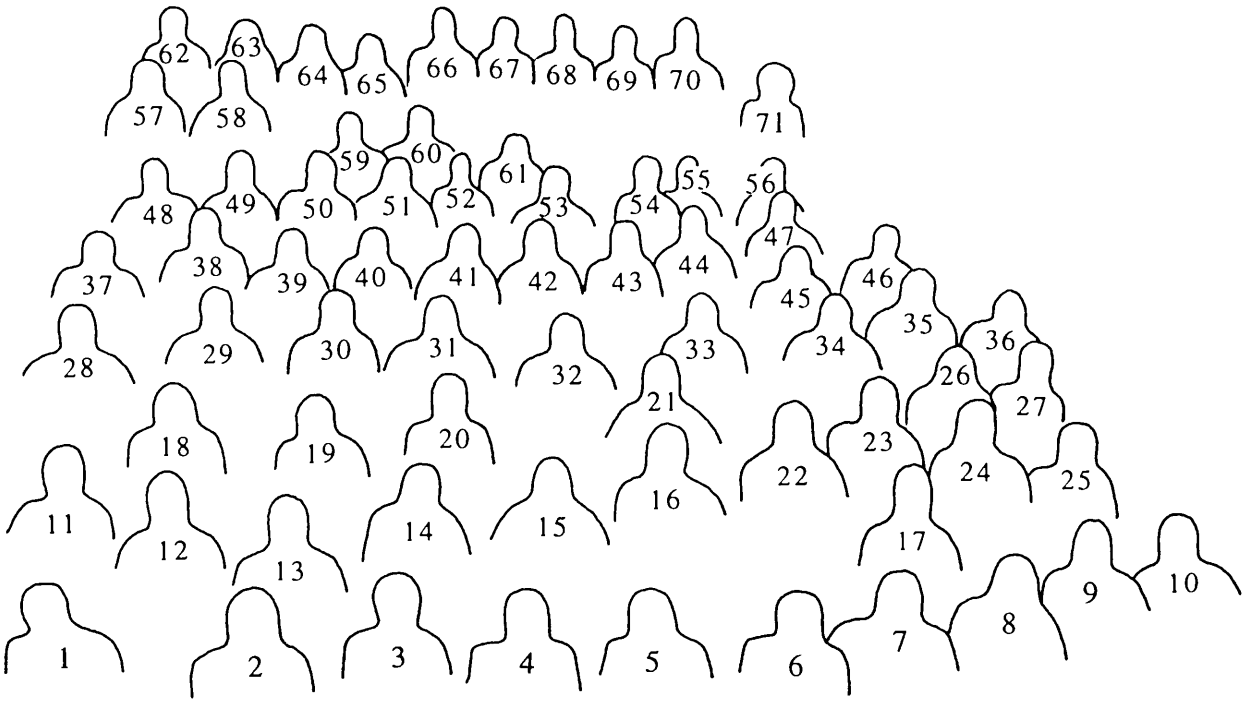

1. M. Kobayashi
2. Y. Saito
3. I. Sato
4. M. Kihara
5. T. Nakajima
6. H. Kobayakawa
7. T. Matsushita
8. S. Fukuda
9. K. Furukawa
10. M. K. Wu
11. H. Kawada
12. G. Kutluk
13. Y. Hori
14. H. Kobayashi
15. S. Anami
16. S. Yamamoto
17. Y. Sato
18. S. Sakanaka
19. T. Kasuga
20. S. Takano
21. Y. Murakami
22. K. Nasu
23. S. Kamada
24. Y. Takiyama
25. Y. Kobayashi
26. T. Kosuge
27. L. Ohmi
28. M. Suzuki
29. J. Y. Choi
30. S. Ohsawa
31. N. Nakamura
32. Y. Otake
33. D. Cookson
34. K. Kobayashi
35. H. Katagiri
36. T. Nogami
37. T. Suwada
38. T. Koide
39. M. Isawa
40. S. Kishimoto
41. H. Maezawa
42. Y Amemiya
43. M. Tanaka
44. M. Nomura
45. K. Ohsumi
46. T. Yokoo
47. T. Kurihara
48. C.O. Pak
49. S. Asaoka
50. K. Tsuchiya
51. A. Ueda
52. T. Honda
53. N. Watanabe
54. T. Kikuchi
55. Y. Kitajima
56. N. Nakajima
57. K. Haga
58. A. Koyama
59. H. Sugiyama
60. K. Hirano
61. T. Urano
62. T. Mori
63. A. Kikuchi
64. M. Kimura
65. K. Ouchi
66. T. Shidara
67. N. Tomita
68. K. Ito
69. K. Iwano
70. A. Mishina
71. M. Noji

PREFACE

It is my pleasure to present the Photon Factory Activity Report No. 13, covering the period from October 1994 to September 1995, which was a very productive year both in terms of user's research and facility development. This was the 13th year of operation for the 2.5 GeV storage ring which became an extremely reliable light source demonstrating as high performace as ever with 370 mA ring current, life-time of 60 hours and emittance of 130 nmrad in the normal multi-bunch operation. In order to further reduce the emittance and remain competitive with the third genaration rings, design work for a major modification, the "High Brilliance Project" was pursued. In addition, efforts to replace some of the older out-dated beamlines with new state-of-the-art beamlines ("Scrap-and-build" projects) made substantial progress. User's research was extremely active with 399 proposals approved in 1995. High-lights of the activities in various fields are summarized in this volume.

Research with parasitic synchrotron radiation operation of the TRISTAN Accumulation Ring (AR) was also acitively pursued. Design work to convert the AR after the termination of the TRISTAN project into a dedicated synchrotron radiation source, characterized by high energy photons and single bunch operation, made progress.

Further facility development projects pursued this year include the TRISTAN Super Light Faclity (TSLF) project which involves a three months experimental operation of the TRISTAN Main Ring for synchrotron radiation, the VUV-Free Electron Laser project, the Slow-positron Source for materials science research, and the upgrade of the injector linac for the KEKB project.

Finally, I would like to note that discussions have been in progress regarding a substantial change in the administrative structure of the laboratory. This involves the reorganization and upgrade of the Photon Factory "facility" into an independent laboratory with the addition of a neutron-based research section. It is my sincere hope that this organizational development will provide a great boost to the future progress of synchrotron radiation research.

Motohiro Kihara
Director, Photon Factory

Acknowledgments

The editors would like to thank Ms. Miyako Kimura and Mrs. Sumie Imai for their help in editing this issue.

KEK Progress Report 96-3 A/M

KEK Reports are available from:

Technical Information & Library
National Laboratory for High Energy Physics
1-1 Oho, Tsukuba-shi
Ibaraki-ken, 305
JAPAN

Phone: +81-298-64-5136
Fax: +81-298-64-4604
e-mail: LIBRARY@KEKVAX.KEK.JP
URL. (Internet): http://www.kek.jp
Telex: 3652-534 (Domestic)
(0)3562-534 (International)
Cable: KEKOHO

You can jump to the article by clicking its title.

CONTENTS

OUTLINE OF THE PHOTON FACTORY

INTRODUCTION

The Photon Factory (PF) is a national synchrotron radiation research facility affiliated with the National Laboratory for High Energy Physics (KEK), supervised by the Ministry of Education, Science and Culture. It is located at the northern end of Tsukuba Science City, which is about 60 km north-east of Tokyo. The PF consists of a 2.5-GeV electron/positron linear accelerator, a 2.5-GeV electron/positron storage ring as a dedicated light source, TRISTAN accumulation ring as a parasitic light source and beamlines and experimental stations for exploiting synchrotron radiation in studies involving research fields such as physics, chemistry, biology, medical sciences, pharmacology, earth sciences and lithography. All of the facilities for synchrotron radiation research are open to scientists of universities and research institutes belonging to the government, public organizations, private enterprises and those of foreign countries. The members of institutions affiliated with the Ministry of Education, Science and Culture are given the highest priority among all users. Applications from other organizations are also accepted.

OVERVIEW OF THE FACILITY

The plan view of the facility is shown in Fig. 1. The 2.5-GeV linac housed in a 450 m long enclosure is used as an injector for both the PF storage ring and the accumulation ring (AR) of the TRISTAN main ring. The PF storage ring was already equipped with the flexibility of storing positrons in place of electrons. Parasitic operation of the AR has been used as a high energy synchrotron radiation source has been going on with its bending magnets and two insertion devices. One of the insertion devices produces elliptically polarized radiation, and the other produces high brilliance radiation in the X-ray region. The AR has been operated for synchrotron radiation users with an energy range from 5.8 to 6.5 GeV.

ORGANIZATION AND STAFF

The organization of KEK is shown in Fig. 2. The PF consists of three divisions: Injector Linac, Light Source and Instrumentation. In addition, a project team has been pursuing the usage of the TRISTAN Main Ring for synchrotron radiation science. The organization of the PF including its personnel is shown in Fig. 3. The Advisory Council for the PF was established to discuss scientific programs and management of the PF. The council consists of twenty-one senior scientists including ten non-KEK members (Tables 1a and 1b). The term of membership is two years. The Program Advisory Committee (PAC) consists of the members listed in Tables 2a and 2b. They receive proposals from users and decide priorities for the experiments.

In Table 3 the names of the staff members are listed in alphabetical order. Also, the numbers of staff members and visiting scientists are summarized in Table 4.

BUDGET AND OPERATION TIME

The budget of the PF is provided by the Ministry of Education, Science and Culture. The annual budget after commissioning of the facilities is shown in Table 5. The numbers of beam channels in each year are shown in Table 6.

The machine operation time is divided into three terms per year. Summary and timetable of the machine operation in FY 1995 are shown in Tables 7 and 8, respectively.

In Table 9, we have shown the total number of proposals approved by the aforementioned PAC.

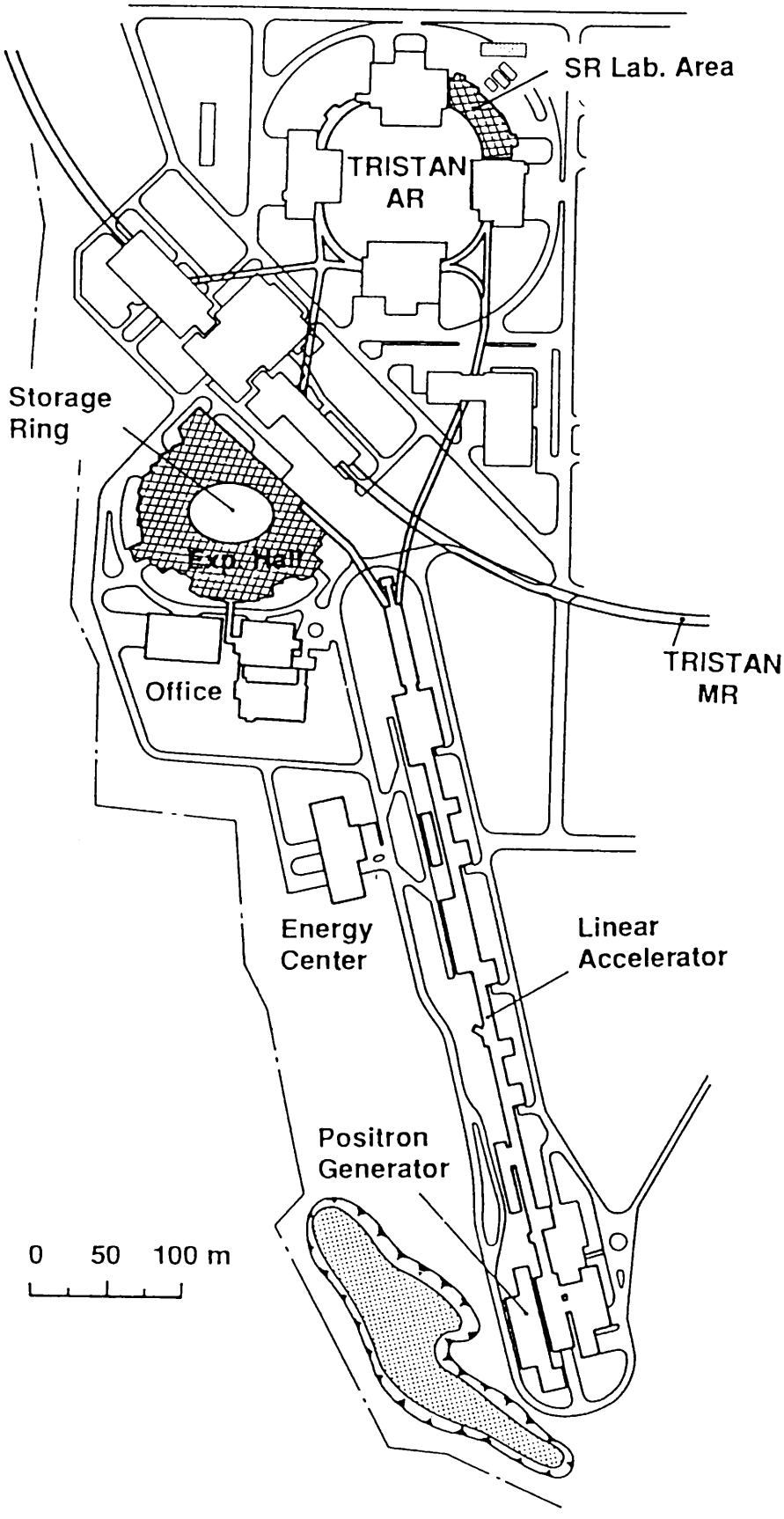

Fig. 1 Plan view of the Photon Factory

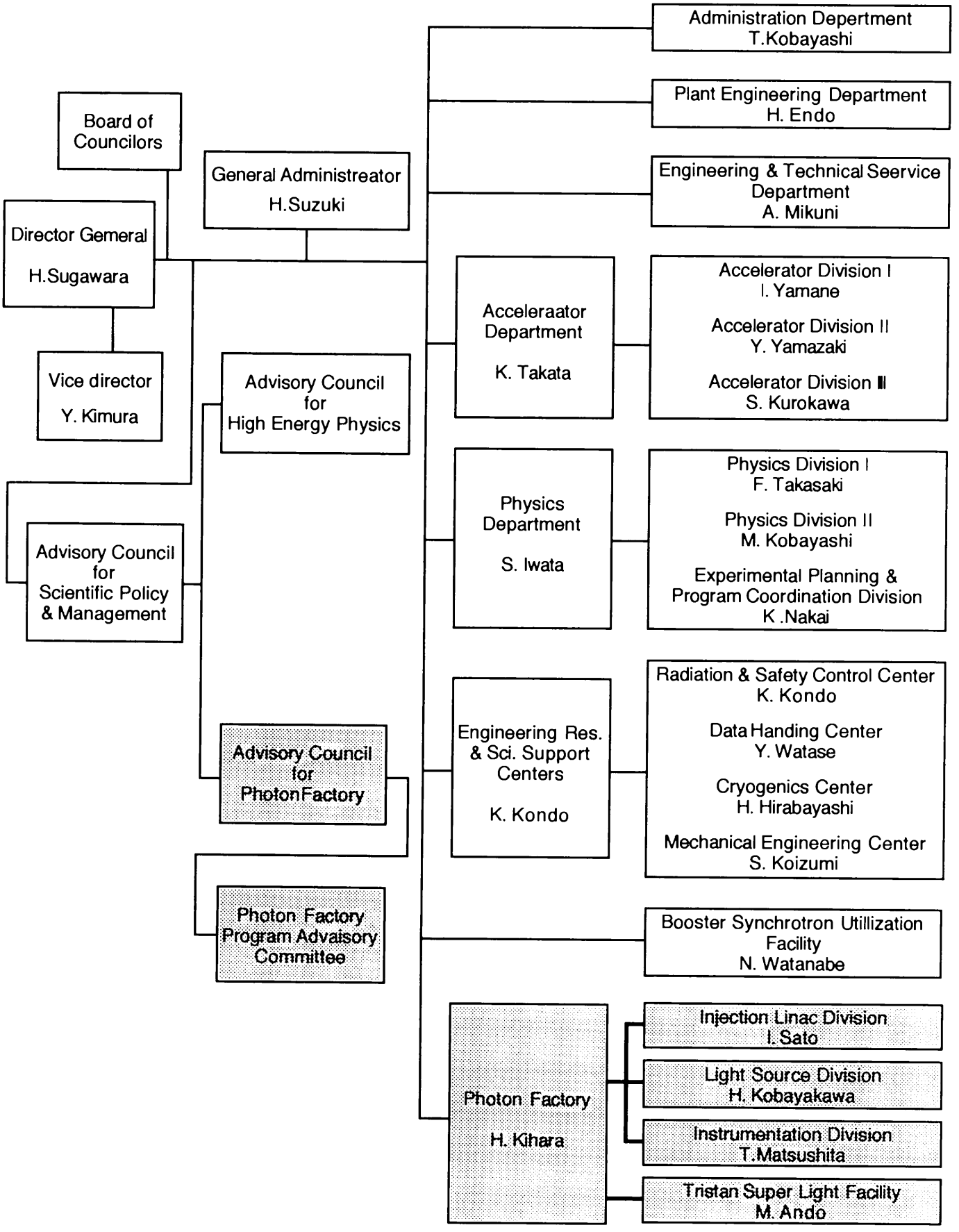

Fig. 2 Organization of KEK

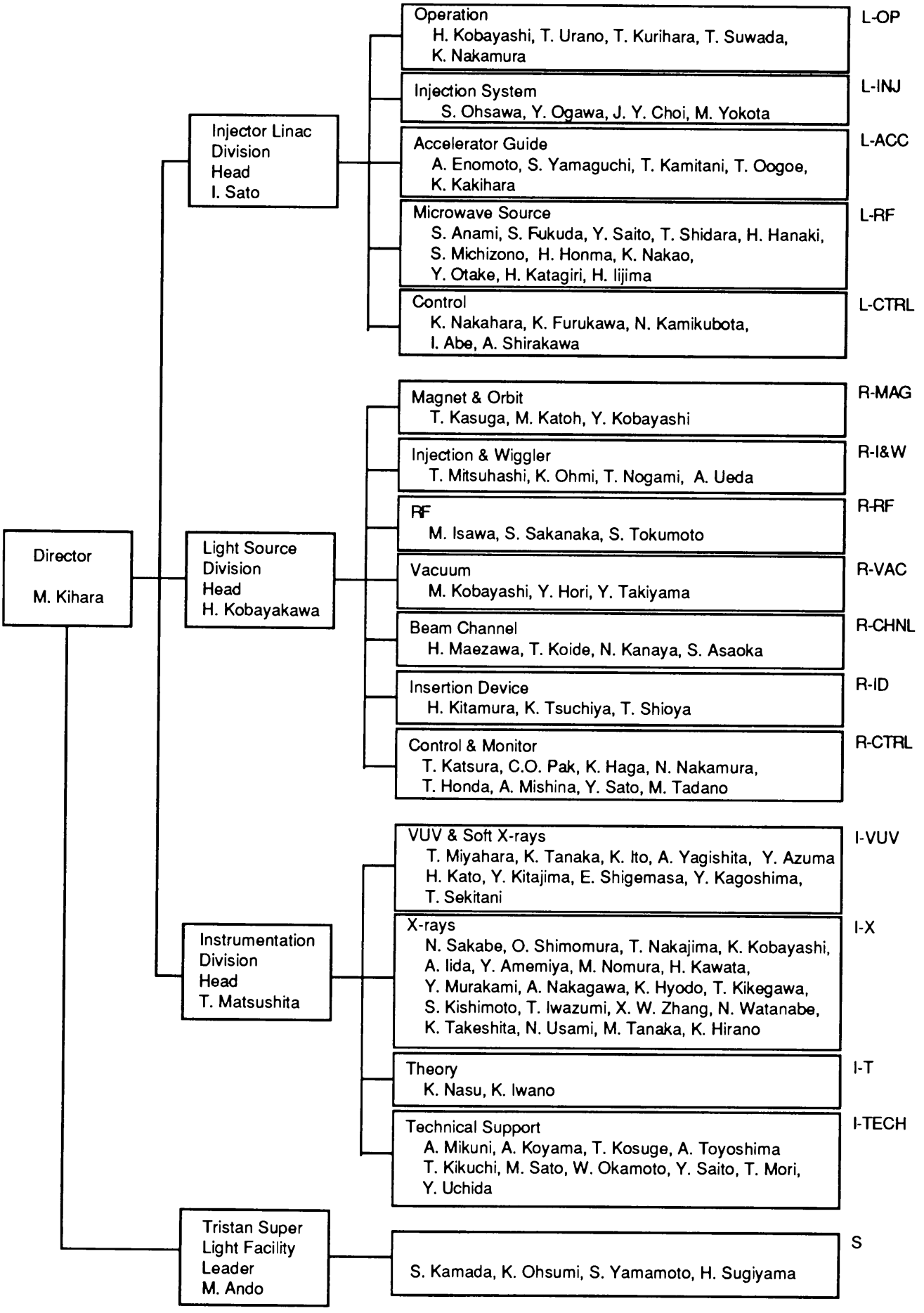

Fig. 3 Organization of the Phton Factory

Table 1a Members of Advisory Council; April '94 ~ March '96

** Chairman * Vice-Chairman

ANAMI, Shozo	Injector Linac Division, PF, KEK
ANDO, Masami	Tristan Super Light Facility, PF, KEK
FUJII, Yasuhiko	Institute for Solid State Physics, University of Tokyo
HIEDA, Kotaro	Faculty of Science, Rikkyo University
ISHII, Takehiko*	Institute for Solid State Physics, University of Tokyo
ITO, Kenji	Instrumentation Division, PF, KEK
KIKUTA, Seishi	Faculty of Engineering, University of Tokyo
KOBAYAKAWA, Hisashi	Light Source Division, PF, KEK
KOBAYASHI, Masanori	Light Source Division, PF, KEK
MAEZAWA, Hideki	Light Source Division, PF, KEK
MATSUSHITA, Tadashi	Instrumentation Division, PF, KEK
MITSUI, Yukio	Department of Bio Engineering, Nagaoka University of Technology
NAKAHARA, Kazuo	Injector Linac Division, PF, KEK
NAKAJIMA, Tetsuo	Instrumentation Division, PF, KEK
NITTONO, Osamu	Faculty of Engineering, Tokyo Institute of Technology
OHTA, Toshiaki	Faculty of Science, University of Tokyo
SATO, Isamu**	Injector Linac Division, PF, KEK
SHIMOMURA, Osamu	Instrumentation Division, PF, KEK
SHIOTANI, Nobuhiro	Tokyo University of Fisheries
SUGA, Shigemasa	Faculty of Engineering Science, Osaka University
SUZUKI, Kenji	Institute for Materials Research, Tohoku University

Table 1b Members of Advisory Council; April '96 ~ March '98

** Chairman * Vice-Chairman

ANAMI, Shozo	Injector Linac Division, PF, KEK
FUJII, Yasuhiko	Institute for Solid State Physics, University of Tokyo
HIEDA, Kotaro	Faculty of Science, Rikkyo University
IIDA, Atsuo	Instrumentation Division, PF, KEK
ITO, Kenji	Instrumentation Division, PF, KEK
KASUGA, Toshio	Light Source Division, PF, KEK
KIKUTA, Seishi	Faculty of Engineering, University of Tokyo
KOBAYAKAWA, Hisashi	Light Source Division, PF, KEK
KOBAYASHI, Hitoshi	Injector Linac Division, PF, KEK
KOBAYASHI, Masanori	Light Source Division, PF, KEK
MAEZAWA, Hideki	Light Source Division, PF, KEK
MATSUSHITA, Tadashi	Instrumentation Division, PF, KEK
MITSUI, Yukio	Department of Bio Engineering, Nagaoka University of Technology
NAKAHARA, Kazuo	Injector Linac Division, PF, KEK
OHTA, Toshiaki	Faculty of Science, University of Tokyo
OSHIMA, Masaharu	Faculty of Engineering, University of Tokyo
SATO, Shigeru	Faculty of Scinece, Tohoku University
SHIMOMURA, Osamu	Instrumentation Division, PF, KEK
SHIOTANI, Nobuhiro	Tokyo University of Fisheries
SUGA, Sigemasa	Faculty of Engineering Science, Osaka University
WAKABAYASHI, Katsuzo	Faculty of Engineering Science, Osaka University

Table 2a Members of Program Advisory Committee; Fiscal Year '94

* Chairman

ASHIDA, Tamaichi	School of Engineering, Nagoya University
KOBAYAKAWA, Hisashi	Light Source Division, PF, KEK
KOSUGI, Nobuhiro	Institute for Molecular Sicnece, Okazaki Nat'l Research Institute
MATSUSHITA, Tadashi*	Instrumentation Division, PF, KEK
NASU, Keiichiro	Instrumentation Division, PF, KEK
OYANAGI, Hiroyuki	Electrotechnical Laboratory
SAKAI, Nobuhiko	Faculty of Science, Himeji Institute of Technology
SAKATA, Makoto	School of Engineering, Nagoya University
SATO, Isamu	Injector Linac Division, PF, KEK
SATO, Yukinori	Research Institute for Scientific Measurements, Tohoku Univ.
TANAKA, Nobuo	Faculty of Bioscience and Biotechnology, Tokyo Institute of Technology
TANIGUCHI, Masaki	Faculty of Science, Hiroshima University
TSUJI, Kazuhiko	Faculty of Science and Technology, Keio University
UEKI, Tatsuo	Institute of Physical and Chemical Research
WAKABAYASHI, Katsuzo	Faculty of Engineering Science, Osaka University

Table 2b Members of Program Advisory Committee; Fiscal Year '95

* Chairman

ASHIDA, Tamaichi	School of Engineering, Nagoya University
JO, Takeo	Faculty of Science, Hiroshima University
KAKIZAKI, Akito	Institute for Solid State Physics, University of Tokyo
KATAOKA, Mikio	Faculty of Science, Osaka University
KOBAYAKAWA, Hisashi	Light Source Division, PF, KEK
MATSUSHITA, Tadashi*	Instrumentation Division, PF, KEK
OHSUMI, Kazumasa	Instrumentation Division, PF, KEK
OYANAGI, Hiroyuki	Electrotechnical Laboratory
SAKAI, Nobuhiko	Faculty of Science, Himeji Institute of Technology
SATO, Isamu	Injector Linac Division, PF, KEK
SATO, Yukinori	Research Institute for Scientific Measurements, Tohoku Univ.
TSUJI, Kazuhiko	Faculty of Science and Technology, Keio University
TSUKIHARA, Tomitake	Institute for Protein Research, Osaka University
YAMAMGUCHI, Toshio	Faculty of Science, Fukuoka University
WAKABAYASHI, Katsuzo	Faculty of Engineering Science, Osaka University

Table 3 Staff members of the Photon Factory

Name		Responsibility*	e-mail address
Research Staff			
KIHARA, Motohiro		Director	KIHARAM@KEKVAX.KEK.JP
ANAMI, Shozo		L-RF	ANAMI@KEKVAX.KEK.JP
CHOI, Jae-Young		L-INJ	CHOIJ@KEKVAX.KEK.JP
ENOMOTO, Atsushi		L-ACC	ENOMOTOA@KEKVAX.KEK.JP
FUKUDA, Shigeki		L-RF	SFUKUDA@KEKVAX.KEK.JP
FURUKAWA, Kazuro		L-CTRL	FURUKAWA@KEKVAX.KEK.JP
HANAKI, Hirofumi		L-RF	HANAKI@KEKVAX.KEK.JP
KAMIKUBOTA, Norihiko		L-CTRL	KAMI@KEKVAX.KEK.JP
KAMITANI, Takuya		L-ACC	KAMITANI@KEKVAX.KEK.JP
KOBAYASHI, Hitoshi		L-OP	HITOSHIK@KEKVAX.KEK.JP
KURIHARA, Toshikazu		L-OP	TKURIHAR@KEKVAX.KEK.JP
MICHIZONO, Shin'ichiro		L-RF	MICHIZON@KEKVAX.KEK.JP
NAKAHARA, Kazuo		L-Head	NAKAHAR@KEKVAX.KEK.JP
OGAWA, Yujiro		L-INJ	OGAWAYJ@KEKVAX.KEK.JP
OHSAWA, Satoshi		L-INJ	OHSAWA@KEKVAX.KEK.JP
SAITO, Yoshio		L-RF	
SATO, Isamu	Mar. 31, 96 R	L-Head	
SHIDARA, Tetsuo		L-RF	SHIDARA@KEKVAX.KEK.JP
SUWADA, Tsuyoshi		L-OP	SUWADA@KEKVAX.KEK.JP
URANO, Takao		L-OP	URANO@KEKVAX.KEK.JP
YAMAGUCHI, Seiya		L-RF	SYAMA@KEKVAX.KEK.JP
HAGA, Kaiichi		R-CTRL	HAGA@KEKVAX.KEK.JP
HONDA, Tohru		R-CTRL	HONDAT@KEKVAX.KEK.JP
HORI, Yoichiro		R-VAC	HORI@KEKVAX.KEK.JP
ISAWA, Masaaki		R-RF	ISAWA@KEKVAX.KEK.JP
KANAYA, Noriichi		R-CHNL	KANAYA@KEKVAX.KEK.JP
KASUGA, Toshio		R-MAG	KASUGAT@KEKVAX.KEK.JP
KATOH, Masahiro		R-MAG	KATOHM@KEKVAX.KEK.JP
KATSURA, Tomotaro		R-CTRL	KATSURA@KEKVAX.KEK.JP
KITAMURA, Hideo		R-ID	
KOBAYAKAWA, Hisashi		R-Head	KOBAYAKA@KEKVAX.KEK.JP
KOBAYASHI, Masanori		R-VAC	KOBYASIMR@KEKVAX.KEK.JP
KOBAYASHI, Yukinori		R-MAG	YUKINORI@KEKVAX.KEK.JP
KOIDE, Tsuneharu		R-CHNL	
MAEZAWA, Hideki		R-CHNL	MAEZAWAH@KEKVAX.KEK.JP
MITSUHASHI, Toshiyuki		R-I&W	MITSUHAS@KEKVAX.KEK.JP
NAKAMURA, Norio	Mar. 1, 96 L	R-CTRL	NORIO@KEKVAX.KEK.JP
OHMI, Kazuhito		R-I&W	OHMI@KEKVAX.KEK.JP
PAK, Cheol On		R-CTRL	PAK@KEKVAX.KEK.JP
SAKANAKA, Shyogo		R-RF	SAKANAKA@KEKVAX.KEK.JP
TSUCHIYA, Kimichika		R-ID	TSUCHIYA@KEKVAX.KEK.JP
AMEMIYA, Yoshiyuki	Apr. 1, 96 L	I-X	AMEMIYA@KEKVAX.KEK.JP
AZUMA, Yoshiro		I-VUV	AZUMA@KEKVAX.KEK.JP
HIRANO, Keiichi		I-X	HIRANO@KEKVAX.KEK.JP
HYODO, Kazuyuki		I-X	HYODO@KEKVAX.KEK.JP
IIDA, Atsuo		I-X	AIIDA@KEKVAX.KEK.JP
ITO, Kenji		I-VUV	ITO@KEKVAX.KEK.JP
IWANO, Kaoru		I-T	IWANO@KEKVAX.KEK.JP
IWAZUMI, Toshiaki		I-X	IWAZUMI@KEKVAX.KEK.JP
KAGOSHIMA, Yasushi		I-VUV	KAGOSIMA@KEKVAX.KEK.JP
KATO, Hiroo		I-VUV	HIROO@KEKVAX.KEK.JP
KAWATA, Hiroshi		I-X	KAWATA@KEKVAX.KEK.JP
KIKEGAWA, Takumi		I-X	KIKEGAWA@KEKVAX.KEK.JP
KISHIMOTO, Syunji		I-X	KISIMOTO@KEKVAX.KEK.JP
KITAJIMA, Yoshinori		I-VUV	KITAJIMA@KEKVAX.KEK.JP

(continued)

Name		Responsibility*	e-mail address
KOBAYASHI, Katsumi		I-X	KOBAYASK@KEKVAX.KEK.JP
MATSUSHITA, Tadashi		I-Head	MATSUS@KEKVAX.KEK.JP
MIYAHARA, Tsuneaki		I-VUV	MIYAHARA@KEKVAX.KEK.JP
MURAKAMI, Youichi		I-X	MYOUICHI@KEKVAX.KEK.JP
NAKAGAWA, Atsushi	May. 1, 95 L	I-X	NAKAGAWA@KEKVAX.KEK.JP
NAKAJIMA, Tetsuo	Mar. 31, 96 R	I-X	TETSUO@KEKVAX.KEK.JP
NASU, Keiichiro		I-T	KNASU@NASUWS1.KEK.JP
NOMURA, Masaharu		I-X	NOMURAM@KEKVAX.KEK.JP
SEKITANI,Tetsuji	Apr. 1, 95 L	I-VUV	SEKITANI@KEKVAX.KEK.JP
SHIGEMASA, Eiji		I-VUV	SIGEMASA@KEKVAX.KEK.JP
SHIMOMURA, Osamu		I-X	SHIMOMURA@KEKVAX.KEK.JP
SUZUKI, Mamoru	Apr. 1, 95 J	I-X	SUZUKI@PFWEIS.KEK.JP
TAKESHITA, Kunikazu		I-X	TAKESHIT@KEKVAX.KEK.JP
TANAKA, Ken'ichiro	Apr. 1, 95 L	I-VUV	TANAKAK@KEKVAX.KEK.JP
TANAKA, Masahiko		I-X	MASAHIKO@KEKVAX.KEK.JP
TOMITA, Norikazu	Nov. 1, 95 J	I-T	TOMITA@NASUWS4.KEK.JP
USAMI, Noriko		I-X	USAMI@KEKVAX.KEK.JP
WATANABE, Nobuhisa		I-X	NOBUHISA@KEKVAX.KEK.JP
YAGISHITA, Akira		I-VUV	YAGISITA@KEKVAX.KEK.JP
ZHANG, Xiaowei		I-X	XIAOWEI@KEKVAX.KEK.JP
ANDO, Masami		S-Leader	ANDO@KEKVAX.KEK.JP
KAMADA, Susumu		S	KAMADA@KEKVAX.KEK.JP
OHSUMI, Kazumasa		S	OHSUMIK@KEKVAX.KEK.JP
SUGIYAMA, Hiroshi		S	HIROSHIS@KEKVAX.KEK.JP
YAMAMOTO, Shigeru		S	SHIGERU@KEKVAX.KEK.JP
Supporting Staff			
ABE, Isamu		L-CTRL	ABEI@KEKVAX.KEK.JP
HONMA, Hiroyuki		L-RF	
IIJIMA, Hitoshi		L-RF	
KAKIHARA, Kazuhisa		L-ACC	KAKIHARA@KEKVAX.KEK.JP
KATAGIRI, Hiroaki		L-RF	KATAGIRI@KEKVAX.KEK.JP
NAKAMURA, Kie		L-OP	KIE@KEKVAX.KEK.JP
NAKAO, Katsumi		L-RF	NAKAOK@KEKVAX.KEK.JP
OOGOE, Takao		L-ACC	OOGOE@KEKVAX.KEK.JP
OTAKE, Yuji	Apr. 1, 96 L	L-OP	OTAKE@KEKVAX.KEK.JP
SHIRAKAWA, Akihiro		L-CTRL	SIRAKAWA@KEKVAX.KEK.JP
YOKOTA, Mitsuhiro		L-INJ	YOKOTA@KEKVAX.KEK.JP
ASAOKA, Seiji		R-CHNL	
MISHINA, Atsushi		R-CTRL	MISHINA@KEKVAX.KEK.JP
NOGAMI, Takashi		R-I&W	NOGAMI@KEKVAX.KEK.JP
SATO, Yoshihiro		R-CTRL	YOSHIHIR@KEKVAX.KEK.JP
SHIOYA, Tatsuro		R-ID	SHIOYA@KEKVAX.KEK.JP
TADANO, Mikito		R-CTRL	TADANO@KEKVAX.KEK.JP
TAKIYAMA, Youichi		R-VAC	TAKIYAMA@KEKVAX.KEK.JP
TOKUMOTO, Shuichi		R-RF	TOKUMOTO@KEKVAX.KEK.JP
UEDA, Akira		R-I&W	UEDA@KEKVAX.KEK.JP
KIKUCHI, Takashi		I-TECH	KIKUCHI@KEKVAX.KEK.JP
KOSUGE, Takashi		I-TECH	KOSUGE@KEKVAX.KEK.JP
KOYAMA, Atsushi		I-TECH	KOYAMA@KEKVAX.KEK.JP
MIKUNI, Akira		I-TECH	MIKUNI@KEKVAX.KEK.JP
MORI, Takeharu		I-TECH	MORIT@KEKVAX.KEK.JP
OKAMOTO, Wataru		I-TECH	OKAMOTOW@KEKVAX.KEK.JP
SAITO, Yuuki		I-TECH	YSAITO@KEKVAX.KEK.JP
SATO, Masato		I-TECH	SATOM@KEKVAX.KEK.JP
TOYOSHIMA, Akio		I-TECH	TOYOSIMA@KEKVAX.KEK.JP
UCHIDA, Yoshinori		I-TECH	UCHIDA@KEKVAX.KEK.JP

*: Refer to Fig. 3 for abbreviations.
J: Date when he/she joinded the PF.
L: Date when he/she left the PF.
R: Date when he/she retired from the PF.

Table 4 Annual numbers of staff & visiting scientists

Position	Department	1985	1986	1987	1988	1989	1990	1991	1992	1993	1994	1995
Chief Director		1	1	1	1	1	1	1	1	1	1	1
	Injector Linac	3	4	4	4	3	3	4	3	3	3	4
Professor	Light Source	3	4	4	4	4	5	5	4	5	5	5
	Instrumentation	2	3	4	5	5	5	6	8	9	8	8
Associate	Injector Linac	2	1	2	3	5	7	6	7	7	7	6
Professor	Light Source	5	3	3	3	5	4	3	3	3	3	3
	Instrumentation	8	7	9	7	10	9	8	10	10	11	10
Research	Injector Linac	10	11	10	10	9	8	9	9	9	10	10
Associate	Light Source	8	9	12	12	9	11	11	12	12	12	12
	Instrumentation	10	13	13	14	11	15	15	15	18	18	17
Technical	Injector Linac	6	7	8	9	10	11	11	11	11	11	10
Staff	Light Source	6	7	7	8	10	10	10	10	10	9	9
	Instrumentation	4	8	9	11	10	9	10	10	10	10	10
Visiting	Injector Linac	2	2	2	2	2	2	2	2	1	0	1
Scientist	Light Source	4	4	4	4	4	4	4	4	3	3	4
	Instrumentation	6	6	6	6	6	6	7	6	6	3	6
Total		80	90	98	103	104	110	112	115	118	114	116

Table 5 Budget in each fiscal year (in million yen)

Item	1985	1986	1987	1988	1989	1990	1991	1992	1993	1994	1995
Salary	510	561	561	642	757	764	859	898	939	1,029	1,163
PF Storage Ring (channel, insertion device, etc.)	153	131	647	0	0	196	103	0	0	0	428
PF Experiments	184	190	196	237	341	367	399	375	366	366	366
PF Operation & Maintenance	653	820	907	962	1,078	1,107	1,107	1,042	1,015	1,096	1,096
Computer Rentals	135	136	136	141	145	145	145	145	145	140	145
Positron Source & Electric Plant Operation	41	138	208	258	300	308	300	253	224	175	157
Cooling System & Electric Operation	180	211	214	217	231	235	240	218	212	218	217
Electricity	338	381	331	355	425	423	423	423	418	431	431
PF-Industrial Cooperative Experiments	95	185	166	302	219	171	174	154	132	86	81
AR Construction and Experiments			398	267	387	250	260	148	145	145	145
B Factory (Linac Upgrade)										400	1,567
Miscellaneous	127	162	120	301	243	287	388	564	877	567	609
Total	2,416	2,915	3,884	3,682	4,126	4,253	4,398	4,220	4,473	4,653	6,405

Table 6 Yearly account of beam channels

Belonging	1985	1986	1987	1988	1989	1990	1991	1992	1993	1994	1995
PF	10	12	13	13	15	15	17	20	21	21	21
Institutes	1	1	3	4	4	4	4	3	2	2	2
Industry	4	4	4	4	4	4	4	4	4	4	4
Total	15	17	20	21	23	23	25	27	27	27	27

Table 7 Summary of operation in FY 1995 (April 1995 - March 1996) (hours)

Cycle	Linac	PF Ring	Users' time	AR	Dedicated to SR at AR
1	1947	1803	1483	1739	1752
2	2568	2520	2048	2160	2136
Total	4515	4323	3531	3899	3888

Table 8 Timetable of the Machine Operation in FY 1995.
PF:PF ring AR:TRISTAN accumulation ring
MR:TRISTAN main ring

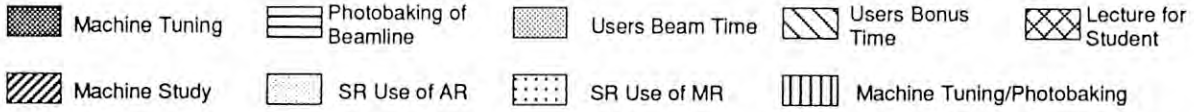

cycle		MON	TUE	WED	THU	FRI	SAT	SUN	MON	TUE	WED	THU	FRI	SAT	SUN	MON	TUE	WED	THU	FRI	SAT	SUN
	Time	9 17	9 17	9 17	9 17	9 17	9 17	9 17	9 17	9 17	9 17	9 17	9 17	9 17	9 17	9 17	9 17	9 17	9 17	9 17	9 17	9 17
1	Date	3/27	28	29	30	31	4/1	2	3	4	5	6	7	8	9	10	11	12	13	14	15	16
	Linac																					
	PF																					
	AR																					
	MR																					
1	Date	17	18	19	20	21	22	23	24	25	26	27	28	29	30	5/1	2	3	4	5	6	7
	Linac																					
	PF																					
	AR																					
	MR																					
1	Date	8	9	10	11	12	13	14	15	16	17	18	19	20	21	22	23	24	25	26	27	28
	Linac																					
	PF																					
	AR																					
	MR																					
1	Date	29	30	31	6/1	2	3	4	5	6	7	8	9	10	11	12	13	14	15	16	17	18
	Linac																					
	PF																					
	AR																					
	MR																					
2	Date	9/11	12	13	14	15	16	17	18	19	20	21	22	23	24	25	26	27	28	29	30	10/1
	Linac																					
	PF																					
	AR																					
	MR																					
2	Date	2	3	4	5	6	7	8	9	10	11	12	13	14	15	16	17	18	19	20	21	22
	Linac																					
	PF																					
	AR																					
	MR																					
2	Date	23	24	25	26	27	28	29	30	31	11/1	2	3	4	5	6	7	8	9	10	11	12
	Linac																					
	PF																					
	AR																					
	MR																					
2	Date	13	14	15	16	17	18	19	20	21	22	23	24	25	26	27	28	29	30	12/1	2	3
	Linac																					
	PF																					
	AR																					
	MR																					
2	Date	4	5	6	7	8	9	10	11	12	13	14	15	16	17	18	19	20	21	22	23	24
	Linac																					
	PF																					
	AR																					
	MR																					
2	Date	25	26	27	28	29	30	31	1/1	2	3	4	5	6	7	8	9	10	11	12	13	14
	Linac																					
	PF																					
	AR																					
	MR																					

SEMINARS, MEETINGS AND WORKSHOPS

Thirty seminars were given by an in-house staff and visiting cientists who visited the PF during the period from October 1994 to September 1995. Seven users' meetings and workshops were held during the same period, including the annual PF symposium.

PF Seminars

Chen, C. T. (AT&T Bell Laboratories) Advanced Soft-X-Ray Spectroscopies and Their Applications	October 20, 1994
Mouri, N. (Institute for Solid State Physics, University of Tokyo) Physics of Solid Under High Pressure	October 20, 1994
Couprie, M. E. (LURE) Status of the Super-ACO FEL	November 4, 1994
Shinohara, K. (University of Lund) Biological Application Soft X-ray Microscopy – Present and Future	November 18, 1994
Leckey, L. (School of Physics, La Trobe University) Angle Resolved Photoemission Using Toroidal Display Analyser	December 16, 1994
Kosugi, N. (Institute for Molecular Science) Vibrational Spectroscopy of Core Excited States of Simple Molecules	December 20, 1994
Sarma, D. D. (Indian Institute of Science) Electronic Structure of and Metal-Insulator Transition in 3d Transition Metal Perovskit Oxides	December 22, 1994
Batterman, B.W. (CHESS, Cornell University) Present Status and Future of CHESS	January 10, 1995
Aberg, T. (Helsinki University of Technology) Inelastic XUV Scattering: The Radiative and Radiationless Channel	January 17, 1995
Shiki, S. (Institute for Solid State Physics, University of Tokyo) Soft X-ray and Raman-scattering Study of Solids	January 20, 1995
Samarey, F. (PF, KEK) Neutron Diffraction Study of Bacteriorhodopsin	February 17, 1995
Lin, C.-D. (Kansas State University) Multiple Excitations in Atoms —A New Perspective	February 21, 1995
K. Tanaka (Faculty of Science, Hiroshima Univ.) Photochemical Surface Reactions Induced by Core-electron Excitation	February 28, 1995
Hamaya, N. (Faculty or Science, Ochanomizu University) Mecanism of Phase Transition in Rare Earth Metals at High Pressure: Structural Approach with the Rietveld Methos	March 17, 1995

Hammersely, A. (ESRF)
Calibration and Testing of an X-ray Image Intensifier/ CCD Read-out Detector, with Application to Monochromatic Protein Crystallography — March 20,1995

Colella, R. (Physics Department, Purdue University)
Multiple Bragg Scattering and the Phase Problem — April 10,1995

Yan, Y. (Institute of High Energy Physics, Chinese Academy of Science)
Design of Soft X-ray Monochromators — April 14, 1995

Schmidt-Böcking, H. (Universität Frankfurt)
What can Atomic Collision Physics Contribute to Future Progress in Physics? — April 19, 1995

Iwano, K. (PF, KEK)
Lopsided Energy Sharing Between a Photoelectron and an Auger Electron in Solids — May 26, 1995

West, J. (RISM, Tohoku University and Daresbury Laboratory)
Molecular Photoionization Experiments at the Daresbury Synchrotron Radiation Source — June 27, 1995

Suzuki, M. (PF, KEK)
Structure Analaysis of Macrophage Migration Inhibitry Factor (MIF) — June 30, 1995

Nakagawa, A. (Gratuate School of Science, Hokkaido University)
Structure Determination of Coenzyme B_{12} Protein, Methylmalonyl-coenzyme A — July 21, 1995

Nagaoka, R. (Light Source Division, Sincrotrone Trieste)
Commissioning and Operation of ELETTRA and Overview of Scientific Activities at the Sincrotrone Trieste — July 27, 1995

Hodgson, K. O. and Hedman, B. M. (Department of Chem. and Stanford Synchrotron Radiation Laboratory, Stanford University)
Recent Development in Structural Molecular Biology Research using Synchrotron at SSRL — August 4, 1995

Manuel, A. A. (Department de Physique de la Matiere Condensee, Universite de Geneve
Fermi Surface Study by Positron Annihilation and Compton Profiles — August 25, 1995

Bell, F. (Sektion Physik, Universitat Munchen)
3D-Electron Momentum Densities by (γ, eγ) Spectroscopy — September 4, 1995

Lama, F. (Instituto di Struttura della Materia)
Construction of the Circular Polarization Baemline in Trieste — September 5, 1995

Hall. R. I. (CNRS & University P et M Curie)
Threshold Photoelectron Spectroscopy of Molecules — September 5, 1995

Cherepkov, N. A. (State Academy of Aerospace Instrumentation, St. Petersburg)
Photoionization of Polarized Atoms and Oriented Molecules — September 13, 1995

Jho, T. (Faculty of Science, Hiroshima University)
— September 22, 1995

Users' Meetings

Powder Diffraction Group Users' Meeting	December 16, 1994
The 12th Photon Factory Symposium (Annual Users' Meeting)	January 12-13, 1995
Workshop on Experiments with Synchrotron Radiation at the TRISTAN MR	February 16-17,1995
Workshop on Generation and Applications of Coherent X-rays	March 4-5, 1995
Lectures on the Elements of Experiments with Synchrotron Radiation	March 15-16, 1995
Workshop on BL2 Soft X-ray Undulator Beamline	July 18, 1995
The 2nd PF Slow-Positron Source Workshop	August 22, 1995

Publications

PHOTON FACTORY NEWS ISSN 0916-0604 Vol.13, No.1-4

GRADUATE UNIVERSITY FOR ADVANCED STUDIES

The Graduate University for Advanced Studies was established in 1988. It has the following three schools:

School of Cultural Studies
School of Mathematical and Physical Sciences
School of Life Sciences.

KEK has participated in the Graduate University to form the Department of Synchrotron Radiation Science and the Department of Accelerator Science, both of which belong to the School of Mathematical and Physical Sciences.

Students in the Department of Synchrotron Radiation Science are expected to study the basic theory of generation of synchrotron radiation, its characteristics, interaction of radiation with matter, and then engage in research by utilizing various facilities at the PF. Areas of thesis research include the development of radiation sources, optical elements, and instruments for diffraction, scattering, spectroscopy, and irradiation experiments as well as exploration of new areas of application of synchrotron radiation to science and technology.

PROPOSAL GUIDELINES FOR EXPERIMENTERS AT PHOTON FACTORY

1. HOW TO SUBMIT A PROPOSAL

Photon Factory is open to everybody in scientific research. A proposal should be filed on an application form which is available on request from the Research Cooperation Section of the Administration Department of KEK. An applicant should carefully read the guide before filing an application. A spokesperson should get the agreement of the members to join the team.

An overseas applicant is requested to find an appropriate "contact person in Japan (CPJ)", who will mediate between the applicant and KEK*. Please contact the person in charge of the experimental station you want to use, if you do not know any appropriate CPJ. He/she will select the person appropriate for the applicant's research plan. A list of the people in charge of the experimental stations can be found in this report.

All experimental proposals are subject to approval of the Photon Factory Program Advisory Committee (PF-PAC). In Table 9, we have shown the total number of proposals approved by this PAC. The CPJ will be informed about the decision.

* The contact person in Japan will help you translate Japanese and English, assist with visa applications and your experiments. In order to assure his/her agreement the signature or seal imprint of the CPJ is required.

2. CATEGORY OF PROPOSALS

2.1 for university researchers etc.

There are four categories of application; G(eneral), S(pecial), P(reliminary) and U(rgent). The character, process of approval and terms of validity are different among those categories.

G is the category for general experiments using synchrotron radiation. Deadlines of application and valid terms are as follows:

Deadlines: May 2, 1997 (a) and November 7, 1997 (b)

Valid terms:

from October, 1997 to September, 1999 for (a)
from April, 1998 to March, 2000 for (b)

P is the category for preliminary experiments in order to determine the feasibility of proposals for categories G or S and for the new comers in this field. There are some limitations as listed below.

1) The maximum beamtime for one project is less than about 120 hours.
2) One spokesperson can have only one project at a time.
3) More than three proposals of this category cannot be approved for an experimental station at a PF-PAC.

Deadlines: May 2, 1997 (a) and November 7, 1997 (b)

Valid terms:

from October, 1997 to September, 1998 for (a)
from April, 1998 to March, 1999 for (b)

S is the special category for those experiments that may have extremely high scientific value and may need much machine time. Among those could be experiments for the development of a difficult technique or those requiring special operation of the storage ring. Photon Factory supports the projects of this category financially within certain limits; the funds cannot be used for travel expenses or salary. At least one Japanese scientist should be included in a team. The process of judgement is different from other categories. An applicant has to present his/her proposal orally before the PF-PAC. Deadline and valid term are as follows:

Deadline: March 21, 1997 (a) and September 19, 1997 (b)

Valid term:

from Octorber, 1997 to September, 2000 for (a)
from April, 1998 to March, 2001 for (b)

The progress report should be presented at the "Photon Factory Symposium" which takes place every year.

U is the category for urgent proposals which cannot be postponed until the next deadline, and which are of extremely high scientific value. Once approved, these projects may exclude already assigned beamtime for other projects. Applicants can apply at any time but the valid terms are limited as follows:

a project approved between October and March: until end of March
a project approved between April and September: until end of September.

Results of a project should be reported at the "Photon Factory Symposium."

2.2 for researchers in private companies etc.

Photon Factory is also open for scientists working in private corporations within certain limits. However, a fee is charged for beamtime.

3. ACCOMMODATION

KEK provides guest houses at low cost for visiting scientists. In the case of domestic experimenters, please contact the person in charge of your experimental station. Overseas experimenters should ask the CPJ to book rooms. KEK supports travel and living expenses for domestic experimenters within certain limits but does not do so for overseas experimenters.

4. OTHERS

(1) Experimenters must obey the safety rules at KEK and PF.
(2) Further procedure may be requested in order to carry out an experiment.
(3) If there are question regarding procedures please contact
Research Cooperation Section, Administration Department, National Laboratory for High Energy Physics,
Oho, Tsukuba 305, Japan
FAX: +81-298-64-4602

Table 9 Number of proposals approved by the PAC.

Research Field	1983	1984	1985	1986	1987	1988	1989	1990	1991	1992	1993	1994	1995
(A) EXAFS	42	26	35	40	61	66	57	71	69	67	81	75	85
(B) Biology	18	18	28	28	32	38	57	61	75	89	92	121	121
(C) X-Ray	24	29	75	54	73	65	61	80	92	109	111	134	127
(D) VUV & Soft X-Ray	19	12	27	26	28	28	36	27	45	44	55	52	66
Total	103	85	165	148	194	197	211	239	281	309	339	382	399

List of proposals accepted in FY 1995

Proposal Number	Spokesperson	Title
95-G001	Y. Iwasawa Graduate School of Science, Univ. of Tokyo	The study of the interaction of metal particles on the support by PTRF-EXAFS at low temperature
95-G002	Y. Iwasawa Graduate School of Science, Univ. of Tokyo	Design of active site for selective oxidation of alkane utilizing the ensemble of main group elements and noble metals
95-G003	N. Toshima Faculty of Engineering, Univ. of Tokyo	Structural analysis of noble metal/light transition metal bimetallic clusters by EXAFS
95-G004	M. Ichikawa Catalysis Research Center, Hokkaido Univ.	Ship-in-bottle synthesis of non-heme metal sulfide clusters in zeolite and their EXAFS analysis
95-G006	Y. Izumi Graduate School at Nagatsuta, Tokyo Institute of Technology	Electrochemical synthesis of Pd and Ru Clusters on fullerene: structures and catalysis
95-G007	M. Anpo College of Engineering, Univ. of Osaka Prefecture	XAFS studies on photocatalysts (Ti, V, Mo) included in the framework of zeolites
95-G009	G. S. Yong Department of Chemical Engineering, Yonsei Univ.	In-situ EXAFS study on the nucleation and growth of supported metal (Ni) catalysis
95-G010	T. Yamaguchi Faculty of Science, Fukuoka Univ.	Concentration effect on hydration number of lanthanoid (III) ions by XAFS
95-G011	Y. Takasu Faculty of Textile Science and Technology, Shinshu Univ.	EXAFS analysis of the structure of noble metal oxides with low crystalinity
95-G012	S. Yanagida Faculty of Engineering, Osaka Univ.	Surface structure of quantum-confined ZnS, CdS nanocrystallites in solution
95-G013	T. Ohta Graduate School of Science, Univ. of Tokyo	In situ XAFS studies of Co_3O_4 and $NiCo_2O_4$ film electrodes
95-G014	M. Matsuo College of Arts and Sciences, Univ. of Tokyo	XAFS study on chemical states of metallic elements at solid-liquid interface
95-G015	T. Nakato Hokkaido Univ.	XAFS analysis of layered niobates and titanates intercalated with a ruthenium complex
95-G016	I. Nakai Faculty of Science, Science Univ. of Tokyo	XAFS study of sulfur and iodine extraordinary accumulated in marine animals
95-G017	I. Nakai Faculty of Science, Science Univ. of Tokyo	Archaeological study of historical objects excavated in Kaman Kalehoyuk by XAFS analyses

Proposal Number	Spokesperson	Title
95-G018	Y. Kawamoto Faculty of Science, Kobe Univ.	Local structure around rare earth ions in sulfide glasses
95-G019	H. Maruyama Faculty of Science, Okayama Univ.	*In situ* XAFS measurements on order-disorder phase transition in Cu_3Au
95-G020	S. Iwata School of Engineering, Nagoya Univ.	Structure analysis of non-equilibrium AuFe and AuCo ordered alloy films grown by MBE
95-G022	I. Nakai Faculty of General Education, Tottori Univ.	Local structure and magnetism of amorphous alloys Y-TM
95-G024	S. Tsunashima School of Engineering, Nagoya Univ.	The influence of iron structure on magneto optical effect of rare earth transition metal multilayers
95-G025	J. Kawamura Faculty of Science, Hokkaido Univ.	Local structure around mobile ions organic-inorganic mixed superionic conductor grasses
95-G026	A. Kolobov ETL, JRCAT-NAIR	In situ EXAFS study of the structure of, and light-induced changes in, nanostructures of amorphous chalcogenides
95-G027	H. Kageyama Government Industrial Research Institute, Osaka	XAFS analysis of nonlinear-optical materials dispersed with ultrafine metallic particles prepared by ion implantation
95-G028	M. Matsuura Miyagi National College of Technology	Local structure change of ZrYAlNi amorphous alloys with two glass transition
95-G029	A. Yoshiasa Faculty of Science, Osaka Univ.	A study on anharamonic vibrations in AgI by I K-edge EXAFS
95-G030	H. Kawazoe Research Lab. of Engineering Materials, Tokyo Institute of Technology	Analysis of chemical state of Tl in $Tl_2Nb_2O_{6+\delta}$ by X-ray absorption spectroscopy
95-G031	S. Takeda Faculty of Science, Kyushu Univ.	Local structure of molten IIIb-Te mixtures
95-G033	K. Koto Faculty of Integrated Arts and Sciences, Tokushima Univ.	EXAFS study of oxide proton conductors with perovskite-type structure
95-G034	K. Tamura Faculty of Integrated Arts and Sciences, Hiroshima Univ.	The local structure of liquid Ge
95-G035	M. Inui Faculty of Integrated Arts and Sciences, Hiroshima Univ.	The local structure of molten AgBr-AgI mixtures

Proposal Number	Spokesperson	Title
95-G038	T. Matsui School of Engineering, Nagoya Univ.	EXAFS study on local structures of perovskite and pyrochlore-type oxides
95-G039	M. Wakaki School of Science, Tokai Univ.	EXAFS study for the structure parameters of spinel type compounds
95-G040	T. Usuki Faculty of Science, Yamagata Univ.	Short-range order of chalcogenide and chalcohalide glasses
95-G041	S. Yanagida Faculty of Engineering, Osaka Univ.	In-situ investigation of electronic/morphological structure of Nd complex in solution
95-G042	H. Maruyama Faculty of Science, Okayama Univ.	XANES and MCXD measurements of 3*d*-transition metal compounds
95-G043	K. Oki Interdisciplinary Graduate School of Engineering Sciences, Kyushu Univ.	Observation of pressure-induced 4f electron transition by high pressure fluorescence XANES measurement
95-G044	O. Shimomura Photon Factory, KEK	Study of valence fluctuation of Yb monocharcogenides
95-G045	E. R. Vance ANSTO	X-ray absorption spectroscopy of actinides and Tc in synroc related titanete phases
95-G047	Y. Higuchi Faculty of Science, Himeji Institute of Technology	X-ray crystal structure analysis of hydrogenase from sulfate reducing bacteria
95-G048	K. Miki Faculty of Science, Kyoto Univ.	X-ray crystallographic studies of chitosanase
95-G049	T. Tsukihara Institute for Protein Research, Osaka Univ.	X-ray crystal structure analysis of single-stranded DNA binding protein
95-G050	T. Nonaka Faculty of Engineering, Nagaoka Univ. of Technology	High resolution X-ray structural analysis of ternary complexes of 7α-hydroxysteroid dehydrogenase
95-G051	Y. Mitsui Faculty of Engineering, Nagaoka Univ. of Technology	Crystallographic refinement of BphC enzyme at 1.8 Å resolution
95-G052	E. F. Pai Faculty of Medicine, Univ. of Toronto	Structural analysis of xanthine oxidase using X-ray crystallography
95-G053	H. Yamaguchi Institute for Protein Research, Osaka Univ.	Cryocrystallography of glutathione synthetase in complex with its intermediate
95-G054	M. Konno Faculty of Science, Ochanomizu Univ.	Binding sties of substrates for methionyl-tRNA synthetase from *thermus thermophilus* HB8

Proposal Number	Spokesperson	Title
95-G055	Y. Yamagata Osaka Univ.	Three-dimensional structure and function by the protein that suppresses spontaneous mutations
95-G056	H. Kato Institute for Chemical Research, Kyoto Univ.	X-ray crystal structure analysis of asparagine synthetase from eschelichia coli
95-G057	T. Nishioka Institute for Chemical Research, Kyoto Univ.	Fast data collection of glutathione synthetase with wide range oscillation on Weissenberg camera
95-G058	T. Shirai School of Engineering, Nagoya Univ.	Crystal structure analysis of alkaline protease (M-protease) from I crystal
95-G059	M. Tanokura Biotechnology Research Center, Univ. of Tokyo	X-ray crystallography of acid proteinase A from *aspergillus* niger var. *macrosporus*
95-G060	T. Horiuchi National Institute for Basic Biology	Crystallographic study of DNA-protein interaction
95-G061	H. Morimoto Faculty of Engineering Science, Osaka Univ.	X-ray crystallographic analysis of the conformation change of hemoglobin
95-G062	M. Nishiyama Biotechnology Research Center, Univ. of Tokyo	X-ray crystallography of sarcosine oxidase
95-G063	K. Hirotsu Faculty of Science, Osaka City Univ.	X-ray crystallographic study of branched-chain amino acid aminotransferase
95-G064	M. Kusunoki Institute for Protein Research, Osaka Univ.	X-ray crystal analysis of B. cereus β-amylase
95-G065	N. Kamiya Institute of Physical and Chemical Research	Crystal structure analysis of nitrile hydratase
95-G066	N. Yasuoka Faculty of Science, Himeji Institute of Technology	Synchrotron radiation study of electron transfer proteins from sulfate reducing bacteria
95-G068	T. Inoue Faculty of Engineering, Osaka Univ.	Structural analysis of the complex between the nitrite reductase and its electron-donnor pseudoazurin
95-G069	Y. Kai Faculty of Engineering, Osaka Univ.	X-ray structure analysis of RuBisCO purified from spinach with polyethylene glycol
95-G070	Y. Katsuya Hyogo Prefectural Instituel of Industrica Research	X-ray crystallographic study of debranching amylase
95-G071	K. Fukuyama Faculty of Science, Osaka Univ.	X-ray crystallographic analysis of cytochrome bc_1 complex
95-G072	N. Tanaka Faculty of Bioscience and Biotechnology, Tokyo Institute of Technology	Crystallographic analysis of cytochrome c-554 from nitrosomonas europaea

Proposal Number	Spokesperson	Title
95-G073	Y. Hata Institute for Chemical Research, Kyoto Univ.	X-ray analysis of reaction mechanism of p. aeruginosa alkaline protease
95-G074	E. T. Adman Department of Biol. Struct., Univ. of Washington	Structural studies of nitrite reductase
95-G075	T. Yamane School of Engineering, Nagoya Univ.	Dynamic analysis of the interaction between hydrolases and their substrates by the time resolved Laue method
95-G076	F. S. Mathews Department of Biochemistry, Washington Univ.	Crystallographic studies of the active forms of a binary and of a ternary electron transfer complex system: methylamine dehydrogenase
95-G077	R. Fletterick Department of Biochemistry, UCSF	Collection of high resolution data for the kinesin motor domain
95-G078	R. Vale Department of Pharmacology, UCSF	Collection of high resolution data for the kinesin and NCD motor domains
95-G079	X. Lee Department of Cancer Biology, Cleveland Clinic Foundation	Structure determination of bactericidal permeability increasing protein
95-G080	E. F. Pai Faculty of Medicine, Univ. of Toronto	Structural analysis of immunoglobulin A protease using X-ray crystallography
95-G081	M. N. G. James Department of Biochemistry, Univ. of Alberta	Protein crystallographic data collection on glycogen debranching enzyme; complex of β-lactamase TEM-1 and BLIP; complexes of P_1 variants of OMTKY3 and SGPB
95-G082	H. Moriyama Faculty of Bioscience and Biotechnology, Tokyo Institute of Technology	Structure analysis on heat denaturation intermediate of IPMDH
95-G083	N. Sakabe Institute of Applied Biochemistry, Univ. of Tsukuba	Studies on millisecond order dynamics of protein crystal structure using synchrotron radiation
95-G084	M. Hirai Faculty of Engineering, Gunma Univ.	Structural properties of ganglioside/phospholipid/protein system
95-G085	H. Okabayashi Faculty of Engineering, Nagoya Institute of Technology	Structural study of aggregates formed by the insect laccifer products
95-G086	M. Kato Faculty of Science and Engineering, Ritsumeikan Univ.	Effect of pressure on the solution structure of globular proteins by small-angle X-ray scattering
95-G087	S. Nojima Japan Advanced Institute of Science and Technology, Hokuriku	Crystallization behavior of block chains in microdomain structure of poly(ε-caprolactone)-polystyrene diblock copolymer
95-G089	N. Matsushima School of Allied Health Profession, Sapporo Medical College	Solution X-ray scattering of porcine amelogenin

Proposal Number	Spokesperson	Title
95-G090	N. Matsushima School of Allied Health Profession, Sapporo Medical College	Solution X-ray scattering of α-zein from maiz and α-gliadin from wheat
95-G091	Y. Sano National Food Research Institute	Reconstitution process of tobacco mosaic virus by time-resolved small-angle scattering
95-G092	T. Fujisawa Institute of Physical and Chemical Research	Time resolved study on the submit dissociation of oligomeric proteins measured by one-dimensional ring cathode detector
95-G093	M. Kataoka Faculty of Engineering, Osaka Univ.	Solution structures of acid partially-denatured state of RNase HI
95-G094	M. Hirai Faculty of Engineering, Gunma Univ.	Structural study of thermotropic phase transition of lysozyme
95-G095	K. Ichimura Dokkyo Univ. School of Medicine	Static and kinetic studies on structural change of transferrin molecule on recognition and allosteric effects
95-G096	S. Takemori Jikei Univ. School of Medicine	Molecular structure changes induced by ATP hydrolysis products and their analogues in isolated skinned fibers of skeletal muscle
95-G097	H. Sakaguchi National Institute of Materials and Chemical Research	Phase transition and structural change of self assembled glycerophospholipids
95-G098	T. Hamanaka Faculty of Engineering Science, Osaka Univ.	X-ray diffraction studies on the light induced structural change of firefly squid visual cell
95-G099	Y. Igarashi Dokkyo Univ. School of Medicine	Structural kinetic studies on the nucleotide binding to GroEL by using stopped-flow X-ray scattering
95-G100	I. Hatta School of Engineering, Nagoya Univ.	Structural formation of water molecules on lipid membranes
95-G101	I. Hatta School of Engineering, Nagoya Univ.	Simultaneous X-ray diffraction and deferential scanning calorimetry in the study of phase transitions of polymers
95-G102	N. Yagi School of Medicine, Tohoku Univ.	Measurement of the axial repeat in the thick filament of skeletal muscle
95-G103	K. Horiuchi Oita Medical Univ.	Contraction of mammalian slow skeletal muscle fibers on photorelease of ATP
95-G104	T. Sano Faculty of Science, Hiroshima Univ.	Kinetic studies on the mechanism of the interaction between the molecular chaperone and the target proteins by stopped flow X-ray scattering method
95-G105	H. Kihara Physics Laboratory, Kansai Medical Univ.	Role of heme protein folding of hemeproteins using fragmental peptides
95-G106	H. Kihaea Physics Laboratory, Kansai Medical Univ.	Solution structure of a thermostable chaperonin from bacillus stearothermophilus and its comparison with GroEL form E. coli
95-G107	H. Kihara Physics Laboratory, Kansai Medical Univ.	X-ray scattering studies of stable and kinetic intermediates in the folding of the alpha subunit of tryptophan synthase and dihydrofolate reductase

Proposal Number	Spokesperson	Title
95-G109	K. Wakabayashi Faculty of Engineering Science, Osaka Univ.	Precise X-ray diffraction studies of the actin and myosin filaments during muscle contraction
95-G110	K. Wakabayashi Faculty of Engineering Science, Osaka Univ.	X-ray solution scattering studies on conformational changes of the myosin head and actomyosin complex during activity
95-G111	K. Hieda College of Science, Rikkyo Univ.	Terminal structures DNA strand breaks induced by K-shell excitation and ionization of phosphorus
95-G112	N. Miyoshi Fukui Medical School	Detection of radical species produced by monochromatic X-ray irradiation of BrdU molecules in nucleas of a cell
95-G113	H. Mori School of Medicine, Tokai Univ.	Clinical application of micro-angiogram by monochromatic synchrotron radiation
95-G114	H. Kato National Institute of Radiological Sciences	Basic research on diagnosis of cancer using synchrotron radiation imaging
95-G115	J. D. Wang Photon Factory, KEK	Observation of helical structures with an imaging microscope using circularly polarized soft X-rays
95-G116	H. Kihara Physics Laboratory, Kansai Medical Univ.	Microspectroscopic elemental analysis on brain tissue of some diseases by X-ray zooming tube
95-G117	K. Ohshima Institute of Applied Physics, Univ. of Tsukuba	Study on direct observation of ferroelectric microregions in $KTa_{1-x}Nb_xO_3$
95-G118	M. Kobayashi Faculty of Science, Himeji Institute of Technology	Temperature dependence of the crystal structure for alkali-doped C_{70}
95-G119	K. Ohsumi Photon Factory, KEK	Crystallographic study on interplanetary dust particles
95-G120	O. Shimomura Photon Factory, KEK	Measurement of electron density distribution of Yb monopnictides and Yb monocharcogenides
95-G121	N. Arai Faculty of Science, Kobe Univ.	Study on spin-peierls transition of $CuGeO_3$
95-G123	T. Ohba School of Science and Engineering, Teikyo Univ.	Structure factor measurements near martensitic transformation temperature in AuCd alloy
95-G124	M. Sakata School of Engineering, Nagoya Univ.	Crystal structural analysis in the electron level of the fullerene compounds by the maximum entropy method
95-G125	M. Sakata School of Engineering, Nagoya Univ.	Study of structural phase transition by imaging of X-ray diffraction data
95-G126	S. Kawasaki Faculty of Textile Science and Technology, Shinshu Univ.	Measurement of minute powder X-ray diffraction pattern of $C_{60}Fx$, $C_{70}Fx$

Proposal Number	Spokesperson	Title
95-G127	N. Kashiwakura Faculty of Engineering, Gifu Univ.	CTR scattering study of elastically bent crystal surface
95-G128	N. Ohnishi Institute for Materials Research, Tohoku Univ.	Crystal structure of zeolites LTA and FAU containing transition metal clusters
95-G129	T. White Ian Wark Research Institute, Univ. of South Australia	Complete structure solution of zirconolite doped with neodymium/ytterbium and thorium/magnesium
95-G130	S. Kohjiya Institute for Chemical Research, Kyoto Univ.	*In situ* observation of inorganic-organic hybrid formation by the Sol-Gel process
95-G131	K. Kajiwara Faculty of Engineering and Design, Kyoto Institute of Technology	Counterion condensation and conformation of flexible polyelectrolytes in solution
95-G133	J. B. Parise Earth and Space Sciences, SUNY	Structure of the high pressure polymorphs of portlandite, $Ca(OH)_2$
95-G134	O. Ohtaka Faculty of Science, Osaka Univ.	In situ observation of high-temperature and pressure phase transition of ZrO_2
95-G135	A. Onodera Faculty of Engineering Science, Osaka Univ.	Phase relation of low-cristobalite at high pressure and high temperature
95-G136	A. Onodera Faculty of Engineering Science, Osaka Univ.	Pressure-induced structural phase transition in AlSb
95-G137	N. Kojima College of Arts and Sciences, Univ. of Tokyo	High pressure X-ray study on the crystal structure of the perovskite-type mixed-valence complexes $Cs_2Au_2X_6$ (X=Cl, Br, I)
95-G138	K. Takemura National Institute for Research in Inorganic Materials	Singularity in the hcp structure under high pressure
95-G139	H. Yusa National Institute for Research in Inorganic Materials	High-pressure powder X-ray diffraction experiments on cesium iodide
95-G140	S. Endo Research Center for Extreme Materials, Osaka Univ.	Crystal structures of two high pressure phases of solid H_2S
95-G141	S. Endo Research Center for Extreme Materials, Osaka Univ.	Determination of the crystal structure of a high pressure phase of TiO_2
95-G142	K. Akimoto School of Engineering, Nagoya Univ.	Lattice strains at the metal-semiconductor interface
95-G143	X. Jiang BSRF Institute of High Energy Physics	Investigation of interfacial structures of δ-doped semiconductors and amorphous multilayers

Proposal Number	Spokesperson	Title
95-G144	T. Takahashi Institute for Solid State Physics, Univ. of Tokyo	Crystal surface structure analysis by absolute reflectivity measurement
95-G145	K. Akimoto School of Engineering. Nagoya Univ.	Ordered structure at the SiGe interface
95-G146	R. Uno College of Humanities and Sciences, Nihon Univ.	Independent determination of the temperature factor of As in GaAs powder sample
95-G147	S. Iida Faculty of Science, Toyama Univ.	Characterization of micro-defects in silicon crystals by high energy synchrotron radiation topography
95-G148	T. Hondo Institute of Low Temperature Science, Hokkaido Univ.	Measurements of dislocation velocities in ice close to the melting temperature
95-G149	K. Kojima Faculty of Liberal Arts and Science, Yokohama City Univ.	Dislocation structures and motions in organic crystals
95-G150	K. Mizuno Faculty of Science, Shimane Univ.	Determination of nature of dislocation loops generated at high-temperature
95-G151	K. Nakayama National Research Laboratory of Metrology	Absolute measurement of lattice spacing by bond method
95G152	S. Kikuta Faculty of Engineering, Univ. of Tokyo	Research and development of nuclear scattering X-ray optics
95-G153	K. Namikawa Tokyo Gakugei Univ.	Study of X-ray parametric scattering stimulated by an intense laser
95-G154	K. Sakurai National Research Institute for Metals	Depth analysis of trace elements in thin films by grazing incidence X-ray fluorescence using SR
95-G155	K. Ishida Faculty of Science and Technology, Science Univ. of Tokyo	Polarization analysis of ATS scattering of FeS_2
95-G156	Y. Waseda Institute for Advanced Materials Processing, Tohoku Univ.	Determination for cation distribution of (Co, Ni, Zn) Fe_2O_4 spinels by the anomalous X-ray scattering method
95-G157	Y. Iwasa Japan Advanced Institute of Science and Technology, Hokuriku	Search for novel C_{60} compounds and structure analysis
95-G158	H. Suematsu Graduate School of Science, Univ. of Tokyo	Crystal structures and phase transitions of higher fullerenes
95-G159	N. Shimojo Institute of Community Medicine, Univ. of Tuskuba	A novel method to evaluate heavy metal toxicity by nondestructive SR-XRF analysis
95-G160	H. Ino Faculty of Engineering, Univ. of Tokyo	XMCS study of the magnetic moment of Sm^{3+} in metals

Proposal Number	Spokesperson	Title
95-G161	J. Chaboy Instituto de Ciencia de Materiales de Aragon, CSIC-Univ. de Zaragoza	X-ray circular magnetic dichroism study of the magnetic moment localization on Rh atoms in Fe-Rh alloys
95-G162	T. Masujima School of Medicine, Hiroshima Univ.	Establishment of X-ray photoacoustic analysis and development of detection method at higher time resolution
95-G163	K. Ishibashi Faculty of Engineering, Kyushu Univ.	Study on the optimization of superconducting tunnel junctions for X-ray detection
95-G164	Y. Kashiwase School of Engineering, Nagoya Univ.	Development of detector and thin-film mirror for nuclear resonance filtering
95-G165	S. Ito Radioisotope Research Center, Kyoto Univ.	Development of two-dimensional position-sensitive proportional counter for high-energy X-rays provided from the single-bunch operation mode
95-G166	S. Aoki Institute of Applied Physics, Univ. of Tsukuba	Evaluation of wolter mirror for X-ray microbeam
95-G167	T. Kron Newcastle Mate-Hospital, Univ. of Newcastle	Use of synchrotron radiation for the study of the variation of dose response of thermoluminescence dosimeters with X-ray energy
95-G168	M. Chiba Faculty of Science, Tokyo Metropolitan Univ.	Study of multi-photon annihilation processes in positronium
95-G169	C. Kennard Department of Chemistry, Univ. of Quneensland	SAXS studies of dental cement
95-G170	C. Kennard Department of Chemistry, Univ. of Quneensland	The location of dopants in kaolinite
95-G172	C. Kennard Department of Chemistry, Univ. of Quneensland	Superlattice formation in iron-chromium and iron-nickel alloys
95-G173	Y. Kagoshima Photon Factory, KEK	Observation of magnetic domains of transition metals and their alloys with a soft X-ray MCD microscope
95-G174	M. Ito Faculty of Engineering, Doshisha Univ.	Measurement and analysis of the coherence of soft X-ray SR from an undulator with a homodyne photon correlation spectroscopy
95-G175	N. Yamada Univ. of Electro-Communications	X-ray absorption spectroscopy of $Y_{1-x}Pr_xBa_2Cu_4O_8$ near oxygen K-absorption edge
95-G176	K. Ichikawa College of Engineering, Univ. of Osaka Prefectures	Resonant X-ray emission spectroscopy in CeO_2 and CeF_3
95-G177	H. Sato Faculty of Science, Hiroshima Univ.	Resonant photoemission spectroscopy of MnY (Y=S, Se, Te)
95-G178	K. Ueda Research Inst. for Scientific Measurements, Tohoku Univ.	Dissociation dynamics of BF_3 after Fls excitation

Proposal Number	Spokesperson	Title
95-G179	M. Oura Institute of Physical and Chemical Research	Study of electronic correlation in two-electron system
95-G180	H. Nanba Faculty of Science, Univ. of Tokyo	Surface reconstruction induced by photoexcitation of adsorbates
95-G181	K. Maki Faculty of Science, Yokohama City Univ.	Chemical state analysis on surface of metal oxide compounds and their thin films by soft x-rays excited photoelectron spectroscopy
95-G182	H. Kato Photon Factory, KEK	Surface electronic structures of transition-metal-adsorbed oxygen-deficient TiO_2 and NiO single crystals
95-G183	K. Hanada Graduate School of Science, Univ. of Tokyo	Evaluation of the device to measure the electron temperature with high time resolution in high temperature plasma
95-G184	C. Y. R. Wu Dept. of Physics & Astronomy, Space Sciences Center, USC	High-resolution, high-temperature absorption spectroscopy of C_2H_2 and opotics-free electron spectroscopy
95-G185	T. Miyahara Photon Factory, KEK	Measurement of spatial coherence and estimation of emittance of synchrotron radiation
95-G186	K. Nakagawa Faculty of Science, Kobe Univ.	Radiation effects of circularly polarized synchrotron radiation for biomolecules with chirality
95-G187	Y. Iwasawa Graduate School of Science, Univ. of Tokyo	Study of the Rf-Mo, Pd-Mo bimetal catalysts repared from the planar hereoplolyanion $[MMo_6O_{24}]^{8-}$ by EXAFS
95-G188	Y. Abe Faculty of Science and Technology, Science Univ. of Tokyo	Investigation on the structures of polytitanosiloxanes and SiO_2-TiO_2 ceramics
95-G190	H. Wakita Faculty of Science, Fukuoka Univ.	XAFS analysis of thermochromic transition metal complexes
95-G191	A. Yoshiasa Faculty of Science, Osaka Univ.	Anharmonic interatomic potentials of tutile, α-quartz and vitreous GeO_2 determined by EXAFS
95-G192	K. Awaga College of Arts and Sciences, Univ. of Tokyo	Crystal structures and magnetic properties of layered copper hydroxy salts
95-G193	S. Sugiyama Faculty of Engineering, Tokushima Univ.	Effects of the structure of apatites on its lattice ion-ion exchanges
95-G194	Y. Kobayashi Institute for Chemical Reaction Science, Tohoku Univ.	A study on the local structure of magnetic particle in transparent alumina matrices
95-G195	T. Nasu Faculty of Education, Yamagata Univ.	Study on the inorganic clusters formed by the simultaneous evaporation with the organic compounds

Proposal Number	Spokesperson	Title
95-G196	R. Ryoo Department of Chemistry, KAIST	High temperature investigation of small Pt clusters supported on zeolite
95-G197	R. Ryoo Department of Chemistry, KAIST	Structural characterization of Pt-based bimetallic clusters supported on KL zeolite
95-G198	H. Yamashita College of Engineering, Univ. of Osaka Prefectural	XAFS studies on metal ion clusters included in semiconductor photocatalysts
95-G199	Y. Iwasawa Graduate School of Science, Univ. of Tokyo	EXAFS studies on the structure of VO complex for oxidation catalysts prepared inside zeolite
95-G200	Y. Iwasawa Graduate School of Science, Univ. of Tokyo	Characterization of novel catalysts based on supported homonoulear and heteronuclear gold cluster by XAFS
95-G201	T. Tanaka Faculty of Engineering, Kyoto Univ.	Structural study of Yb complexes as stable lewis acids in organic synthesis
95-G202	T. Mukoyama Institute for Chemical Research, Kyoto Univ.	X-ray absorption spectroscopy on the shake processes in lanthanoid compounds
95-G203	T. Ishioka Faculty of Science, Toyama Univ.	Coordination structure around the Zn cation in zinc salts of fatty acids
95-G204	S. Tsunashima School of Engineering, Nagoya Univ.	The analysis of controlled structural anisotropy by sputtering condition in RE/TM multilayers
95-G205	T. Moriga Faculty of Engineering, Tokushima Univ.	XAFS study on structure of $Li_{1-x}NiO_2$ substituted by Mn
95-G206	A. Morikawa Faculty of Engineering, Tokyo Institute of Technology	Investigation on coordination sphere of rare-earth cations in zeolite cavity
95-G209	I. Ouchi Faculty of Engineering, Tottori Univ.	Microstructure of alloy films including CoCr by means of XAFS
95-G210	R. Ryoo Department of Chemistr, KAIST	Local Atomic structure of titanium during crystallization of Ti-NaY zeolite
95-G211	Y. Nishiyama Institute for Chemical Reaction Science, Tohoku Univ.	The structure determination of metal particles in HOPG by polarized XAFS spectroscopy
95-G212	H. Maeda Faculty of Science, Okayama Univ.	EXAFS study on the anharmonic interatomic potentials of Cu-halides
95-G214	N. Hamaya Faculty of Science, Ochanomizu Univ.	Valence measurement using XANES for Pt at pressure-induced phase transition

Proposal Number	Spokesperson	Title
95-G215	A. M. Páez Faculty of Chemistry, Univ. of Sevillia	Coupled EXAFS study of YBr_3 solutions by measuring the edges of both ions
95-G216	O. Shimomura Photon Factory, KEK	Study of valence fluctuation of NaCl type rare earth phosphides
95-G217	S. Yanagida Faculty of Engineering, Osaka Univ.	In-situ investigation of electronic/morphological structure of Nd complex in solution
95-G218	K. Kawamura Faculty of Science, Tokyo Institute of Technology	Local Arrangement around rare-earth elements doped in PHB glasses
95-G219	O. Haruyama Faculty of Science and Technology, Science Univ. of Tokyo	Study on the structure change of amorphous alloys associated with the reversible structural relaxation by anomalous X-ray scattering
95-G220	M. Takahashi Inst. of Scientific and Industrial Research, Osaka Univ.	Study of corrosion resistance of thin films in the TiN-AlN system by the yield XAFS method
95-G221	Y. Takeda School of Engineering, Nagoya Univ.	Fluorescence EXAFS study on local structure around Er doped in InP matrix
95-G222	T. Ohta Graduate School of Science, Univ. of Tokyo	The local structures of the dionedioxime complex evaporated films for the third order nonlinear optics
95-G223	I. Watanabe Faculty of Science, Osaka Univ.	Analysis of deposited thin film by conversion electron yield XAFS method
95-G224	T. Yamaguchi Faculty of Science, Fukuoka Univ.	In situ XAFS of different oxidation states of trinuclear Ru cluster complexes
95-G225	M. Izumi Tokyo Univ. Mercantile Marine	Fluorescence XAFS on single crystal of long-chainalkyl $[EDT\text{-}TTF(SC_{18})_2]_2I_3$
95-G226	Y. Izumi Graduate School at Nagatsuta Tokyo Institute of Technology	Study on $Rh_{10}Se$ cluster catalysts for ethanol synthesis from CO_2
95-G227	T. Shiota Electrotechnical Laboratory	XAFS study of MBE-grown $CuInSe_2$ thin layer
945G228	T. Shiota Electrotechnical Laboratory	Molecular and electronic structural analysis of rare earth complexes by XAFS upon their selective chemical reaction with necleic acids
95-G229	K. Kawamura Faculty of Science, Tokyo Institute of Technology	Study on local arrangement of poled tellurite glasses
95-G231	A. Nishijima National Institute of Materials and Chemical Research	Genesis of hydrocracking activity on boron-added Ni-Mo and Ni-W hydroprocessing catalysts studied by XAFS
95-G232	A. Nishijima National Institute of Materials and Chemical Research	XAFS study on electronic structure of perovskite oxide $La_{1-x}A_xCoO_3$ (A = Sr, Ce)

Proposal Number	Spokesperson	Title
95-G233	T. Matsui Nagoya Univ.	EXAFS study on local structures of fluoride uranium oxides
95-G234	A. Yoshiasa Faculty of Science, Osaka Univ.	Interatomic potentials of stishovite, β-quartz and vitreous SiO_2 determined by EXAFS
95-G235	A. Itoh College of Science and Technology, Nihon Univ.	Microstructure analysis of oxide magnetic materials by EXAFS
95-G236	Y. Nakata Inst. of Scientific and Industrial Research, Osaka Univ.	Structure Analysis of Ti-Ni amorphous alloys
95-G237	N. Sakabe Institute of Applied Biochemistry, Univ. of Tsukuba	Evaluation and application studies of novel protein data collection system with newly constructed large size of IP reader
95-G238	I. Tanaka Faculty of Science, Hokkaido Univ.	X-ray crystal structure analysis of DNA-binding domain of OmpR protein of E.coli
95-G239	I. Tanaka Faculty of Science, Hokkaido Univ.	Thermal stabilization of DNA binding protein HU
95-G240	A. Nakagawa Graduate School of Science, Hokkaido Univ.	Structure analysis of Macrophage migration inhibitory factor
95-G241	K. Miki Graduate School of Science, Kyoto Univ.	X-ray crystallographic studies of aldehyde reductase
95-G243	K. Fukuyama Faculty of Science, Osaka Univ.	X-ray crystallographic analysis of the intermediates of *arthromyces ramosus* peroxidase
95-G244	H. Yamaguchi Institute for Protein Research, Osaka Univ.	X-ray structure analysis of *m*-hydroxybenzoate-4-hydoroxylase
95-G245	H. Morimoto Faculty of Engineering Science, Osaka Univ.	The application of the time-resolved Laue method to the conformation change of hemoglobin
95-G246	O. Nureki Graduate School of Science, Univ. of Tokyo	X-ray crystallography of RecA•DNA complex
95-G247	J. R. Shen Institute of Physical and Chemical Research	X-ray crystal structure analysis of photosystem II membrane protein supramolecular complex
95-G248	H. Matsuzawa Faculty of Agriculture, Univ. of Tokyo	Analysis of acquisition mechanism of allosteric characteristic of L-lactate dehydrogenase from lactobacilli
95-G249	K. Hirotsu Faculty of Science, Osaka City Univ.	Reaction mechanism of aspartateaminotransferase
95-G350	W. Wolodko Department of Biochemistry, Univ. of Alberta	The crystal structures of succinyl-CoA synthetase and CoA transferase

Proposal Number	Spokesperson	Title
95-G251	T. Jardetzky Department of Biochemistry, Northwestern Univ.	Structural studies of the high affinity IgE receptor
95-G252	T. L. Bullock Structural Studies Division, MRC Laboratory of Molecular Biology	Subfilament structure of the nematode sperm motility protein, MSP
95-G253	S. Hasnain Daresbury Laboratory	Crystallographic study of copper proteins involved in electron transfer and denitrification
95-G254	S. -X. Lin UHUL	Crystallographic studies of human 17β-hydroxysteroid dehydrogenase
95-G255	M. W. Parker SVIMR	Structural studies of detoxifying enzymes
95-G256	M. W. Parker SVIMR	Structural studies of membrane-associating proteins
95-G257	R. W. Pickersgill IFR Reading Laboratory	Elucidation of the structure of glycosyl-hydrolases and pectic enzymes
95-G258	T. L. Blundell Department of Crystallography, Birkbeck College	Structure, function and engineering of proteinases
95-G259	B. W. Mattews Institute of Molecular Biology, Univ. of Oregon	Weissenberg data collection of β-galactosidase from E. coli
95-G260	E. N. Baker Dept. of Chemistry and Biochemistry, Massey Univ.	Structures of proteins of Alcohol and carbohydrate metabolism
95-G261	G. -Y. Lu College of Life Sciences, Peking Univ.	The collection of diffraction data of bar-headed goose hemoglobin and antibacterial polypeptide LC1
95-G262	T. Konno Graduate School of Natural Science, Kobe Univ.	Solution X-ray scattering studies on subunit-assembly properties of hemoglobin and nAChR
95-G263	M. Iwakura	X-ray solution scattering studies of circular and circular permuted dihydrofolate reductase
95-G264	K. Akasaka Faculty of Science, Kobe Univ.	Solution X-ray scattering studies on non-native structures of SSI and apomyoglobin
95-G265	N. Sasaki Faculty of Science, Hokkaido Univ.	Molphological change of bone mineral during calcification of connective tissue physiological and pathological calcification
95-G266	Y. Muroga School of Engineering, Nagoya Univ.	Change in the radius of gyration accompanied by conformational transition of α-tropomyosin
95-G268	Y. Sano National Food Research Institute	Studies on functional properties of tobacco mosaic virus RNA
95-G269	Y. Goto Faculty of Science, Osaka Univ.	Structural characterization of thermal unfolding state of proteins

Proposal Number	Spokesperson	Title
95-G270	N. Niimura Japan Atomic Energy Research Institute	The initial stage of bio-macromolecule (DNA, Lysozyme, BPTI) crystallization
95-G271	M. Kataoka Faculty of Science, Osaka Univ.	Solution structure of PYP (Photoactve Yellow Protein) and its change upon illumination
95-G272	M. Kataoka Faculty of Science, Osaka Univ.	Effects of deletions on the structure and stability of proteins -In the case of staphylococcal nuclease
95-G273	Y. Izumi Faculty of Engineering, Yamagata Univ.	Solution structures of calmodulin/target peptide complex - effects of target peptides with systematically substituted sites -
95-G274	Y. Izumi Faculty of Engineering, Yamagata Univ.	Comparative study of solution structures between yeast and vertebrate calmodulin
95-G275	V. J. James Department of Biophysics, School of Physics, Univ. of N.S.W.	Synchrotron X-ray diffraction study of the changes in collagen from the dermal layer of the breast with ageing and breast cancer
95-G276	H. Sugi School of Medicine, Teikyo Univ.	Studies on the molecular mechanism of fall in tension following a decrease in stretch velocity in active skeletal muscle fibers
95-G278	K. Ema Faculty of Science, Tokyo Institute of Technology	Dimensional crossover and finite-size effect in the gel to liquid-crystalline phase transition of lipid bilayer membranes
95-G279	N. Yagi School of Medicine, Tohoku Univ.	Ca-induced structural changes in the thin filament
95-G280	N. Yagi School of Medicine, Tohoku Univ.	X-ray diffraction study on single muscle fibers using a multipole wiggler beamline
95-G281	N. Usami Photon Factory, KEK	Distribution of cleavage site produced by inner-shell photoabsorption of iodine in iodinated oligonucleotide
95-G282	A. Yokoya Japan Atomic Energy Research Institute	Characteristics of degradation of sulfur-containing amino acids in aqueous solution with sulfur K-shell photoabsorption
95-G283	K. Shinohara Tokyo Metropolitan Institute of Medical Science	Elemental and molecular analyses of mammalian cells by X-ray contact microscopy with an electronic zooming tube
95-G284	A. Ito Faculty of Engineering, Tokai Univ.	Measurements of XANES spectra for biomolecules and its application to molecular imaging in a mammalian cell
95-G285	K. Tokumori Faculty of Dentistry, Kyushu Univ.	Study on digital dental radiography using monochromatic X-ray generated by synchrotron radiation
95-G286	S. Hasegawa Tokyo Institute of Polytechnics	Development of life size energy subtraction X-ray television system for coronary angiography and estimation of image qualit

Proposal Number	Spokesperson	Title
95-G287	E. Tanaka School of Medicine, Tokai Univ.	Utilization of small vessel angiography by monochromatic synchrotron radiation for cancer diagnosis
95-G288	H. Mori School of Medicine, Tokai Univ.	Distribution of intramyocardial blood flow and vascular density evaluated by monochromatic synchrotron radiation evoked X-ray fluorescence spectrometry
95-G289	T. Takeda Institute of Clinical Medicine, Univ. of Tsukuba	Development of transmit and fluorescent X-ray computed tomography for biomedical diagnosis
95-G290	T. Takeda Institute of Clinical Medicine, Univ. of Tsukuba	Aortographic coronary arteriography with synchrotron radiation
95-G291	T. Akatsuka Faculty of Engineering, Yamagata Univ.	Development and experimental study of scattering computed tomography for biological diagnosis
95-G292	H. Maruyama Faculty of Science, Okayama Univ.	Alternating circularity and MCD measurements using diamond phase retarder
95-G293	S. Sasaki Research Laboratory of Engineering, Tokyo Institute of Technology	Study on valence fluctuation by X-ray anomalous dispersion
95-G294	H. Ino Faculty of Engineering, Univ. of Tokyo	XMBS study of the temperature dependence of Sm^{3+} moment in metals
95-G295	M. Ito Faculty of Science, Himeji Institute of Technology	Development of X-ray magnetic diffraction experiments with phase retarders
95-G296	M. Ito Faculty of Science, Himeji Institute of Technology	Orbital and spin magnetic moments of ferromagnets by X-ray magnetic diffraction
95-G297	A. Iida Photon Factory, KEK	Research of development of wavelength dispersive X-ray fluorescence analysis
95-G298	Y. Amemiya Photon Factory, KEK	Measurements of dielectric constant anisotropy of materials using a tunable X-ray polarimeter
95-G299	Y. Gohshi Faculty of Engineering, Univ. of Tokyo	Decay measurements of X-ray excited optical luminescence
95-G300	N. Haga Faculty of Science, Himeji Institute of Technology	Michrobeam analysis of trace elements of zonal structure in rock-forming minerals
95-G301	T. Hirokawa Faculty of Engineering, Hiroshima Univ.	SRXFA of trace rare-earth elements

Proposal Number	Spokesperson	Title
95-G302	A. Kawahara Faculty of Science, Okayama Univ.	Structure determination of fukalite ($Ca_4Si_2O_6(OH)_2CO_3$)
95-G303	F. Toda Faculty of Engineering, Ehime Univ.	X-ray structure analysis of organic crystals with very small sizes of host-guest inclusion compounds
95-G304	H. Ohsato Faculty of Engineering, Nagoya Institute of Technology	Epitaxial growth of GaN of SiC substrates
95-G305	S. Tsunekawa Institute for Materials Research, Tohoku Univ.	Study on ferroelastic domains by micro-area X-ray diffraction
95-G306	K. Koyama Faculty of Integrated Arts and Science, Tokushima Univ.	Magnetic correlation in $Pr_{1-x}Ln_xBa_2Cu_3O_{7-y}$ (Ln = Y, Nd)
95-G307	H. Yamaguchi Electro Technical Laboratory	X-ray diffraction study on superlattice structure in tetragonal $La_{2-x}Sr_xCuO_4$
95-G308	K. Suzuki Faculty of Engineering, Yokohama National Univ.	Magnetic structure analysis of quasi-two-dimensional magnet $(GdS)_{1.20}TaS_2$ by X-ray magnetic scattering
95-G309	M. Arai Faculty of Science, Kobe Univ.	Study on oxide superconductor $La_{2-x}Sr_xCuO_4$
95-G310	H. Kawada Photon Factory, KEK	Magnetic structures of organic complexes (BEDT-TTF) (FnTCNQ) studied by X-ray magnetic scattering
95-G311	Y. Murakami Photon Factory, KEK	Ordering of change and spin in perovskite compounds of Mn oxide
95-G312	N. Suzuki Univ. of Elector Communications	Structural study of physisorbed film by means of X-ray CTR scattering
95-G313	Y. Takeda School of Engineering, Nagoya Univ.	X-ray CTR scattering study on Hetero-Epitaxially grown AlGaP/InP and AlGaP/InAs interface-structures
95-G314	Y. Takeda School of Engineering, Nagoya Univ.	X-ray CTR study on Er δ-doped layer in InP
95-G315	H. Kawamura Faculty of Science, Himeji Institute of Technology	Pressure-induced structural phase transition of II-VI compound
95-G316	A. Onodera Faculty of Engineering Science, Osaka Univ.	Search for post-NaCl type high pressure phase in III-V nitrides

Proposal Number	Spokesperson	Title
95-G317	O. Shimomura Photon Factory, KEK	Pressure induced structural phase transitions and valence transitions of NaCl type rare-earth compounds
95-G318	T. Kondo Institute for Solid State Physics, Univ. of Tokyo	In situ X-ray observation of the multi-component silicate system under high temperature and high pressure
95-G319	I. Shirotani Faculty of Engineering, Muroran Institute of Technology	Structure and valence fluctuation of $La_{1-x}Ce_xRu_4P_{12}$ at high pressure
95-G320	I. Shirotani Faculty of Engineering, Muroran Institute of Technology	Study of X-ray diffraction of PrP and $PrRu_4P_{12}$ at low temperatures and high pressures
95-G321	T. Fukamachi Faculty of Engineering, Saitama Institute of Technology	Dynamical diffraction when the real part to X-ray polarizability is zero
95-G322	N. Kamijo AIST, Osaka National Research Institute	Fabrication and testing of hard X-ray sputtered-sliced zone plate (II)
95-G323	S. Sasaki Research Lab. of Engineering Materials, Tokyo Institute of Technology	Electron density distributions in high-Tc oxides
95-G324	Y. Kudo Faculty of Science, Tohoku Univ.	Effect of pressure on the crystal structure of phase E, $Mg_{2.27}Si_{1.26}H_{2.4}O_6$
95-G325	S. Tsukui Univ. of Osaka Prefecture	Analysis on Crystal structure of twin-free oxide high-Tc superconductors
95-G326	H. Yoshida Faculty of Technology, Tokyo Metropolitan Univ.	Structure formation dynamics of polymers by the simultaneous differential scanning calorimetory and X-ray scattering method
95-G328	T. Kanaya Institute for Chemical Research, Kyoto Univ.	Insitu SAXS experiments at isothermal crystallization of the weakly crosslinked i-PP
95-G329	Y. Nishimura Osaka National Research Institute	Characterization of ion clustering in solid polymer electrolyte
95-G330	Y. Muroga School of Engineering, Nagoya Univ.	Investigation of local conformation polyelectrolyte by SOR-SAXS
95-G331	Y. Udagawa Research Inst. for Scientific Measurements, Tohoku Univ.	Determination of bethe surfaces by X-ray compton-raman scattering
95-G332	K. Uosaki Faculty of Science, Hokkaido Univ.	In situ structural study of semiconductor single crystal electrode/electrolyte solution interfaces by X-ray absorption spectroscopy at atomic level

Proposal Number	Spokesperson	Title
95-G333	A. Yoshiasa Faculty of Science, Osaka Univ.	High-pressure and high-temperature XAFS study on debye-waller factor in GeO_2
95-G334	N. Ishizawa Research Lab. of Engineering Materials, Tokyo Institute of Technology	Structures of double-perovskite-type compounds $La_{2/3}Ta_2O_6$ and $La_{2/3}Nb_2O_6$
95-G335	Y. Soejima Faculty of Science, Kyushu Univ.	Structure analysis using EDAFS of super lattice diffraction in $PbZrO_3$
95-G336	F. Marumo College of Humanities and Sciences, Nihon Univ.	Distribution and amount of oxygen diffects in $CaLnAlO_4$ (Ln: Gd, La, Y)
95-G337	H. Yamaoka Institute of Physical and Chemical Research	Characterization of mosaic Si crystals with 100 keV synchrotron radiation
95-G338	S. Nanao Institute of Industrial Science, Univ. of Tokyo	A structural analysis of F-type Al-Cu-Ru single quasicrystals by X-ray anomalous scattering
95-G339	W. Ustsumi Japan Atomic Energy Research Institute	In situ observation of graphite to diamond transformation using a catalyst
95-G340	I. Shirotani Faculty of ENgineering, Muroran Institute of Technology	Structural anomaly of one-dimensional platinum complexes at high pressure
95-G341	T. Yagi Institute of Solid State Physics, Univ. of Tokyo	Exploring research on a new high pressure and high temperature phase of iron
95-G342	K. Nishikawa Faculty of Education, Yokohama National Univ.	Study on clustering of supercritical solution systems
95-G343	Y. Masumoto Institute of Physics, Univ. of Tsukuba	Small angle X-ray scattering of clusters and microcrystals of CuI and CuBr
95-G344	K. Osamura Faculty of Science, Kyoto Univ.	Structure change during phase decomposition in metallic materials
95-G345	T. Hashimoto Graduate School of Engineering, Kyoto Univ.	Phase transition and structure formation in block polymers
95-G346	T. Hirai Faculty of Textile Science and Technology, Shinshu Univ.	Structure change of solution induced by electric field and the effect of polymer as additive
95-G347	K. Hasegawa College of Engineering, Hosei Univ.	Test of integrating type PSPC

Proposal Number	Spokesperson	Title
95-G348	T. Cho Institute of Physics, Univ. of Tsukuba	Extension of a new theory of semiconductor X-ray detector sensitivities, and its experimental verification and applications
95-G349	K. Hirano Photon Factory, KEK	Phase-contrast X-ray computed tomography with an X-ray interferometer
95-G350	K. Namikawa Tokyo Gakugei Univ.	Spectroscopic study of magnetic multilayer films by means of X-ray magnetic resonant scattering
95-G351	M. B. Salamon Department of Physics, Univ. of Illinois	Direct detection of coherent RKKY oscillation in a Co/Ir superlattice
95-G352	M. Koike Electrotechnical Laboratory	Experimental characterization of bragg-fresnel X-ray optical devices
95-G353	T. Matsushita Photon Factory, KEK	Structural analysis of the electrode/electrolyte interface by the X-ray standing wave method
95-G354	H. Hashizume Research Lab. of Engineering Materials, Tokyo Institute of Technology	High-resolution X-ray scattering from mesoscopic structures in mechanofusion alloys and mesoporous solids
95-G355	S. Nanao Institute of Industrial Science, Univ. of Tokyo	Magnetic X-ray absorption in the Fe-Rh alloys
95-G356	S. Nanao Institute of Industrial Science, Univ. of Tokyo	Magnetic circular dichroism in Fe_4N
95-G357	S. Nanao Institute of Industrial Science, Univ. of Tokyo	X-ray magnetic EXAFS in Dy-Fe alloys
95-G358	T. Iwazumi Photon Factory, KEK	Magnetic circular dichroism in fluorescent X-ray profiles
95-G359	T. Iwazumi Photon Factory, KEK	Magnetic circular dichroism study of carbon based organic magnet
95-G360	J. Chaboy CSIC, Univ. of Zaragoza	X-ray circular magnetic dichroism investigation of the influence of hydrogen absorption on the local magnetic moments in R-M intermetallics (R = rare earth; M = transition metal)
95-G361	B. O'Neill Institute for Solid State Physics, Univ. of Tokyo	Study of garnet-rich complex compositions at lower mantle conditions
95-G362	T. Yamanaka Faculty of Science, Osaka Univ.	The kinetic study of the dehydration of hydrous minerals under pressure

Proposal Number	Spokesperson	Title
95-G363	K. Kusaba Institute for Materials Research, Tohoku Univ.	Pressure-induced phase transition of FeS
95-G364	N. Hiramatsu Faculty of Science, Fukuoka Univ.	USAXS observation of bio-related materials with mesoscopic structure
95-G365	S. Nakai Faculty of Engineering, Utsunomiya Univ.	S-k_β resonant emission spectra in S-K absorption threshold
95-G366	T. Mitsuishi Faculty of Engineering, Utsunomiya Univ.	3p-5d core-level resonant photomission of heavy rare-earth compounds
95-G367	T. Hayashi Institute of Applied Physics, Univ. of Tsukuba	Post-collision interaction effects induced by auger cascades in rare gases
95-G368	H. Ishii Faculty of Science, Tokyo Metropolitan Univ.	Resonant photoemission spectroscopy of $PrBa_2Cu_3O_7$ and related oxides
95-G369	E. Shigemasa Photon Factory, KEK	Study on molecular shape resonances using an angle-resolved photoelectron-photoion coincidence technique
95-G370	T. Kojima Institute of physical and Chemical Research	Photoionization and photodissociation of molecular ions
95-G371	S. Kono Research Inst. for Scientific Measurements, Tohoku Univ.	Surface structure analysis by photoelectron diffraction in an electron energy range of 100~400 eV
95-G372	Y. Ouchi School of Science, Nagoya Univ.	NEXAFS studies on the surface structure of organic thin films for liquid crystal alignment
95-G373	M. Yanagihara Research Inst. for Scientific Measurements, Tohoku Univ.	Developments and applications of small d-spacing multilayer elements for soft X-rays
95-G374	K. Seki School of Science, Nagoya Univ.	Study of evaporated films of dyes, organic semiconductors, and other electronically functional organic molecules using polarized NEXAFS spectroscopy
95-G375	H. Kihara Kansai Medical Univ.	Energy resolved study of photoelectron micro-imaging
95-G376	Y. Takeda School of Engineering, Nagoya Univ.	EXAFS study on local-structure around Si doped in AlGaAs
95-G377	Y. Kitajima Photon Factory, KEK	XAFS measurements with variable surface sensitivity by exit angle dependent fluorescence yield

Proposal Number	Spokesperson	Title
95-G378	K. Akimoto Institute of Materials Science, Univ. of Tsukuba	EXAFS analysis of defects in semiconductors
945G379	T. Yokoyama Graduate School of Science, Univ. of Tokyo	Anisotropic anharmonic vibration of the surface metal-Cl bonds on Cl-adsorbed Ni and Cu single crystals
95-G380	Y. Iwasawa Graduate School of Science, Univ. of Tokyo	Shape change in the white line peak of Pd $L_{2,3}$ edge induced by adsorbed and absorbed hydrogen
95-G381	M. Taniguchi Faculty of Science, Hiroshima Univ.	Studies of electronic structures of trigonal and amorphous Se
95-G382	H. Miki Faculty of Science and Engineering, Science Univ. of Tokyo	Correlation of the electron state at step edge on Pt surfaces and the NO chemisorption state
95-G383	A. Misu Faculty of Science, Science Univ. of Tokyo	Piezoreflectivity of Al_2O_3
95-G384	K. Akimoto Institute of Materials Science, Univ. of Tsukuba	Characterization of semiconductor interface by photoemission spectroscopy
95-G385	T. Sekitani Faculty of Science, Hiroshima Univ.	Surface photochemical reaction of alochols by core electron excitation
95-G386	N. Ueno Faculty of Engineering, Chiba Univ.	Local photochemical decomposition of organic molecular thin films core electron excitation
95-G387	K. Maeda Faculty of Education, Kumamoto Univ.	High-resolution measurement for absolute photoabsorption cross sections of Ba
95-G388	M. Taguchi Faculty of Science, Tohoku Univ.	Absorption profile measurements at 121.567 nm/121.534 nm attained by hydrogen/deuterium absorption cells
95-G389	Y. Aiura Elecrtotechnical Laboratory	Photoemission of $LaxSr_{1-x}TiO_3$ single crystals
95-G390	A. Tanaka Graduate school of Science, Tohoku Univ.	Photoemission studies of Ce/V
95-G391	M. Iwami Faculty of Science, Okayama Univ.	Angle resolved photoemission spectroscopy of 6H-SiC polar surfaces
95-G392	C. Y. Park Department of Physics, Sung-Kyun-Kwan Univ.	Interaction of oxygen with alkali metal on Si(111) 7 × 7 surface

Proposal Number	Spokesperson	Title
95-G393	Y. Suda Faculty of Technology, Tokyo Univ. of Agriculture and Technology	Angle-resolved photoemission study of porous Si
95-G394	A. Kakizaki Institute for Solid State Physics, Univ. of Tokyo	ARUPS study of the surfaces electronic structures of LaB_6 and CeB_6
95-G395	A. Kakizaki Institute for Solid State Physics, Univ. of Tokyo	Angle-resolved photoemission spectroscopy of $CoPt_3$ single crystal
95-G396	A. Kakizaki Institute for Solid State Physics, Univ. of Tokyo	Spin-resolved photoemission spectroscopy of Fe and Co/Au system
95-G397	T. Mizoguchi Faculty of Science, Gakushuin Univ.	Electronics structures of ferromagnetic transition metal thin film on GaAs
95-G398	A. Fujimori Graduate School of Science, Univ. of Tokyo	Spin-polarized photoemission of transition-metal pnictide itinerant ferromagnets
95-G399	Y. Saitou Japan Atomic Energy Research Institute	2p core resonance and magnetic circular dichroism in spin resolved photoemission of ferromagnetic nickel
95-G400	S. Shin Institute for Solid State Physics, Univ. of Tokyo	3p and 2p resonant photoemission of V_2O_3
95-G401	M. Fujisawa Institute for Solid State Physics, Univ. of Tokyo	Electronic structures of quasicrystal Al-Cu-Fe studied by soft X-ray emission and absorption spectroscopes
95-G402	Y. Tezuka Institute for Solid State Physics, Univ. of Tokyo	Soft X-ray emission and resonant photoemission study of $Sr2RuO_4$
95-G403	A. Hartmann Surface Science and Technology, Univ. of New South Wales	Electronic structure of low resistance Ga- and High resistance Cu-doped chemical vapour deposition grown ZuO films
95-G404	G. J. Russell School of Physics, Univ. of New South Wales	Electronic structure of HTSC crystal from NEXAFS and PES
95-G405	H. Sato Faculty of Science, Hiroshima Univ.	Soft X-ray emission of alkali halides
95-G406	N. Yamada Univ. of Elector-Communications	X-ray absorption polarization analysis for $PrBa_2Cu_3O_7$ near oxygen K-absorption edge
95-G407	K. Ito Photon Factory, KEK	Photoelectron spectroscopy of molecular hydrogen in the energy region of doubly excited states

Proposal Number	Spokesperson	Title
95-G408	Y. Morioka Institute of Physics, Univ. of Tsukuba	Analysis of potential energies of diatomic molecule ions
95-G409	J. B. West Research Inst. for Scientific Measurements, Tohoku Univ.	Inner valence electron spectroscopy of CO and high resolution resonance measurements on CO_2
95-G410	Y. Baba Japan Atomic Energy Research Institute	X-ray photochemical reaction in condensed phases at low temperature by inner-shell resonant excitation
95-G411	T. Koide Photon Factory, KEK	Magnetic circular dichroism in metallic magnetic superlattices and multilayers prepared by on MBE technique
95-G412	T. Koide Photon Factory, KEK	Magnetic circular dichroism in oxides and halides of 3d metals and valence-fluctuating Ce compounds
95-G413	K. Okuno Faculty of Science, Tokyo Metropolitan Univ.	Study of circular dichroism in double photoionization of rare Gas atoms
95-G414	A. Fujimori Faculty of Science, Univ. of Tokyo	Photoemission magnetic circular dichroism of ferromagnetic transition-metal oxides
95-G415	S. Tsunashima School of Engineering, Nagoya Univ.	The analysis of magnetic polarization at interface of NiFeCo/Cu multilayers by MCD
95-G416	T. Kurihara Photon Factory, KEK	Damage recovery of Cr implanted Al_2O_3
95-P001	T. Ohta Graduate School of Science, Univ. of Tokyo	Exploitation of the liquid-solid interface EXAFS method in the hard X-ray region
95-P002	Z. Y. Wang Faculty of Engineering, Tohoku Univ.	A small-angle X-ray scattering study on the aggregate structures of pigments from photosynthetic bacteria
95-P003	S. Tsunashima School of Engineering, Nagoya Univ.	A study of MCD on Gd in Gd/Fe multilayers
95-P004	H. Hosono Research Lab. of Engineering Materials, Tokyo Institute of Technology	Phase transition of $Tl_2Nb_2O_{6+\delta}$ under high pressure
95-P005	M. Koike Electrotechnical Laboratory	Experimental characterization of monochromatizing- and focusing- X-ray devices
95-P007	K. Yakushi Institute for Molecular Science	Crystal structure of conductive phthalocyanine crystal under high pressure

Proposal Number	Spokesperson	Title
95-P008	K. Akimoto Institute of Materials Science, Univ. of Tsukuba	Band discontinuity measurements by photoelectron spectroscopy
95-P009	H. Yokoyama Electrotechnical Laboratory	Synchrotron X-ray diffraction and reflection studies of langmuir monolayers of azobenzene derivative
95-P010	H. Takechi Fukuoka Institute of Technology	Structural analysis on soft ferrite treated by mechanical alloying
95-P011	I. Nakai Faculty of Science, Science Univ. of Tokyo	XAFS analysis of deintercalated $LiMO_2$ (M = Ni, Co)
95-P012	H. Kihara Kansai Medical Univ.	High resolution topography of dislocations in silicons by use of X-ray zooming tube
95-P013	T. Hashimoto College of Arts and Sciences, Univ. of Tokyo	Variation of crystal system of $BaPb_{1-x}Bi_xO_{3-\sigma}$ on composition and its effect on conduction behavior
95-P014	S. Saeki Faculty of Engineering, Fukuoka Univ.	Development of perfect crystalline polymer in the vicinity of zero gravity state
95-P015	S. Nanao Institute of Industrial Science, Univ. of Tokyo	Phase transformation of quasicrystal under the high pressure and high temperature
95-P016	H. Kihara Kansai Medical Univ.	Unfolding and refolding kinetics of adenylate kinase by means of stopped-flow X-ray scattering
95-Y001	K. Iinuma NEC Corp.	Soft X-ray lithography, photo-chemical reaction experiments and X-ray optics
95-Y002	S. Kaida	XAFS study of nickel hydroxide
95-Y003	K. Kubodera Interdisciplinary Research Lab. NTT	Materials analysis using synchrotron radiation
95-Y004	S. Sato Fujitsu Laboratories Ltd.	Exposure tests by synchrotron radiation in BL-17A, BL-17B, and BL-17C
95-Y005	K. Suzuki Central Research Laboratory, Hitachi Ltd.	BL-8A; soft X-ray diffractometry, X-ray absorption spectroscopy, soft X-ray microprobe. B; EXAFS experiments, total reflection measurement. C; lithography, microprobe experiments, micro X-ray diffractometry
95-Y006	K. Tanaka Mitsui Toatsu Chemicals, Inc.	XAFS analysis of metal catalysts for polymer synthesis
95-Y007	M. Sagara	The structural analysis of Ru-Sn catalysis by XAFS
95-Y008	S. Sato Fujitsu Laboratories Ltd.	Exposure tests by synchrotron radiation in BL-17A, BL-17B, and BL-17C

Proposal Number	Spokesperson	Title
95-Y009	K. Suzuki Central Research Laboratory, Hitachi Ltd.	BL-8A; soft X-ray diffractometry, X-ray absorption spectroscopy, soft X-ray microprobe. B; EXAFS experiments, total reflection measurement. C; lithography, michoprobe experiments, micro X-ray diffractometry
95-Y010	K. Iinuma NEC Corp.	Soft X-ray lithography, photo-chemical reaction experiments and X-ray optics
95-C001	Y. Ohishi Tsukuba Research Laboraty, Sumitomo Chemicals, Inc.	Small angle X-ray scattering study for dynamical strucutre Change of Polymers
95-C002	S. Kimura Microelectronics Research Laboratories, NEC. Corp.	
95-C003	M. Imafuku Advanced Materials & Technology Research Laboratories, Nippon Steel Corporation	
95C-004	S. Kawado Research Center, Sony Corp.	Developement of precies characterizaion techuniques for semicconductor
95-C005	S. Nakagawa Kawasaki Heavy Industries, Ltd.	Basic study of diagnostic applications of SR monochromatic X-rays to medicine
95-C006	S. Yasuami ULSI Reserach Center, Toshiba Corp.	Analysis of microscopic structures using synchrotron radiation
95-C007	H. Hashimoto Toray Research Center	Studies of melts by means of XAFS
95-C008	K. Ogawa Fuji Photo Film Co., Ltd.	Local structure analysis of photographic silver halides
95-C009	N. Ishikawa	
95-C010	Y. Iketaki Research Development Corporation of Japan	
95C011	T. Akai Mitsubishi Chemical Corp.	XAFS studies of metal catarysts for polymer resin synthesis
95-C012	K. Sudo Mitsui Toasu Chemicals, Inc.	Strucural Studies on complexes used for liquied phase autoxidation by XAFS
95-C013	K. Murakami Nicon Corp.	Characterization of X-ray multilayer reflecting mirrors using synchrotron radiation
95-C014	S. Komiya Fujitsu Laboraes Ltd.	Structure analysis of thin film interface
95-C015	K. Kuroda Central Research Laboratory, HitachLtd.	Study of X-ray Imaging

Proposal Number	Spokesperson	Title
95-C016	S. Okude NKK Corp.	Chemical state determination based on synchrotron radiation
95-C017	M. Ohsawa Fuji Electric Corporate Reserach and Deelopment, Ltd.	Highly sensitive structure analysis of thin films by synchrotron Radiation
95-C018	T. Kiyokura Interdisciplinary Research Laboratory, NTT	
95-C019	D. Amano Sumitomo Heavy Industries, Ltd.	Basic research on the design study of insertion devices
95-C020	A. Komura Hitaachi Zosen Corp.	Development of monochromator for high brilliance Synchrotron Radiation

G : General
P : Preliminary
Y : Approved for charged beam time.
C : Collaborations between the Photon Factory and institutes of private companies.

Introduction

INTRODUCTION

The Photon Factory at the National Laboratory for High Energy Physics is a national user's facility for scientific research utilizing synchrotron radiation. User's proposals for experiments utilizing synchrotron radiation at the Photon Factory are accepted internationally from any interested party. The facility is funded and operated by the Monbusho (Japanese Ministry of Education, Science, Sports and Culture). The organization consists of three divisions, the Injector Linac Division, Light Source Division and the Instrumentation Division. Altogether the Photon Factory operates the linear injector, two light sources including the 2.5 GeV storage ring and the 6.5 GeV TRISTAN Accumulation Ring as well as a major fraction of their beamlines and experimental stations.

The construction of the main facility, the 2.5 GeV dedicated storage ring started in 1978 and user's experiments started in 1982. Now in the 13th year of operation, this ring has become an extremely reliable light source with very high performance. Currently the ring is filled up to 370 mA, with the life-time of 60 hours and an emittance of 130 nmrad in normal multi-bunch operation. Usually injection is done once a day in the morning. In order to further reduce the emittance down to 27 nmrad and remain competitive with third generation rings, the "High Brilliance Project" has been underway. This involves adding 34 new quadrupole magnets and 32 new sextupole magnets to the storage ring. The installation is scheduled for a 9 months shut-down in 1997.

As of 1995, 61 experimental stations are in operation at the 2.5 GeV storage ring and the construction of new stations still continues. Recently, efforts to replace some of the older beamlines with outdated designs by new state-of-the-art beamlines have been in progress ("Scrap-and-build" projects). Such beamlines include BL4C for X-ray magnetic Bragg scattering, BL6B for protein crystallography, BL12C for XAFS, BL16B high resolution 24m SGM, and BL18C for powder diffraction in non-ambient conditions.

The TRISTAN Accumulation Ring (AR) is the injector for the TRISTAN Main Ring which is an electron-positron collider for high energy physics research. Parasitic operation of the AR at 6.5 GeV for synchrotron radiation started in 1987. Two insertion devices have been installed and 6 experimental stations have been built. Research projects utilizing the unique characteristics of this light source, high energy and single bunch operation have been actively pursued at the AR. From next year, replacement of the TRISTAN Main Ring with the KEKB facility and the upgrade of the injector LINAC will free the AR from operation as an injector. Possibilities of the subsequent conversion of the AR into an upgraded dedicated light source are being considered.

User's research has been extremely active with 399 proposals approved in 1995. Highlights of the activities in various fields are summarized in the "Scientific Disciplines" chapter.

Further facility development projects currently in progress include the following.

TRISTAN Super Light Facility (TSLF) Project: A three months experimental operation of the TRISTAN Main Ring (MR) for synchrotron radiation with very high brilliance (TRISTAN Super Light Facility) is scheduled for late 1995. This involves 10GeV operation of the MR to achieve extremely low emittance and the usage of a 5.2 meter long undulator. All of the beamline components including the monochromator have been designed, fabricated and installed.

VUV-FEL Project: Development of a short-wavelength free electron laser in the vacuum ultra-violet region has been continuing since 1992 at the BL2 straight section of the 2.5 GeV Photon Factory storage ring.

KEKB Project: The Injector Linac Division of the Photon Factory takes the responsibility to upgrade the Injector Linac for the KEKB project. The B-factory, which is the biggest future project for KEK, is a new high-energy electron-positron collider with asymmetric energies of 8 GeV and 3.5 GeV. The

upgrade of the Linac (presently 2.5 GeV) is necessary to supply beams at the required energies.

Slow-positron Source: A group in the Injector Linac Division has been developing a slow-positron source, for potential applications in materials science research. A slow positron flux of 1×108 e^+/s has been achieved with a 2.0 GeV, 2-kW primary electron beam from the linear injector.

Collaborative research has been as active as ever this year. Synchrotron Radiation Laboratory of the Institute for Solid State Physics of the University of Tokyo has been operating three experimental stations, BL18A, BL19A and BL19B. Research Center for Spectrochemistry of the University of Tokyo has operated their own experimental stations BL7A, and BL7B for many years and has mostly conducted surface science research. Research on advanced material characterization has been conducted at BL13 as collaborative projects between the Photon Factory and NIMC. Four industrial companies, NTT, Hitachi, NEC and Fujitsu have been operating their beamlines. The Australian National Beamline Facility has also been successfully commissioned.

Scientific Disciplines

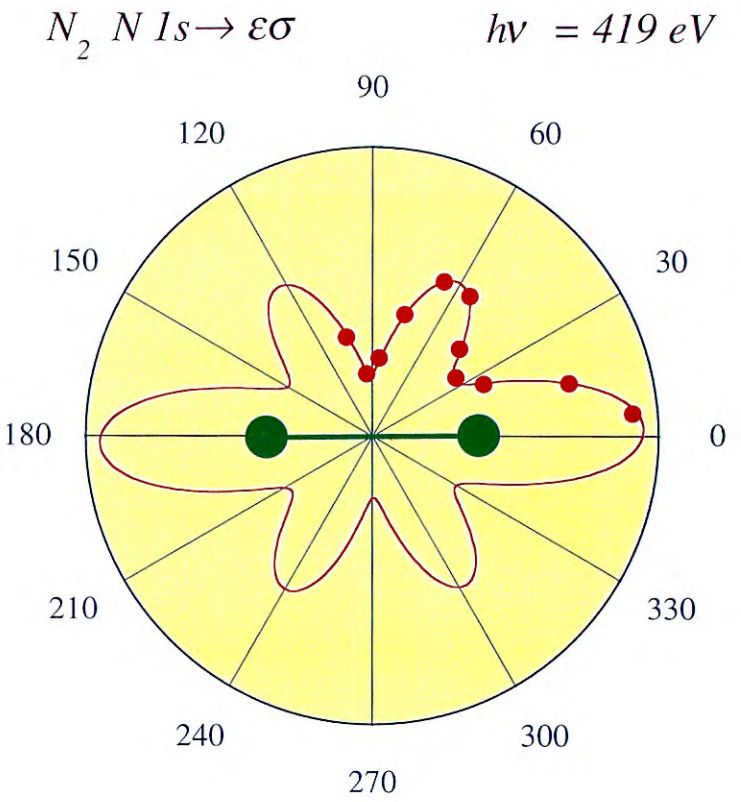

Angular distributions of 1 $s\sigma$ photoelectrons from fixed-in-space molecules at the shape resonance for a parallel transition.

CONTENTS

A. ELECTRONIC PROPERTIES OF CONDENSED MATTERS (Soft X-Rays)

In FY 1995, modification of linear polarization into circular polarization was accomplished in the low photon energy region below 30eV (94-G180), though circularly polarized light in the VUV and soft x-ray region produced by a helical undulator continued to be used for studies on magnetism. Polarization technique has been used also in emission spectroscopy to clarify whether the memory of the polarization of the incident light is preserved or not in the emitted light. In future the polarization analysis of emitted light will have more chance to be used to study various relaxation processes following core excitations.

Photon stimulated desorption (PSD) following inner-shell excitation has become a much more popular and established technique compared in FY 1994. Some discussions have been presented on how the excess energy is delocalized or remains localized before breaking a chemical bond (95-G410, 94-G360).

Angle resolved photoemission has been employed basically in two directions. One is to map the bulk and surface band structures in the k space in various materials (94-G191, 94-G186, 94-G366, 95-G384), where the photoelectrons were assumed not to be diffracted after excitation. The other is to study surface structures by observing the diffracted photoelectrons (94-G189, 95-G374, 94-G368, 94-G198). These two aspects are complementary because the electronic structure depends on the atomic arrangement in solids or surfaces, while the latter corresponds to the minimum electronic energy in the ground state.

Absorption spectroscopy (XAS) and angle-integrared photoemission spectroscopy (XPS) has still been a powerful technique though it seems "old-fashoned" under the presence of new methods such as emission spectroscopy. An apparent advantage of XAS and XPS is that it gives a good S/N ratio of the obtained signals even using incident photons with very good energy resolution and good polariztion characteristics. For instance a very small difference beteen O 1s absorption spectra at different temperatures was detected to study magnetic transition in $LaCoO_3$ (94-G361). A small concentration dependence was also observed in $La_{1-x}Sr_xCuO_{2.5}$ (94-G361), where polarization dependence was measured for a one-dimensional organic compound.

Total photoelectron yield method has been also employed instead of real XAS measurements especially when the real absorption measurement is difficult due to the thickness or the surface roughness of samples. It was used both for ordinary XAS measurement (95-G374) and magnetic circular dichroism (MCD) measurement (95-G411).

Some other activities have made their purposes focused not on the electronic or atomic structure of materials but on determination of the inelastic mean free path of photoelectrons in solids (94-G365) or on the depth profile analysis of ion implanted layers (95-G410).

An excellent attempt was made on the MCD microscope (95-G173) using a zone plate, where Ni 2p core level was measured with a partial photoelectron yield detected instead of real XAS.

In addition to the activities mentioned above great effort has been made to perform so-called high resolution photoelectron spectroscopy using an electron energy analizer SES200. Some primary studies have been carried out at BL3B and at BL2B under the proposal No. 92-S002. The typical overall resolution was 40 meV at the 4d-4f giant resonance region of rare earth elements. More than 20 samples were the target of the studies at low temperature (typically 20 K). The results are not included in this volume but will be presented in the next volume

B. ATOMIC AND MOLECULAR SCIENCE

With the high activities of atomic and molecular science at the Photon Factory as the background, The Oji International Seminar on Atomic and Molecular Photoionization was held at the Seminar Hall of Tsukuba Center Inc., from 4th through 7th 1995. The semiar was attended by 95 scientists, including 46 overseas researchers, from many areas worldwide to discuss the most advanced studies in photoionization of atoms and molecules mainly using synchrotoron radiation. In the concluding remarks at the Seminar, Professor M. Ya. Amusia mentioned to the audiences that "It was particularly good to have it in a place where so many valuable investigations in the domain of photoionization were performed and where so many exciting plans for future research in this field are created."

1. ATOMIC SPECTROSCOPY

Energy- and angle-resolved electron – electron coincidence measurements give us direct information on electron correlation. Therefore coincidence measurements are attracting the attention of many atomic and molecular physicists. However to perform the coincidence measurements, one must overcome the experimental difficulties. At the Photon Factory great efforts have been devoted over a few years, to perform the energy- and angle-resolved electron – electron coincidence measurements in double photoionization. Recently coincidence measurements were successfully done at BL-28A, which is equipped with a helical undulator to produce circularly polarized soft x-rays. The first attempt of the coincidence measurements was applied to study circular dichroism in fragmentation patterns for two-step double photoionization of Xe atom. That is, angular correlation patterns between $4d_{5/2}$ photo- and subsequent N_5-$O_{23}O_{23}$ $^1S_0$ Auger electrons in Xe have been measured for right and left circularly polarized light with 110eV energy. Figure 1 shows the polar plots of the angular correlation patterns. Comparing Figure 1(a) with (b), it is clearly demonstrated that the angular distribution of N_5-$O_{23}O_{23}$ $^1S_0$ Auger electrons in coincidence with the $4d_{5/2}$ photoelectrons, the direction of which is indicated by an arrow, is different for right and left circular polarization. Namely the fragmentation patterns for right and left circular polarization are symmetric relative to the photoelectron detection direction. The patterns are predicted by the polarization parameters and the amplitudes and phase shifts of dipole matrix elements for relevant photoionization channels. Theoretical predictions expressed by solid curves in Figure 1 reproduce the experimental results fairy well. Because the symmetry treatment for the two

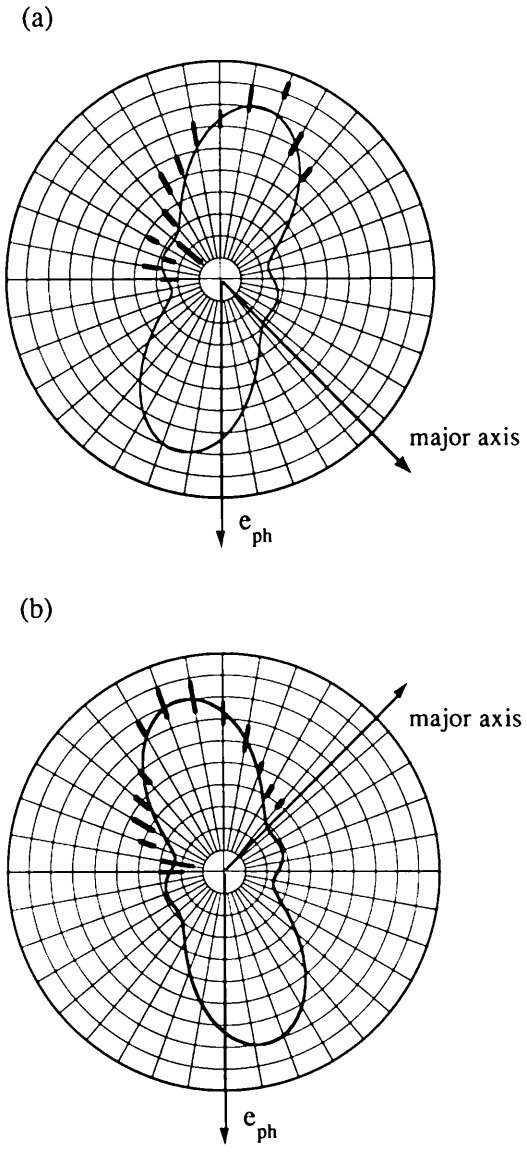

Fig. 1 Polar plots of angular correlation between the $4d_{5/2}$ photoelectrons and the N_5-$O_{23}O_{23}$ $^1S_0$ Auger electron of xenon in a plane perpendicular to the photon beam direction for right circularly polarized photon (a) and for left circularly polarized photon (b), the energy of which is 110 eV. The major axis of the polarization ellipse is indicated by an arrow in each figure. The $4d_{5/2}$ photoelectrons are observed in the direction of e_{ph}. The intensities of true coincident N_5-$O_{23}O_{23}$ $^1S_0$ Auger electrons are given with error bars. K. Soejima, M. Shinbo, A. Danjo, K. Okuno, E. Shigemasa, and A. Yagishita.

-step double photoionization is valid, the agreement between the experimental and theoretical results implies that the values of the dipole matrix elements, which are used here, are correct.

The continuous improvement of a merging beam apparatus for photoabsorption spectroscopy of free ions enables one to study the photoabsorption of rare gas ions at BL-3B. Figure 2 shows the 4d photoabsorption spectrum of singly charged Xe ions. To recognize the change of spectral profiles from neutral Xe atoms to Xe^+ ions, the Xe 4d spectrum is also shown in Figure 2. One can see the dramatic change of the spectral profiles for the 4d giant resonance between neutral Xe atoms and Xe^+ ions. In the Xe^+ specteum, two broad structures are revealed. According to MCDF calculations, the second broad structure having the peak at about 100eV consists of numerous two-electron transitions, 4d→4f and 5p→np, oscillator strengths of which

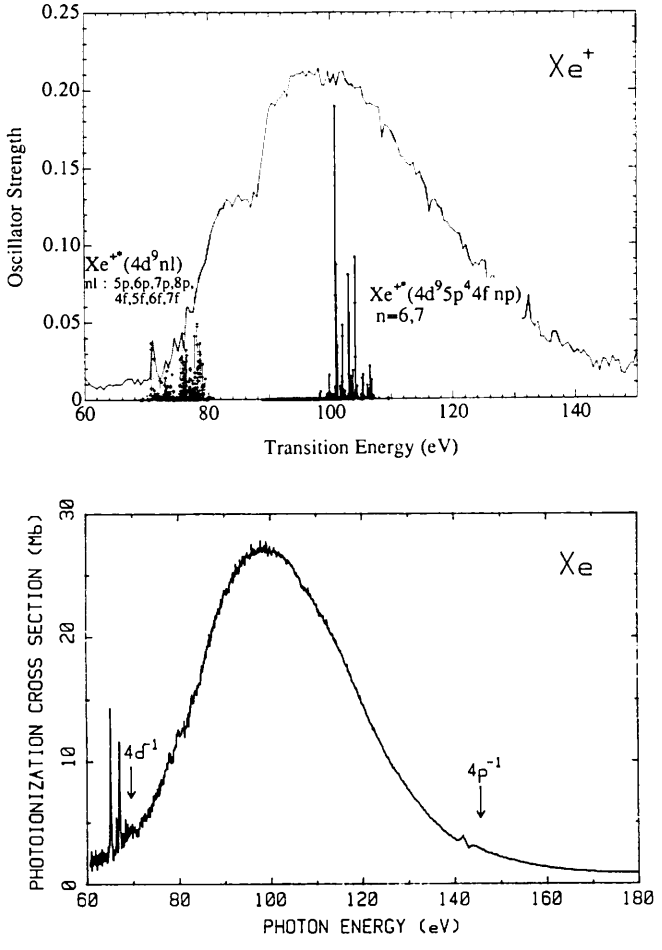

Fig. 2 4d photoabsorption spectra of Xe^+ ions and Xe atoms. M. Sano, Y. Itoh, T. Koizumi, T. M. Kojima, S. D. Kravis, M. Oura, T. Sekioka, N. Watanabe, Y. Awaya, and F. Koike.

are indicated by bars in the figure. In these configurations, the 4f orbital is fully collapsed. Then the two-electron transitions exhaust about 50% of the oscillator strength for 4d photoabsorption. The strongest 4d→5p transitions at about 56eV are not shown in the figure. The first broad structure around 84eV in the continua is considered to be part of a shape resonance. One can see the overall profile of the shape resonance in the spectrum for neutral Xe atoms. In neutral Xe atoms, the two-electron transitions can not induce the 4f orbital collapse. Then the oscilator strengths for the two-electron transitions, 4d→εf and 5p→np, are very weak in Xe atoms. The weak structure around 80eV is due to two-electron transitions. It should be emphasized that the 4f orbital collapse is very sensitive to the outermost electrons.

2. MOLECULAR SPECTROSCOPY

2.1 Valence Electronic Excitaton

Even for the simplest molecule, H_2, having two valence electrons, the potential curves are rather complicated. To search for autoionizing states embedded in continnum states of H_2 molecules, intensive studies by angle-resolved proton spectroscopy have been done at BL-20B. The kinetic energy spectra of protons emitted from hydrogen molecules are shown in Figure 3. Two sets of the spectra were measured at 0° and 90° relative to the electric vector of the linearly polarized incident light. Peak A in the spectra at 90° shifts to the higher energy side with increasing photon energy and attains its maximum intensity at $h\nu = 35$eV. That is, the peak energy moves from 6eV to 9eV when the photon energy changes from 32eV to 38eV. As the origin of peak A, two candidates are considered; direct process leading to repulsive H_2^+ $2p\sigma_u$ ionic state and indirect process via autoionization. If the peak is to be ascribed to direct photoionization, then the dipole matrix elements would have to be very large just when the photoelectron energy is close to zero in order to reproduce the narrow width of peak A. Steep energy dependence of the dipole matrix elements is unlikely. Then one should take the indirect process into account. The peak A appears above the threshold of the H_2^+ $2p\sigma_u$ state, so a Q_2 autoionizing state should be considered. The Q_2 state associated with the $2p\sigma$ state of H_2^+ have two possible decay pathways; it can autoionize either to $2p\sigma_u$ or to $1s\sigma_g$ state. The decay pathways between poten-

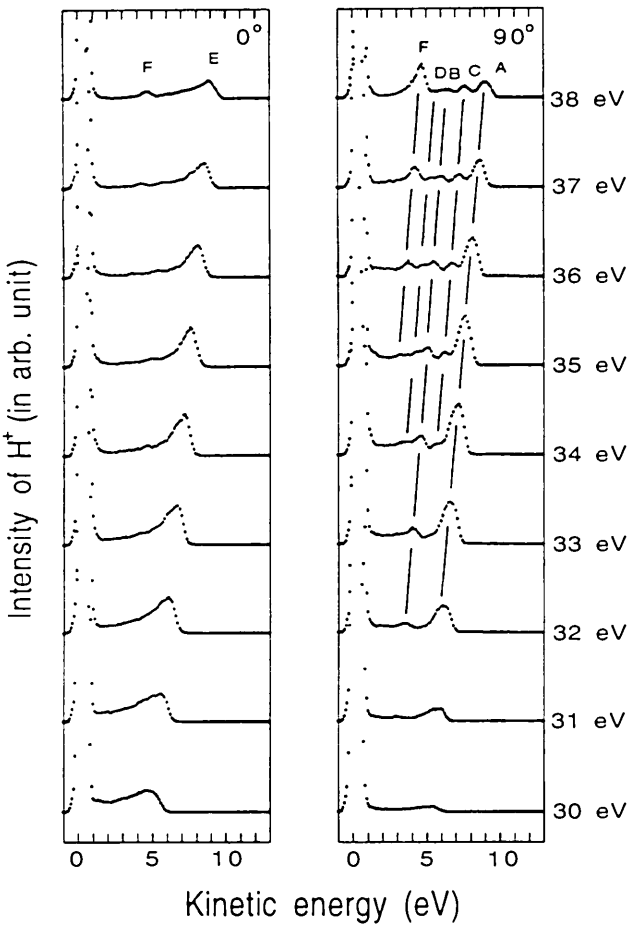

Fig. 3 Kinetic energy distributions of protons produced via dissociative photoionization of molecular hydrogen for incident photon energies 30-38 eV observed at 0° and 90° with respect to the electric vector of the incident radiation. Peaks A-D are attributed to autoionization of $Q_2\ ^1\Pi_u$ states to the H_2^+ $2p\sigma_u$ and $1s\sigma_g$ states. Peaks E is due to direct ionization to the H_2^+ $2p\sigma_u$ and autoionization of the $Q_2\ ^1\Sigma_u^+$ state, and peak F due to direct ionization of the $2p\pi_u$ states. K. Ito, R. I. Hall, and M. Ukai.

tial curves are illustrated in Figure 4. For autoionization to the $2p\sigma_u$ state the kinetic energy release is KE1 + KE2. The energy release decreases monotonically with increasing internuclear distance. Conversely, the energy release KE3 via autoionization to the $1s\sigma_g$ state increases with increasing internuclear distance. As can be seen in Figure 4, It is evident that KE3 is always smaller than KE1 + KE2. In fact, another peak designated as B appears from $h\nu = 32$ eV along with the appearence of the peak A. As demonstrated here, one can obtain the information of veiled potential curves from detailed analyses of angle-resolved proton spectroscopy.

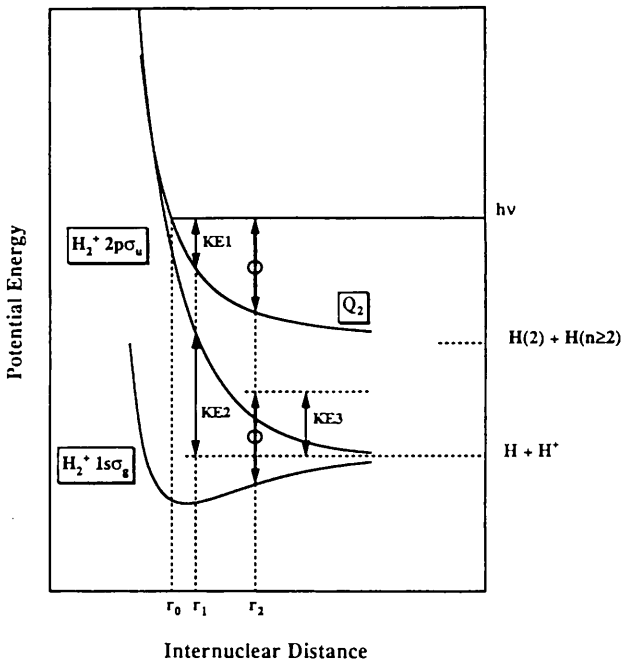

Fig. 4 Schematic of the autoionization of a Q_2 state with an excitation energy of $h\nu$. This state can autoionize either to the $2p\sigma_u$ or $1s\sigma_g$ states of H_2^+. The energy released by the dissociation process is KE1 + KE2 and KE3 for the former and the latter autoionization process, respectively. K. Ito, R. I. Hall and M. Ukai.

2.2 Core Electronic Excitation

Symmetry-resolved soft x-ray spectroscopy, developed at the Photon Factory, has been applied to linear triatomic molecules to investigate their molecular and electronic structures in core-excited states, at BL-2B. Figure 5 shows the high-resolution symmetry-resolved O K-edge spectra of N_2O. At the π^* resonance of peak 1, the symmetry decomposition in the spectra was insufficient. When the N_2O molecule is bent, the π^* orbitals lose the degeneracy in $C_{\infty v}$ symmetry, and have two components, a″ (out-of-plane π^*) and a′ (in-plane π^*) in C_s symmetry. In the O 1s→a′ π^* (in-plane) excited state the caluculated bond lengths N-N and N-O are slightly shortened and largely lengthened, respectively, from those of the ground state, and the molecule is strongly bent within the range of the N-N-O angle about 112~115°. On the other hand, in the O 1s→a″ π^* (out-of-plane) excited state the molecular structure has a linear stable one as well as in the ground state. The O 1s→a′ π^* excited state is much lower in energy than the O 1s→a″ π^*. The energy lowering by bending the linear molecules in the degenerate state is called the Renner-Teller effect.

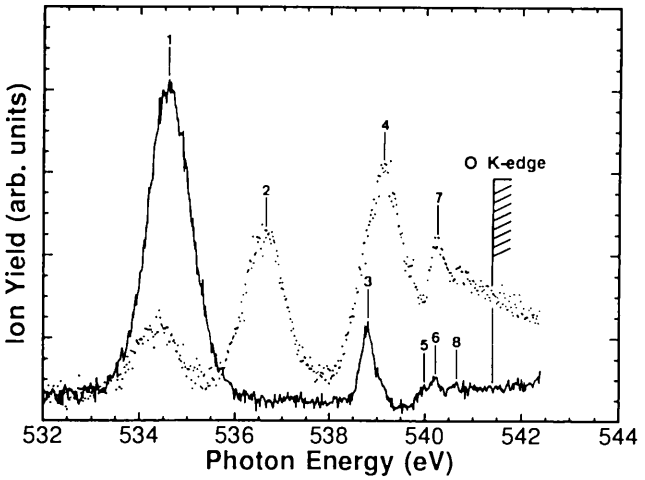

Fig. 5 O K-edge high-resolution ion yield spectra of N_2O. The spectrum expressed by the solid line was observed at 90° with respect to the polarization direction, and the spectrum by the dotted line at 0° . J. Adachi, N. Kosugi, E. Shigemasa, and A. Yagishita.

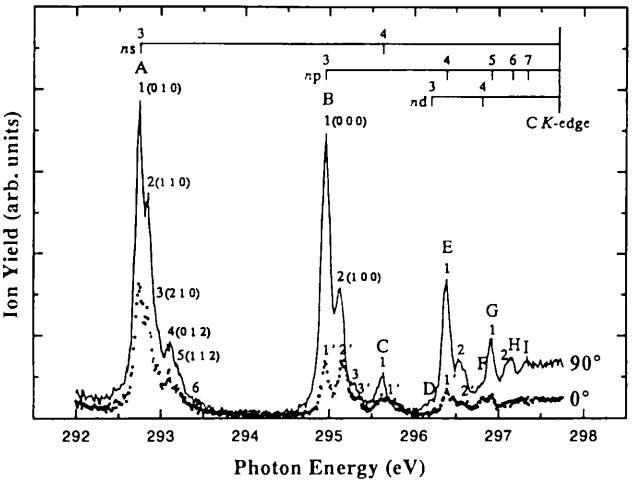

Fig. 6 Angle-resolved ion-yield spectra in the C 1s→ Rydberg region of CO_2, measured with the high resolution of 70 meV. The solid line spectrum is observed at the 90° direction with respect to the polarization direction, and the dotted line at the 0°. J. Adachi, N. Kosugi, E. Shigemasa, and A. Yagishita.

According to the Franck-Condon principle, the bending mode is not excited in the transition to the a″ π^* state, but is strongly excited in the a′ π^* state that is lower in energy than the a″ π^* state. Then, it is considered that the fragment ion intensities, observed at the parallel direction (0°) relative to the electric vector of the incident light, arise mainly from the bending mode in the a′ π^* state stabilized by the Renner-Teller effect. The peaks numberd from 2 to 8 in Figure 5 are assigned to the O 1s→Rydberg transitions with the help of theoretical calculations for the vertical transitions. In the Rydberg transition region, the symmetries of the excited states are perfectly resolved. This means that the bending motion has no contribution to the Rydberg excited states. This is the reflection of the fact that the molecular geometries of the Rydberg states are nearly identical to the geometry of the ionized state with a linear structure and the Rener-Teller effect is negligibly weak even in degenerate π-type Rydberg states. The anomalous feature in the Rydberg series, very large intensities and widths of Peak 2 (3sσ) and 4(4sσ), should be noticed in Figure 5. The irregularity is cased by the Rydberg-valence mixing through avoided crossings between the potential energy curves of the Rydberg and valence states. The most probable valence state contributing to the mixing is the s-type σ^* located below the ionization threshold.

Figure 6 shows the high-resolution symmetry-resolved C 1s→Ryberg excitation spectra of CO_2. The C 1s→ns(n=3,4), npπ, σ(n=3−7), and nd(n=3,4) are clearly observed, some of which show vibrational structures. Contrary to one's expectations from the Ryderg spectra of diatomic molecules, the dipole-forbidden C 1sσ_g →3sσ_g Rydberg transition is the strongest among the Rydberg transitions, and the fragment ions are ejected predominantly towards the direction unexpected from the symmetry consideration, i.e., the perpendicular direction (90 °) relative to the electric vector of the incident light. Because the C 1σ_g→3sσ_g Rydberg state has a stable linear geometry and the linear 3sσ_g Rydberg state can not be reached by photoabsorption, the unexpected experimental results should be related to the symmetry of the dipole-allowed intensity-lending states mixed with the 3sσ_g state through the vibronic coupling. The results indicate directly that the dipole-allowed state mixed with the 3sσ_g Rydberg state has π_u symmetry, that is, the 3sσ_g state is strongly coupled with the bending mode. The dipole-allowed intensity-lending state with the σ_u symmetry is the π^* resonance state located at 290.77eV corresponding to C 1s→unoccupied 2π_u transition. Except for the 3sσ_g and 4s π_g Rydberg states, the symmetries of the Rydgerg sates are resolved in Figure 6, because stretching vibrations are mainly excited in these states.

C. X-Ray Imaging

1. Phase-constrast X-ray computed tomography

At BL-14B, phase-contrast X-ray computed tomography (CT) has been developed[1-3]. This novel technique uses an X-ray interferometer. In reconstructing tomographic images, the spatial distribution of X-ray phase shift, or the phase-mapping image, caused by an object needs to be measured. For this purpose, a fringe scanning method[4] that is used in visible light interferometry was employed for the definitive determination of phase shift. Tomograms that display the inner distribution of the refractive index were reconstructed from phase-mapping images using a standard CT algorithm.

The advantage of phase-contrast X-ray imaging is its high sensitivity to weakly X-ray absorbing objects. Conventional techniques for inner observation using X-rays depends on X-ray absorption to create image contrast. However, the absorption coefficients of light elements, such as hydrogen, carbon, nitrogen, and oxygen, are insufficient for creating image contrast. In contrast, the X-ray phase shift cross section is almost a thousand times greater than the X-ray absorption cross section for light elements[5]. Hence, phase-contrast X-ray imaging is a promising technique for observing the structure inside biological soft tissues without the need for staining and without serious radiation exposure.

The structure of the X-ray interferometer is a typical triple Laue-case[6]; i.e., three parallel crystal slabs are monolithically cut out from the block of a perfect silicon crystal having the same gaps (Figure 1). The slabs function as X-ray half mirrors when the Bragg diffraction condition is satisfied. Consequently, Mach-Zehnder type interfering beam paths are created. When an object is placed in the path of one beam (object beam), one can see an interference pattern corresponding to the spatial distribution of the phase shift caused by an object.

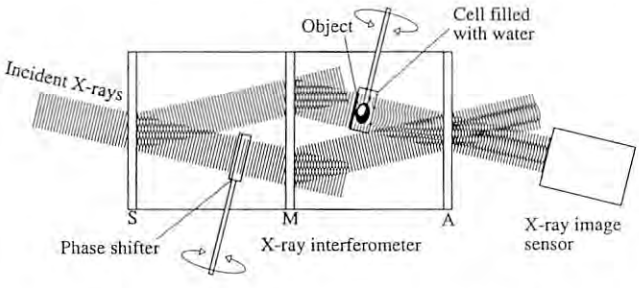

Fig.1 X-ray interferometer and beam paths.

The fringe scanning method uses a phase shifter as shown in Fig. 1. When the phase difference between the object beam and the reference beam is varied by rotating the phase shifter, one can see the interference fringes move. The displacement of the fringe definitively depends on the phase shift caused by the object. Therefore, a phase-mapping image can be obtained by analyzing the fringe movements. The fringe scanning method provides an algorithm for producing a phase-mapping image from several interference patterns observed by varying the phase difference step by step.

The experimental setup is shown in Figure 2. X-rays from a vertical wiggler were introduced to the X-ray interferometer through a double-crystal monochromator. The vertical wiggler source was convenient for setting up high-throughput optics using the X-ray interferometer because the beam is linearly polarized and divergent in the vertical direction. A collimator crystal was used to widen the beam section in this case. A sample was immersed in a water-filled cell placed in the object beam path to observe it in a wet environment. For a CT scan, the sample was rotated in the cell step by step. A plastic phase shifter was placed in the reference beam path for the fringe scans. A ten-step fringe scan was performed at every angular setting of sample rotation. Interference patterns were detected with an X-ray sensing pickup tube[7] whose optimal spatial resolution was eight microns. Because this is an image detector, a

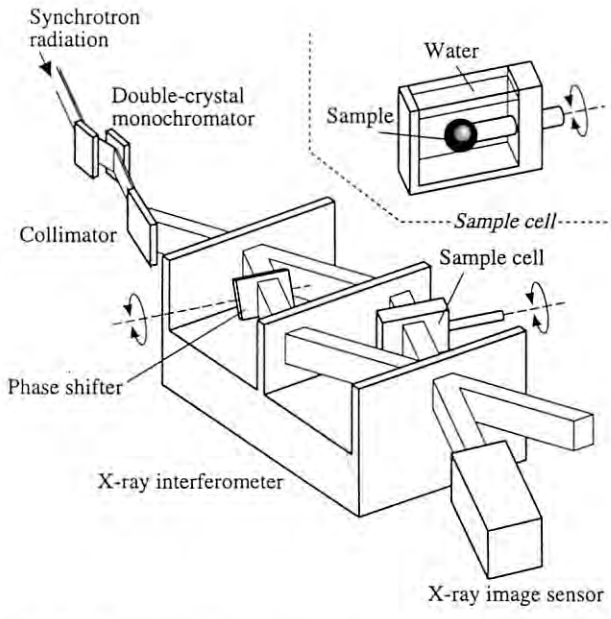

Fig.2 Experimental setup for phase-contrast X-ray CT.

series of tomograms can be reconstructed using one CT scan.

Figure 3(a) is a phase-contrast X-ray tomogram of a cancerous rabbit liver obtained using 0.7-Å X-rays. Two hundred phase-mapping images were acquired over 180-degree rotation of the sample to create the tomogram. The left part of the image corresponds to the cancer lesion. The opposite side is normal liver tissue. Moreover, structures in the tumor can be seen. The bright-contrast area can be identified as a degenerated lesion, while the dark area is nondegenerated. Fibrous structures are also depicted in the marginal region of the tumor. Figure 3(b) is a three-dimensional expression of the entire body of data made by stacking all tomograms. To show the inside, one quadrant has been cropped.

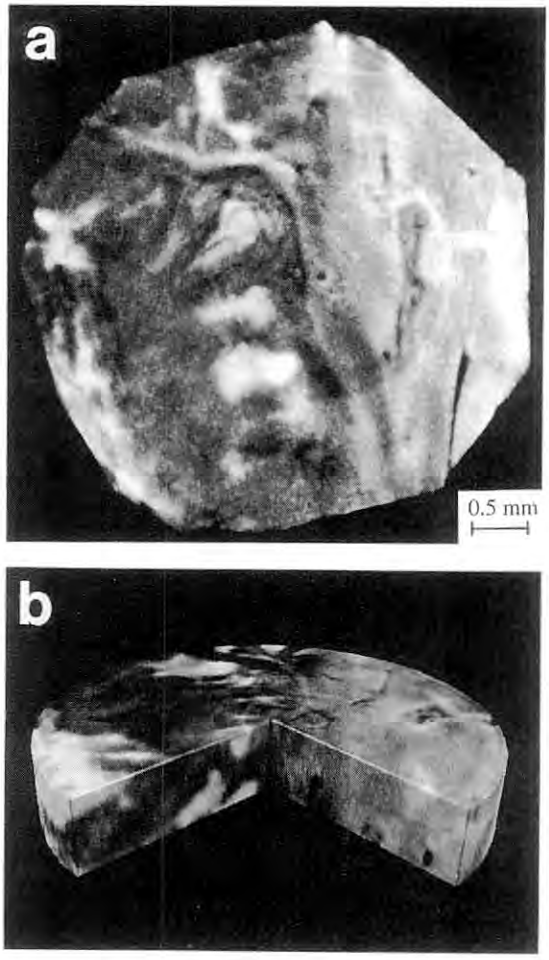

Fig.3 (a) A phase-contrast tomogram of a cancerous rabbit liver. The left half corresponds to the cancer lesion. (b) 3D expression of the entire body of data has been made by stacking all tomograms (one quadrant has been cropped to show inside).

Thus, high sensitivity of the phase-contrast X-ray CT has been well demonstrated. This technique is expected to provide us with a new opportunity for investigating biological tissues and organic materials.

References

1) A. Momose, Nucl. Instrum. Meth. A352, 622 (1995).
2) A. Momose, T. Takeda, and Y. Itai, Rev. Sci. Instrum. 66, 1434 (1995).
3) A. Momose, T. Takeda, Y. Itai, and K. Hirano, Nature Medicine 2, 473 (1996).
4) J. H. Bruning, et al., Appl. Opt. 13, 2693 (1974).
5) A. Momose and J. Fukuda, Med. Phys. 22, 375 (1995).
6) U. Bonse and M. Hart, Appl. Phys. Lett. 6, 155 (1965).
7) Y. Suzuki, et al., Rev. Sci. Instrum. 60, 2299 (1989).

2. Ecological study of the migration of eel by SR - X-ray fluorescence imaging of otoliths[1)]

In spite of the popularity of eels as a Japanese favorite cuisine, only a few people know that the spawning area of the freshwater eels is in the North Equatorial Current west of the Mariana Islands, which was recently discovered by Tsukamoto[2)]. Japanese eels migrates 2000km from the spawning area to the Japanese rivers in 4 to 6 months. Because of the long distance and long term of the migration, it was difficult to pursue their life history. Synchrotron radiation X-ray fluorescence (XRF) imaging was used to clarify the secret of the migratory history of the eels.

The inner ear of fish contains a set of two tiny particles of calcium carbonate $CaCO_3$, known as otoliths, which functions as the organ of equilibrium: if the head moves, the otoliths change position. In shifting, they pass over sensitive nerve endings and send immediate impulses to the brain. The otoliths grow with the age of fish; the source of Ca and CO_2 is from water, the environments. Consequently, based on daily growth increments on the otoliths, we can estimate the ages of fish by measuring the tree ring pattern developed in the otoliths. It is easily presumed that calcium carbonate precipitates together with trace elements in environments with daily growth increments. Chemical analyses of otoliths of various fish including

marine habitats and river habitats indicated that concentration of Sr in the otolith of marine habitat fishes is more than two to three times higher than that of the fresh water habitat fishes. It is known that the Sr concentration of sea water is 8 ppm and that of fresh water is 0.057 ppm. The former is more than 100 times as large as that of the latter and this reflects on the Sr concentration in the otolith. Based on this principle, two dimensional analysis of Sr/Ca ratio in otoliths of various eels were carried out using SR-XRF system.

A total of 27 specimens including 17 European eels, Anguilla anguilla, collected in the North Sea and the River Elbe, and 10 Japanese eel Anguilla Japonica from the East China Sea and the Tone River were analyzed. Sagittal otolith of each fish were embedded in polyester resin and prepared for the measurements by polishing the sample from the both sides to the mid plane of 30 mm with the polishing paper. XRF measurements were made at BL 4A with the energy dispersive XRF system. Sample were excited by X-ray of 17keV obtained by a Si(111) double-crysal monochromator. A fine parallel beam of 120 μm$\times$100μm size was obtained by a set of vertical and horizontal slits. Two dimensional analysis of samples was made in air by step scanning the sample on a XY stage and XRF intensities of Sr Kα and Ca Kα were measured with counting time of 3 sec/point with step size of 50 μm. The integrated intensity of the Sr Kα line was subtracted by that of the CaKα line to produce a normalized intensity. The two dimensional image of Sr in the sample was represented by 12 colors from red, yellow, green to blue (or black to white in monochrome) corresponding to the Sr/Ca intensity ratio.

Two dimensional images of the Sr/Ca ratio in otoliths showed remarkable difference between marine habitat samples (e.g. Fig.4(a) :East China Sea) and freshwater habitats samples (e.g. Fig.4 (b) :River Tone). All river samples contained an elevated Sr region of 200$-$300μm in diameter in the core region of otolith corresponding to an early life stage, while low Sr levels occurred in the otolith's peripheral region indicating freshwater habitat. All specimens collected in the North Sea and East China Sea showed a second peripheral region of elevated Sr which was not observed in the river specimens. This observation indicates that these eels have not spent yellow and silver (juvenile and adult) stages in freshwater habitats. This is in remarkable contrast to the expected catadromous pattern shown by both Elbe and Tone river eels, which shows

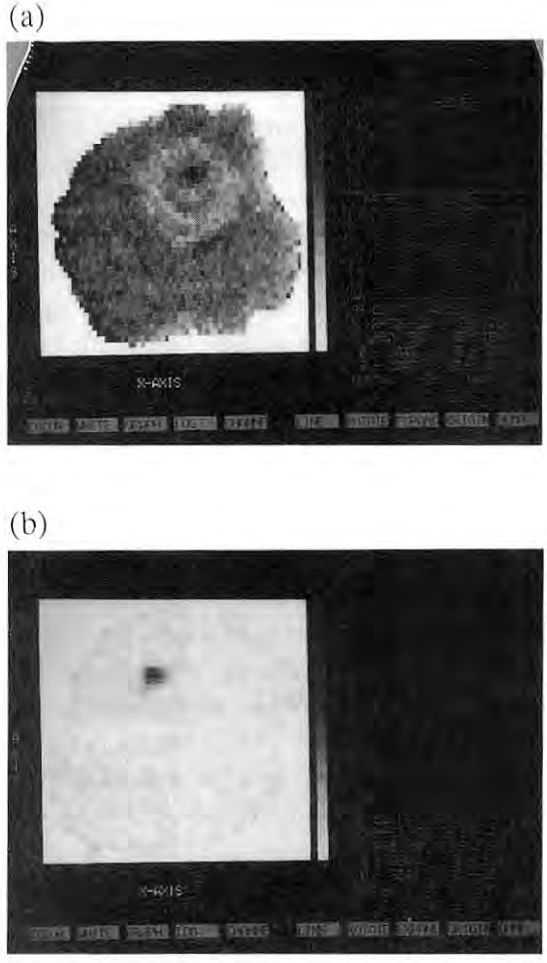

Fig.4 Two dimensional SR-XRF imaging of Sr/Ca in otoliths of (a) marine habitat sample (East China Sea) and (b)freshwater habitats sample (River Tone)

freshwater residence during juvenile and adult stages. Fish migration is generally explained by a difference in food abundance between marine and freshwater habitats. Therefore it might be predicted that sea residency by freshwater eels would occur more frequently at high latitudes where productivity of the freshwater habitat is lower compared with that of adjacent coastal regions. This is the first report of facultative catadromy or "sea-locking" in eels, which phenomenon might give a key to the understanding of evolutionary process of fish migration.

References

1) K. Tsukamoto, I. Nakai, and W-.V-. Tesch (1996) in preparation.
2) K. Tsukamoto (1992) Nature 356, 789-791.

D. Radiobiology using Synchrotron Radiation

High intensity and complete tunability from ultraviolet to X-ray region are very useful characteristics of synchrotron radiation in researches aiming at the elucidation of whole processes included in radiobiology. Research in radiobiology has been actively done since the commissioning of the Photon Factory. A variety of processes are included in radiobiological effects, some of which are familiar to physicists, some to chemists and others to biologists. In this sense, radiobiology can be said to be interdisciplinary. Today, radiobiology is attracting much attention, not only due to basic scientific interest, but also due to the practical points of view, such as the radiotherapy of cancer using heavy particles, or protection from environmental radiation of low dose rates. Two topics in radiobiology recently studied or in progress are briefly introduced in this section. First is one of the researches which need the use of radioisotopes for DNA sequencing. Since open radioisotopes became available in the BL-27 area in 1993, various research utilizing radioisotopes are being actively done.

1. Study of the Sites of Strand Breaks in DNA by Auger effect

Before SR X-rays became available, the biological effects of the Auger effect have been studied intensively by using Auger-emitting isotopes such as ^{125}I. On the other hand, it has been known that the X-rays can induce Auger effects through photoabsorption of non-Auger emitting element. Monochromatic X-rays from synchrotron radiation is very useful to investigate the enhancement of the biological effect by the Auger process since it enables us to precisely extract the true enhancement from other biological effects induced by various mechanisms including energy-independent enhancement by halogenation. Use of monochromatic X-ray in the study of Auger effects on halogenated DNA has an advantage that the halogenation of biomolecules occurs only artificially and hence we can select the element at which the Auger effects will occur. Lethality of bromine-incorporated yeast cells irradiated with monochromatic synchrotron X-rays above the bromine K-absorption edge was reported to be enhanced by 7% Auger-enhancement than with irradiation of X-rays below the edge[1]. This enhancement became greater up to 20% when irradiated under the presence of cysteamine as a radical scavenger. This result means that the lesions induced by Auger processes are produced through mechanisms rather than radical-mediated mechanism. In order to understand the mechanisms of the Auger enhancement observed in the biological system, researches in the molecular level is necessary. Not only the efficiency of the production of the strand breaks, but also the molecular structure or microscopic distribution of the strand breaks around the Auger site must be investigated, since the damages by Auger process may be different in repair susceptibility. From this point of view, DNA sequencing methods using radioisotope, ^{32}P, was adopted for analyzing the microstructure of the DNA strand, since this methods is suitable for analyzing the local structure of the lesions due to its extremely high resolution enough to discriminate even slight difference of the end structure of the cleaved site. It was found by using this method that there exist only two types of 3' termini of the radiation-induced strand breaks, phosphate and phosphoglycolate. Study on the distribution and microscopic structure of the strand breakage site in brominated oligonucleotides irradiated with the monochromatic X-rays around the bromine K-edge started recently at the Photon Factory in order to elucidate the molecular mechanism of Auger enhancement using the similar technique, since radioisotopes became available at the facility. Use of radioisotope is essential for the sequencing methods. One of the advantage of using cold bromine and tunable X-rays is that the net Auger enhancement can be estimated, being discriminated from the X-ray energy-independent enhancement by halogenation of DNA.

A 21mer single-stranded synthetic oligonucleotide containing one bromine atom per each molecule was used. The sequence is as follows;

5' TTT TTT TTT T^{Br}UT TTT TTT TTT 3'.

All the bases of the nucleotide were designed to be thymine except for the center (11th) of the strand, bromouracil, in order to prevent from forming undesirable secondary structure within one molecule or between molecules. The 5' end of the oligonucleotide was labeled with ^{32}P. For irradiation of the aqueous solution, the oligonucleotide solution was diluted to 40 pmole/ml and irradiated in an acrylic cell through a thin Kapton film window. For irradiation under dried condition, 2 μl of the solution was spotted on the acrylic plate and irradiated after dried. In both samples, the oligonucleotides were used without further purification, which means large amount of solutes in buffer and reac-

tion mixture were included in the sample. In the case of aqueous DNA, the glycerol in the kinase-reaction buffer must be act as a radical scavenger, which may be convenient for reducing the energy-independent radical reaction. The final concentration of the glycerol is 1% (about 0.1 M), which may be reasonable for radical scavenging condition. On the other hand, in the dried condition, contaminants such as glycerol can act as electron absorber, namely, the secondary electrons ejected from a bromine atom in certain oligonucleotide cannot attack other oligonucleotide due to the large amount of solutes. Irradiation was performed at the BL-27B installed in the radioisotope-usable area. The second crystal of the monochromator was bent in order to get more photon flux. X-ray energies used were 13.51 and 13.45 keV, between which the bromine K-shell absorption edge (13.47 keV) was located. Exposure rate was measured by a free-air ionization chamber[3] at the sample position. The beam intensity during irradiation was monitored by a transmission-type ionization chamber. The dose rate used in this experiment was about 10 kGy/hr.

Irradiated samples, mixed with the sequencing gel-loading buffer, were loaded into the 19% polyacrylamide-urea gel, the dimension of which was 200mm × 400mm. The gel was electrophoreses at 2000 V for 180 min to separate individual bands of the products. After electrophoresis, the gel was fixed, dried and then attached to an image plate (BAS-III, Fuji Film) overnight in order to get the radioactivity image. The image plate was then read by a reader (BAS2000, Fuji Film). The captured data was analyzed to obtain the quantity of each band. For assignment of the fragments produced by the irradiation, the oligonucleotides treated with Maxam-Gilbert sequencing reaction were also electrophoreses. The sequence of the oligonucleotides for Maxam-Gilbert reaction was

5' TTT TTT GTT TTT TTT TTT GTT 3'.

Since the 7th and 19th nucleotides are less susceptible to the cleavage reaction by hydrazine under the condition of the Maxam-Gilbert T reaction, the band images of 6mer and 18mer fragments which have phosphate at their 3' ends become dimmer than other bands. This characteristic pattern of the band distribution was used to confirm our band assignment.

An image of the electrophoresed gel of the brominated oligonucleotide irradiated under aqueous condition is shown in Fig. 1. The density profiles of the Lane 2 and 6 were shown in Fig. 2. In the samples irradiated with either energy, several intense bands appeared

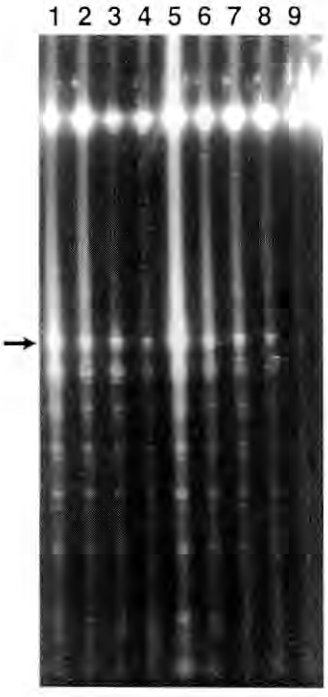

Fig. 1 Image of the electrophoresed gel of brominated oligonucleotides irradiated with monochromatized X-rays at 13.51 keV (above the bromine K-edge, Lane 1-4) and at 13.45 keV (below the edge, Lane 5-8), in aqueous solution. The irradiated doses were 720 Gy (Lane 1, 5), 240 Gy (Lane 2, 6), 80 Gy (Lane 3, 7), 28 Gy (Lane 4, 8) and 0 Gy (Lane 9). The arrows indicate the most and the next most intense band, assigned as 9mer and 8mer fragment, respectively.

around the half size of the original molecules. The most intense band (indicated as "9" in the Fig. 1), accompanied by a satellite band just below, was assigned as 9mer fragment, not 10mer which could be expected as the product cleaved at the brominated nucleotide. The 3' end structure of the main band was phosphate and the satellite was phosphate-like group, presumably, phosphoglycolate which was already detected at the termini of the radiation-induced strand breaks by Henner et al.[2]. The next most intense band, appeared below the 9mer fragment, was assigned as 8mer fragment (indicated as "8" in the Fig. 1). Obtained profiles were very similar with the results by Martin et al. in which the site of the strand breaks of double-stranded oligonucleotide containing ^{125}I was analyzed[4].

Regarding the dependence of distribution of the products on the irradiated energy, the production ratio of the most intense band (9mer fragment) against a band far from the bromine site was compared with the irradiated energy. Ratio of the product amount of 9mer

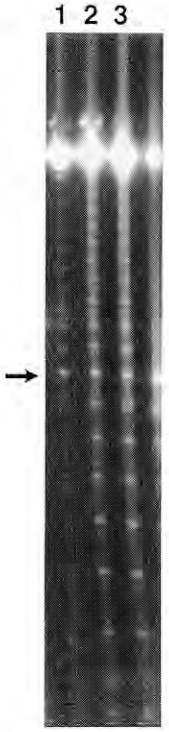

Fig. 2 Image of the electrophoresed gel of brominated oligonucleotides irradiated with monochromatized X-rays at 13.51 keV (above the bromine K-edge, Lane 2) and at 13.45 keV (below the edge, Lane 3), under dried condition. The irradiated dose was 5 kGy at each energy. Lane 1 was a unirradiated oligonucleotide. The positions of the arrows are the same as that in the Figure 1.

fragment against 5mer fragment was almost same. This means that the product distribution does not change with inner shell ionization of bromine. Fragment distribution, common to both irradiation energies, is considered to be derived not from bromine Auger process, but from debromination of the DNA due to the attack of water radicals.

The same oligonucleotides were also irradiated under the dried condition in order to increase the atomic fraction of bromine in the sample and to increase number of Auger events relatively. The image of the product distribution on the gel was shown in Figure 3. Two characteristics are remarkable when compared with the aqueous samples. First is that each fragment was produced with almost similar efficiency. The 9mer band, which was produced with the highest efficiency in the aqueous samples, was not so intense. This result indicates that the site of the strand breaks is not correlated with the site of bromination in the oligonucleotides irradiated under dried condition. The second is that the fragments having phosphoglycolate termini were much less produced than those having phosphate termini, which was a good contrast to the sample irradiated in aqueous condition. Difference in the distribution pattern due to the net Auger effect was not clearly observed in the dry condition, either.

As shown above, DNA sequencing gel technique, combined with use of radioisotopes, is a powerful tool to determine the precise site and the local structure of the strand breaks. Owing to the progress of the oligonucleotide synthesis technique, the oligonucleotide having halogenated base(s) at the defined site(s) can be commercially available. This method enabled us to investigate the correlation between the Auger-emission site and the strand breakage site. Up to now, results directly related to the Auger process have not been obtained. Further experiments with newly designed samples are under way.

2. Production yield of adenine from ATP irradiated with monochromatic X-rays in aqueous solution of different concentrations.

Study of radiation-induced chemical reactions in aqueous system and determination of the yields of various species, both intermediates and end-products is very important in understanding cellular mechanism of radiation, since yields of these species may, in some part, determine production efficiencies of the molecular damage and hence, the induction efficiencies of biological effects in aqueous system. One of the examples is the oxidation yield of ferrous solution (Fricke solution), which gives a measure of absorbed dose in aqueous solution through the yield of water radicals. The yield was found to decrease with the energy of X-rays from 15 keV down to 1.8 keV[5]. All X-ray photons in this energy region are absorbed via photoelectric effect and the kinetic energy of the photoelectrons is equal to the photon energy minus the binding energy of the electrons. In aqueous system almost all absorption events can be considered to occur at the oxygen atom in water molecule. With lower energy photons, nearly monoenergetic photoelectrons having less energy are produced. Lower energy electrons produce ionization and/or electrons with higher density (high LET). In aqueous solution, radicals produced by the energy deposition of electrons react with various solutes in the system and even do so with other radicals to annihilate or to become less hazardous. This leads us to the com-

monly accepted idea that higher LET radiation gives lower radical yields and hence lower yields of chemical consequences, radicals produced densely have higher probability to annihilate by the reaction between them. Our results on the photon energy dependence of the yield of ferric ions are in accordance with this idea.

On the contrary we already reported that the Auger effect occurring at the phosphorus atom gives higher yield of production of adenine from ATP, extent of which was higher in the more concentrated solution[6]. Biological effects were also found to be enhanced by the Auger effects at phosphorus atom[7]. Considering that the Auger effect produces ionizations with high density around the atom, these results led us to a hypothesis that there are two type of reaction fields in irradiated aqueous system; one can be called "hot area" where reactions between radicals can occur, the other called "cold area" where biologically important molecules are attacked by radicals which have diffused out of "hot area". Size of the hot area can be estimated as small as the order of nm. Hence, only solute molecule with high concentration could participate in the reactions in the area. The hypothesis may predict that the higher chemical yield in higher LET radiation field might be observable only in concentrated solutions. Since intracellular circumstance is dense aqueous solution, although not homogeneous, our observation on the biological enhancement by the Auger effect of phosphorus seems to be explained with the hypothesis above.

In order to test the hypothesis, we measured the production yield of adenine from ATP irradiated with monochromatic X-rays from 2 keV to 15 keV with two concentrations differing 100 folds. In the dilute sample, probability of solute molecule participating in the reactions in the hot area seems very small, and hence the yield in dilute samples could be considered as the results of the reactions in the cold area. Observed energy dependence of the yield in dilute solution was similar to the Fricke solution, while that of the concentrated solution was not. And also the dependence on the Auger effects was completely opposite, namely, enhanced in concentrated solution but suppresses in dilute solution.

Recently, biological effects of high LET radiation such as heavy particles attract much attention not only due to basic interest but also from the practical points of view such as radiotherapy of cancer and health problem in manned space projects. Study on the reaction mechanism in concentrated aqueous solutions irradiated with low energy X-rays is expected to give us a clue to understanding the effect of high LET radiation on cells, although attention should be paid to the inhomogeneity in intra-cellular circumstances.

References

(1) Usami N, Kobayashi K, Maezawa H, Hieda K, Ishizaka S., Int. J. Radiat. Biol., **60**, 757-768 (1991).

(2) Henner, W.D., Rodriguez, L.O., Hecht, S.M., Haseltine, W.A, J. Biol. Chem., **258**, 711-713 (1983).

(3) Kobayashi, K., Hieda, K., Maezawa. H., Ando, M., Ito, T. J. Radiat. Res., **28**, 243-253 (1987).

(4) Martin. R.F., D'Cunha, G., "Biophysical Aspect of Auger Processes" AAPM Symposium Series No.8, 153-163 (1992).

(5) Watanabe, R., Usami, N. and Kobayashi, K., Int. J. Radiat. Biol., **68**, 113-120 (1995)

(6) Watanabe, R., Ishikawa, M., Kobayashi, K. and Takakura, K., "Biophysical Aspects of Auger Processes", AAPM Symposium Series No.8, 24-36, (1992).

(7) Kobayashi, K., Hieda, K., Maezawa, H., Furusawa, Y., Suzuki, M., and Ito, T., Int. J. Radiat. Biol., **59**, 643-650 (1991).

E. STRUCTURAL PROPERTIES OF CONDENSED MATTERS

1. DETERMINATION OF THE ENDROHEDRAL NATURE OF THE METALLOFULLERENE Y@C_{82}

Endohedral Metallofullerenes are novel forms of fullerene-related materials which encage metal atom in a carbon cage. The synthesis of metallofullerene encapsulating various metal atoms within the carbon cage has stimulated wide interest because of their unusual structure and electronic properties. As for the endohedral nature, there has been some debate about whether the metal atoms are really located inside of the cage or not. Several theoretical and experimental studies suggest that the metal atoms are distributed inside the fullerenes, but, some ambiguities remained. The fullerene specialists had hoped that was the case. The X-ray structural analysis based on the SR powder data measured at BL-6A2(95G-124) succeeded in determining the endohedral nature of the metallofullerene YC_{82}.

For the structural analysis, the novel method combining the Maximum Entropy Method and the Rietveld Method was used to analyse the complicated powder pattern of YC_{82} crystal[1]. The cell parameters of YC_{82} crystal were a = 18.401(2), b = 11.281(1), c = 11.265(1) Å, β = 108.07(1)° (monoclinic $P2_1$). The result shows the section of the charge density of YC_{82} molecule with the relief map(Fig.1). The powder pattern fitting based on the charge density is excellent and the R-factor based on the integrated intensities is 1.4%(Fig.2).

In Fig.1, the remarkably high density inside the circular lower rim was found to be yttrium atom. This shows the conclusive evidence that a metal atom is indeed trapped within the carbon cage, i.e., the YC_{82} is the Y@C_{82}, which is the shorthand notation for yttrium in an C_{82} carbon cage. In the figure, the yttrium atom does not reside in the center of the carbon cage but is very close to the carbon cage as suggested by the theoretical study[2]. The present result proved the endohedral nature of metallofullerene without doubt and further revealed the strong off-centered nature of the mono-metallofullerene Y@C_{82}. *(M.Sakata, Univ. Nagoya)*

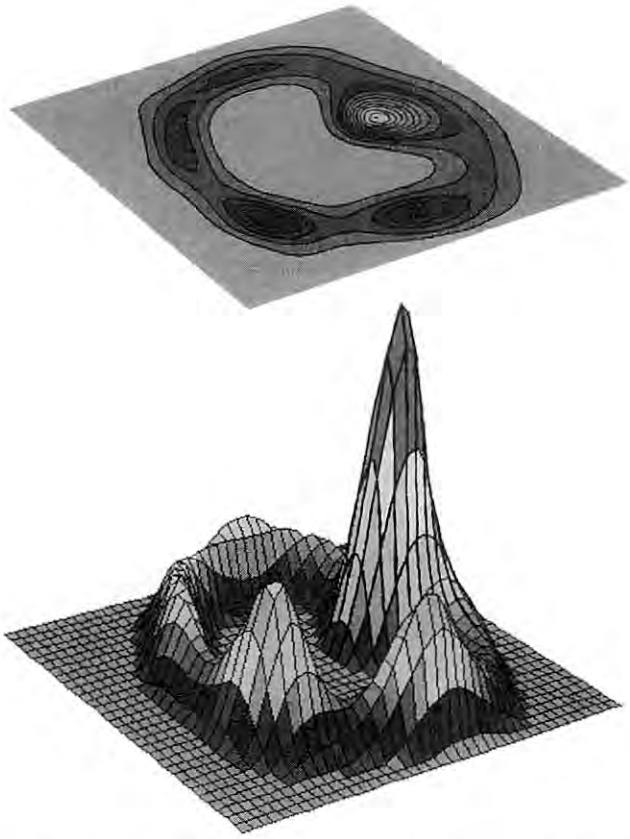

Fig. 1 The MEM charge density of Y@C_{82} with the relief map.

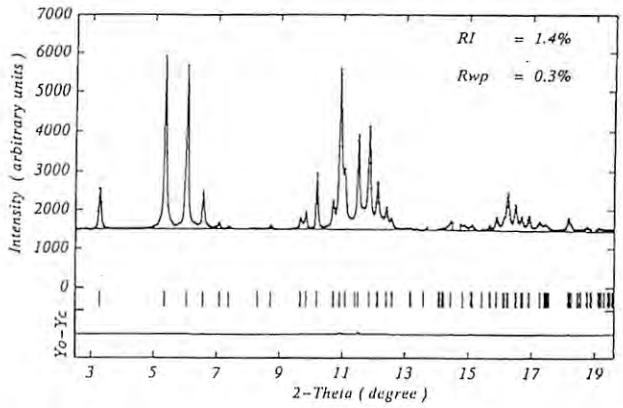

Fig. 2 The powder pattern fitting result for Y@C_{82} based on the calculated intensities from the MEM charge density.

Reference

1) M. Takata, B. Umeda, E. Nishibori, M. Sakata, Y. Saito, M. Ohno and H. Shinohara: Nature, 377 (1995) 46.

2) S. Nagase and K. Kobayashi: Chem. Phys. Lett., 214 (1993) 57.

2. THE DENSE HYDROUS MAGNISIUM SILICATES (DHMS)

Water has a crucial influence on the seismic and rheological properties of the earth's mantle. The existence of the dense hydrous magnesium silicates (DHMS)[1] whose stability fields suggest their possible occurrence in the subducting slab at transition zone depths(410-660km) of the earth's mantle was first reported by Ringwood and Major[2]. The structural studies on these dense high pressure phases suffer difficulties caused by a problem associated with the X-ray diffraction intensity measurement on a very small crystal of relatively low degree of crystallinity. Structural studies on two DHMS's, superhydrous phase B, $Mg_{20}Si_6H_8O_{36}$ and phase F, $Mg_{3.35}Si_{5.5}1H_{7.26}O_{18}$ were carried out at the beamline BL-10A using the vertical type four-circle diffractometer.

The crystal structure determination and the study of the effect of pressure on the superhydrous phase B(Fig.1) of about 30mm in diameter were carried out up to 6.5 GPa using a single diamond anvil cell mounted on the four-circle diffractometer. The bulk modulus thus obtained was $K_{0T}=145$ GPa. The crystal structure of phase F(Fig.2) of about 30mm in diameter, synthesized at 17 GPa and 1000°C using a multi-anvil high pressure device was determined with X-ray intensity data measured with the monochromatized synchrotron radiation of the wave length of 0.7065 Å by the Si(111). The structure contains layers with many similarities to the superhydrous phase B. The layers of oxygen atoms are stacked in the ABCBAC -type double cubic closest packing arrangement. (*Y. Kudoh, Tohoku Univ.*)

References

1) A. B. Thomson, Nature 358 (1992) 295.
2) A, W. Ringwood and A. Major, Earth. Planet. Sci. Lett. 2 (1967) 130.
3) Y. Kudoh, T. Nagase, S. Ohta, S. Sasaki, M. Kanzaki and S. Tanaka, in S. C. Schmidt, J. W. Shanner, G. A. Samara and M. Ross, Eds., High-Pressure Science and Technology-1993, American Institute of Physics (1994) 469.
4) Y. Kudoh, T. Nagase, S. Sasaki, S. Tanaka and M. Kanzaki, Phys. Chem. Minerals 22 (1995) 295.

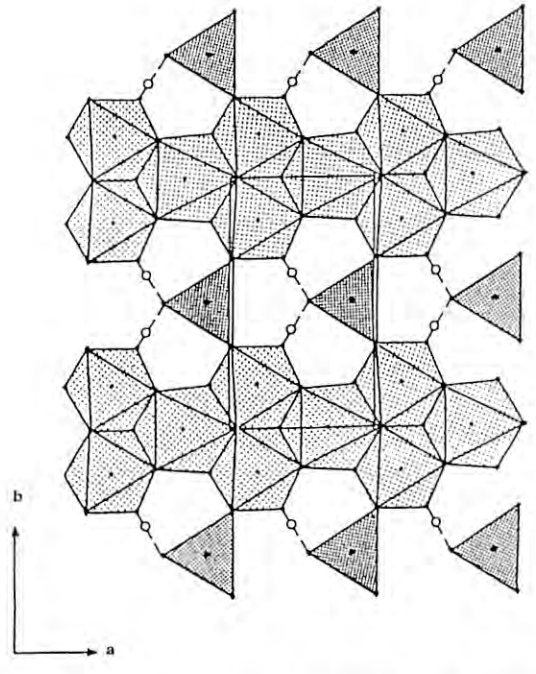

Fig. 1 Partial view of the superhydrous phase B structure. The hydrogen bonds connecting SiO_4 tetrahedra and MgO_6 octahedra are shown. (Produced with the data of Kudoh et al.3))

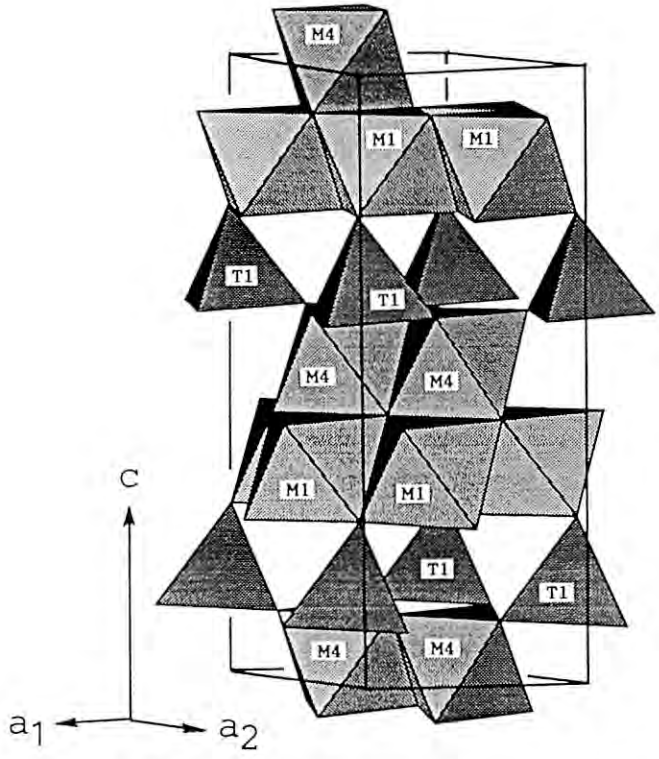

Fig. 2 Partial view of the phase F structure. Periclase-like layers of $(Mg,Si)O_6$ octahedra are crosslinked by SiO_4 tetrahedra and $(Mg,Si)O_6$ octahedra. (From Kudoh et al.4))

3. SINGLE-CRYSTAL STRUCTURE ANALYSIS UNDER EXTINCTION-FREE CONDITION

Both experimental and theoretical approaches to the electron density distribution study become more important in the field of materials science. However, several kinds of effects limit the accuracy of the observed kinematical structure factors from imperfect crystals. They are extinction, multiple scattering, absorption, counting statistics, thermal diffuse scattering, etc. The extinction and absorption can be reduced significantly by using a smaller crystal and/or a shorter wavelength. Since both solutions tend to decrease the diffracted intensities, the use of synchrotron radiations is strongly recommended for accurate structure analyses.

After a number of progressive studies which have been carried out using the horizontal-type four-circle diffractometer at the beam line 14A in 1990s, the extinction-free condition has been finally realized in the single crystal structure analysis.

As given in the user's report[1] on $CaYAlO_4$ (95G334) in this issue, three-dimensional diffraction data from a small single crystal of about 10 μm size using synchrotron radiation have been found to be scarcely affected by secondary extinction with a minimum value for the secondary extinction transmission factor Ys of 0.988 for the 200 strongest reflection. The value should be compared to 0.5855 calculated for a spherical specimen with diameter of 112 μm mounted on the Ag rotating-anode four-circle diffractometer. The analysis of the extinction-free data on $CaYAlO_4$ has revealed important information about the composition, atomic positions and the electron density distribution.

Due to recent hardware and software developments[2] at the BL-14A four-circle diffractometer, the improvement of the counting dynamics up to some 10^8 cps has been enabled by the use of the avalanche photodiode detector. The new device has contributed in removing almost completely the dead time correction which was inevitable for the NaI detector previously. It looks obvious that scientists can see the electron density of a crystal in quite near future without any complicated corrections. (*N.Ishizawa, TIT*)

References

1) K. Morita, K. Suda, N. Ishizawa and N. Kodama, Photon Factory Activity Report 1995
2) S. Kishimoto, N. Ishizawa, T. P. Vaalsta, in preparation (1996)

4. HIGH PRECISION DIFFRACTION IMAGING OF THE ELECTRON DENSITY IN CRYSTALLINE SOLIDS

X-ray diffraction imaging can explain a wide range of physical properties of materials. The technique becomes especially powerful if the atomic coordinates and vibration amplitudes are complemented by accurate measurements of the deformation density Dr -- the change in electron density due to the formation of the crystalline material. Because measurements of Dr are notoriously sensitive to instrumental errors and to inadequacies in specimen preparation, it is necessary to check the reliability of the results obtained, preferably by techniques that do not depend on the accuracy of diffraction measurements. Comparison of Dr maps measured by diffraction imaging with those from theoretical calculations tests the validity of both experiment and theory. A multipole representation of the static deformation density for $MgCO_3$ shown in Fig. 1 (a), recently determined with the BL14A four-circle diffractometer[1], is close to that evaluated from a density functional calculation[2] shown in Fig. 1(b).

This comparison indicates that the accuracy now being achieved should extend the applications of high precision diffraction imaging. Crystals containing heavier elements in the periodic table can be investigated with greater confidence. High precision diffraction imaging will help clarify the nature of phase transitions and structural disorder. It has recently raised some intriguing questions regarding the strength of the cation-cation interactions in the C-type rare earth oxides. The method also has the potential to provide more detailed insights into ferroelectric behaviour. It is also possible that it will provide more information on the nature of the exchange interactions that govern the magnetic properties of materials. That information will complement direct measurements of the much smaller cross-sections that originate in magnetic cross sections directly. (*E. N. Maslen, Univ. Western Australia*)

References

1) E. N. Maslen, V. A. Streltsov, N. R. Streltsova and N. Ishizawa, Acta Cryst. **B51** (1995) 929.
2) M. Catti, A. Pavese, R. Dovese and V. Saunders, Phys. Rev. **B47** (1993) 9189.

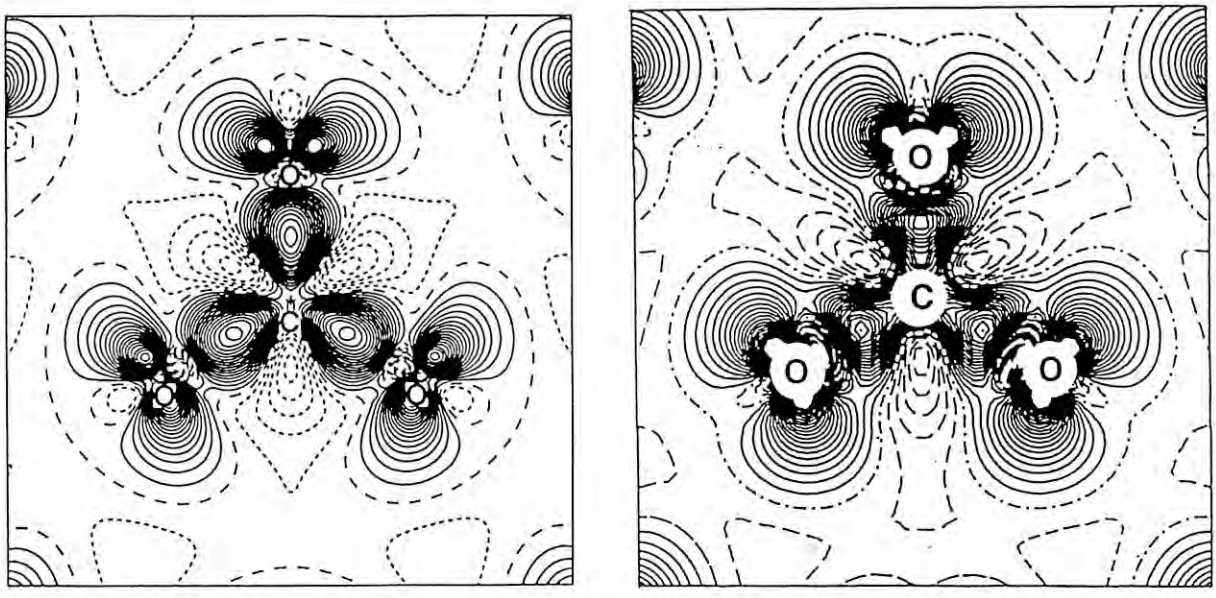

(a) (b)

Fig. 1 Representations of the deformation density in $MgCO_3$
(a) from X-ray diffraction measurements on the BL14A diffractometer.
(b) by a density functional calculation. Contour interval 0.005 e. $bohr^{-3}$.

5. OBSERVATION OF AMORPHIZATION OF SERPENTINE AT HIGH PRESSURE AND HIGH TEMPERATURE VIA IN SITU X-RAY DIFFRACTION MEASUREMENTS

The occurrence of deep-focus earthquakes at 100-670km depths in the mantle has puzzled earth scientists for more than 50 years. The pressure-induced amorphization of serpentine has been considered as one of the most likely mechanism. However, the amorphization of serpentine was observed only at room temperature using a diamond anvil cell[1]. The temperature/pressure conditions for the amorphization of serpentine have been examined on the basis of in situ X-ray diffraction measurements using the combination of synchrotron radiation and a double-stage multianvil high pressure apparatus[2].

Natural antigorite was used as the serpentine starting material. A "hybrid anvil system", utilizing four tungsten carbide (WC) and four Advanced Diamond Composite (ADC) anvil[3], was adopted for the second stage anvil (MA8) system. The assembled anvil cube was pressurized in cubic presses (MAX80 and MAX90)[4] at KEK. An energy dispersive method was adopted for the X-ray diffraction measurements under high pressure and high temperature.

Figure 1 summarizes one of the results obtained in the five runs so far conducted at pressures up to 28 GPa, and at temperatures up to 1500℃. No amorphization of antigorite was observed upon compression to 28 GPa at the room temperature (Fig. 1, (A) and (B)), in contrast to those reported in the earlier study[1] using diamond anvil cell. As the temperature increases, however, the diffraction peaks of serpentine became smaller and were completely lost at temperatures 200-400℃ in a few minutes (Fig. 1(C)). A rapid crystal growth of high pressure phases then followed upon further increasing temperature above 400℃ (Fig. 1, (D) and (E)). The results of the present experiments demonstrated that the amorphous regime of serpentine was limited to pressures above ca. 14 GPa, and temperatures lower than 400℃. Such low temperatures are unrealistic for subducting oceanic lithosphere, and it is therefore concluded that the amorphization of serpentine is an unlikely mechanism for deep-focus earthquakes. (*T. Irifune, Tohoku Univ.*)

References

1) C. Meade and R. Jeanloz, Science, **252**, 68 (1991)
2) T. Irifune, K. Kuroda, N. Funamori, T. Uchida, T. Yagi, T. Inoue, N. Miyajima, Science **272**, 1468 (1996)
3) T. Irifune et al. Proc. Jpn Acad., **68**, 161 (1992)

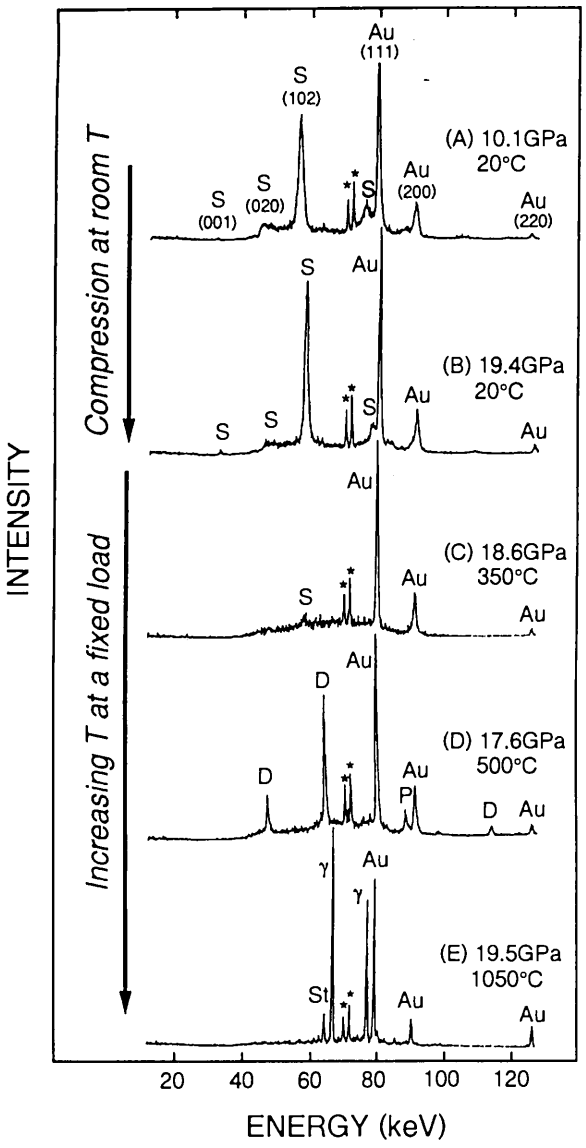

Fig. 1 An example of the changes of X-ray diffraction patterns for serpentine as a function of pressure and temperature. S=serpentine (antigorite), Au =gold used as a pressure marker; D=phase-D; V=$(Mg,Fe)_2SiO_4$; St=SiO_2 stishovite;. Stars denote the characteristic X-ray lines of gold.

4) O. Shimomura et al. in High-Pressure Research: Application to Earth and Planetary Sciences (ed. Y. Syono and M. H. Manghnani, TERRAPUB/ AGU] 3 (1992)

6. SINGULARITY IN THE HCP STRUCTURE AT C/A=$\sqrt{3}$

Hcp metals are known to have c/a axial ratios close to the "ideal" value of 1.633. The axial ratios of Zn and Cd, however, deviate considerably from 1.633 (Zn c/a=1.856, Cd c/a=1.886). The deviation from the ideal hcp structure is explained by the gain in the band-structure energy through lattice distortion. Pressure modifies the band structure and may change the axial ratios of these metals. High-pressure structural studies of these metals serve as a rigorous test for total energy and band-structure calculations. A recent high-pressure Mösbauer experiment on Zn showed a discontinuous change in the so-called Lamb-Mösbauer factor at about 6.6 GPa and 4 K[1]. The discontinuity was interpreted on the basis of a drastic change in the lattice dynamics. Scalar-relativistic augmented plane wave calculations further indicated that a pressure-induced change in the topology of the Fermi surface, the electronic topological transition (ETT), is responsible for the anomaly in the lattice dynamics[1]. In order to study the effect of pressure on the axial ratios of Zn and Cd, and to investigate the possible correlation with the ETT, we have carried out angle-dispersive powder x-ray diffraction experiments with high precision. The experiments were done at room temperature on BL-6B with the use of a diamond-anvil cell and an imaging plate. X-rays were monochromatized to an energy of 18.00 keV. The lattice parameters a and c were determined with precision of 0.04%. Figure 1 shows the variation of the c/a ratios of Zn[2] and Cd[3] plotted as a function of the relative volume V/Vo, where Vo denotes the volume of each metal at normal pressure. Both metals remain in the hcp structure to the highest pressures (Zn: 126 GPa, Cd: 174 GPa). The axial ratios continuously decrease

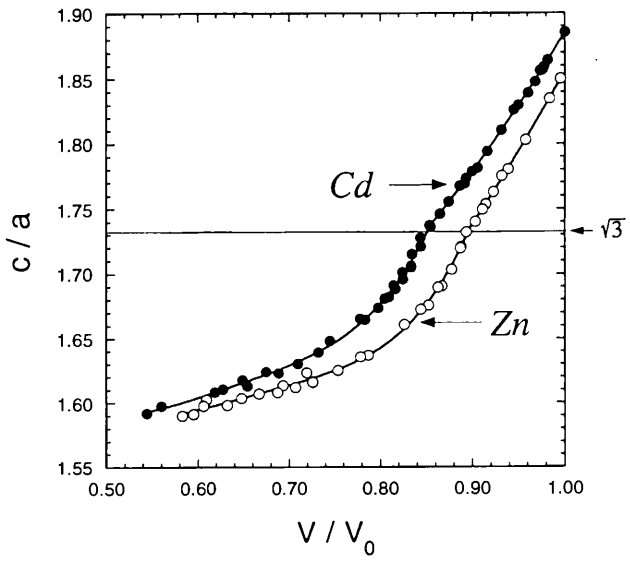

Fig. 1 Volume-dependence of the a/c axial ratios of Zn and Cd. Vo denotes the volume for each metal at normal pressure.

with pressure to a value of 1.59. One notices, however, clear changes in the curvature of the volume-dependence of the axial ratios at a common value of c/a $= \sqrt{3}$. The corresponding pressures for this anomaly are 9.1 and 12.5 GPa for Zn and Cd, respectively.

In the case of Zn the anomaly of the Mösbauer spectra occurred at 6.6 GPa and 4 K, lower than the pressure for the anomaly of the axial ratio at room temperature (9.1 GPa). If we estimate the axial ratio of Zn at high pressure and low temperature, however, it is very close to $\sqrt{3}$ at 6.6 GPa and 4 K[2]. The two anomalies are therefore most probably correlated. On the other hand, it is difficult to explain the fact that the anomaly in the axial ratio occurs exactly at c/a $= \sqrt{3}$. Even in the free electron model, the Fermi sphere for an hcp divalent metal does not change the positions at which it intersects the Brillouin zone boundaries, when the c/a axial ratio varies through $\sqrt{3}$. Furthermore, since the real Fermi surfaces of Zn and Cd differ from the free-electron model, there is no reason for the ETT to occur at such a special value of the axial ratio.

The present finding suggests that the anomaly may be a rather universal feature for the hcp structure. The hcp structure with c/a $= \sqrt{3}$ has high symmetry both in real and reciprocal spaces. The hcp lattice in real space can be represented by an orthorhombic unit cell containing four atoms (Fig. 2(a)). If the c/a axial ratio is $\sqrt{3}$, the a_0 and b_0 axes become equal making the cell tetragonal. In reciprocal space, the reciprocal lattice vectors AA and AL have the same length when c/a $= \sqrt{3}$ (Fig. 2(b)). Perhaps this special symmetry may influence the elastic properties of the hcp lattice giving rise to the anomaly in the lattice dynamics. Further high-pressure experimental studies on these metals, including transport properties and phonon spectra, are highly encouraged. (*K. Takemura, NIIRIM*)

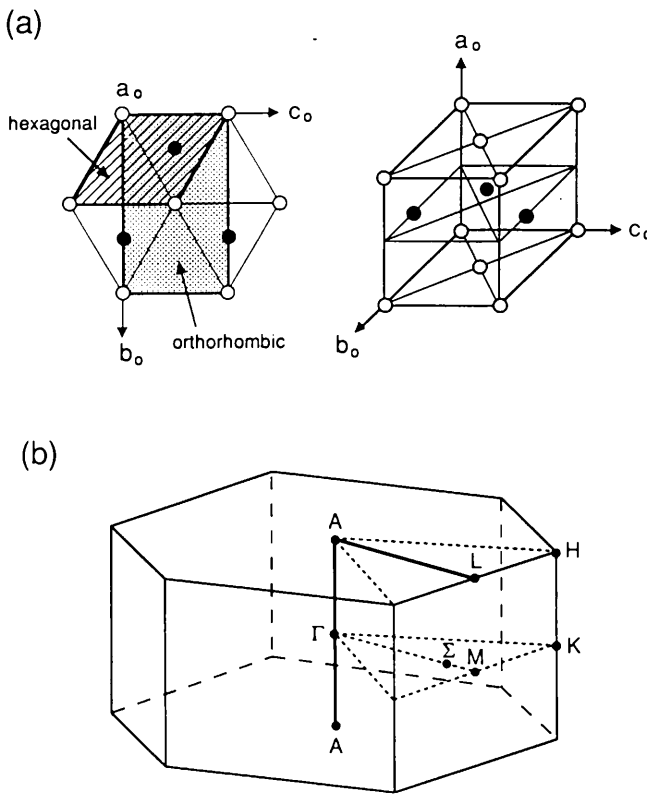

Fig. 2 (a) The hcp structure in real space. The a_0, b_0 and c_0 axes indicate the orthorhombic representation of the hcp unit cell. (b) The first Brillouin zone for the hcp structure with symmetry points.

References

1) W. Potzel, M. Steiner, H. Karzel, W. Schiessl, M. Koferlein, G.M. Kalvius, and P. Blaha, Phys. Rev. Lett. 74, 1139 (1995).
2) Takemura K., Phys. Rev. Lett. 75, 1807 (1995).
3) Takemura K., in the present Activity Report.

F. STRUCTURAL PROPERTIES OF SOLID SURFACES AND ADSORBATES

Although scanning-microscopic techniques such as STM and AFM are quite useful to observe surface structures, methods based on diffraction of photons or electrons are essential to determine atomic structure precisely. Synchrotron radiation is a suitable source of hard and soft X rays to investigate surface and interface structures by means of X-ray Diffraction, X-ray Standing Wave, X-ray Absorption Fine Structure or X-ray Photoelectron Diffraction techniques. There are a number of studies progressing at the X-ray and soft X-ray beamlines of the Photon Factory, which include experimental stations constructed by collaborations with other universities, laboratories and private companies. Here will be presented some recent topics at the Photon Factory but please refer also to the "Collaborations" and "User's Reports" sections.

1. IN-PLANE STRUCTURE OF As ADSORBED Si SURFACES DETERMINED WITH GRAZING-ANGLE X-RAY STANDING WAVES

The grazing-angle X-ray standing wave technique has been applied, for the first time, to surface structure determinations in ultrahigh vacuum environment, at the Photon Factory. The technique employs diffraction vectors nearly parallel to the surface, while keeping the high-position sensitivity of the standing-wave method, thus enabling to locate adsorbed atoms in the in-plane direction with high accuracy without any triangulation. Experiments were performed on the Si(111):As-1 × 1 surface placed in a purposely designed UHV chamber[1] and profited from the vertically polarized synchrotron X rays available at BL-14B[2]. The emission profiles observed from monolayer As atoms on the Si substrate near the $\bar{2}20$ Bragg reflection show very good agreement with those calculated assuming highly ordered As atoms occupying the three fold-symmetry sites on the bulk-like Si(111) surface (Fig. 1). Profile fits confirmed that displacement from this position is less than 3% of the Si ($\bar{2}20$) interplanar spacing. The determined coherent fraction was greater than 0.8, indicating a highly ordered As structure. The result obtained here is consistent the previously proposed model with As atoms substituting for the Si atoms at the topmost site of the Si(111) double plane. The technique is being extended

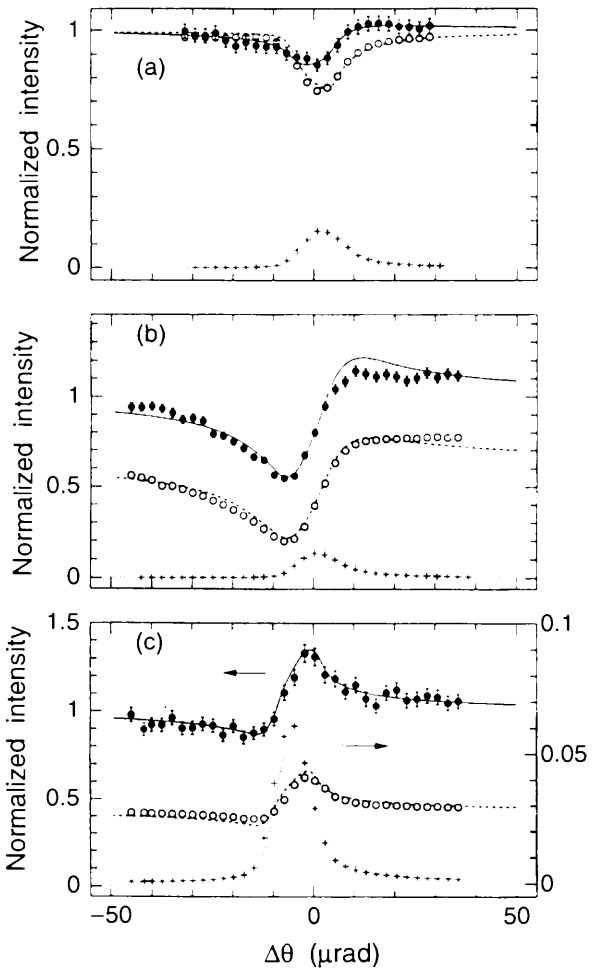

Fig.1 As fluorescence signals (closed circles), specular-beam fluxes (open circles) and diffracted fluxes (crosses) observed from a Si(111): As-1 × 1 surface near the grazing-angle $\bar{2}20$ Bragg condition of Si at glancing-incidence angles 1.12 (a), 1.86 (b) and 2.64 mrad (c) for the primary X-ray beam of 16.84 keV.

to As-deposited Si(100) surfaces[3], where the structures of the 1×2 and 2×1 domains are explored, in addition to the As-As dimer bond length and disorder.

References

1) O. Sakata and H. Hashizume: Rev. Sci. Instrum. **66** (1995) 1364.
2) O. Sakata and H. Hashizume: Acta Cryst. A **51** (1995) 375.
3) O. Sakata, S. Kumano, Y. Tanaka, N. Matsuki, A.M. Nikolaenko and H. Hashizume: Photon Factory Activity Report #13 (this volume).

2. STRUCTURE CORRELATION OF SiGe / Si SUPERLATTICE INTERFACES

Growth of SiGe/Si superlattices shows unusual roughening behaviors indicating that the top interfaces of SiGe alloy layers are rough and this roughness is not replicated in Si layers grown on top of the alloy, but successive SiGe layers show roughness that can be correlated with that of underlying SiGe layers. The structure properties of this behavior were investigated by X-ray reflectivity and diffuse scattering measurements on various samples at BL-20B. Interesting features were observed from a sample containing 10 periods of Si(50Å)/Si $1-x$ Ge_x(50Å) bilayers with $x=0.1$, grown by MBE on a slightly miscut Si(111) substrate. Specular profiles, with suppressed even-order Bragg peaks, evidencing equally thick Si and SiGe layers, show rms roughness of 8Å and 9.5Å for the SiGe/Si and Si/SiGe interfaces respectively when fit by a model using the distorted-wave Born approximation (DWBA). Offset $\omega-2\theta$ scans show oscillatory profiles with features related to those in the specular profiles, indicating that the roughness structures in the different interfaces are correlated. The correlations manifest themselves as diffuse scattering peaks, S_1 and S_2, commonly observed on a series of ω scans made at different q_z values. S_1 is located at a fixed q_x value corresponding to a 3700Å lateral wavelength, which is ascribed to a bunched step structure replicated by the successive Si and SiGe layers deposited on the vicinal substrate

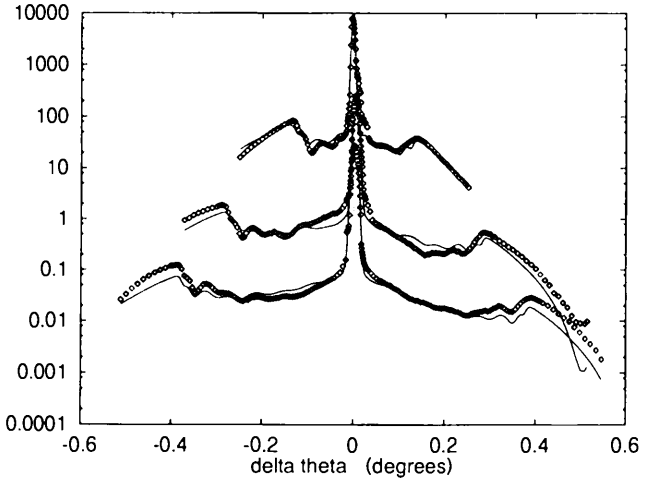

Fig.2 ω-scan profiles (data points) at $2\theta=0.7$ (top), 1.0° (middle) and 1.2° (bottom), together with DWBA fits (lines), for a $Si_{0.9}Ge_{0.1}$/Si heterostructure. Specular peaks at the center and Yoneda peaks towards the right and left ends.

Si(111) surface. The 0.6° miscut angle and the 3700Å wavelength indicate that 10 single-height atomic steps are bunched together to produce ten-layer height steps. S_2 is believed to arise from a partially correlated 3D island structure on the top interfaces of the SiGe layers. The q_x positions of this peak indicate 1900-2300Å for the island size, which is consistent with electron-microscopy observations.

3. MODEL-INDEPENDENT DETERMINATION OF NEAR-SURFACE LATTICE STRAIN FROM X-RAY ROCKING-CURVE DATA

There have been a series of works which determined the depth profiles of near-surface lattice distortions in single crystals from triple-crystal X-ray diffractometry data without replying on models. The highest depth resolution achieved reaches 25Å. The technique uses a logarithmic dispersion relation to determine the phase of the structure factor with information available a priori on the sample structure. Phase information was obtained from the observed rocking-curve profile via a logarithmic Hilbert transform and the a priori information was used to select the zeros to be included in the solution, thus solving the ambiguity problem intrinsic to the inverse scattering problem. The experiments profited from the low background of the evacuated BIGDIFF diffractometer, used with a four-bounce crystal analyzer, on the Australian National Beamline Facility (BL-20B) to measure rocking curve profiles of a symmetric Bragg reflection over a six-decade intensity range[1]. In the 1D case, the vertical lattice spacing in 90-160Å-thick epitaxial SiGe layers in a SiGe/Si superlattice was found to be much smaller than predicted by Vegard's law[2]. For the 2D case silicon crystals implanted with high-energy B^+ ions through a periodical mask pattern were investigated, where the solutions obtained by applying the phase retrieval technique to a series of satellite reflections were Fourier synthesized to build 2D strain maps[3,4]. Localized strains perpendicular to the surface arising from deposited ions in near-surface layers were displayed with spatial resolutions of 0.016 and 0.265 μm in the depth and lateral directions respectively (Fig. 3), which are higher than those achieved so far with other X-ray imaging methods.

References

1) A. Nikulin, A.W. Stevenson, H. Hashizume, S.W.

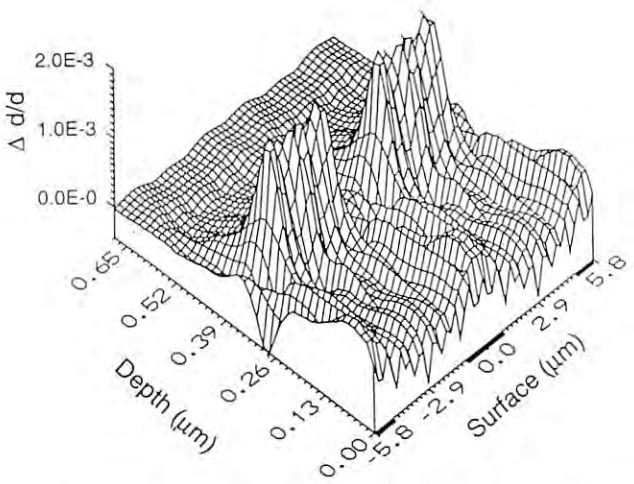

Fig.3 2D strain map reconstructed for the Si(111) crystal implanted with 100 keV boron ions through a periodic surface oxide mask pattern. 11 satellite reflections are used to produce the image.

Wilkins, D. Cookson, G. Foran and R.F. Garrett: J. Appl. Cryst. **28** (1995) 57.

2) A. Nikulin, A.W. Stevenson and H. Hashizume: Phys. Rev. B **53** (1996) 8277.

3) A. Nikulin, O. Sakata, H. Hashizume and P.V. Petrashen: J. Appl. Cryst. **27** (1994) 338.

4) A. Nikulin, T.E. Gureyev, A.W. Stevenson, S.W. Wilkins and H. Hashizume: J. Appl. Cryst. **28** (1995) 803.

4. PHOTOELECTRON DIFFRACTION STUDY OF In/Si(001) INTERFACE

Photoelectron diffraction (PED), where the angular distributions and / or the $h\nu$-dependences of photoelectron intensities are measured, is a 'local' structural probe, which has the uniqueness of elemental-, chemical- and even site-specificity. PED for surface structural analyses has grown up as one of the most promising research fields using soft X-ray synchrotron radiation (SR) in last decade. This is stimulated also by the recent development of the high-resolution and high-brightness soft X-ray beam lines on the new 3rd generation SR sources.

In Photon Factory, there has been almost no report on the surface structure studies by PED up to now, although interesting PED works using the circularly-polarized SR and the 2-dimensional analyzer has been performed by Daimon et al. for bulk Si.

An extensive angle-scan PED investigation using SR from BL-18A was applied to study the structures of well-ordered surface phases of 2×3, 2×2 and 4×3 induced by In adsorption on Si(001)[1-4]. Although the (group-III metal)/Si(001) interface is one of the most important metal/semiconductor interface system in the device technology, its surface structures have been uncertain. Furthermore, the 2×2 and 2×3 reconstructions, which are common to all group-III metal adsorbates, have attracted much interest recently due to their unique dimer structures[5].

The full angular distributions of In 4d photoelectron intensities (so called angle-scan PED patterns) were measured by rotating the sample and the angle-resolved analyzer at photon energies ($h\nu$'s) of 70.9, 99.1 and 100 eV for the Si(001)2×2-In surface (Fig. 4) and also for the 2×3-In and 4×3-In surfaces at $h\nu=$ 100 eV. For the 2×2-In surface, a rigorous R-factor analysis was done using a recently-developed full-multiple-scattering-simulation method of PED (see Fig. 4) to give detailed structural parameters of the surface dimer structures formed, e.g., In dimer length 2.84 ± 0.1Å and In-Si layer spacing 1.44 ± 0.1Å[1,2]. It was found that the determined structures are consistent to the theoretical prediction by total energy minimization and the very recent experimental results by tensor-LEED. In the comparison of the PED patterns of different surface phases, a striking similarity was found between the PED patterns for the 2×2 and 2×3 phases. It shows that the local structures around In adsorbates of these two phases are almost identical and PED in this energy range is sensitive almost only to the nearest neighbors from an In emitter. This very local sensitivity can be an advantage for a local structure probe since it would reduce the number of parameters to be optimized in simulations. Similar PED results for the 4×3-In phase is now under analysis.

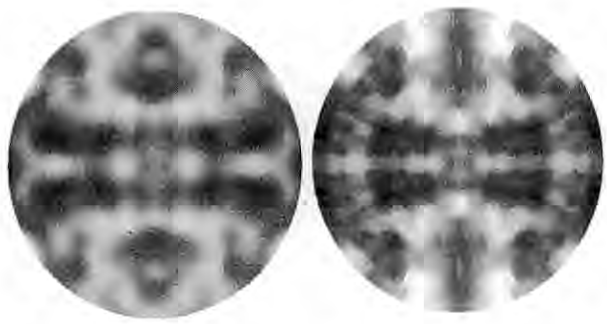

Fig.4 The angle-scan PED patterns of In $4d_{3/2}$ for the Si(001)2×2-In surface taken at $h\nu=100$ eV. The simulated PED pattern is in the left panel; experimentally measured one in right.

In addition, a large difference was found in the PED patterns for the two spin-orbit components of In 4d levels, In $4d_{5/2}$ and In $4d_{3/2}$. It indicates that there is a strong angular variation (up to 40% of the statistical value of 1.5) of the spin-orbit branching ratio (BR) for In 4d from In overlayers on Si(001)[1-3]. In order to clarify its origin, extensive BR measurements have been performed in the angle-scan PED for the In 4d of the 2 ×2, 2×3 and 4×3 phases at hν's of 70.9, 99.1 and 100 eV. It was found that the BR angular anisotropy depends on both local structures of surface and hν's. A careful analysis of these results unambiguously showed that the anisotropy of BR is a manifestation of the difference in the photoelectron final-state wave-functions for the two spin-orbit components through PED[3,4].

To summarize, low-energy ($\lesssim$ 100 eV) PED using SR was successfully applied to the structure determination of semiconductor surfaces. This work is now being extended to higher hν's of 100~400 eV using BL-7A. The new tool of PED using SR is expected to be applied to a wider variety of surfaces and to evolve into photoelectron holography. However, further developments are highly required for an efficient data taking, i.e. developments of higher-resolution and higher-flux soft X-ray beam lines along with multi-detection photoelectron spectrometers.

References

1) X. Chen, H.W. Yeom, T. Abukawa, Y. Takakuwa, T. Shimatani, Y. Mori, A. Kakizaki, and S. Kono: J. Electron Spectrosc. Relat. Phenom., 80 (1996) 147.
2) H.W. Yeom, T. Abukawa, Y. Takakuwa, X. Chen, S. Fujimori, T. Okane, Y. Ogura, T. Miura, S. Sato, A. Kakizaki, and S. Kono: submitted to the 5th International Conference on the Structure of Surfaces, Aix en Provence, France (1996).
3) H.W. Yeom, T. Abukawa, Y. Takakuwa, X. Chen, S. Fujimori, T. Okane, Y. Ogura, T. Miura, S. Sato, A. Kakizaki, and S. Kono: submitted to Phys. Rev. B (1996).
4) H.W. Yeom: Ph. D thesis, Tohoku University (1996).
5) H.W. Yeom, T. Abukawa, Y. Takakuwa, M. Nakamura, M. Kimura, A. Kakizaki, S. Kono: Surf. Sci. **321** (1994) L177; ibid. **340** (1995) L983; ibid. **341** (1995) 328; Phys. Rev. B **53** (1996) 1948.

5. NEXAFS STUDY ON SURFACE AND INTERFACIAL STRUCTURE OF ORGANIC MOLECULES

Surface and interfacial properties of organic molecules have been the subject of considerable recent interest. Various surface sensitive (or specific) techniques, such as electron spectroscopy with UHV system, nonlinear optical spectroscopy, STM, IR-RAS etc. have been applied to the related problems. Recently, NEXAFS (Near Edge X-ray Absorption Fine Structure) has been recognized as a useful probe of the structure and orientation of organic molecules. Their spectroscopic nature and the surface sensitivity by virtue of the short escape depth of photoelectron may provide wide variety of information which can not be obtained by other means.

Surface structure of rubbed polyimide films, which is widely used as aligning layers for liquid crystal display devices, was firstly investigated with use of NEXAFS[1]. An effective depth (50Å) of the rubbing process was successfully detected. C K-edge spectra at various incident angles have revealed that the structure of BPDA polyimide differs with the number of alkylene unit, that is, even numbered BPDA forms a trans-transoid conformation contrary to the case of odd numbered BPDA having a trans-cisoid type as shown in Fig. 5. Assuming a selective adsorption of the liquid crystal molecule on

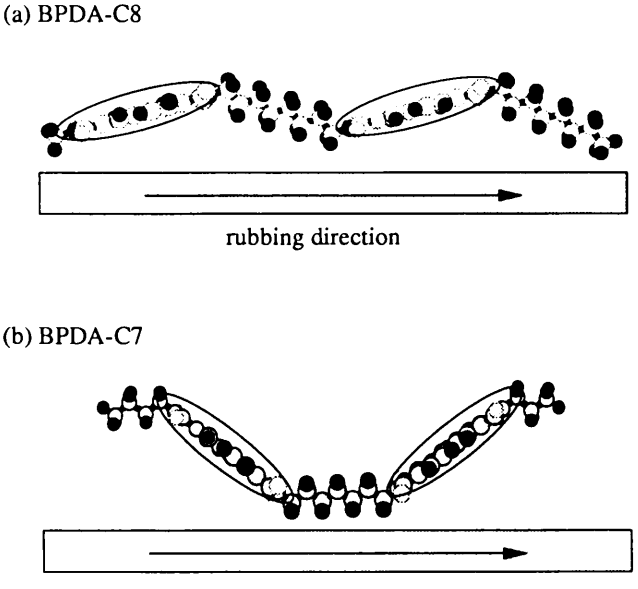

Fig.5 Conformations of (a)BPDA-C8 (trans-transoid) and (b)BPDA-C7 polyimides (trans-cisoid) at film surfaces. Arrows represent the mechanical rubbing direction applied on the film surface.

to the polyimides, the experimental results on the average direction of the liquid crystal alignment was well explained[2].

The surface structure of liquid has also been intensively studied. Recently, surface freezing of liquid n-alkane was discovered by X-ray reflection measurement[3]. Surface freezing effect refers to the phenomena where a liquid surface first freezes while descending temperature and the ordered thin layer at the surface remains on the liquid bulk substance for a few degrees above T_m (melting point). NEXAFS spectra have successfully detected the existence of the surface freezing of n-$C_{50}H_{102}$ (pentacontane) as illustrated in Fig. 6[4]. The temperature variation of σ^* (C-H) resonance peak at the region A is attributable to the range of the surface freezing effect. Incident angle dependence of NEXAFS has revealed that the molecular long axis uniformly aligns perpendicularly to the air/liquid interface.

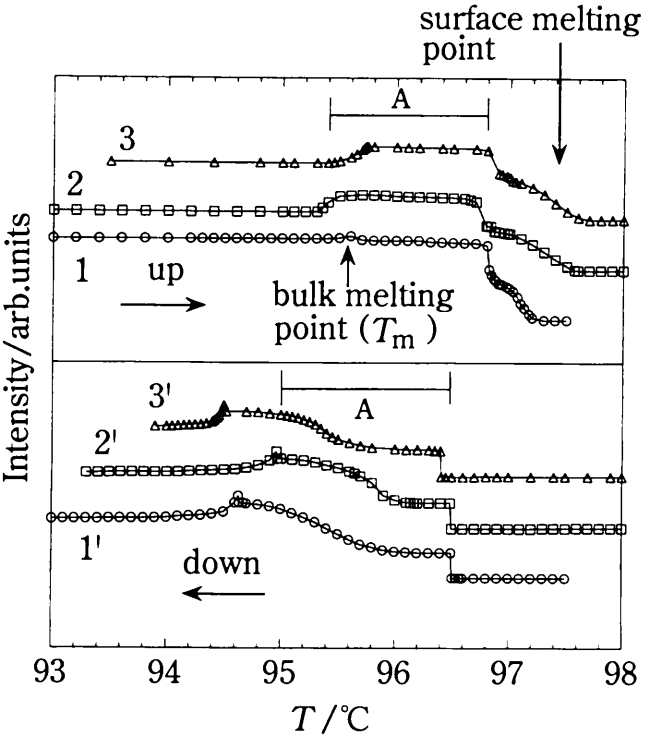

Fig.6 Temperature variation of σ^* (C-H) resonance peak. In the process of increasing temperature, bulk melts first at Tm followed by the surface melting. Intensity variation at region A is due to the surface freezing effect.

References

1) Y. Ouchi, I. Mori, M. Sei, E. Ito, T. Araki, H. Ishii, K. Seki and K. Kondo: Physica B **208 & 209** (1995) 407.

2) Y. Ouchi, K. Seki, and K. Kondo, Proc. of 15th International Display Research Conference, Asia Display '95: S17-1.

3) X.Z. Wu, E.B. Sirota, S.K. Sinha, B.M. Ocko, and M. Deutsch: Phys. Rev. Lett., **70** (1993) 958.

4) Y. Yamamoto, R. Mitsumoto, E. Ito, T. Araki, Y. Ouchi, K. Seki, and Y. Takanishi: J. Electron Spectrosc. **78** (1996) 367.

G. STRUCTURE AND FUNCTION OF PROTEINS

Introduction

As in the previous year [1], many protein structures have been solved using the well-established macromolecule-oriented Weissenberg camera [2] installed at the beam line BL6A [3]. Moreover a new type multifunctional camera has recently been constructed by N. Sakabe and installed at the beam line BL18B. The new type multi-functional camera, which has been financially supported by a grant-in-aid for scientific research on priority area No. 05244105 (see the section C) below), has several fundamental advantages over the old type camera installed at BL6A which may be briefly described as follows [4].

1) Two cylindrical cassettes with the radii of 430 mm and 1290 mm are, available.

2) On the larger cassette, two special-size imaging plates (IPs) with a dimension of 400 mm × 800 mm can be set side-by-side.

3) A specific IP reader, named IPR4080, has been developed in a collaborative effort between the team at the Photon Factory led by N. Sakabe and a team at Fuji Film Co. Ltd to read out intensity data from the above-mentioned special-size IPs.

4) Thanks to the characteristics 1) through 3) mentioned above, the maximum possible resolution has been extended to 1.13 Å (vertical direction) and 2.4 Å (horizontal direction) when using the cassette of 430 mm radius and X-ray beam of 1.0 Å wavelength. The corresponding figures are 2.02 Å (vertical direction) and 3.4 Å (horizontal direction) when using the cassette of 1290 mm radius.

5) In addition to the horizontal film cassette movement, which is essential for Weissenberg-type geometry, the capacity for vertical cassette movement has been added. Thanks to this characteristics, the overlaps of diffraction spots can be much more efficiently avoided than in the case of the old type Weissenberg camera although this capacity has not yet been exploited due to the limit in software capacity.

6) The new camera can be conveniently used to record Laue diffraction patterns as a function of time. Hence the camera is multifuncitonal perhaps deserving the name of the time-resolved Laue cum Weissenberg camera.

Among many achievements performed more or less taking advantage of the facilities at the beam lines BL6A and BL18B, the following three topics will be highlighted here : A) the elucidation of the structure of cytochrome c oxidase from bovine heart, B) the more rational approaches to the solution of the phase problem in protein crystallography making use of selenomethionyl proteins and C) the efforts toward the elucidation of the dynamical structural change occurring in protein crystals making use of the time-resolved Laue diffraction method.

1. The elucidation of the structure of cytochrome c oxidase from bovine heart.

The crystal structure of bovine heart cytochrome *c* oxidase has been solved by T. Tsukihara et al [5,18] based on the X-ray diffraction intensity data collected at the Photon Factory. The enzyme is a large multicomponent membrane protein complex with molecular size of 200 kilodaltons comprising 13 different polypeptide subunits (Fig.1). Located in the subunits are two heme A moieties, two redox active copper sites, one zinc and one magnesium ions. The main function of the cytochrome oxidase, the terminal enzyme in the respiratory chain, is energy conservation. Situated in the inner mitochondrial membrane in eukaryotic organisms, cytochrome *c* oxidase is a proton pump that uses redox chemistry to drive protons from the mitochondrial matrix across the membrane. The electrochemical potential thus generated causes protons to

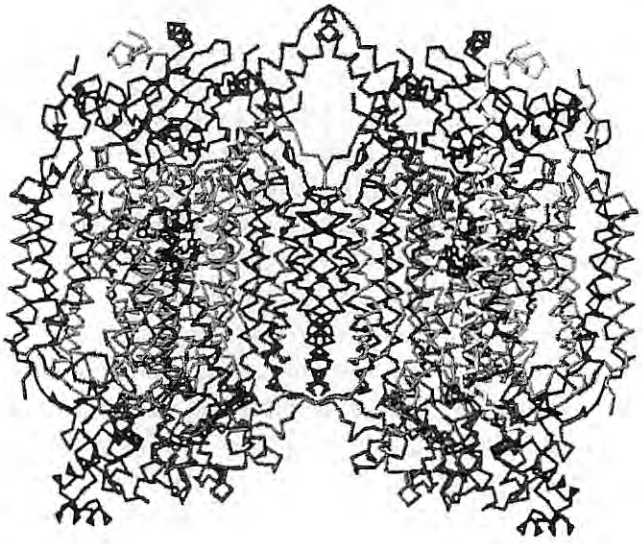

Fig.1 Three-dimensional structure of cytochrome *c* oxidase from bovine heart having a molecular weight of 400 kilodaltons [5].

flow back into the matrix resulting in the synthesis of ATP, the biological molecular device to store energy.

With 13 different subunits, the mammalian cytochrome *c* oxidase is by far the most complex membrane protein to yield a defined structure. This remarkable achievement is the result of a long-term (20 years) and painstaking collaboration between the biochemical group led by S. Yoshikawa and the crystallographic group led by T. Tsukihara.

From the technical point of view, the most remarkable feature about this crystal strucutre analysis is that the asymmetric unit (or the independent region in the unit cell) comprising two subunits has a total molecular weight of 400 kilodalton, one of the largest number solved by *de novo* crystal structure analyses employing the well-established MIR (multiple isomorphous replacement) method [6]. As described in the previous review [1], the largest number ever solved by the MIR method is 1600 kilodalton (four tetrameric molecules of β-galactosidase each of 400 kilodalton) achieved by B. Matthews and his colleague [19] using the beam line BL6A of the Photon Factory. It used to be the commonly accepted view that, for solving the structures of crystals having such large asymmetric units, use of specifically designed (and synthesized) extra-heavy-atom compounds is a requisite to solve the phase problem. In the recent achievement by T. Tsukihara et al [5], however, simply the kinds of heavy-atom reagents, which have been conventionally used ($IrCl_6$ and CH_3HgCl), turned out to give sufficient phase information up to 5 Å resolution and further extension up to atomic resolution was possible by employing the modern techniques of electron density modification and so-called hitogram matching (for details of these techniques, see, for example, the textbook by J. Drenth [6]). Attachment of bulky extra-heavy-atoms to protein surfaces tends to break good isomorphism (less than, say, 0.2% in lattice parameter change) which is essential for successful MIR procedures. Thus, apart from the difficulty in obtaining extra-heavy-atom compounds, the use of conventional heavy-atom reagents is much desirable. It should be emphasized here that the successful use of conventioinal heavy-atom reagents in solving such a huge structure has been made possible mainly because of much higher precision of the X-ray intensity data which resulted in accurate estimation of the differences between the intensities from the protein crystals and those from the heavy-atom-labeled protein crystals.

The much more accurate intensity measurement, in turn, has been made possible through 1) the availability of Synchrotron X-ray beam, which are much more intense and has much smaller divergence and 2) the availability of the IP detector which has much wider dynamic range and much less fog level. Thus the macromolecule-oriented Weissenberg camera [2,3] installed at the Photon Factory, as well as other two-dimensional detectors installed at other Synchrotron Radiation Sources in the world, has not only shortened the data acquisition time but also served in dramatically improving the quality of the acquired data. In any case, the achievement of T. Tsukihara [5] is a tremendous encouragement for world-wide protein crystallographers and is bound to lead to the elucidation of many other crystal structures of protein complexes of comparable size, which would make our understanding of the mechanism of various biological machineries much wider and deeper. Finally the structure of another cytochrome *c* oxidase from the bacterium *Paracoccus denitrificans*, which is much simpler (consisting of four (rather than 13) subunits) but performs similar biological function, has independently been solved by S. Iwata et al of the laboratory of H. Michel [7]. It should be noticed that, in this work also, the X-ray diffraction intensisty data were collected by using the Weissenberg camera installed at BL6A of the Photon Factory.

2. The more rational approaches to the solution of the phase problem in protein crystallography making use of selenomethionyl proteins.

Among various approaches to solve the phase problem in protein crystallography without resort to trial-and-error searches for good isomorphous heavy-atom derivatives, the method employing selenomethionyl (SeMet) residues (the amino acid residue where the S(delta) atom of the sidechain of normal methionine (Met) is replaced by a selenium atom) appears to be most powerful and generally applicable. In this method pioneered by W.A. Hendrickson and his colleagues [8], 1) SeMet residues in place of normal Met residues are incorporated into the polypeptide chain of the target protein by cultivating a Met-requiring species of the bacterium *E. coli* transfected with the relevant gene in the medium containing abundant SeMet, 2) the relevant SeMet protein is crystallized and 3) X-ray diffraction intensities are collected from (in principle) a single crystal at three different wavelengths set around the absorption edge of the selenium atom so as to optimize the estimation of the in-

tensity difference due to anomalous scattering effect of the selenium atom. The method known as the MAD (multiple wavelength anomalous dispersion) method can be thought of as *in situ* multiple isomorphous replacements (MIR) generated by the variation in scattering factors that accompanies change of wavelength. Unlike the MIR method, however, here isomorphism is perfect and, in principle, a single crystal can suffice. The potential for such experiments has long been recognized, but effective use awaited synchrotron radiation where very fine tuning of the wavelength of the incident X-ray beam can be a practical prodecure.

During the period covered by the present Activity Report, one successful example employing the SeMet MAD method emerged [9] where the crystal structure of the macrophage migration inhibitory factor (MIF) from rat liver (with a molecular weight of 12.3 kilodalton) has been solved (Fig.2). Using the Weissenberg camera at BL18B, three sets of X-ray diffraction data were collected using a set of wavelengths 0.9794 Å (peak), 0.9797 Å (edge) and 0.9005 Å (remote). The final crystallographic R-factor at 2.2 Å resolution was 0.197 for 94.7% of the experimental data between 5-2.2 Å without considering solvent molecules.

Using the same technique, T. Senda et al [10] prepared the SeMet-substituted protein specimen of an extradiol ring-cleavage type dioxygenase from a *Pseudomonas* species (the BphC enzyme). The BphC enzyme consists of 8 identical subunits each of 32 kilodalton resulting in a total molecular weight of 250 kilodalton (Fig.3). The enzyme is a constituent of an aromatic ring-cleavage pathway which can degrade, among various substrates, the PCB (polychlorinated biphenyl) compounds, one of the most notorious environmental pollutants. Although Senda et al solved the phase problem essentially by the conventional MIR method based on a set of X-ray diffraction data collected in laboratory, they found that the presence of 9 selenium atoms (as markers of the Met residues) were of tremendous help in correctly interpreting the electron density map. In a later analysis, T. Senda has noticed [11] that even the set of laboratory X-ray data (native Met protein vs. SeMet protein) has a considerable phasing power if not sufficient to lead to a complete tracing of the polypeptide chain. As usual, the structure of the BphC enzyme was finally refined against the 1.8 Å resolution data collected at BL6A of the Photon Factory.

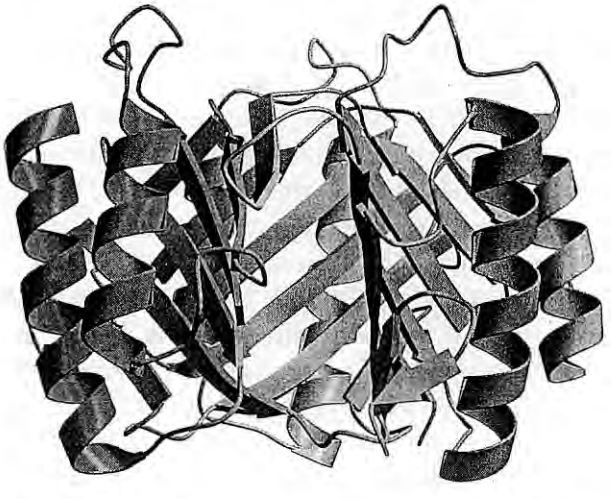

Fig.2 Three-dimensional structure of macrophage migration inhibitory factor from rat liver solved by the MAD method (see text) [9].

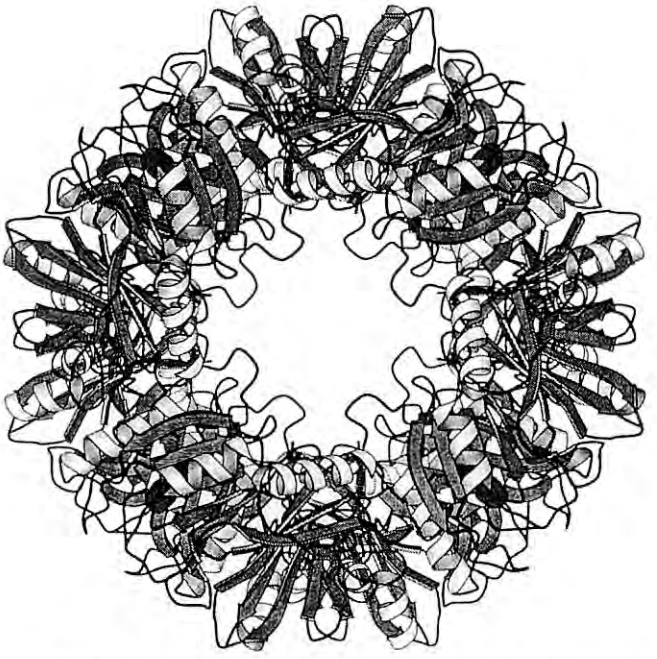

Fig.3 Three-dimensional structure of the octameric molecule of a PCB-degrading enzyme, BphC, having a total molecular weight of 250 kilodaltons [10].

3. The efforts toward the elucidation of the dynamical structural change occurring in protein crystals making use of the time-resolved Laue diffraction method.

As mentioned in the Introduction, the new multifunctional camera installed at BL18B is so designed as to have a capacity for recording both Laue and Weissenberg X-ray diffraction patterns. Several Laue pat-

terns can be recorded on a single IP detector with a certain time interval. Attempts at utilizing the classical Laue diffraction methods for the elucidation of protein structures changing as a function of time have become realistic only with the advent of synchrotron radiation as a source of continuous and intense X-ray beam [12]. The new time-resolved Laue cum Weissenberg camera has been installed at BL18B constructed by N. Watanabe at the Photon Factory. This project has fully been supported by the Ministry of Education, Science and Culture of Japan through grants-in-aid for scientific research on priority area Nos. 05244101, 05244102 and Nos. 05244104, 05244105 represented by Prof. N. Sakabe (Tsukuba University). The priority area is scheduled to be active through the period 1993 to 1996. The priority area is now enjoying the participation of nealy 50 reaearch groups specializing in diffraction physics, instrumentation, software development, crystallography, spectroscopy, enzyme biophysics, enzyme biochemistry and organic synthesis.

For the sake of space limit, only one achievement, which has been performed by T. Nonaka, will be highlighted here. The obvious preliminary experiments along this line of efforts is the attempt to deduce a protein structure based on a set of static Laue diffraction data. Obviously the data set must be recorded with a single Laue exposure (without changing the crystal orientation) so that the experiment is a meaningful preliminary step toward the final purpose of carrying out time-resolved experiments. To collect a set of X-ray diffraction data sufficiently covering the independent area of the reciprocal space in a single-shot experiment, the target crystals must have high (Laue) symmetry and the direction of the incident X-ray beam must be very carefully chosen. With this point in mind, T. Nonaka has made an extensive survey over the polymorphic crystals reported so far for a classical enzyme RNase A (ribonuclease A from bovine pancreas) and its modified form, RNase S [13]. Using the crystals of RNaseA crystallized in the highest available symmetry (Laue group $\bar{3}$m), Nonaka was able to collect a 2.5 Å, 45% complete data set from a crystal of RNase A complexed with a substrate analogue 3'-UMP in a single-shot Laue experiment (0.7-2.0 Å wavelength range) by a single-shot Laue exposure enduring only 20 msec [14]. As shown in Fig.4, this data set exhibited an excellent difference electron dnesity for the bound ligand, 3'-UMP, when difference Fourier map was calculated against the data taken from a crystal of the enzyme (RNase A) alone. Although the latter data were collected by a conventional Weissenberg method using monochromatic X-ray beam and thus were almost perfect with respect to the coverage of the reciprocal space, it is remarkable that, in a favourable condition, a single-shot Laue exposure can yield such an image as shown in Fig.4, which clearly has enough potential to give at least partial information as to the structural change in the active site of the enzyme occurring upon certain triggering impacts.

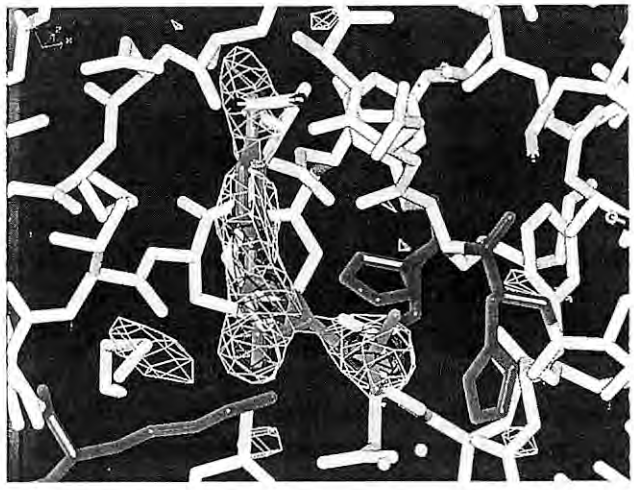

Fig.4 Difference electron density (caged) corresponding to the bound ligand (caged skeleton) as revealed by a 20 msec single-shot Laue diffraction exposure [14].

As is now well known, however, one of the most difficult problems inherent to time-resolved Laue diffraction experiments is how to give the triggering impact to the target crystals. The consensus now appears to be that the method employing the so-called "caged" compounds is the best one. In this method, the "caged" compounds are specifically designed to protect the reaction group through covalent binding with a chemical group (most popularly the ortho-nitro benzyl group) which, in turn, is liberated from the reactive group upon irradiation with UV or visible light (most popularly the light at 340 nm wavelength). In practice, however, the method employing the "caged" compounds is bound up with various inherent difficulties : non-uniform irradiation by light due to absorption through the light path in crystal and the solubility limit of the "caged" compounds, to mention only a few factors. Various attempts to break through these difficulties are now in progress for the crystals of RNase A as well as for other protein crystals.

Other attempts at realizing time-resolved Laue diffraction experiments are in progress in several other groups working for the above-mentioned Japanese

priority area project. Among them, two reports are included in the present Activity Report. One is from the group of N. Tanaka [15] ("Development of temperature-jump system for protein crystallography which coupled with Laue photography") and the other is from the group led by J. Oda [16,17] ("High resolution and rapid diffraction data collection studies of glutathione synthetase from *Eschericia coli* B").

(Y. Mitsui, Nagaoka University of Technology)

References

1) T. Tsukihara, *Photon Factory Activity Report* **12** (1994) 529.
2) N. Sakabe, *J. Appl. Crystallogr.* **16** (1983) 542.
3) N. Sakabe, *Nucl. Instrum. Methods*, **A303** (1991) 448.
4) N. Sakabe, S. Ikemizu, K. Sakabe, T. Higashi, A. Nakagawa, N. Watanabe, S. Adachi and K. Sasaki, *Rev. Sci. Instrum.* **66** (1995) 1276.
5) T. Tsukihara, H. Aoyama, E. Yamashita, T. Tomizaki, H. Yamaguchi, K. Shinzawa-Itoh, R. Nakashima, R. Yaono and S. Yoshikawa, *Science* **269** (1995), 1069.
6) J. Drenth, *Principles of Protein X-ray Crystallography*, Springer.
7) S. Iwata, C. Ostermeier, B. Ludwig and H. Michel, *Nature* **376** (1995) 680.
8) W.A. Hendrickson, J.R. Horton and D.M. LeMaster, *EMBO J.***9** (1990) 1665.
9) M. Suzuki, H. Sugimoto, A. Nakagawa, I. Tanaka, J. Nishihara and M. Sakai, *Nature Structural Biol.* **3** (1996) 259.
10) T. Senda, K. Sugiyama, H. Narita, T. Yamamoto, K. Kimbara, M. Fukuda, M. Sato, K. Yano and Y. Mitsui, *J. Mol. Biol.* **255** (1996) 735.
11) T. Senda, *J. Crystallogr. Soc. Japan* 38 (1996) **14** (in Japanese).
12) J. Hadju and I. Anderson, *Ann. Rev. Biophys. Biomol. Structure*, **22** (1993) 467.
13) T. Nonaka and Y. Mitsui, *Tampakushitsu, Kakusan, Kohso* (Proteins, Nucleic Acids and Enzymes), **40** (1995), 1635 (in Japanese).
14) T. Nonaka, *J. Crystallogr. Soc. Japan*, **38** (1996) 35 (in Japanese).
15) H. Moriyama, N. Igarashi, A. Ikezaki and N. Tanaka, *Photon Factory Activity Report* **13** (1995) Project No. 95G-082.
16) A. Aoyagi, H. Kato, J. Hiratake, T. Nishioka and J. Oda, *Photon Factory Activity Report* **13** (1995) Project No. 95G-057.
17) J. Hiratake, J. Kato and J. Oda, *J. Amer. Chem. Soc.* **116** (1994), 12060.
18) T. Tsukihara, H. Aoyama, E. Yamashita, T. Tomizaki, H. Yamaguchi, K. Shinzawa-Itoh, R. Nakashima, R. Yaono and S. Yoshikawa, *Science*, **272** (1996), 1136.
19) R.H. Jacobson, X-J, Zhang, R.F. DuBose and B. Matthews, *Nature* **369** (1994), 761.

H. THEORETICAL RESEARCHES

The theoretical group of Photon Factory was established in 1993. The staff consists of one professor and two research associates. Until now two students, one of whom is from Bangladesh, have received the Ph.D. degrees, and now two students are registered. In the following, a brief research is presented.

1. Lopsided Energy Sharing between a Photoelectron and an Auger Electron in Solids

1.1. Introduction

The phenomena of the Auger decay have been observed in many systems since the discovery by Auger in 1925. As it is well known, the essence is rather simple: a core hole created by some reason is destroyed by the electron in a higher level and, accordingly, another electron is emitted from the atom. Here, we are interested in the cases of photoexcitation, in which the core hole is made by exciting a core electron into the continuum states by photons. When the energy of the photon is larger than the threshold energy, the electron becomes a photoelectron and propagates almost freely until it is detected. In this simplest framework, the kinetic energy of the photoelectron is determined by that of the photon, and that of the Auger electron is always constant representing a fixed level scheme.

In actual cases, the above framework is too simple. We must take into account the following two *final-state* interactions associated with the present excited states: the core attraction by the ionized atom and the Coulomb repulsion between the two propagating electrons. With these interactions, their kinetic energies are no more constant because the two electrons can share kinetic energies and a part of the energy is transferred from one to the other. Then, a new question arises. That is, in which direction does the energy transfer tends to occur within the restriction of energy conservation? From the photoelectron to the Auger electron or vice versa?

The experiments performed so far, seem to give the answer: the photoelectron *lopsidedly* loses some energy and the Auger electron receives it. In particular, the most outstanding case is where the energy of the former is close to the threshold. In fact, the energy loss of the former becomes largest in that case. Thus, it is our main concern to clarify why such lopsidedness occurs in the dynamics of energy sharing.

In order to answer this problem, we first investigated each effect separately because it was too difficult to treat those entangled effects at the same time from the beginning. As for the core attraction, we already clarified last year that it leads to an energy gain of the Auger electron and a loss of the photoelectron. This year, we have extended our formulation to include the electron-electron (e-e) repulsion and clarified its effect completely. Briefly speaking, the e-e repulsion gives an almost reverse effect, namely, part of the kinetic energy of the Auger electron is transferred to the photoelectron. In this case, the physical image is somewhat difficult to understand intuitively. In fact, the way of sharing is determined by the initial phase of the two-electron wave function.

Now, we know that the two effects are competing, and so the remaining question is what type of dynamics is realized in consequence of such competitions. In order to answer this question quantitatively, we will take into account both effects and examine the energy spectrum for propagating electrons in various cases as shown later.

1.2. Model

In actual calculations, we prepare electronic states, using a rather simple model as shown in Fig.1. Here we take into account only two core levels: a deep one and a shallow one. Thus this is a minimum model to study the Auger decay. The continuum states are also chosen as the most simple ones. Namely, only s-waves are included, by assuming that the spherical symmetry is good enough around the atom. In order to obtain those

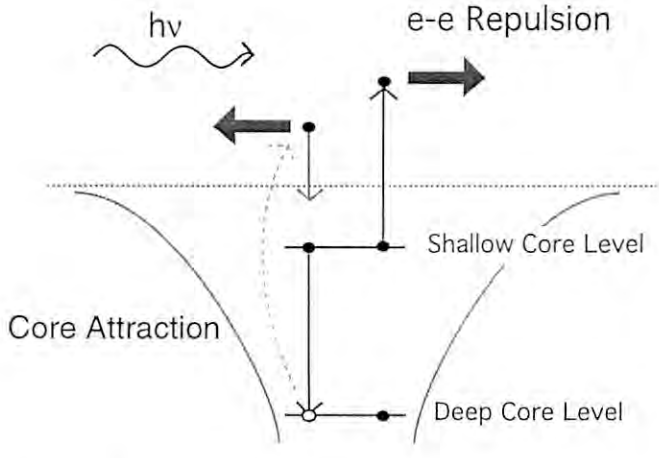

Fig.1 A schematic picture of a 'minimum model' to study a dynamics of a photoelectron and an Auger electron.

wave functions, we solve a semi-infinite one-dimensional tight-binding Hamiltonian with appropriate attraction potentials.

1.3. The Electron-Electron Repulsion and More

In the following, we show one typical example that well illustrates the dynamics. In this case, the kinetic energy of the photoelectron is much larger than that of the Auger electron. Generally speaking, when the photoelectron has only a small kinetic energy, the effect of the core attraction is rather large and superior to that of the e-e repulsion. In this case, the former is weakened by rapid propagation of the photoelectron. The competition that we mentioned at the beginning, therefore, becomes severer. In the rest of this section, we use the notation that the screening lengths for the core attraction and the e-e repulsion are expressed as ξ_1 and ξ_2, respectively.

In Fig.2, we show several photoelectron line shapes. For all the line shapes, the nominal energies are common and set at 6.5 au and 1.0 au (au=27.2eV) for the photoelectron and the Auger electron, respectively.

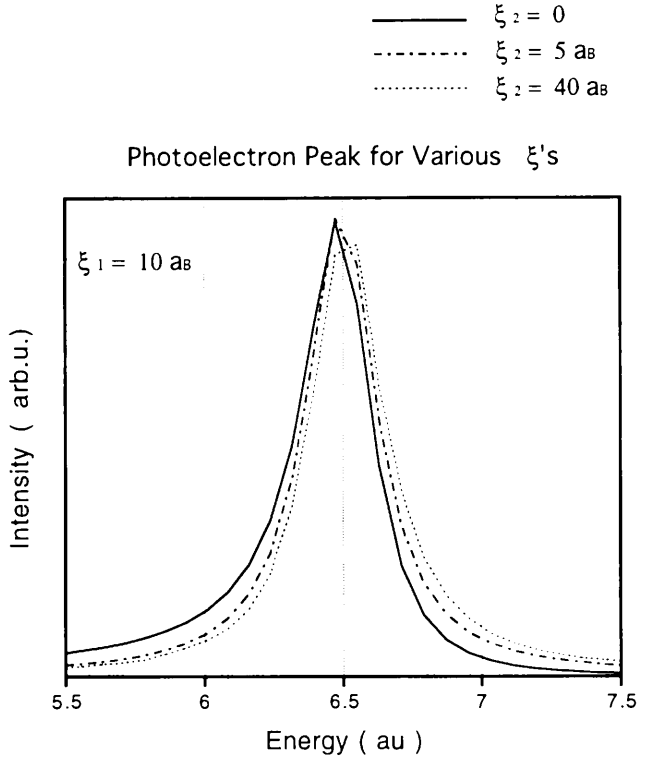

Fig.2 The photoelectron line shapes in various cases of screening. In all of them, the screening length for the core attraction is fixed at ten times the Bohr radius, while that for the e-e repulsion is zero, five and forty times the Bohr radius for the solid, chain and dashed curves, respectively.

Different line shapes correspond to various screening cases. In all of them, ξ_1 is fixed at ten times the Bohr radius. The screening length for the e-e repulsion, ξ_2, on the other hand, is zero, five and forty times the Bohr radius for the solid, chain and dashed curves, respectively. As it is clearly seen, the spectral shape varies continuously with the increase of ξ_2. When ξ_1 is much larger than ξ_2, we find the asymmetry that the lower energy side is enhanced and the higher energy side is reduced. On the other hand, when ξ_1 is much smaller than ξ_2, we find another asymmetry that the lower energy side is reduced and the higher energy side is enhanced. This means that the direction of the net energy transfer between the electrons is very sensitive to the two parameters, and various types of dynamical energy sharing is realized. In the case of an isolated atom, such screening cases might be somewhat unrealistic, but, in the case of solids, we can expect a variety of situations. In particular, the core hole is essentially a static charge, while the Auger electron is a dynamical charge when they are seen from the photoelectron. Thus, the choice of different values for ξ_1 and ξ_2 become more realistic.

2. Three Band Theory for Three Types Self-Trapped Excitons in Alkali Halids

As the most basic processes of radiation damage, excitons and their subsequent lattice relaxation processes in non-metallic solids have been a subject of considerable interest in these twenty years. In particular, charge-separation processes of an exciton into an electron and a hole, together with local lattice relaxation, have been the problem of great interest. It is well known that, from this charge-separated state, various photo-chemical reactions can occur, such as the photographic effect, the optical composition and decomposition, and defect formations. As a typical example for these various photo-chemical reactions, lattice relaxation processes of an exciton in alkali halides have been studied very intensively.[1)]

In the past several years, substantial progress has been made to clarify origins of various emission bands coming from the self-trapped exciton (STE). Kan'no et al.[2)] discovered the presence of three kinds of emission bands from their experiments on mixed alkali halides, i.e. emission bands of a small Stokes-shift (type I), of a large shift (type III), and of an intermediate one (type II). These three types of emission bands are inferred to

come from different lattice configurations of the STE. The type I emission seems to come from a hole localized in dimerized two halogen (X)'s with an electron loosely trapped around it. In this case, the X-X distance becomes short, and the symmetry of the STE is reduced from O_h to D_{2h}, but still keeping even parity. The dimer ion (X_2^-) in alkali halide crystals is usually called "V_K" center and hence this type STE with even parity is called "$V_K + e$"[3]. Meanwhile, the type III emission seems to come from an X_2^- ion which is pushed out along ⟨110⟩ direction from their regular halogen ion sites. In this case the electron constituting an exciton is trapped in a halogen vacancy thus created. This is a charge-separated STE without parity. They have also proposed the type II that corresponds to an intermediate case between the types I and III.

The present report is devoted to a theoretical investigation on STE's in alkali halides, by using the following three band model.[4] The electron moves over diffuse orbitals centered always at the regular halogen lattice sites, in addition to the s-orbitals on the alkali ion sites. We call this diffuse orbital v-orbital hereafter. While, the hole moves over the p-orbitals which are always centered at X-ions. As for the interionic potentials, Mayer-Huggins model will be adopted. In the perfect lattice, the energy of the v-orbital is much higher than that of the s-orbitals. However, when an X ion is pushed out from the regular lattice site because of the lattice relaxation, the v-orbital of this site is pulled down well bellow the s-orbital, resulting in the F center which consists of an electron trapped at the halogen-vacancy.

Our Hamiltonian[4], which is not explicitly given here to save the space, includes the site energies, transfer energies of the electron and the hole constituting an exciton, the Coulombic interactions between the electron and the hole, and the interactions between ions. The state of electron is assumed to be written by a linear combination of the s-orbitals and the v-orbitals. It is also assumed that envelope of these s-orbltals is a Gaussian whose center and width will be determined by the variational method. The hole is assumed to spread over only in the p_σ orbitals and its wave function will also be determined by the variational method. Thus the total energy can be calculated for every ionic configuration by the variational methods, and these calculations are iterated until we get a minimum energy. Three types of energy minima A, B and C with different lattice deformations are finally found. The type A is a one-center STE, the B is a deformed V_K+e and the C is a charge-separated STE. These results are obtained in a very wide range of parameter values. In Fig.3, the ionic configurations of A, B and C on [110] plane are schematically shown, together with distributions of the hole and the electron. In these figures, larger open circles (indicated by X^-) denote iodide ions and smaller ones (indicated by A^+) denote alkali ions. Closed circles schematically show fractions of the hole distribution on each iodide ions. While, a large open circle (indicated by e) schematically denotes the radius and center

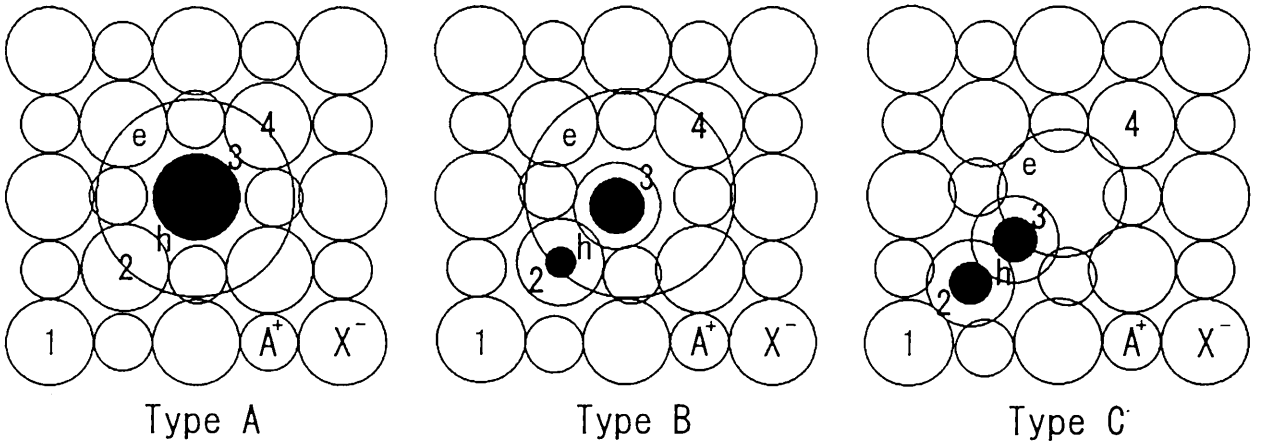

Fig.3 The A, B and C types of the STE with distributions of the hole and the electron on [110] plane. Larger open circles (indicated by X^- denotes the positions of iodines and smaller ones denote the alkali ions. Closed circles show frations of hole distributions on the iodine ions, i.e. ratios of the closed and open circle's radii denote the fractions. While, a large open circle (indicated by e) denotes the radius and center of the Gaussian.

of the Gaussian. In the type A, the hole is localized almost on iodine 3 and the electron is distributed almost in the s-orbitals on the alkali ions, but scarcely in the v-orbitals. It is also seen that the alkali ions adjacent to iodine 3 are displaced outward. Thus, the type A can be called a one-center STE with D_{2h} symmetry. In the type B, the hole is shared by iodine 2 and 3 which are displaced inward with each other. It should be noticed that the hole is much more shared by iodine 3 than iodine 2. While, the electron distribution is almost same as that of the type A. The type B is resemble to the "$V_K + e$" mentioned before, but the D_{2h} symmetry is clearly broken. Thus, we can call it a *deformed* ($V_K +$ e). In the type C, the hole is almost equally shared by iodines 2 and 3, which are both largely displaced toward iodine 1. The lattice site which iodine 3 is originally occupied has now become vacant. While the electron enters into this v-orbital and its neighboring s-orbitals. This type C can be called a charge-separated STE and corresponds to the "off-center type STE", which is proposed through the Hartree-Fock calculations for alkali-chlorides clusters by Leung et al.,[5] Table I shows values of energies of A, B, and C minima for different parameters corresponding to the case of NaI(a), KI(b) and RbI(c), respectively. It is seen from this table that the type A is always the highest and the type C is absent in (a) and (b).

Now we will discuss these theoretical results in connection with experiments. According to Kan'no et al.[2] it is well known that only type I emission is observed in NaI, while both types I and II are observed in KI, and all types I, II and III can be observed in RbI. From these facts, we can presume that Kan'no's types I and type III correspond to our B and C, respectively. A state corresponding to the type II is not found in our present result. Recent studies by femtosecond pump and probe spectroscopy [6),7)] have suggested that in the initial stage of the self-trapping, a new precursor state is expected to be formed. Iwai et al.[8] have proposed that this precursor state is a one-center type self-trapped hole. Our type A may correspond to this precursor state, and further studies are necessary on this problem. A strong asymmetry of the type B can be attributed to the Coulombic attraction between the electron and the hole. If some screening effects between the electron and the hole were taken into account, the asymmetry may be weakened. The short-range nature of the transfer integral of s-orbital is also responsible for this asymmetry. More precise consideration of these factors is necessary.

Table I Energies (eV) of the type A, B, and C minima. Parameters are set to correspond to NaI(a), KI(b) and RbI(c).

	a	b	c
A	−2.9897	−3.2155	−3.2407
B	−3.0864	−3.3751	−3.4241
C			−3.4683

References

1) Y. Toyozawa: Highlights of Condensed-Matter Theory (North-Holland, 1985).
2) K. Kn'no, K. Tanaka and T. Hayashi: Rev. Solid State Sci. **4** (1990) 383.
3) M. Kanzig: Phys. Rev. **99** (1955) 1890.
4) S. Nagasaka and K. Nasu: 1826. J. Phys. Soc. Jpn. **65** (1996).
5) C.H. Leung, G. Bradford and K.S. Song: J. Phys. C **18** (1985) 4459.
6) J.C. Philips: Phys. Rev. **133** (1964) A452.
7) T. Shibata, S. Iwai, T. Tokizaki, K. Tanimura, A. Nakamura and N. Itoh: Phys. Rev. **B 49** (1994)13255.
8) S. Iwai, T. Tokizaki, A. Nakamura, T. Shibata, K. Tanimura, A. Shluger and N.Itoh: J. Lumines. **60-61** (1994) 720.

Experimental Facilities

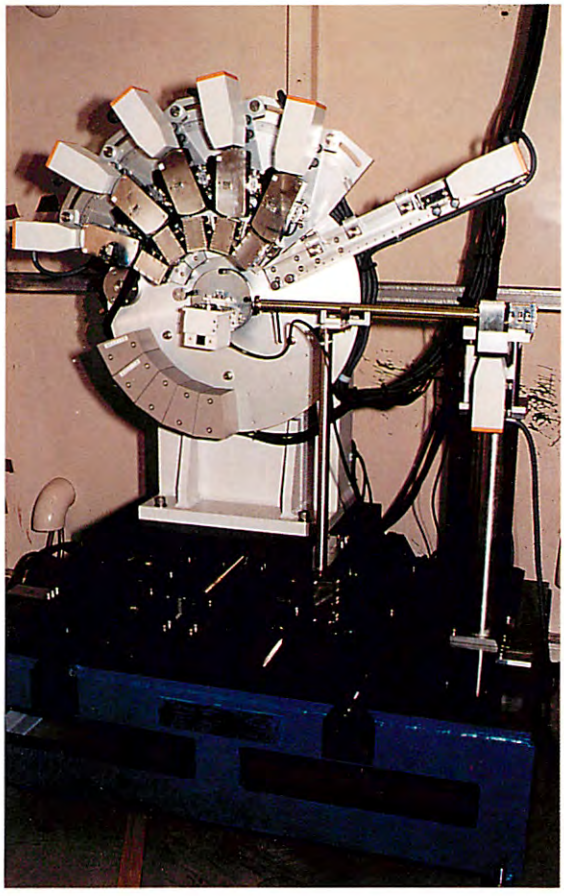

New powder diffractometer with a multiple-detector system

You can jump to the article by clicking its title.

CONTENTS

A. BEAMLINES

1 IMPROVEMENT OF OPTICAL ELEMENTS IN BL-4C

New optical elements were installed in BL-4C during the 1995 summer shutdown. The outline of the beam line was previously described in Volume 12[1]. The sagittal focusing monochromator was replaced by a flat double-crystal monochromator which would ensure good energy tunability. In order to focus the monochromatic beam, the cylindrical mirror was bent, bringing about a high photon density. The beam line was opened on the 7th of November and new experiments on X-ray magnetic Bragg scattering were started. The performance of the beam line is as follows.

Monochromator (Photon Energy): 6 - 23 keV,
Si(111) (Energy Resolution): $(\Delta E/E) \approx 5 \times 10^{-4}$
Mirror: rhodium-coated silicon
Size: 1000 × 100 × 60 mm
Radius of curvature: 53 mm × 5 km
Horizontal Acceptance: 3 mrad
Beam size: 0.6 mm (vertical) × 1.0 mm (horizontal),
Movement of Beam Position: 0.2 mm (vertical),
(E = 6 - 23 keV) 0.15 mm (horizontal)
Beam Intensity: (mirror focus)/(without mirror) = 160
(E = 17.7 keV)
(mirror focus)/(sagittal focus) = 17
(E = 15.9 keV)
Momentum Resolution: $(\Delta q/q) < 10^{-3}$ (Si(111), λ=1.1Å)
New Accessories: Polarimeter for magnetic scattering
He flow type cryostat (T = 2.0 K-350 K)
Magnet (H = 2 kOe at a gap of 60 mm)

Reference
1) Photon Factory Activity Report 1994, #12, E-1 (1994).

2 BL-6B, BEAMLINE FOR THE TARA PROJECT

BL-6B is to be constructed as a beamline for macromolecular crystallography using a Weissenberg camera and an imaging plate. The layout of the new beamline is shown in Fig. 1. The beamline consists of a Pt coated bent plane Si single crystal mirror and an asymmetrically cut cylindrical Si (111) monochromator. The mirror and the monochromator are located at 19.5 m and 23.0 m from the source, respectively. The expected size of the focused beam is to be 0.1 mm by 0.1 mm, FWHM. The Weissenberg camera equipped in the experimental hutch has a radius of 573 mm, and the two large 400 mm × 800 mm imaging plates can be mounted on the film cassette. Half of the beam-time of the station will be dedicated to members of the TARA project.

3 BL-12C PERFORMANCE OF A NEW XAFS BEAMLINE

The design and the mechanical performance of the double crystal monochromator was described in previous volumes[1,2]. In brief, the beamline consists of a double crystal monochromator and a bent cylindrical mirror. These kinds of optics allow it to be used separately from the focusing and beam size variation adjustments functions during energy scanning, which were experienced when sagittal focusing double crystal monochromator was used.

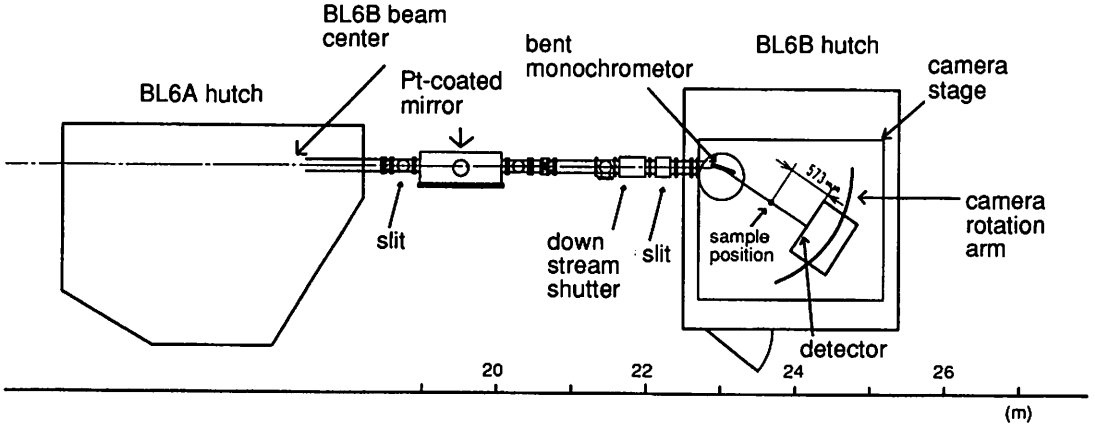

Fig. 1 Layout of BL-6B

Si(111) crystals are used below 16 keV and Si(311) are used above this energy level. The mirror is removed when higher energy X-rays, above 23 keV, are required. A slit defining vertical beam size (Slit 2) was added between the monochromator and the mirror, which defines the energy resolution of the beam. The slit placed before the monochromator could be used for the same purpose, which inevitably would derive the temperature gradient on the first crystal at the edge of the beam even if it is fairly well cooled. Thus, lose the energy resolution.

The beam size, measured by scanning a narrow slit, was 1.3 mm (hor.) x 0.6 mm (ver.) in FWHM, which is a little bit larger than expected. The difference is due to the imperfect shape of the mirror; the both ends of the mirror are not bent ideally. The flux gain is shown in Table 1. As shown in Fig. 2, both the high flux with fairly high energy resolution, Mode(a), and

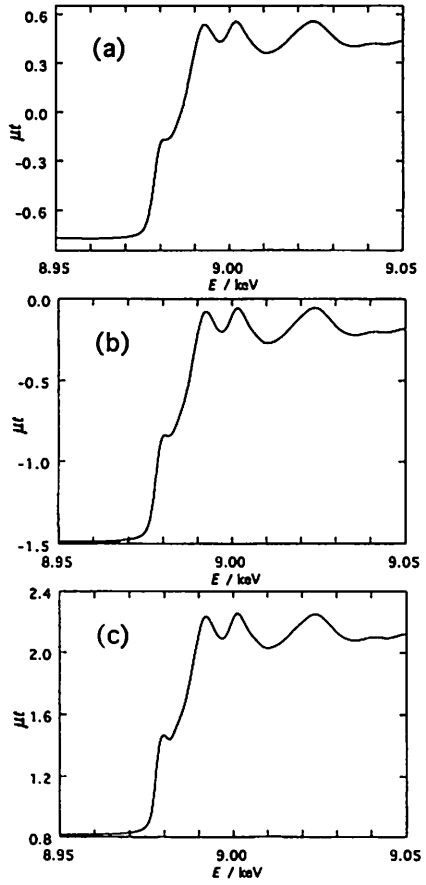

Fig. 2 XANES spectra of a copper foil taken with a Si(111) monochromator at different opening conditions of Slit 2. The photon fluxes were 7.2×10^{10} s^{-1} (a), 4.8×10^{10} s^{-1} (b) and 6.4×10^{9} s^{-1} (c) when the stored current was 300 mA. Thus, both high energy resolution (c) and high flux modes (a) can be easily chosen.

Table 1 Observed flux gain by the focusing mirror.

slit size	5×1	1×1	0.5×0.5	
non foc.	5.8×10^{9}	1.1×10^{9}	2.7×10^{8}	
focused	1.1×10^{11}	7.4×10^{10}	2.7×10^{10}	a)
gain	20	65	101	
focused	8.9×10^{10}	4.8×10^{10}	1.6×10^{10}	b)
gain	15	44	59	

The gain is the ratio of the intensity which passes through the receiving slit, the amount of which is indicated in the table with and without a focusing mirror. a) Slit 2 fully opened; b) Slit 2 adjusted so as to measure the usual XAFS spectra as indicated in Fig. 2b.

the high energy resolution with fairly high flux, Mode(c), can be selected by adjusting the opening of Slit 2. These modes are suited for EXAFS and XANES experiments, respectively. The higher orders were less than 10^{-4} of the fundamental beam when the monochromator was detuned so that the intensity of the monochromatized beam was 60 % of the maximum. The detailed design and performance of the beamline was reported elsewhere[3].

With the help of a 19-element solid-state detector, BL-12C has extended the objects of XAFS experiments both in the sample concentration, size, and quantity.

References

1) Photon Factory Activity Report 1993, #11, I-4 (1994).
2) Photon Factory Activity Report 1994, #12, E-1 (1995).
3) M. Nomura and A. Koyama, KEK Report 95-15 (1996).

4 BL-16B HIGH RESOLUTION 24-M SGM BEAMLINE

Commissioning of BL-16B has recently begun. BL-16B combines a high-resolution 24-m spherical grating monochromator (H-SGM) with a 26-period multi-pole wiggler/undulator resulting in high energy resolution and high flux in the VUV and soft X-ray regions. The H-SGM was successfully installed during the 1995 winter shutdown. The first photons came out through the monochromator in the middle of May 1995. With a resolving power of approximately 2000 in a range of photon energy from 40 to 500 eV more than 10^{11} photons/sec were measured in a beam size of less

than 1mm². The best resolutions obtained so far, at substantially lower photon flux, are higher than 10000 at 250 eV, and 8000 at 400 eV. The way is paved for new experiments in the spectroscopic research field of gaseous and solid state samples. Resolution is close to the theoretically expected values, but flux is at least one order of magnitude lower than the calculated values. This is probably due to the insufficient focusing property of the second mirror M_1, overestimation of the grating efficiencies in the calculations, and carbon contamination of the optical elements.

The beam-line consists of a Kirkpatrick-Baez premirror system, a 24 m spherical grating monochromator with a movable exit slit, and refocusing mirrors. Undulator radiation is focused horizontally by the first cylindrical mirror M_0 with 3/5 demagnification. The second mirror M_1 is a spherical mirror, which focuses vertically with 1/10 demagnification onto an entrance slit. With three interchangeable gratings of 400 l/mm, 900 l/mm, and 2000 l/mm, the H-SGM is designed to cover the photon energy range from 40 to 600 eV.

The energy resolution of the monochromator has been tested by photoabsorption measurements of rare gas atoms and diatomic molecules. The total-ion yield spectrum of N_2 at the N1s→π* resonance is shown in Fig. 3 as an example. Both entrance and exit slits were set for maximum resolution at 5 μm. Unfortunately it was difficult to determine absolute values for the resolution from the absorption measurements because the natural linewidths for inner-shell excited states is not well-established. Comparing this with all available data for the N1s→π* resonance in N_2 suggests that the energy resolution is below 50 meV at 400 eV. The degree of linear polarization of the monochromatized radiation was determined to be more than 96 % by photoelectron angular distribution measurements from He atoms. Further detailed information on the performance of the H-SGM is being prepared for publication.

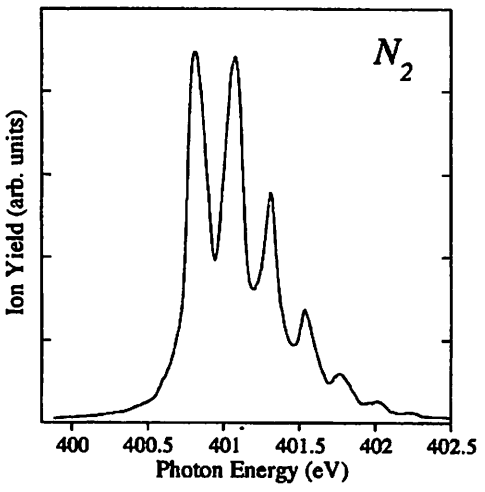

Fig. 3 Total-ion yield spectrum of N_2 at the N1s→p* resonance.

B. NEW INSTRUMENTATION

1 18C POWDER DIFFRACTION IN NON-AMBIENT CONDITIONS

BL18C, designed for the powder diffraction experiment in non-ambient conditions such as high pressure and/or low temperature, was constructed during the summer shutdown in 1995. The beamline consists of a double-crystal monochromator and horizontal and vertical focusing mirrors.

The double-crystal monochromator is a fixed-exit type equipped with a double flat crystal, which covers an energy range of 5 to 25 keV. The second crystal is long enough to receive the monochromatized beam from the first crystal without any translational motion in the X-ray direction. The position of the second crystal is adjusted up and down to keep the beam height constant. The measured shift of the beam position between 7.7 keV and 25 keV was 25 μm in the horizontal direction and less than 5 μm in the vertical direction.

Both mirrors are cylindrical types without a bending mechanism, and made of SiO_2 with a Pt coating. The critical energy is designed to be 25 keV. The mirror size is designed to have a sample acceptance of 1 mrad. The horizontal mirror is located 18.4m from the source with a radius of 1070 m and the vertical mirror is located at 18.9 m with a radius of 760 m, while the sample position is 21.5 m from the source. The focused beam size at 25 keV was 40 μm in the vertical direction and 80 μm in the horizontal direction (Fig. 4).

A diamond anvil high pressure cell or a circulation type refrigerator (cooled down to 10 K) is attached to a vertical type single axis goniometer. Diffracted X-rays are recorded on a round imaging plate and can be read out in three minutes. For more precise measurements, a flat imaging plate is also available. Typical measuring

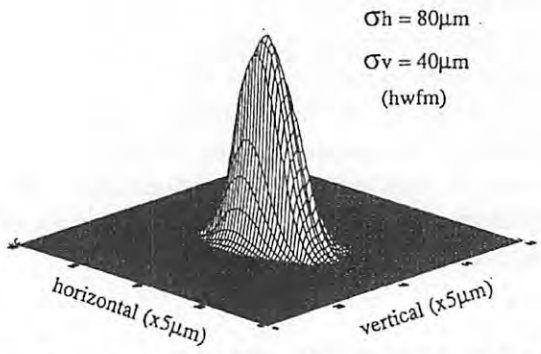

Fig. 4 Direct beam profile at the focused point at BL18C.

time for DAC experiments is 10 min., which is 10 times shorter than that of the BL6B. Details of the diffractometer are described elsewhere in this volume.

The station has been open since February, 1996.

2 A NEW POWDER DIFFRACTOMETER WITH MULTIPLE-DETECTOR SYSTEM

A new powder diffractometer has been installed at the BL-4B$_2$ experimental station[1] that equips two kinds of detector systems, a multiple-detector system (hereafter called MDS) and a multi-purpose detector (MPA) for conventional single-arm scanning (Fig. 5). The optics design of the MDS is based on flat-specimen-reflection geometry using parallel-beam, and a 2θ-scan technique in the asymmetric diffraction at a fixed incident angle. In the case of parallel-beam optics, asymmetric diffraction from a flat specimen gives virtually the same angular resolution and enhanced intensity compared with symmetric diffraction[2]. Thus a number of detectors can be set at arbitrary 2θ angles and function simultaneously.

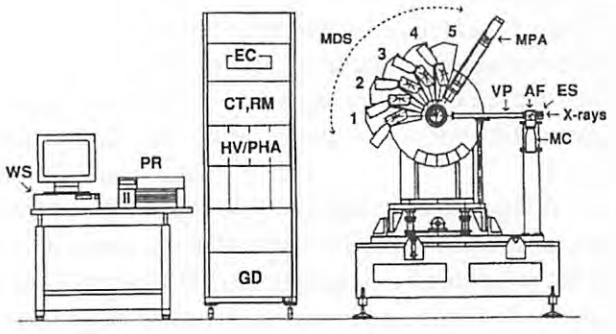

Fig. 5 A schematic diagram of new powder diffractometer with a multiple-detector system.

The present MDS consists of five detector arms. Each arm has Soller slits with a 2° aperture, a flat Ge(111) crystal analyzer, and a scintillation counter, and is set radially at 25° intervals on the 2θ-axis of the goniometer. These five detectors can simultaneously record the whole powder pattern divided into five segments with an equal 2θ span. The flat-specimen reflection geometry has several advantages over Debye-Scherrer geometry with capillary specimens: 1) high counting rates and good particle statistics, 2) low noise and a high peak-to-background ratio, 3) correction-free for the absorption by sample materials containing heavy elements. Moreover, a wide range of angular resolutions can be obtained by using different analyzers, and angular positions and intensities can be accurately measured. The 6th arm, MPA, can be equipped with various kinds of analyzers, such as the long horizontal parallel slits[3], flat and channel-cut crystal analyzers, etc.

The beam-line BL-4B$_2$ has a double-crystal Si(111) monochromator and a focusing mirror. The (111) reflection from Si powder recorded an angular resolution of 0.022 to 0.025° in the full-width at half-maximum and more than 100,000 counts/sec. for λ = 0.7 to 1.5Å. High angular resolution is of essential importance for crystal structure solution and refinement using powder diffraction data. An MDS with a parallel processing function for data collection could achieve both high angular resolution and rapid scanning.

References

1) H. Toraya, H. Hibino & K. Ohsumi (1996). J. Synchrotron Rad. **3**, 75-83.
2) H. Toraya, T.C. Huang & Y. Wu (1993). J. Appl. Cryst. **26**, 774-777.
3) H. Toraya, M. Takata, H. Hibino, J. Yoshino & K. Ohsumi (1995). J. Synchrotron Rad. **2**, 143-147.

3 POWDER DIFFRACTOMETER AT LOW TEMPERATURE AND/OR HIGH PRESSURE

A newly designed powder diffractometer for non-ambient conditions such as low temperature and/or high pressure was installed at BL-18C. Figure 6 shows the side view of the diffractometer. The curved imaging plate (IP) is used as a detector as well as a flat IP. The curved IP reader is installed in the diffractometer. The cryostat and/or diamond anvil cell (DAC) can be

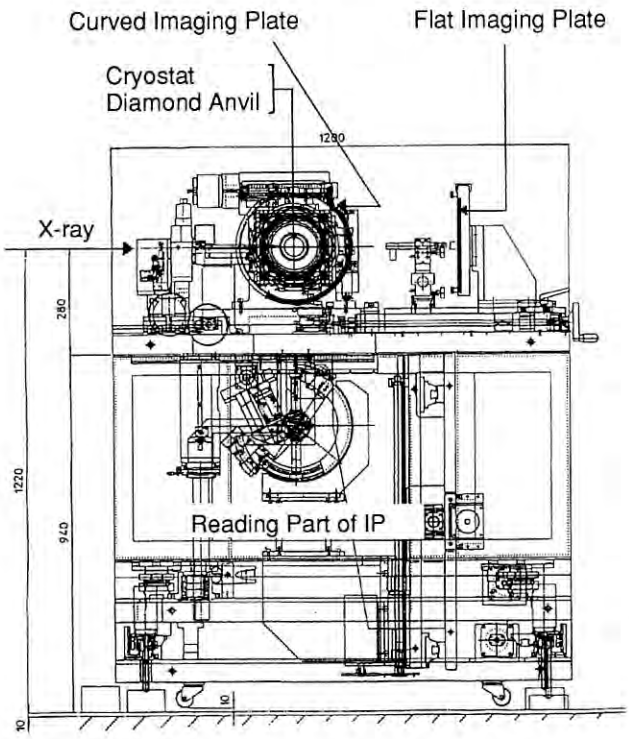

Fig. 6 Side view of the powder diffractometer in non-ambient conditions.

attached to an xy-stage on a goniometer. The specifications are as follows.

1. Optics
   (1) Remote attenuator
   (2) XY-remote slit: 0.25 μm /pulse
   (3) Ion chamber as incident beam monitor: length 5 cm
   (4) Remote shutter
   (5) Collimator diameters: 40, 60, 80, 100, 200, 500, 1000 mm
   (6) Remote xyz-stage for DAC: ±5 mm, 2 μm/pulse
   (7) Goniometer: ω-rotation ±180°, 0.004°/pulse, y-direction 200 mm, 4 μm/pulse
   (8) Remote yz-stage for cryostat: ±4 mm, 4 μm/pulse
   (9) CCD camera for sample alignment
   (10) Base: q-rotation ±2°; y-direction ±20 mm, 4 μm/pulse; z-direction 20 mm, 0.02 μm/pulse
2. Imaging Plate
   (1) Curved IP
      a. Size: 4400 mm × 200 mm (-123° to +45°)
      b. Pixel size: 100 μm × 100 μm
      c. Sensitivity: 1 X-ray photon
      d. Dynamic range: 1 - 72946
      e. Camera radius: 150 mm
      f. IP reader: He-Ne laser (10 mW), spot size of 30 μm on IP film
   (2) Flat IP
      a. Size: 250 mm × 200 mm, 400 mm × 200 mm
      b. Pixel size: 100 μm × 100 μm
      c. Sensitivity: 1 X-ray photon
      d. Dynamic range: 1 - 9999
      e. Camera radius: 135 mm - 420 mm, 4 μm/step
3. Cryostat
   a. Closed cycle cryostat: 3 W/10 K, range 10 K - 350 K
   b. Controller: sensor Si-diode, computer controlled ±0.1 K (10 K - 25 K), ±0.2 K (25 K - 350 K)
4. CPU: Workstation (SUN/SPARC; 2 sets) Some standard software

C. AR UPGRADE

The synchrotron radiation operation at the Accumulation Ring (AR) has remained parasitic because of its important role as the injector to the TRISTAN Main Ring (MR). The upcoming KEK B-factory is a new high-luminosity electron-positron collider to be constructed in the TRISTAN MR tunnel, and the electron and positron beams will be supplied to the KEK B-factory directly from the linac, which will also be upgraded for high energy injection. Therefore, the AR could be converted to a dedicated synchrotron light source. Discussions about the future plans for the AR began in 1993. It was settled upon that the future role of the AR would be as a single bunch and high flux synchrotron light source. The specifications of this project are summarized in Table 2. The characteristic point of this project is a dedicated machine for single bunch operations with a very high ring current (6-6.5 GeV, 200 mA).

Table 2 Specifications of the upgraded AR.

	Upgraded AR	Present AR
Energy (GeV)	6.0 - 6.5	6.5
Ring Current (mA)	200	40
Emittance (nmrad)	150 - 180	280
Coupling (%)	1 - 2	1
Single Bunch	Yes	Yes
Life Time (hr.)	10	3
Numbers of Insertion device beam lines	8	2
Numbers of Bending magnet beam lines	5	2

It has been well known that bunch property is one of the important characteristics of synchrotron radiation. Recently, single or few bunch operations have been absolutely necessary for some experiments. For example, it makes doing time domain measurements possible like Mössbaur spectroscopy, and also time of flight spectroscopy of ions and electrons created by pulsed X-ray photons. These experiments have been already carried out at the AR-NE3 and NE1 beamlines. Another example is the structural analysis of dynamics like a photo-reaction on protein crystallography using the Laue method. Such dynamics investigations will be done by XAFS and small angle X-ray scattering to clarify what kind of electronic states and structures exist at the intermediate stages of the reaction. Figure 7(a) shows flux spectra of a single pulse from the upgraded AR (200 mA) and Photon Factory (50 mA). The upgraded AR will provide 10^8 photons/pulse at a sample spot (0.5×0.3 mm^2) with an energy resolution of 10^{-4} at 10 keV in the X-ray region. The intensity of the above pulsed X-ray would be sufficient for X-ray scattering and/or XAFS experiments, even single shot, because the typical value of the reflectivity of X-ray diffraction from the sample would be ~10^{-4}.

The upgraded AR will provide not only a single bunch X-ray source but also a high flux hard X-ray source. Figure 7(b) shows usual flux spectra from the upgraded AR (200 mA) and the Photon Factory (300 mA). As shown in this figure, the upgraded AR will provide almost 1 order of magnitude (or more) higher flux than those from the Photon Factory in a hard X-ray region (>10 keV). The high flux enables us to measure weak X-ray scattering phenomena such as magnetic scattering, and structural analysis under extreme conditions (like high pressure, surface etc.), and also to establish medical applications such as Coronary Angiography.

A workshop on "Single Bunch and High Flux Synchrotron Light Sources - AR" was held in the middle of October 1995 where the new science that will become possible with the upgraded AR and also the hardware aspects were discussed. The project will start from 1997 and construction will be completed in 2000.

a

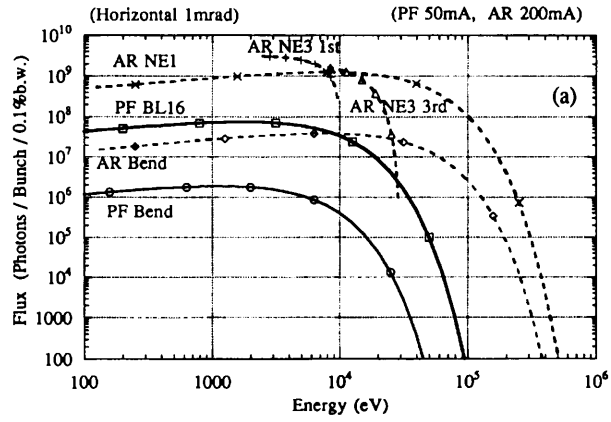

b

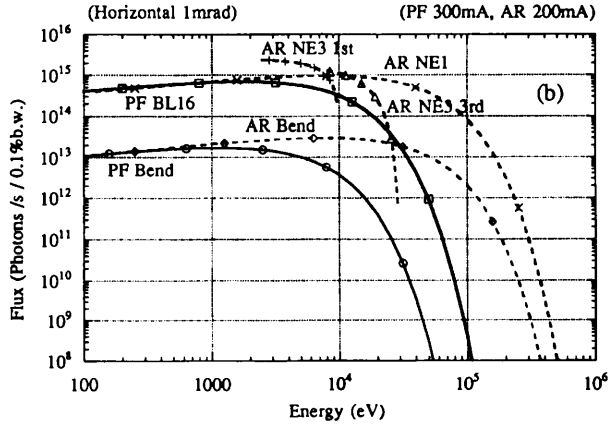

Fig. 7 (a) The solid (dotted) lines correspond to flux spectra of single pulse operation from the insertion device beam lines and bending magnet beamlines at the Photon Factory (50mA) and the upgraded AR (200mA).
(b) Flux spectra from the upgraded AR (200mA) (dotted lines) and Photon Factory (300mA) (solid lines).

Accelerator Operations, Researches and Developments

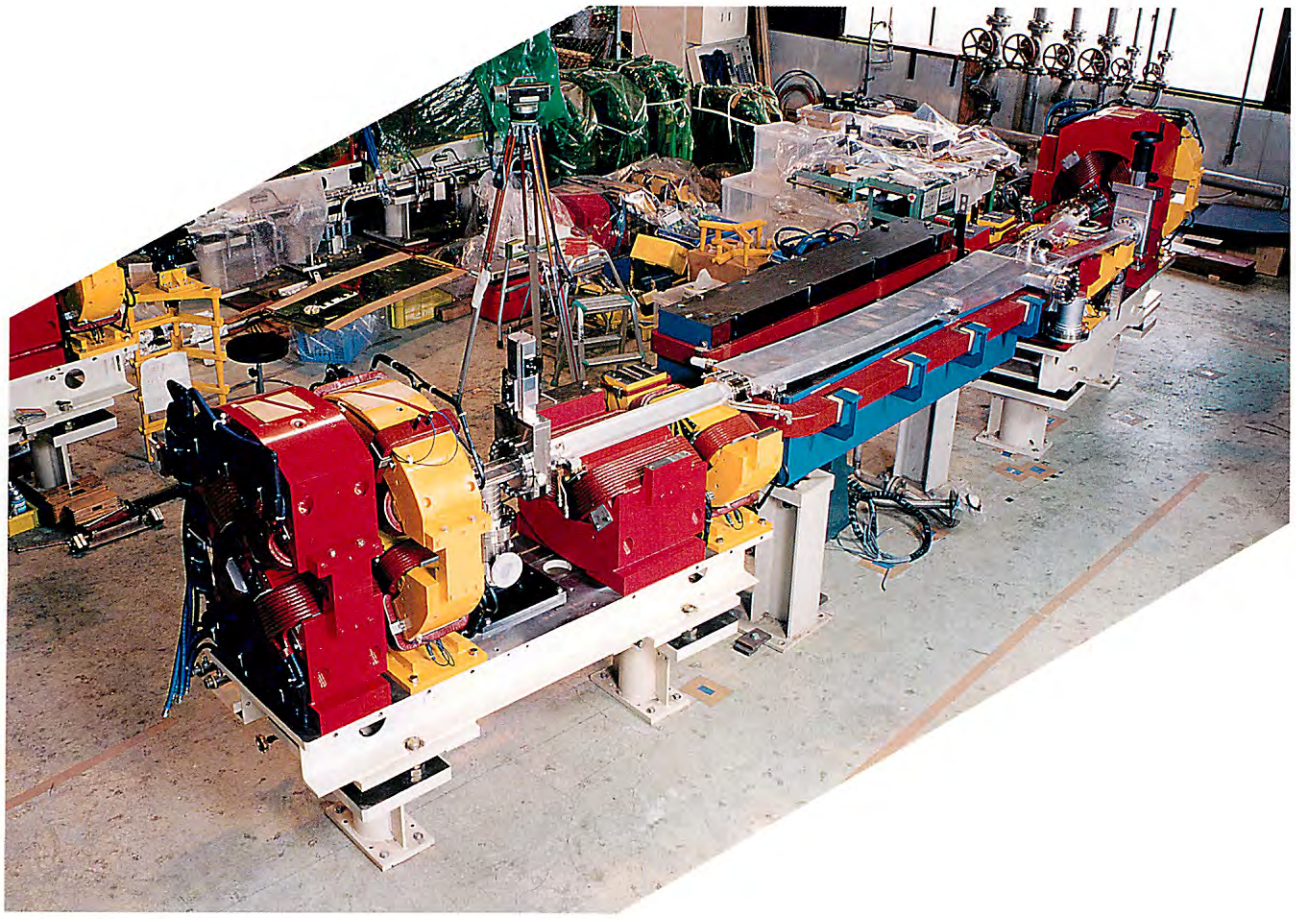

New magnets and vacuum ducts for the high brilliance project of the PF ring.

You can jump to the article by clicking its title.

CONTENTS

A. INJECTOR LINAC

During this period, the linac has been stably operated with a total operation time of 4710 hours and a high operation rate of 99.3%. Operation statistics for this period are listed in Table 1. There were no severe failures which took comparatively long recovering time during this run.

Table 1 Operation and failure time during this period.

Date	Operation time (hrs)	Failure time (hrs)	Operation rate (%)
1994			
Sep. 26 - Dec. 22	2091	10.6	99.5
1995			
Feb. 27 - Jun. 16	2619	22.6	99.1
total	4710	33.2	99.3

The cumulative usage hours of klystrons and the averaged fault rate with averaged applied anode voltage are shown in Tables 2 and 3, respectively. Cumulative status of klystrons up to the end of this term are summarized in Table 4.

Table 3 Averaged fault rate and averaged applied voltage to klystrons.

Period	Fault rate (/day·tube)	Applied voltage (kV)	Total operation (tube·days)
1985/8-1986/7	1.0	238	5,600
1986/8-1987/7	1.0	239	7,740
1987/8-1988/7	1.0	240	9,990
1988/8-1989/7	0.6	241	10,510
1989/8-1990/7	0.3	244	10,690
1990/8-1991/7	0.2	246	10,750
1991/8-1992/7	0.1	248	10,140
1992/8-1993/7	0.1	247	10,010
1993/8-1994/7	0.1	245	10,580
1994/8-1995/7	0.1	246	9,210

Table 2 Cumulative usage hours of klystrons during the past years.

Period	Total	Unused	Failed		Living		MTBF
	No.of tubes	No.of tubes	No.of tubes	Mean age (hours)	No.of tubes	Av.op.time (hours)	(hours)
up to 1985/7	79	2	28	3,600	49	6,200	13,400
up to 1986/7	91	3	39	4,400	49	7,400	13,100
up to 1987/7	106	4	52	4,400	50	9,600	13,600
up to 1988/7	120	2	67	4,500	51	11,400	13,500
up to 1989/7	140	5	82	6,400	53	12,400	14,400
up to 1990/7	158	6	98	8,500	54	11,200	14,700
up to 1991/7	176	14	107	10,100	55	11,100	15,800
up to 1992/7	191	24	113	10,800	54	13,400	17,100
up to 1993/7	203	19	123	10,800	56	15,300	17,700
up to 1994/7	217	30	130	10,900	57	17,800	18,700
up to 1995/7	230	34	138	11,200	58	19,000	19,200

Table 4 Cumulative status of BI-cathode klystrons up to July 1995 corresponding to the year of production. Unused tubes are those which have never been used in the klystron gallery. STB (stand-by) tubes are those which have been used in the gallery and can be used there again.

Year of	Total	Unused	Living					Failed					Cumulative	MTBF
product	No. of tubes	No. of tubes	No. of tubes	(STB	Working) e-	e+	Av.op.time (hours)	No. of tubes	Causes (arcing	window	others)	Mean age (hours)	operation (tube-hours)	(hours)
1987	7	0	4	0	4	0	38,017	3	0	1	2	22,913	220,808	73,603
1988	20	1	13	3	7	3	27,654	6	1	4	1	17,290	463,242	77,207
1989	18	1	8	0	7	1	28,753	9	0	7	2	15,255	367,315	40,813
1990	18	4	8	1	6	1	19,315	6	0	5	1	9,329	210,488	35,081
1991	15	1	8	2	5	1	7,058	6	1	4	1	4,241	81,910	13,652
1992	12	2	8	0	7	1	11,632	2	0	2	0	6,295	105,643	52,821
1993	14	10	4	0	4	0	3,381	0	0	0	0	—	13,524	—
1994	13	13	0	0	0	0	—	0	0	0	0	—	0	—
total	117	32	53	6	40	7	19,984	32	2	23	7	12,618	1,462,930	45,717

B. PF STORAGE RING

1. SUMMARY OF THE STORAGE-RING OPERATIONS

The PF storage ring had been operated with positron beams since 1988. Since the injector linac is now undergoing a large reconstruction phase for the KEKB project, it can not deliver positron beams until 1998. We thus returned to electron-beam operation in June, 1995. In parallel with user runs, much preparation work for upgrading of the PF ring to a low-emittance configuration is under way. In this project (hereafter called the high-brilliance project), the beam emittance will be reduced to 27 nm·rad, about one fifth of the present value. This will result in about ten-times brighter synchrotron radiation from the existing insertion devices. The current status of this project, together with the development of various accelerator components, is described in the next section. The current topics of accelerator studies at the PF ring are described in section 3. FEL research in the UV / VUV region is also under way at BL-2. Recent progress is described in a later chapter (see PROJECTS).

During 1995 we maintained the usual machine-operation cycle involving runs and stops of three months each. Figure 1 and Table 1 summarize the operation statistics of the PF storage ring. The failure times of the machine are given in Fig. 2. The injection intervals and average currents are shown in Fig. 3. The initial stored current was 370 mA for user-runs, and the maximum stored current was 550 mA. The average stored current was about 300 mA during 24-hours of operation.

The electron-beam operations were almost similar to those of the positrons, except for slightly shorter beam lifetimes. Figure 4 is a plot of $I \cdot \tau$ (beam current $\times$ lifetime), which shows this tendency. The beam lifetime was 50-60 hours (at 300 mA), which was 80% of that with positron beams. We can understand the cause of this as follows. In order to prevent the trapping of ions in the beams, we operated with a partial-filling mode that contained 1/6 of the vacant buckets in the ring; however, some amount of ions were still being

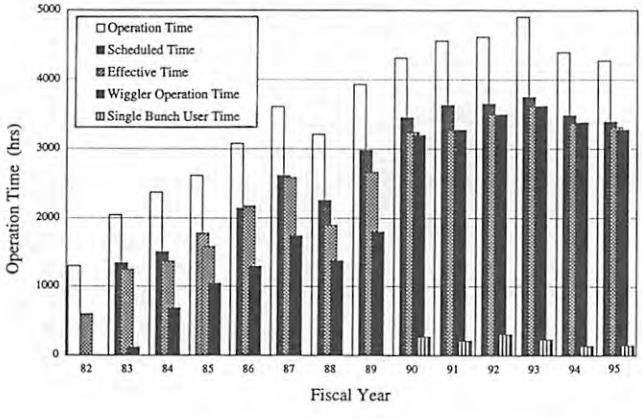

Fig. 1 Operation times of the storage ring.

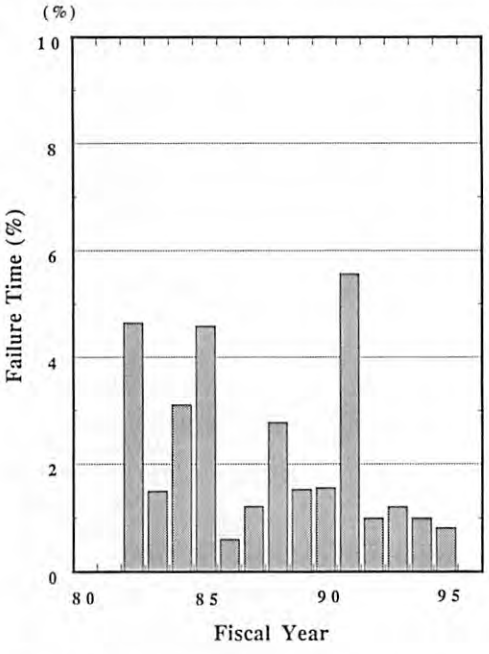

Fig. 2 Rate of failure time of the storage-ring operation.

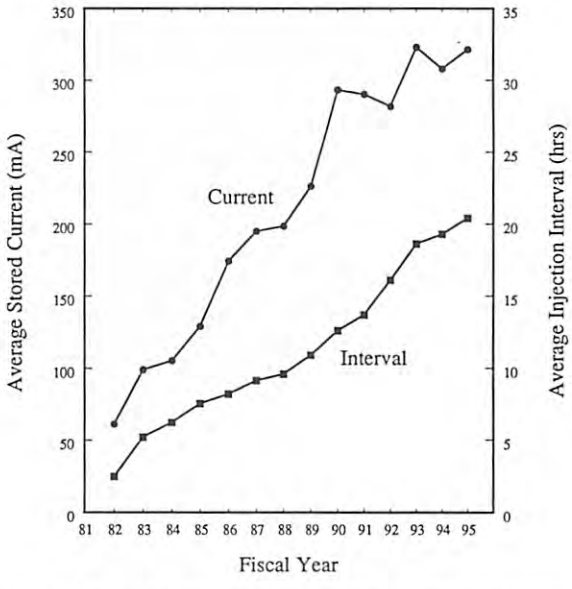

Fig. 3 Average stored currents and injection intervals.

trapped, which induced a vertical instability. In order to suppress this instability, an additional octupole field was applied. This reduced the dynamic aperture, and, thus, shortened the beam lifetimes.

In single-bunch runs, the initial current was 65 mA, and the beam lifetime was typically 20-30 hours (at 50 mA). A bunch-cleaning operation was routinely performed by continuous running of the rf knock-out tuned at the betatron frequency of satellite bunches. The ratio of the satellite bunch to the main one was maintained to an order of 10^{-6} during routine user-runs.

Under multibunch operations with electrons, we sometimes observed a sudden beam-loss of 1-2 mA. Since the amount of loss was small, the users have so far suffered no significant disturbances. Sudden decreases in the lifetimes were observed under the single-bunch runs. These phenomena are supposed to be due to the trapping of micro particles in the beams.

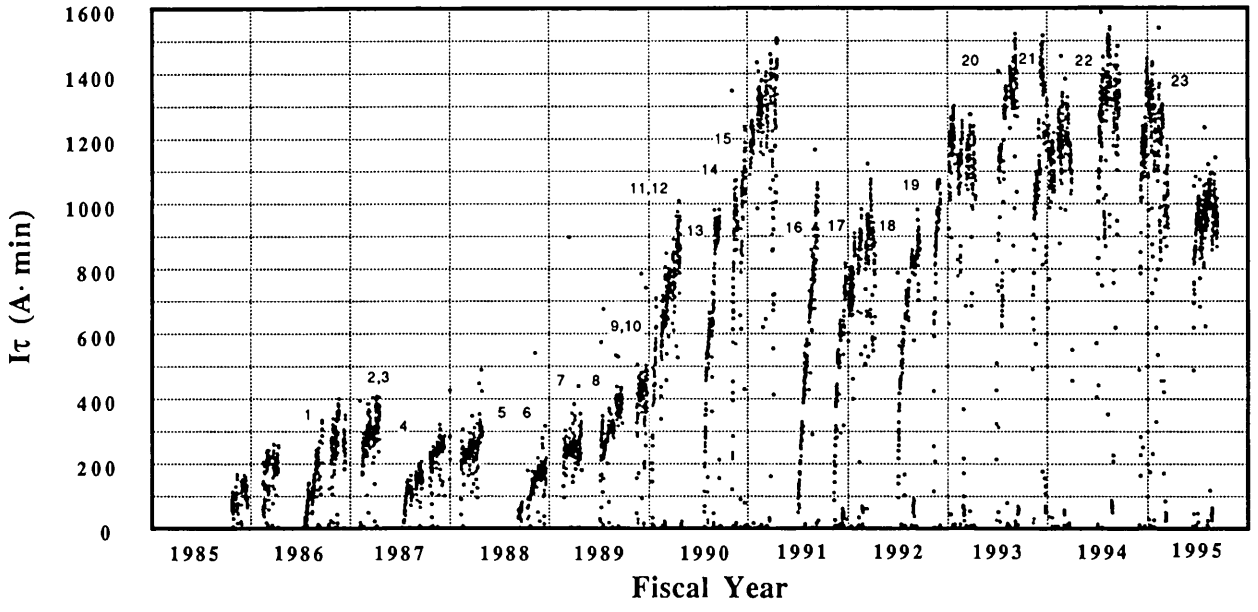

1: Vent for reducing beam emittance Rearrange magnet system

2: Operation with reduced emittance

3: MPW16

4: Vent for positron injection Renovation of the rf-cavity for reducing beam instabilities

5: Vent for insertron devices MPW13 and EMPW28 Positron operation

6: MPW13

7: EMPW28

8: New VW14

9: New U2

10: Thermal insulation

11: Lowβ operation

12: Single bunch run 3Gev test run

13: Vent for Isolation valves, RFQ

14: New tunes

15: VW14 chamber

16: B01 chamber, Isolation valves with rf-shield

17: Water leak(absorber for VWradiation)

18: Optical klystron, Feedback system

19: B04-05 feedback cavity

20: B21 Mirror, B04-05 scraper

21: B01 crotch absorber

22: B10,11,12 crotch absorber BL6,11 renewal

23: Electron operation

Fig. 4 Plot of $I \cdot \tau$.

Table 1 Statistics of the storage-ring operation during fiscal year 1995 (from Apr. 1995 to Mar. 1996)*.

	Multi-bunch	Single-bunch	Total
Ring Operation Time (hours)	—	—	4275.0
Scheduled user time (hours)	3387.0	144.0	3531.0
Net user time T (hours)	3310.6	142.4	3452.4
Time used for injection (hours)	66.5	6.8	73.3
Integrated current in T (A·hours)	1064.1	6.1	1070.2
Average current in T (mA)	321.4	43.0	—
Number of injections	162	14	176
Interval between injections (hours)	20.4	10.2	—

* Note that a part of this duration, from Oct. 1995 to Mar. 1996, is primarily beyond the scope of this report.

2. HIGH-BRILLIANCE PROJECT

2.1 Overview

The high-brilliance project[1-4] of the PF ring is in progress. By doubling the number of quadrupole and sextupole magnets in the FODO cells (normal-cell sections), the beam emittance, which is now 130 nm·rad, will be reduced to 27 nm·rad. This will result in a higher brilliance of the synchrotron radiation, typically by a factor of ten at the beamlines for the insertion devices. To this aim, about one third of the ring will be reconstructed. Along with this, many accelerator components, which are now 15 years old, will be upgraded. These improvements will make the PF storage ring to be competitive with the third-generation synchrotron light sources.

Reconstruction of the ring will start in January, 1997, and the upgraded PF storage ring will be recommissioned in October, 1997. In order to minimize the reduction of the user-time during these fiscal years (1996 and 1997), all of the accelerator components are to be fabricated prior to the long shutdown. To restart the user-runs quickly after the reconstruction, the new lattice was designed to allow almost the same optics as the present one, if necessary.

Much preparation work for the reconstruction is under way. New quadrupole and sextupole magnets, as well as their power supplies, were manufactured during 1994 and 1995. Magnetic field measurements will be completed at the end of fiscal year 1995. New beam-ducts for the normal-cell sections will be manufactured in fiscal year 1995 and 1996. The present beam-position-monitors (BPMs) are to be replaced with new ones to match the new vacuum ducts. The signal-processing system is being replaced so as to achieve very fast COD measurements, which will allow us a fast stabilization of the beam orbit by using a global feedback system. A single-pass BPM system, used during the recommissioning phase, is under development. A new beam-loss monitor system was installed in 1995. A transverse feedback system, which can cure beam instabilities, is under development.

The beamline frond-ends are being reconstructed so as to be compatible with the new lattice configuration, as well as to withstand higher heat loads. The reconstruction has already started, and will be finished prior to the reconstruction of the ring. New traveling-wave kicker magnets for beam injection are under development. They are to be compatible with the new optics, together with having a fast response. A new rf-acceleration cavity has also been developed. This cavity is a HOM-damped type, which was designed to reduce the impedances due to higher-order-mode (HOM) resonances. The present four cavities will be replaced by the HOM-damped ones. The control system of the storage ring will also be upgraded so as to match modern computer technologies.

In the following subsections, the design and development of each accelerator components are described.

References

1) M. Katoh and Y. Hori. (ed.), KEK Report 92-20 (in Japanese).
2) M. Katoh et al., Proc. of the 4th European Particle Accelerator Conference (EPAC94), London, 1994, p.636.
3) Photon Factory Activity Report #12, 1994, p.A-4.
4) M. Katoh and Y. Hori, to be presented in the 5th European Particle Accelerator Conference (EPAC96), Barcelona, 1996.

2.2 Lattice and Magnets

The basic lattice structure of the PF ring is FODO[1]. The normal FODO cells occupy about one-third of the ring, and it determine the beam emittance. We designed a new low-emittance configuration[2,3], in which the quadrupoles and sextupoles in the normal cells are doubled in number and are reinforced. No change is required for the bending magnets, which minimizes the influence on the existing SR beamlines. Figures 5(a) and 5(b) show the optical functions in the new and present normal-cells, respectively. The optics of the whole ring was designed for three cases of phase advance: 90, 105, 135 degrees. In the case of 135 degrees, we will obtain the lowest emittance of 27 nm·rad. The principal parameters of the new optics are given in Table 2. The new and present configurations of the normal cell are shown in Figs. 6(a) and 6(b), respectively.

Even in the new lattice configuration, we can reproduce almost the same optics as the present one by turning off and changing the polarities of some of the magnets. This will allow us to quickly restart operation using our familiar optics.

All of the quadrupoles and the sextupoles in the normal-cells are to be replaced with newly fabricated ones[4], which have shorter lengths, smaller bores and higher field gradients in order to save space for other accelerator components. Each core of these magnets has a gap at the outside (so-called Collins-type core) in

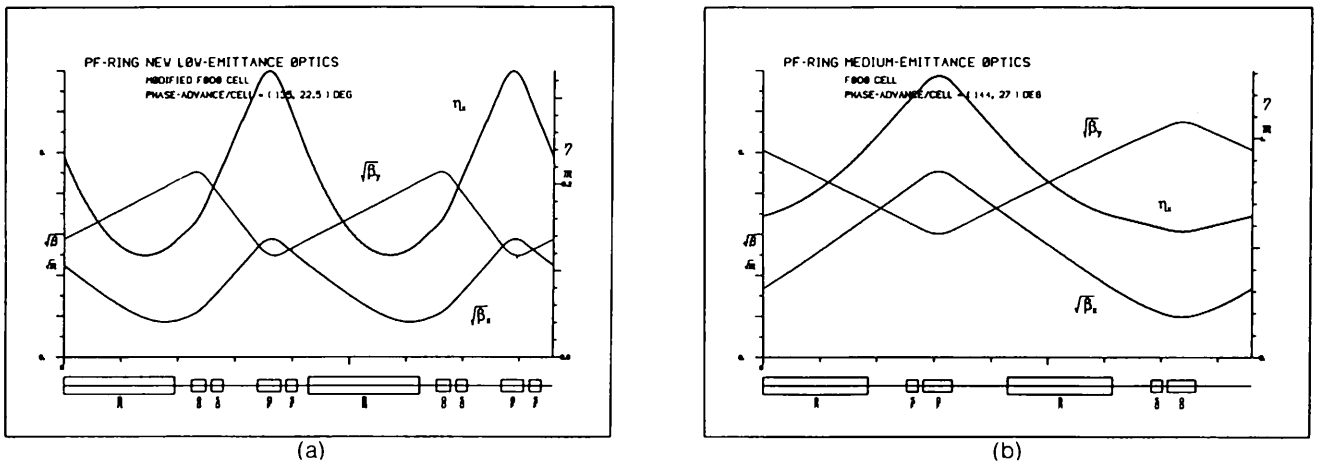

(a) (b)

Fig. 5 Optical functions in the normal cell. (a) For the new low-emittance configuration. Two FODO cells are shown. Phase advances are 135 and 22.5 degrees for the horizontal and vertical directions, respectively. (b) For the present configuration. One FODO cell is shown.

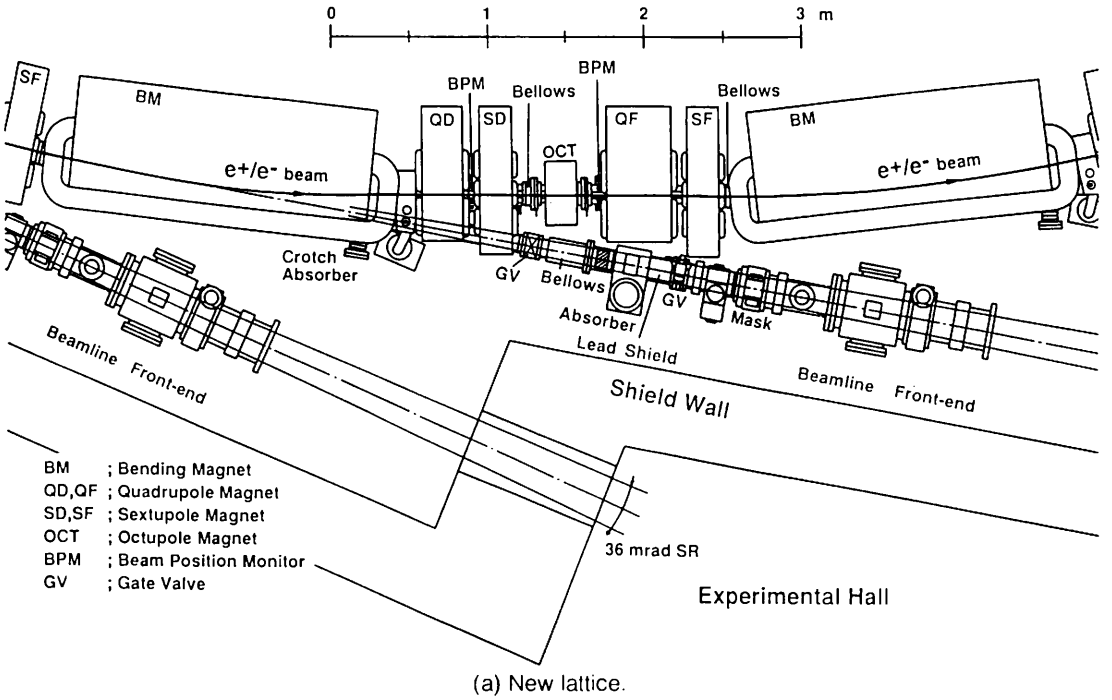

(a) New lattice.

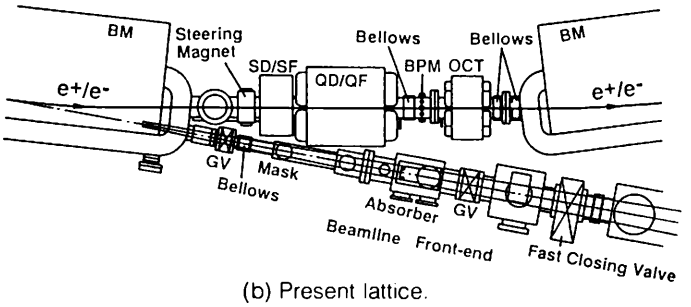

(b) Present lattice.

Fig. 6 Configuration of the normal cell.

order not to disturb the synchrotron-radiation extraction to the existing beam lines. Each sextupole has auxiliary windings used for vertical steering and for correcting the field asymmetry. The maximum field strengths of the magnets are strong enough to allow 3-GeV operation under the new optics. The parameters of the new magnets are summarized in Table 3.

Mass production of all the magnets has been completed. End-shim corrections, applied to obtain a wide good-field region, were determined by a measurement using the prototype magnets. Field measurements of the new magnets are under way. Some preliminary results have indicated that the individual deviation in the field gradient would be less than 1×10^{-3} in r.m.s. The new magnets will be aligned on a common girder with a precision of 100 microns, prior to installation to the ring. New power supplies, eight for the quadrupoles and three for the sextupoles, have been fabricated.

References

1) PHOTON FACTORY ACTIVITY REPORT 1982/83, p.IV-5.
2) M. Katoh et al., Proc. of the EPAC94, London, 1994, p.636.
3) M. Katoh and Y. Hori, to be presented in the EPAC96.
4) Y. Kobayashi et al., Proc. of the 10th Symposium on Accelerator Science and Technology, Hitachinaka, Japan, 1995, p.121.

2.3 Vacuum System

In the PF ring, the beam lifetime is mainly determined by the vacuum pressure in the beam duct, which, in turn, is governed by the photo-desorption of molecules from the duct walls. Since the photo-desorption yield decreases as the integrating irradiated photons on the duct, long and stable operation of the storage ring results in a good vacuum, and, thus, in a long lifetime.

The present vacuum system was originally designed in 1979, and was largely modified in 1985 so as to be able to accumulate higher beam currents[1]. It was designed to allow in situ baking (that is, baking after installed in the ring) in order to obtain a low base pressure, as well as to reduce the initial photo-desorption yield. To avoid mechanical stress on the duct during baking, we have arranged a bellows to the neighbor of each beam-position-monitor (BPM).

In the normal-cell sections of the new lattice, each

Table 2 Principal parameters of the new and present optics.

	New low-ε optics*	Present optics
Natural beam emittance (nm·rad)	27	130
Betatron tune (horizontal)	10.85	8.44
(vertical)	4.20	3.30
Natural chromaticity (horizontal)	-16.1	-13.5
(vertical)	-13.3	-9.0
Natural energy spread	7.3×10^{-4}	7.3×10^{-4}
Momentum compaction factor	0.0043	0.016
RF voltage (MV)	1.5	1.7
Synchrotron tune	0.011	0.023
Bunch length in r.m.s. (cm)	0.84	1.52

* Phase advance per cell, 135 degrees.

Table 3 Parameters of the new magnets.

	QF*	QD**	SX***
Core length (m)	0.4	0.25	0.20
Bore radius (mm)	40	40	45
Maximum field strength	24 T/m	24 T/m	600 T/m^2
Maximum excitation current (A)	900	900	450
Number of turns per pole	19	19	17
Power dissipation (kW)	17	13	6

* Focusing quadrupole. ** Defocusing quadrupole. *** Sextupole.

space between the bending magnets is occupied by two quadrupole and two sextupole magnets. The remaining open space for the BPMs, bellows and flanges, is very small. Because there is no space for the bellows, it is very difficult to adopt the same design principle as the present one. For the new system, we have basically given up in situ baking of the vacuum ducts, except for the pumps, vacuum gauges and valves, which are not irradiated by photons. Alternatively, the ducts are pre-baked, and are filled with pure nitrogen-gas until they are installed. A sufficiently-low pressure will be established after they are exposed to enough synchrotron photons. We expect that this beam cleaning will take place within a reasonable conditioning time.

In this design principle, it is very important to evaluate the required conditioning period. To this aim, we are investigating the beam cleaning effect[2] for several test ducts, which are to be treated in different ways, using beamline BL-21. The resulting data will be useful for predicting whether we will need in situ baking or not. If the beam cleaning is much slower than expected, we will have to bake the vacuum ducts in situ. In such a case, we will loose the BPMs during the baking.

A new beam duct (called a Q-duct) for the normal-cell section has been designed. It fits in the reduced bore diameter of the new quadrupole and sextupole magnets. The Q-duct is extruded from aluminum alloy, after which BPM assemblies are directly attached by electron-beam welding. A cross section of the new Q-duct is shown in Fig. 7. The present ducts in the bending magnets (called B-ducts) are re-used with a small modification. In order to check the overall combination, we assembled a prototype normal-cell lattice comprising the magnets and the ducts. Figure 8 shows a test duct mounted in the prototype lattice. Some conflicts were found, which will be removed in the design for mass production. The fabrication of the Q-ducts will be completed during fiscal year 1995, and other ducts will be produced in fiscal year 1996.

Under the new optics, the bunch length becomes about half the present one, which would result in some enhancement of the wake-field effects, such as a parasitic mode loss. In order to reduce such effects, the inner walls of the beam ducts are to be made as smooth as possible, especially for the newly installed and modified ones. For this purpose, we have designed an RF-shielded bellows and an RF contact for flange gaps. Ceramic ducts for kicker magnets are also replaced with new ones, which will have almost the same cross section as the Q-duct.

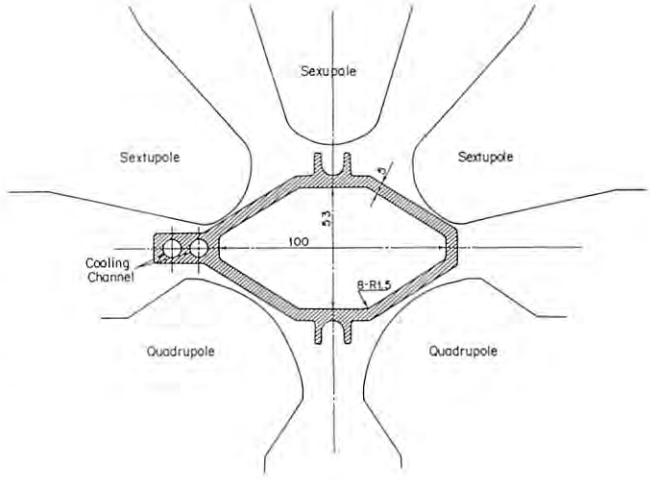

Fig. 7 Cross-sectional view of the new Q-duct.

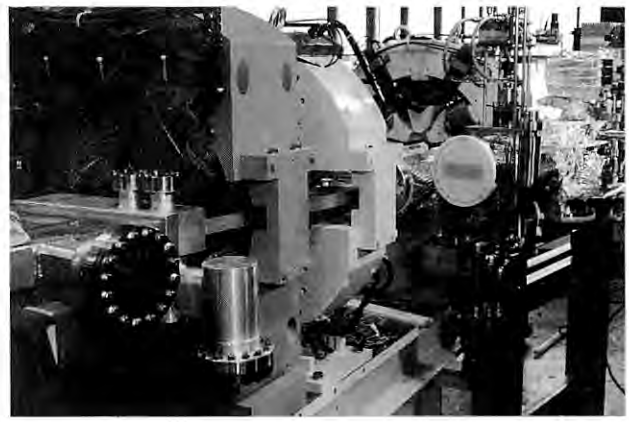

Fig. 8 Prototype beam duct mounted on a test bench.

References

1) Photon Factory Activity Report 1984/85 #3, p.IV-10.
2) Y. Hori and M. Kobayashi, VACUUM **47**, p.621 (1996).

2.4 Beam Monitor System

A. BPM System

Accompaning the high-brilliance project, the beam-position-monitor (BPM) system will be renewed. The purpose of the BPM system is to accurately measure the beam position in order to correct for any closed-orbit distortion (COD), to stabilize the beam position using feedback, and to correct such optical functions as the dispersion function. The new system was designed to enable precise and fast measurements to correct the

COD, as well as to feed back the orbit position during user-runs. It comprises electrostatic pickup units and a signal-processing system.

The pickup units for the normal-cell sections are to be doubled in number. There will be 42 BPMs newly installed, making a total of 65 BPMs. A cross-sectional view of the new BPM unit is shown in Fig. 9. It was designed to fit in the narrow space between the magnets. A commercial product (from KYOCERA corp.) was adopted for the electrode assembly, which consists of a button electrode (10.3 mm in diameter), a feedthrough and an SMA-type connector. The button is set at the center of the assembly within ± 50 μm. Each BPM unit is fixed to an end of the quadrupole magnet. All of the BPMs will be tested at a calibration bench where the electric center of each BPM will be identified with an overall accuracy of about 100 μm using a coaxially strung metallic wire.

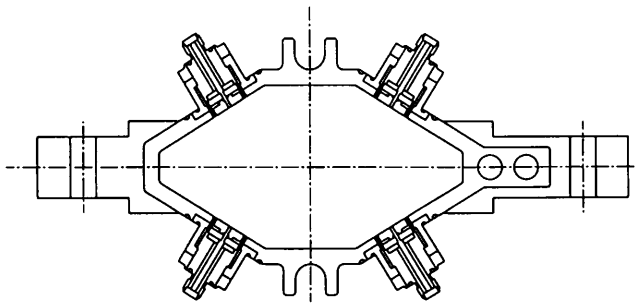

Fig. 9 Pickup unit of the newly installed BPMs.

A schematic of the layout of the signal-processing system is shown in Fig. 10. These circuit units are to be distributed in 12 local control racks around the ring. The beam signals from the pickup electrodes are to be transmitted to the processing system, and at the front end of the system, one of the signals will be selected by RF switches. To improve the reliability, the currently-used mechanical coaxial switches will be abandoned, and PIN-diode switches are to be adopted. The fluctuation of the insertion loss over many switchings is less than ± 0.01 dB, which corresponds to a position error of ~ 3 μm. The signal detection circuit consists of a super-heterodyne circuit with synchronous detection. The bandwidth of the signal detection is determined by the response time (~ 3 msec by 10 to 90% rise time) of a low-pass filter in the final detection stage. In the fastest mode, this system is capable of measuring the COD within about 2 msec, which is determined by the sum of the switching time, the response time of the detection circuit and the conversion time of an analog-to-digital (A/D) converter. This very fast acquisition will allow us fast suppression of the beam movement for frequencies

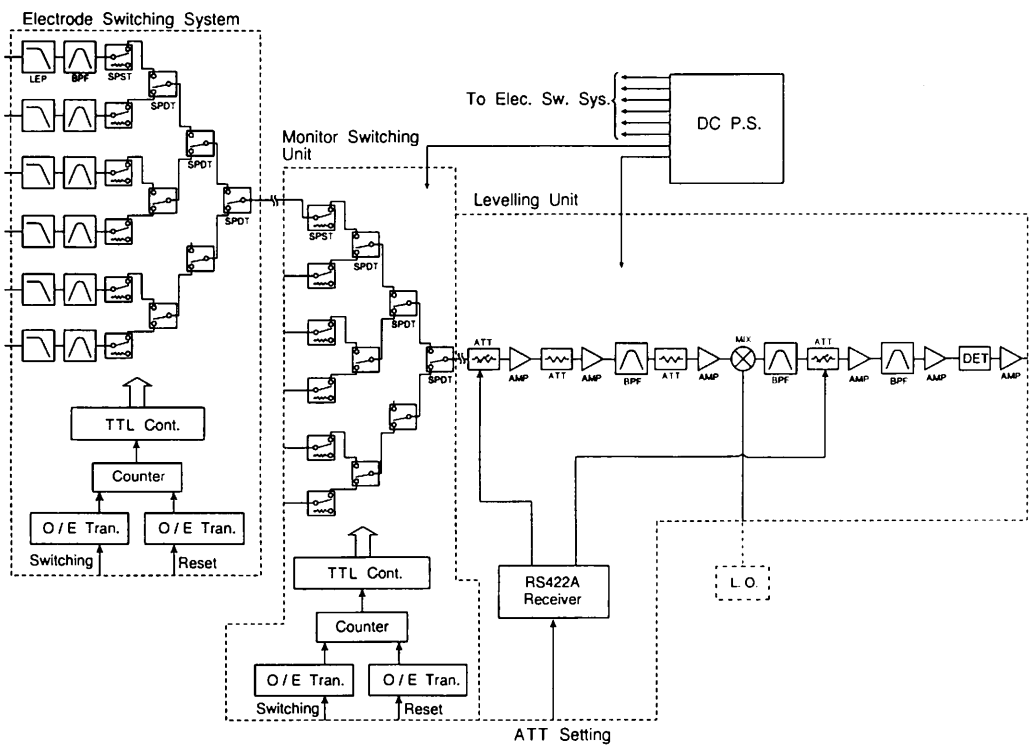

Fig. 10 Schematic diagram of the signal-processing system.

of up to 100 Hz using a global feedback system[1].

B. Single-pass BPM System for the Injected Beams

During the recommissioning phase, precise steering of the beam orbit will be needed in advance of beam storage, since the dynamic aperture is small. A single-pass beam-position-monitor system, for this use, is under development[2,3]. This system will allow us to measure the beam positions of an injected beam at every turn during a few revolution periods without accumulating the beam.

When this system is used, the signals from the button-type electrodes (that are common to the BPM system) are connected to this system. The signal-processing scheme is shown in Fig. 11. Signals from eight BPM units, each of which has four button electrodes, are combined into four channels, which correspond to the four buttons. The signals are then detected using a real-time digitizing oscilloscope (Tektronix TDS684A) which has four-channel A / D converters. We have chosen to use a commercial oscilloscope (or digitizer) as a fast, reliable and cost-effective solution for signal detection. The bipolar waveshape of the bunch signals can be well resolved at a sampling rate of 5×10^9/s. The beam positions are deduced from the ratio of the peak-to-peak height of the four signals. The beam positions at 8 locations can be measured during 4 or 5 turns. The relative resolution of the detective position was estimated to be a few hundred microns.

The result of a test measurement using this system is shown in Fig. 12. In this figure, the filled circles are the measured beam positions of the injected beam in the first turn, and the solid line in Fig. 12(a) is the design orbit for the injected beam. The measured beam positions agreed well with the calculated orbit. In the vertical direction, shown in Fig. 12(b), only a small orbit distortion was measured, as expected.

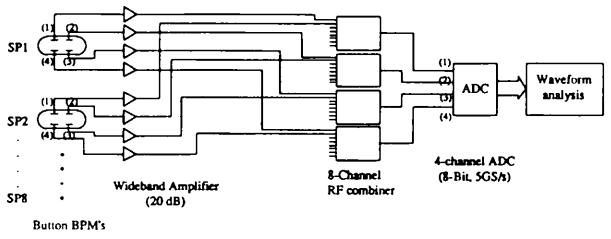

Fig. 11 Signal-processing scheme of the single-pass BPM system.

C. Beam Loss Monitor

Twenty beam-loss monitors (BLMs) made by BERGOZ were installed near to the beam duct. This monitor is useful for studying the trapping phenomenon of micro-particles or ions, as well as to help in recommissioning the ring. The BLMs on the outer side of the duct detect the bremsstrahlung due to residual-gas molecules, ions or small particles in the duct, and those on the inner side detect showers due collisions of lost electrons with the duct wall. The BLMs do not detect the X-ray component in the SR. A block diagram of the BLM system is shown in Fig. 13. Events detected by a BLM are counted with a VME scaler, and the data are processed using a workstation. An example of the beam-loss rates is shown in Fig. 14.

References

1) Photon Factory Activity Report #12, 1994, p.A-6.
2) T. Honda, KEK Preprint 95-128, 1995.
3) T. Honda and M. Katoh, to be presented in the EPAC96.

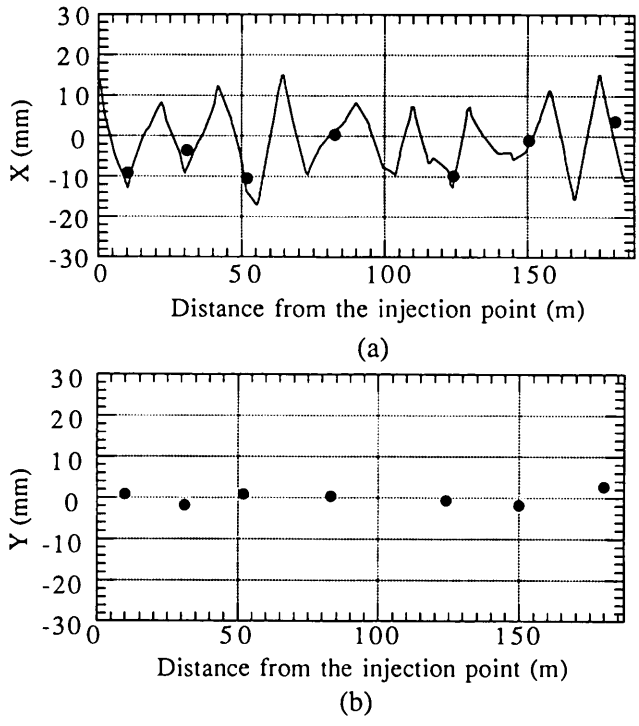

Fig. 12 Measured orbit of the injected electron beam in the first turn. The horizontal axis indicates the location along the ring measured from the injection point. (a) Horizontal beam positions. The solid line is the calculated injection orbit. (b) Vertical beam positions.

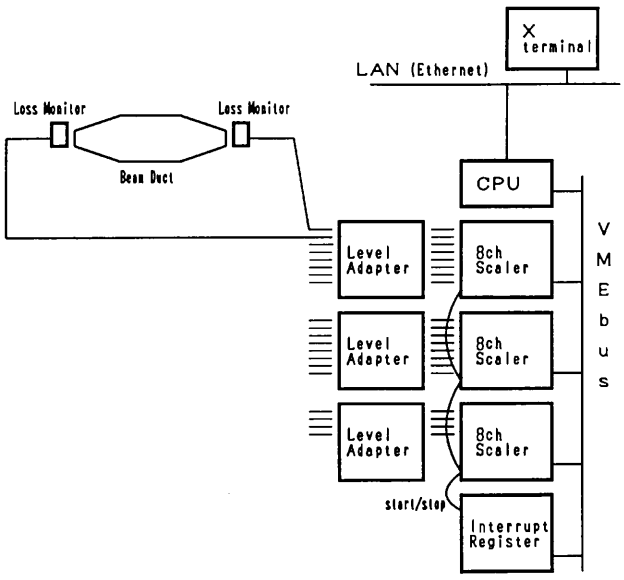

Fig. 13 Block diagram of the BLM system.

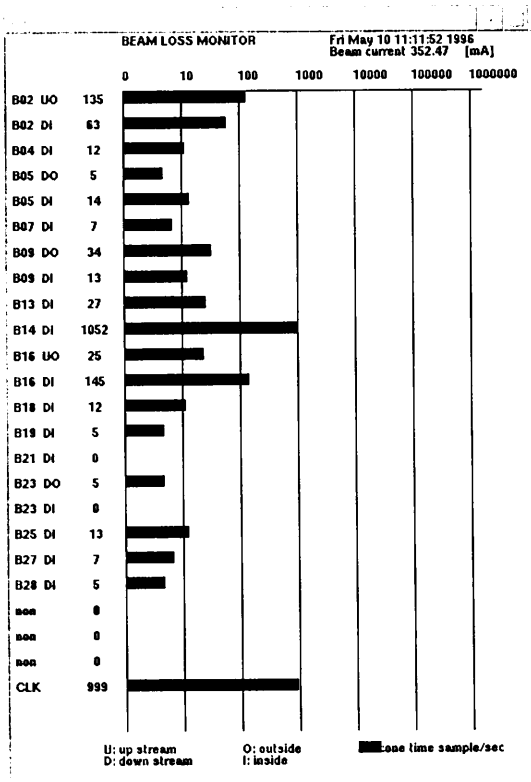

Fig. 14 Typical observation of the beam-loss rate during beam storage (beam current, 352 mA). The ordinate shows the location of the monitor, and the abscissa shows the count rate.

2.5 Beamline Front Ends

In the new lattice configuration, reinforced quadrupole and sextupole magnets in the normal-cell sections interfere with present beamline front-ends. About half of the beamlines (BL-6, 7, 8, 9, 10, 11, 12, 19, 20 and 21) should be modified. In addition, constant improvements of the PF ring have brought about a potential possibility of user operations with higher beam currents (>500 mA) or with higher energies (at 3 GeV with >200 mA). This has prompted the renewal of the front-end components so as to be capable of handling higher heat loads. Based on these needs, we have decided to thoroughly upgrade the front ends of the above-mentioned beamlines. This renewal has been carried out step by step, as summarized in Table 4. Six beamlines have been completed and the other three will be finished before installation of the new magnets planned in 1997.

In the beamlines, the beam stopper / absorbers located at the uppermost stream should withstand the most severe heat loads. For radiation from the bending magnets, the incoming power per unit area on the beam axis is given by

$$P_d = \frac{7e_0}{64\pi\varepsilon_0}\frac{I\gamma^5}{\rho L^2}, \qquad (1)$$

where the power distribution is approximated by a belt-like distribution, I is the beam current, γ the Lorentz factor, ρ the bending radius, L the distance from the source point, e_0 the electron charge and ε_0 the permittivity of vacuum. For multipole wiggler radiation, the surface heat load is given by

$$P_d = \frac{7e_0}{16\varepsilon_0}\frac{NKI\gamma^4}{\lambda_0 L^2}, \qquad (2)$$

where the power distribution is approximated by a rectangular distribution, λ_0 is the period of undulation, N the number of periods and K the deflection parameter. Table 5 summarizes the values of $P_d L^2$ for all radiation sources under the most severe condition of 500 mA at 3 GeV.

The beam stoppers / absorbers were re-designed based on a safety-sided estimation with bold modeling. For an inclined copper plate of the stopper, the temperature difference between the heat-loaded front surface and the water-cooled rear surface is roughly given by

$$\Delta T = \frac{P_d D\cos\theta}{\chi}, \qquad (3)$$

where D is the thickness of the plate, θ the angle between the beam axis and the surface normal, and χ the

thermal conductivity of copper ($\approx$ 400 W / m·K). Based on our design criterion of $\Delta T_{max} < 150$ K, we have chosen D = 5 mm and $\theta = 70^\circ$ for the bending-magnet source, and D = 7 mm and $\theta = 86^\circ$ for the multipole wiggler / undulator sources.

The newly designed beam stopper / absorber for the bending-magnet source is shown in Fig. 15(a), and that for the insertion-device sources in Fig. 15(b). Figure 16(a) shows the new front end for the bending-magnet source (BL-7), and Fig. 16(b) shows that for the insertion-device source (BL-19). Figure 16(a) also shows the boundary conditions given by the high-brilliance magnet configuration.

Table 4 Renewed beamline front ends.

	Fiscal	Installation*	Remarks
BL-6	1993	Summer 1994	Bending-X
BL-7	1995	Winter 1996	Bending-VSX, X
BL-8†	1995	Winter 1996	Bending-VSX, X
BL-9††	1994	Summer 1995	Bending-VSX, X
BL-10	1994	Summer 1995	Bending-X
BL-11	1993	Summer 1994	Bending-VSX
BL-12	1994	Summer 1995	Bending-VSX, X
BL-19	1995	Summer 1996	Undulator-VSX
BL-20	1994	Winter 1995	Bending-V, X

* Summer: Jul. - Sep., Winter: Jan. - Mar.
† Hitachi.
†† NEC.

Table 5 Values of $P_d L^2$ for $I_{max} = 0.5$ A and $E = 3.0$ GeV.

Source		λ_0 (m)	N	K_{max}	$P_d L^2$ (W)
Undulator-2		0.06	60	2.25	1.06×10^{10}
MPW-13		0.18	13	25.0	8.48×10^{9}
MPW-16		0.12	26	16.8	1.71×10^{10}
MPW-19	A	0.05	46	1.3	5.62×10^{9}
	B	0.072	32	2.7	5.64×10^{9}
	C	0.1	23	5.0	5.40×10^{9}
	D	0.164	14	9.5	3.81×10^{9}
MPW-28		0.16	11	14.9	4.81×10^{9}
VW-14	3-p*	0.4	1	187	2.20×10^{9}
	5-p**	0.4	2	187	4.39×10^{9}
Bending		8.66***			2.53×10^{8}

* 3 pole mode ** 5 pole mode *** bending radius of curvature

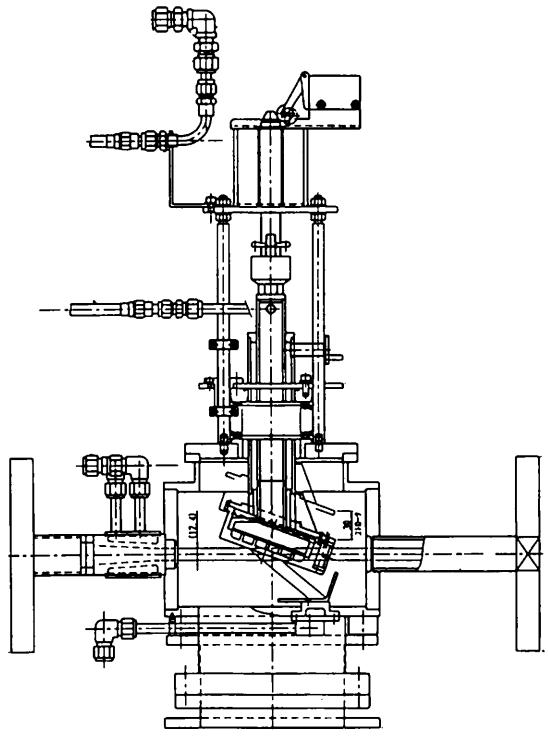

(a)

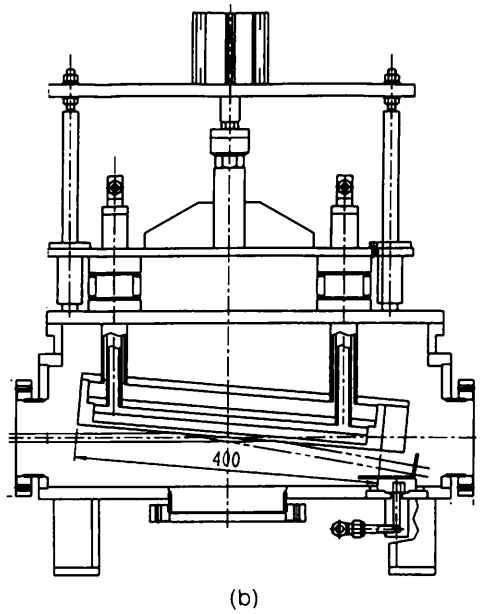

(b)

Fig. 15 (a) The beam stopper / absorber with 70° -inclination-angle for the normal-cell bending-magnet sources. (b) The beam stopper / absorber with 86° -inclination-angle for the insertion-device sources.

(a)

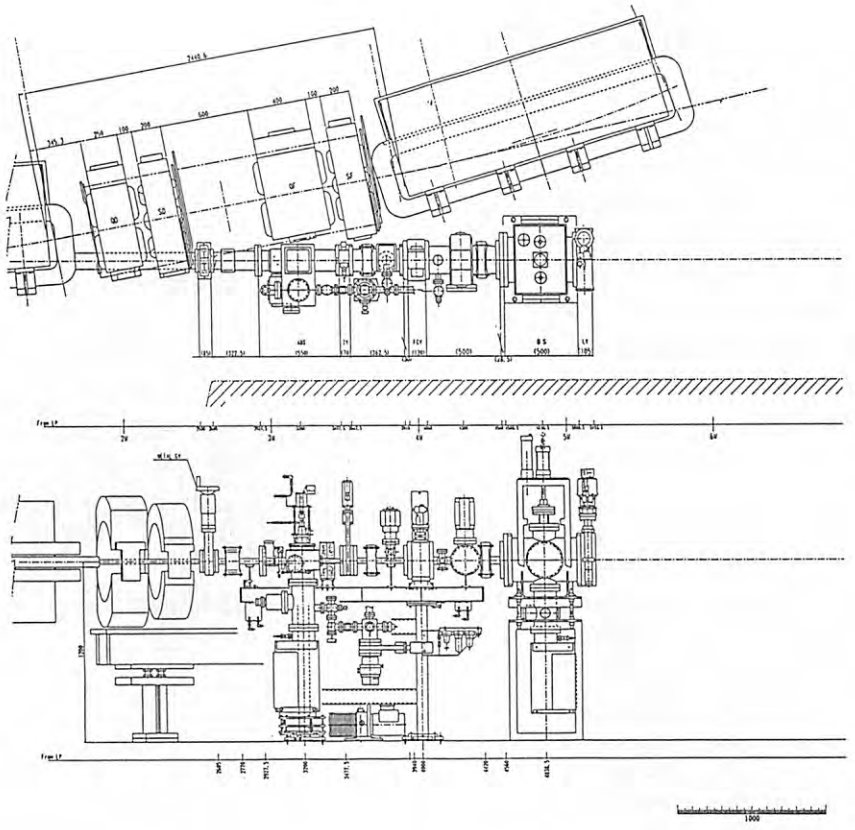

(b)

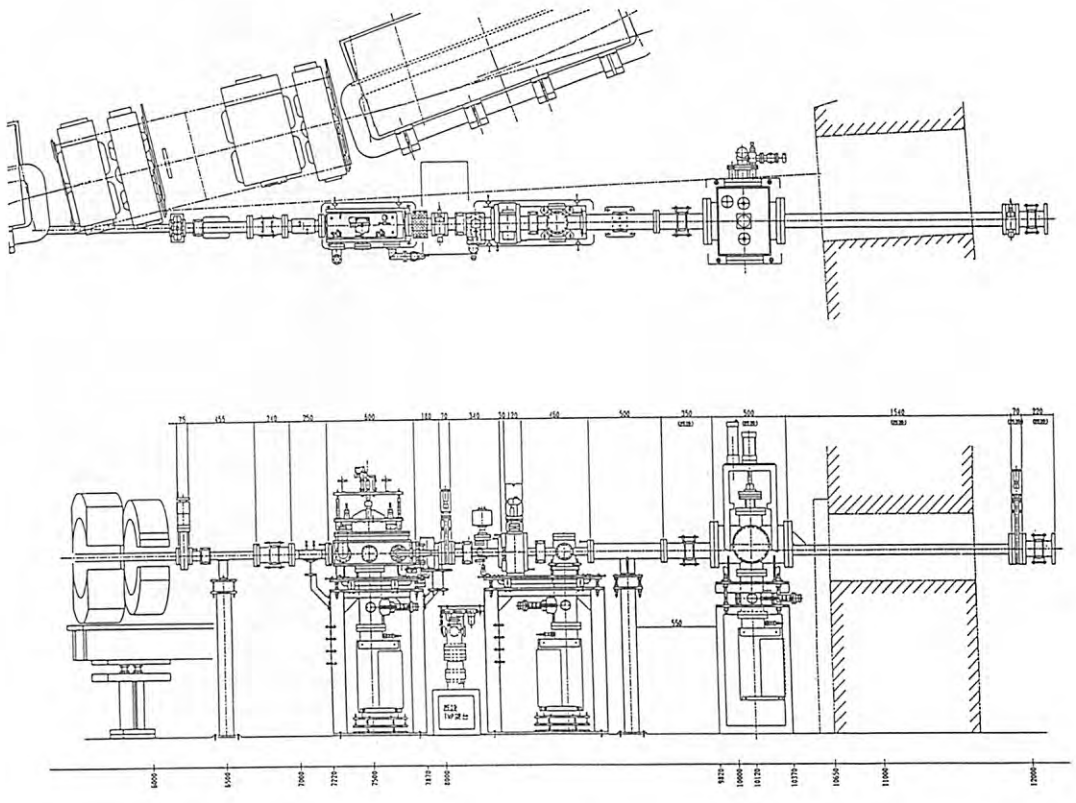

Fig. 16 (a) Plan view of the front end for the normal-cell bending-magnet sources. The example is that for BL-7. (b) Plan view of the front end BL-19.

2.6 Injection System

A new injection system was designed for the high-brilliance project. It comprises four kicker magnets, used to produce a pulsed bump orbit, and two septum magnets, used to deflect the injected beams. We designed the excitation of the kicker magnets to complete within one revolution period. This produces a sufficiently wide aperture for the injected beams during the first few turns. For this purpose, we have designed a traveling-wave kicker magnet which has a characteristic impedance of 6.25 Ω. A drawing of the traveling-wave kicker magnet is shown in Fig. 17. The present septum magnets are used as they are. Table 6 summarizes the requirements for the injection magnets for three cases of the phase advance of the new optics.

In order to test the design of the traveling-wave kicker magnet, we constructed a cold model. For the model magnet, poli-viniliden-fluorite (PVDF) was used as the capacitor dielectric to obtain a large dielectric constant. The parameters of the model magnet are listed in Table 7. A general view of the magnet is shown in Fig. 18. The total capacitance and inductance of the 29-cell magnet were measured using an HP4284A precision LCR meter. The results of the measurement are shown in Figs. 19 and 20, respectively. In the frequency range from 1 kHz to 100 kHz, the measured capacitance and inductance were about 37.5 nF and 1.6

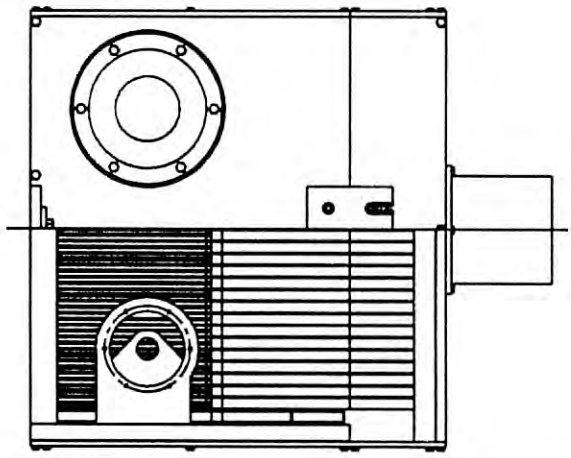

Fig. 17 Design of the 6.25-Ω traveling-wave kicker magnet.

Table 6 Deflection angles required for the injection magnets under low-emittance optics. Those for three phase advances per cell are shown.

	90° optics	105° optics	135° optics
K1	3.20 mrad	3.30 mrad	3.50 mrad
K2	-2.24 mrad	-2.30 mrad	-2.71 mrad
K3	3.14 mrad	3.40 mrad	3.91 mrad
K4	1.79 mrad	1.78 mrad	1.71 mrad
S1	87 mrad		
S2	122 mrad		

K1-K4: kicker magnets, S1,S2: septum magnets.

Fig. 18 General view of the model magnet.

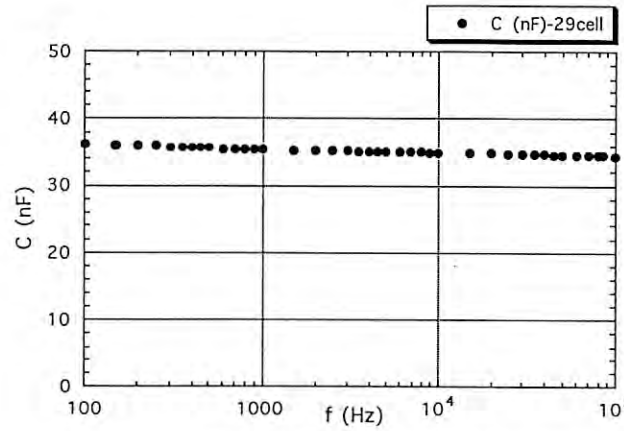

Fig. 19 Measured capacitance of the model magnet.

Table 7 Design parameters of the model kicker magnet.

Magnetic length	324 mm
Gap height	60 mm
Gap width	170 mm
Characteristic impedance	6.25 Ω
Field propagation time	181 nsec
Number of cells	29 cell
Inductance per cell	38.9 nH
Capacitance per cell	996 pF

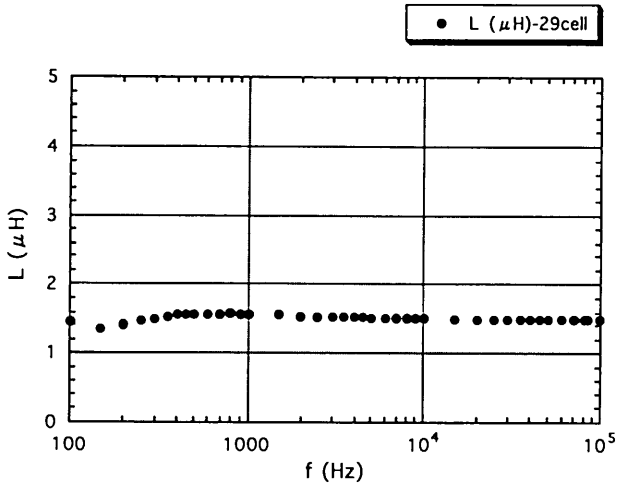

Fig. 20 Measured inductance of the model magnet.

μH, respectively. Using these values, the characteristic impedance of the magnet was concluded to be 6.5 Ω in the range of 10^2-10^5 Hz. The measured impedance was 4% larger than the designed value. This discrepancy is considered to be caused by some floating inductance near to the input and output terminals.

According to this design, the fabrication of the kicker magnets is under way. The power supplies for the 6.25-Ω kicker magnets were newly designed, and have already been completed.

References

1) T. Mitsuhashi et al., Proc. of 10th Symposium on Accelerator Science and Technology, Hitachinaka, 1995, p.94.

2.7 New RF Cavity

In the PF ring, the longitudinal and transverse coupled-bunch instabilities are one of the most serious problems that limit the beam current and beam quality at high currents[1]. This instability is mainly caused by the wakefield excited by the preceding bunches in the RF cavities or in other structures. An effective way to avoid this instability is to damp (to reduce the Q-values of) the higher-order-mode (HOM) resonances in the RF cavities. To this aim, a HOM-damped cavity has been developed[2-5] by a collaboration between the Photon Factory and the Institute for Solid State Physics (ISSP) of the University of Tokyo. Several cavities of this type are to be used for the high-brilliance project of the PF ring; they will also be used for the third-generation VUV and SX synchrotron radiation source project (VSX Light Source)[6], which is being proposed by the University of Tokyo.

The basic design is a 500-MHz, single-cell copper cavity which has relatively-large beam ports (140 mm in inner diameter), as shown in Fig. 21. Because of its simple structure together with an effective cooling design, this cavity has a possibility of operation at very high power with sufficient reliability. The HOM power, excited in the cavity, is guided out of the cavity through the beam ports, and then dissipated in microwave absorbers located beside the cavity (see Fig. 22). Each absorber is a cylinder of silicon-carbide (SiC), which is fit in the beam duct by a shrink-fit technique. We have determined the diameter of the beam port so as to obtain the highest cutoff-frequency possible while obtaining a reasonable shunt impedance. Although there remains several low-frequency HOMs, the coupled-bunch instability driven by them can be avoided by tuning their frequencies appropriately, which has been successfully applied in the PF ring. Low-power measurements on two cold-model cavities showed a satisfactory damping performance of the HOMs[4].

A prototype cavity was first manufactured and then tested under high power. The principal cavity parameters obtained are given in Table 8. Figure 23 shows the prototype cavity mounted on a test bench. After conditioning for 60 hours, an input power of 150 kW was successfully fed to the cavity without any serious

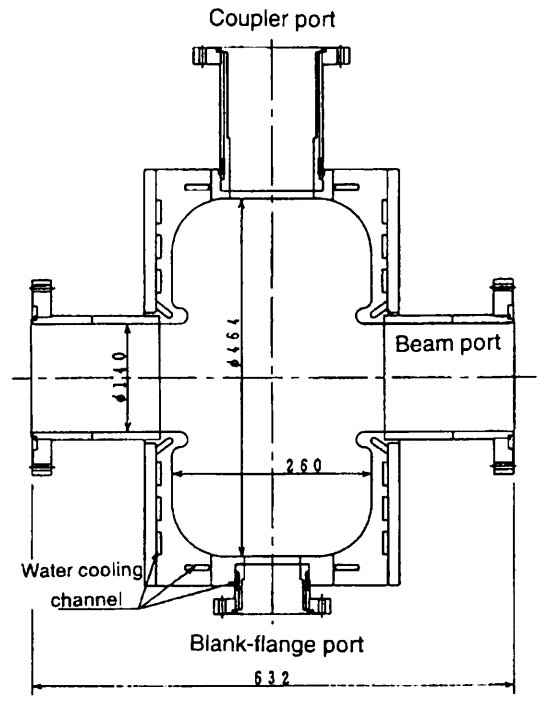

Fig. 21 Cross section of the HOM-damped cavity.

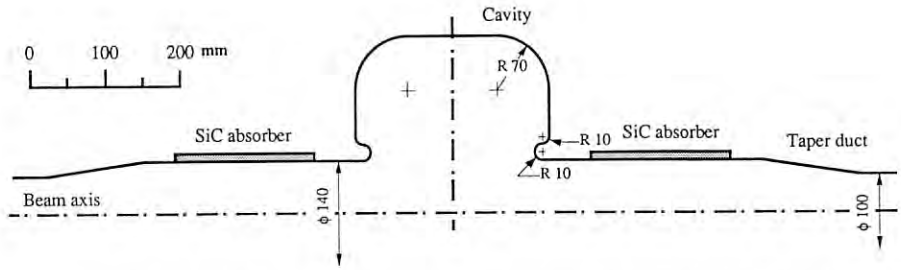

Fig. 22 Inner shape of one cavity unit, which includes the cavity, microwave absorbers and taper ducts.

Fig. 23 High-power test cavity mounted on a test bench.

Table 8 Obtained parameters of the damped cavity.

RF frequency	500.1 MHz
Shunt impedance	6.8 MΩ
Unloaded-Q	39,000
Coupling coefficient (β)	2.35
Maximum wall loss	140 kW

problems[5]. This demonstrated the capability of operation at very high power, at least up to about five-times the required dissipated power. A beam duct, equipped with an SiC absorber, has also been developed[7,8]. The present four cavities will be replaced by new ones of this type. This will result in a great improvement in the beam quality at high currents.

References

1) For example, Photon Factory Activity Report #7, 1989, p.R-7.
2) T. Koseki et al., Proc. of 4th EPAC, London, 1994, p.2152.
3) T. Koseki et al., Rev. Sci. Instrum., 66 (1995), 1926.
4) T. Koseki et al., Proc. of the 1995 Particle Accelerator Conference (PAC95), Dallas, 1995, p.1794.
5) T. Koseki et al., to be presented in the EPAC96.
6) Y. Kamiya et al., Proc. of the EPAC94, London, 1994, p.639.
7) M. Izawa et al., Rev. Sci. Instrum. 66, 1995, p.1910.
8) M. Izawa et al., to be presented in the EPAC96.

2.8 Control System

The present control system uses four 32-bit minicomputers (FACOM S-3000 series from Fujitsu Ltd.), which are linked to each other through a token ring-type network[1]. There is a need to update the system so as to match today's computer technologies. In addition, the upgrade of the PF ring requires a large modification of the software and interfaces in order to control the new devices. Taking this opportunity, there is a plan to renew the control system.

An overview of the new control system is as follows (see Fig. 24). VME systems are used to perform the real-time processing of various equipment of the storage ring (Equipment Control Layer). Unix workstations are used to process upper-level control programs (Application and Presentation Layer). A server computer is also incorporated for cpu-consuming calculations, like simulation or database processing etc. A large-capacity disk is connected to the server in order to save operation data.

An ATM has been adopted for the backbone of the network system. Twelve switching hubs, each of

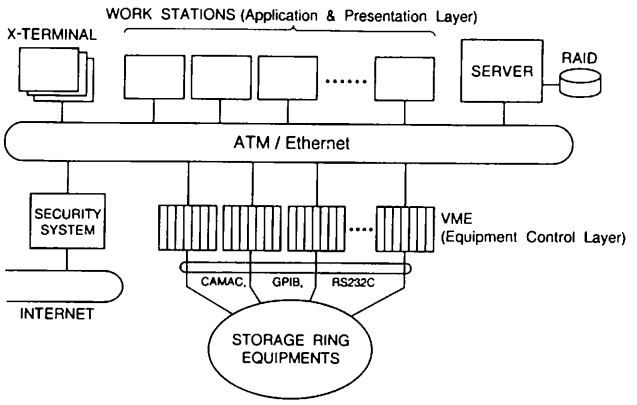

Fig. 24 Schematic view of the new control system.

which has twelve 10BASE-T ports, are connected to an ATM switch by optical fiber cables in 155Mbps. The VMEs and workstations are connected to the 10BASE-T port as an ordinary Ethernet node. The ATM has advantages for multimedia, such as visual and audio information.

The operator console of the new system will have window-based graphical user interfaces. Advanced GUI (Graphical User Interface) tools are useful to construct such control screens. We have adopted VAPS (from Virtual Prototypes corp.) as such a tool. The VAPS provides software tools for editing graphical objects to make interface screens and for linking them to control processes distributed over the network.

The interfaces to various equipment remain the same as they are (CAMAC, GPIB and RS-232C). These are accessed via the VMEs in the new system. The software drivers of these interfaces are located in the VMEs. The service routines used in the control programs on the workstations are made almost the same as those on the present minicomputers. The software differences between the old and new system are absorbed in the VME system. This makes the conversion of upper-level programs easier.

References

1) C. O. Pak, Nucl. Instr. Meth. A277 (1989), 501.

3. MACHINE STUDIES

3.1 Study on the Vertical Instability in a Positron Multibunch Beam

A. Experimental Study

Under positron multibunch operations of the PF ring, we have suffered from a vertical instability[1-3] which arises only with positron beams, and not with electron beams. This instability is very hard to suppress; even with a cure by strong octupole fields, it enlarges the vertical beam size under routine operations. The principal features of this instability are: 1) coupled-bunch oscillation, 2) a low threshold current of 15-20 mA, 3) broad distribution of the betatron sidebands, and 4) that it is not suppressed by filling positrons partially in RF buckets. Figure 25 shows the typical beam spectrum during positron multibunch operation, which was observed with a button-type BPM electrode.

The vertical instability has been extensively studied by Izawa et al.[4]. The following remarkable features were found: 1) The distributions of the betatron sidebands in the positron and electron beams were quite different. 2) It was very difficult to find any cavity higher-order-modes (HOMs) or resonances of the other components which would have a very large transverse-coupling impedance together with a low-Q value. 3) When an electrostatic potential was applied to 88 BPM electrodes in the ring, the vertical beam size was reduced by a factor of about 15%, although the instability was not completely suppressed. From these facts, it was strongly suggested that the vertical instability is not caused by the well-known transverse wakefield induced by the electromagnetic beam-wall interaction. As an alternative possibility, they proposed that this instability would be caused by electrons in the vacuum chamber. They explained the distribution of the betatron sideband spectrum which is characteristic of this instability by using the conventional coupled-bunch theory[5]. Although their analysis was phenomenologically, they showed that the range of the interaction was relatively short, typically eight-times the bunch spacing.

B. Theory and Simulations

The mechanism of the interaction between bunches, which induces the instability in positron beams, was clearly explained by Ohmi[6]. In positron storage rings with high current and multi-bunches, a considerable number of photoelectrons are produced at the beam chamber. The beam chamber will be filled with photoelectrons by successively passing bunches. The photoelectrons will not be trapped by a bunched positron beam due to their light mass. However, a sufficiently dense distribution of the photoelectrons will produce coupling between the bunches, which will lead to the instability. Here, we will outline the instability mechanism, the details of which are given in reference 6).

The number of synchrotron photons emitted by a

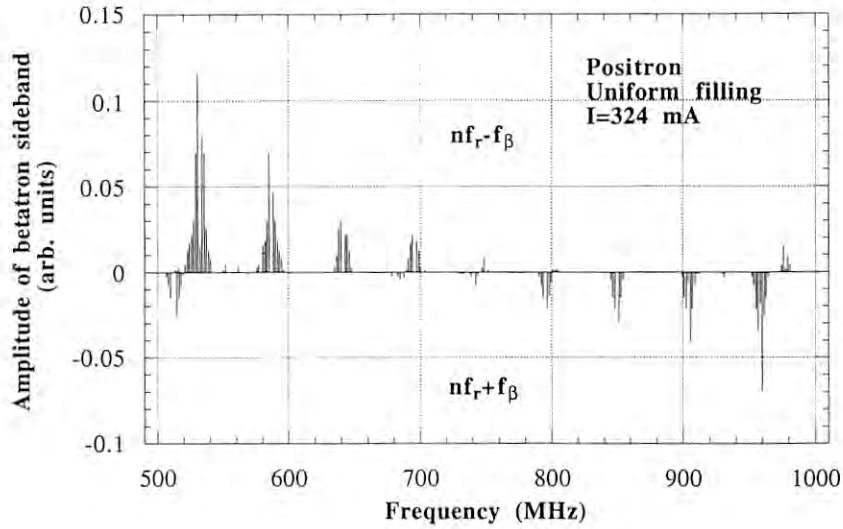

Fig. 25 Distribution of the betatron sidebands observed during positron multibunch operation with uniform filling. Beam current, 324 mA. The amplitude of the betatron sideband is plotted against the frequency, where the upper side of the figure shows the sidebands expressed as $nf_r - f_\beta$, where f_r is the revolution frequency, $f_\beta = \delta_{\nu\beta} f_r$ ($\delta_{\nu\beta}$ the fractional part of vertical tune), while the lower side shows the sideband expressed as $nf_r + f_\beta$.

positron in one revolution is expressed as

$$N_\gamma = \frac{5\pi}{\sqrt{3}}\alpha\gamma, \qquad (4)$$

where α and γ are the fine-structure constant (= 1/137) and the relativistic factor, respectively. In the case of the PF ring (E = 2.5GeV, γ = 4892), N_γ is 324. If we assume that the photoelectron production efficiency is 0.1, the number of photoelectrons produced is $N_{p.e.}$ = 32 by a positron during one revolution. The total number of photoelectrons is 4×10^{10} by a bunch during a revolution. The photoelectrons propagate in the beam chamber and are absorbed into its surface at about 10-100 ns after their production.

A computer simulation was performed to investigate the interactions between the photoelectrons and the beam. We consider a model beam-chamber with a diameter of 10 cm. All of the RF buckets are assumed to be filled uniformly. A rigid-beam approximation is used for the positron beam, while photoelectrons are expressed by macro particles. Photoelectrons (macro particles) are produced during each passing of the bunch at the position of beam chamber illuminated by the synchrotron radiation. The photoelectrons propagate in the chamber while feeling an attractive electromagnetic force from the following bunches. Although the photoelectrons are eventually absorbed, their stationary distribution is formed in the beam chamber. Figure 26 shows an example of the stationary distribution

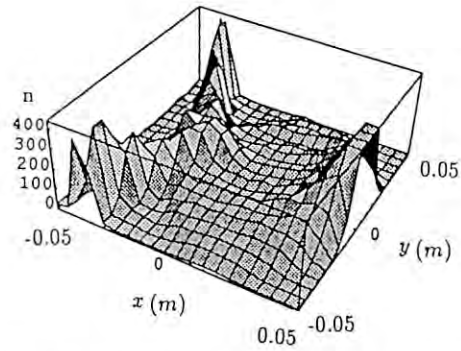

Fig. 26 Stationary distribution of photoelectrons. z-axis shows the number of photoelectrons at a transverse position (x, y) of beam chamber (arbitrary unit).

obtained from a simulation.

If a bunch (loading bunch) is shifted to the positive y- (vertical) direction, the photoelectrons are attracted toward the new position, which leads to a disturbance in the photoelectron distribution. The following bunches then feel kicks in the positive y-direction from the displaced distribution. We can interpret this momentum kick as being a transverse wake force, similar to that due to an electromagnetic wakefield. Figure 27 shows the calculated wake force. Due to this wake force, the transverse motion of the bunches becomes coupled, and the coupled-motion can be unstable. The unstable mode of oscillation, as well as its growth rate, is predicted by the conventional coupled-bunch theory[5]. The result is

shown in Fig. 28, where the photoelectron production rate is assumed to be 0.1. The growth rate predicted is much higher than the radiation damping rate of 120 s^{-1}. If the growth rate depends linearly on the beam current, the threshold current of the instability is 10-times lower than that given by the experiment. We consider that this discrepancy would be caused by the magnetic fields used in the ring, since they could relax the growth of the instability.

References

1) Photon Factory Activity Report #7, 1989, p.R-7.
2) Photon Factory Activity Report #8, 1990, p.R-5.
3) H. Kobayakawa, Rev. Sci. Instrum. **63**, 509 (1992).
4) M. Izawa, Y. Sato, and T. Toyomasu, Phys. Rev. Lett. **74**, 1995, pp.5044-5047.
5) A.W. Chao, Physics of Collective Beam Instabilities in High Energy Accelerator (Wiley-Interscience Publication, New York, 1993).
6) K. Ohmi, Phys. Rev. Lett. **75**, 1995, pp.1526-1529.

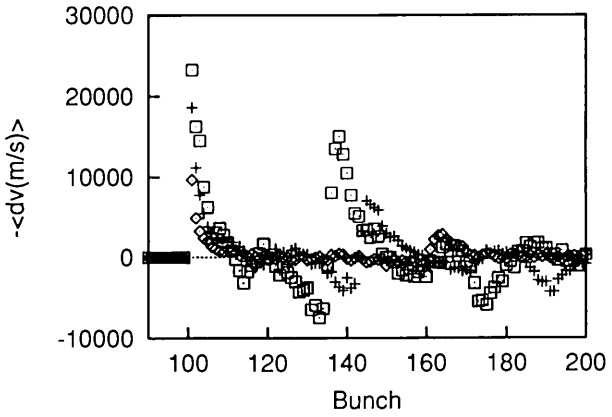

Fig. 27 Wake forces produced by the photoelectrons. Three kind of plots show the wake forces for stored current of 100, 200 and 300 mA. Higher current causes stronger force.

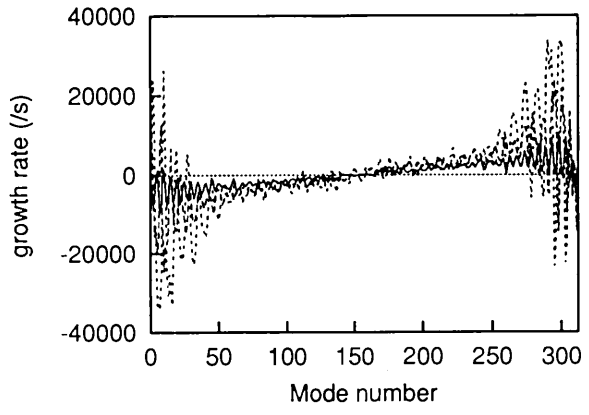

Fig. 28 Calculated growth rate of the coupled bunch instability for each stored current. The growth rate becomes higher for higher stored current.

3.2 Transverse Phase Space Monitor System

We have developed a beam-monitor system which can detect a transverse betatron oscillation of a single bunch, turn by turn. By measuring the beam positions at two differently-located BPM electrodes, we can experimentally obtain beam tracks on the transverse phase space. This system, together with a fast kicker magnet[1], allows us to perform attractive studies on the beam dynamics, similar to the particle tracking simulations on computers.

A block diagram of the system is shown in Fig. 29. The system comprises two position detection circuits, each of which has six independent channels, and a timing circuit used to synchronize the detection with a trigger-signal of the fast kicker magnet. Each channel consists of a bandpass filter, RF amplifiers, a peak detector with sample hold, a 8 -bit flash ADC and a 256-kbyte memory. The digitized signals are sent to the memory within a revolution period (624 nsec). After the data are filled in the memory, they are sent to an on-line computer (HP v743) through a GP-IB interface.

We selected PM02 and PM03, located at a 5 m long straight section, for the BPM electrodes by considering the following requirements: (1) no nonlinear magnets exist between the BPMs; (2) the phase advances of the betatron oscillation should be more than 45 degrees for both the horizontal (x) and vertical (y) directions, and (3) the beta functions ($ß_x$, $ß_y$) at the BPMs should be suitably large (5 ~ 10 m) and the same. In deriving the beam positions from the signals, the non-linear dependence of the signals at large amplitudes is precisely corrected off-line using a calculated mapping data of the BPM. Since there are no magnets between the BPMs, the beam angles (x', y') are simply obtained from the two beam positions.

Since the position resolution, the linearity and the dynamic range of the monitor are essential for beam studies, these were carefully investigated with a stored single-bunch beam of 5 mA. Figure 30(a) shows the horizontal beam positions without any kicks, which were measured with PM02 during 16384 turns. The position resolution can be seen from its histogram, shown in Fig. 30(b), which indicates the standard deviation of the horizontal positions being less than 0.1 mm. The resolution for the vertical direction was about 0.1 mm; these results were the same as in the PM03. At

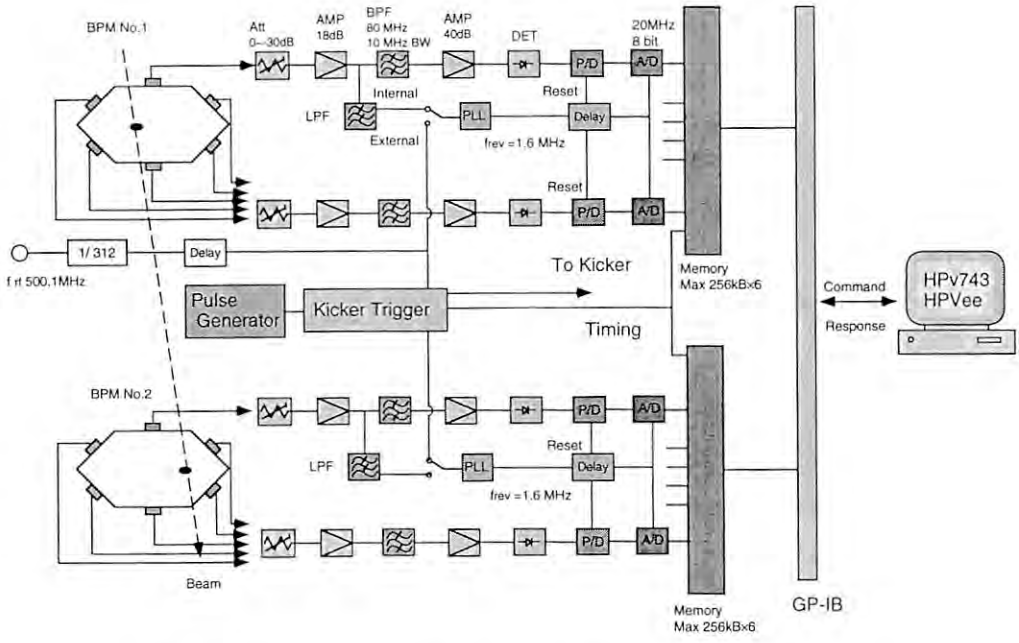

Fig. 29 Block diagram of the transverse phase-space monitor system

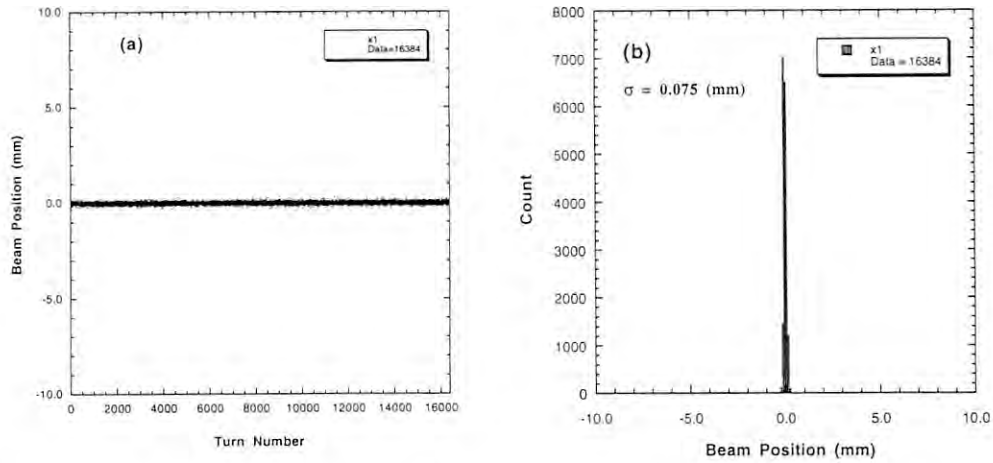

Fig. 30 (a) Horizontal beam position in one BPM measured turn by turn without a kick. (b) Histogram of the beam position.

present, these resolutions have been achieved when the stored beam current is more than 1 mA. The investigation of the dynamic range and the linearity is shown in Fig. 31. The horizontal axis indicates a high-voltage supplied to the kicker magnet, which is proportional to the kick angle. The vertical axis indicates the initial amplitude of the betatron oscillation induced by the kick. The dynamic ranges were more than 14 mm (in horizontal direction) and 9 mm (in vertical direction), respectively, which covers the physical aperture of the ring. Moreover, the linearity of the system was confirmed up to this limitation.

Using this system, interesting experiments on the beam dynamics are under way[2]. As an example, Fig. 32(a) displays a horizontal phase-space plot measured near to a 3rd-order resonance ($\nu_x = 8.33$). The beam tracks on the phase space, denoted by points, form a triangle due to the 3rd-order resonance effect. As another example, a vertical phase-space plot measured near to a 4th-order resonance ($\nu_y = 3.25$) is shown in Fig. 32(b). This shows the phenomenon that the beam was trapped on the 4th-order resonance island.

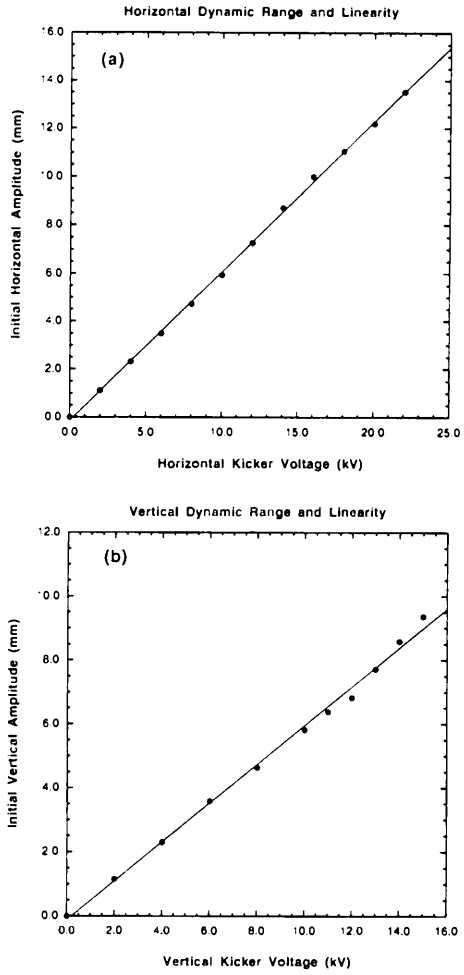

Fig. 31 Estimations of the dynamic range and linearity of the system: (a) horizontal direction, (b) vertical direction.

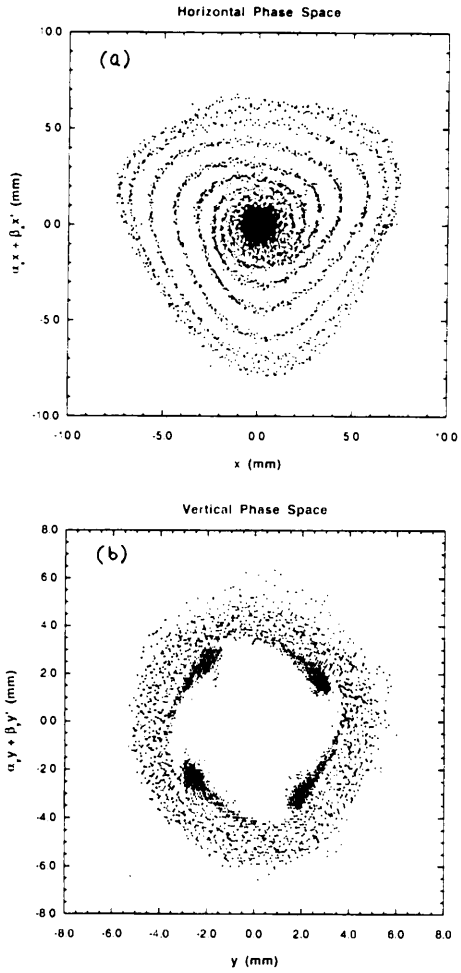

Fig. 32 (a) Horizontal phase-space plot measured near to the 3rd-order resonance (ν_x=8.33). (b) Vertical phase-space plot measured near to the 4th-order resonance (ν_y=3.25).

References

1) Y. Kobayashi et al., Proceedings of the 1993 Particle Accelerator Conference, p.215.
2) Y. Kobayashi, to be presented in the EPAC96.

3.3 Development of a Precise Beam-profile Monitor using Visible Synchrotron Light

A precise beam-profile monitor, by means of imaging visible synchrotron light, was designed and constructed at the Photon Factory[1,2]. This monitor allows the accurate measurement of a small-beam size. The monitor can be used to measure the beam emittance under the low-emittance optics of the PF ring. It consists of a beryllium mirror for extracting visible synchrotron light and a diffraction-limited focusing system.

The extraction mirror must withstand the maximum incident power of the synchrotron radiation (SR), given in Table 9, without experiencing a serious permanent deformation. Because of the small absorption of un-

Table 9 Parameters concerning the SR from the bending magnet.

Bending radius	8.66 m
Dipole field	0.96 T
Angular power density of SR (at 350 mA)	13.2 Watt/mrad
Beam size*	σ_x : 352 μm, σ_y : 74 μm

* Under the low-emittance optics (135° per cell).

wanted X-rays, beryllium (Be) was chosen as the mirror material to extract visible synchrotron light. The mirror was water-cooled, and has an effective area of 50 mm × 50 mm. An outline of the Be-mirror is shown in Fig. 33.

The flatness of the mirror surface is always watched by a Fizeau-type interferometer within a precision of $\lambda/20$. A result of the interferometry of the mirror surface, measured under no irradiation of SR, is shown in Fig. 34. A permanent deformation of the mirror, which was caused by baking at 150°C, was observed. The mirror was deformed in a cylindrical way in the horizontal direction by 2.36 mm (by peak to valley). With the irradiation of SR, a further deformation due to the head load is added.

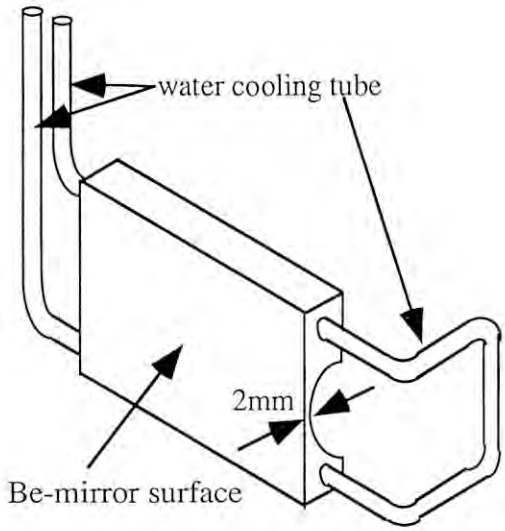

Fig. 33 Design of the Be-mirror.

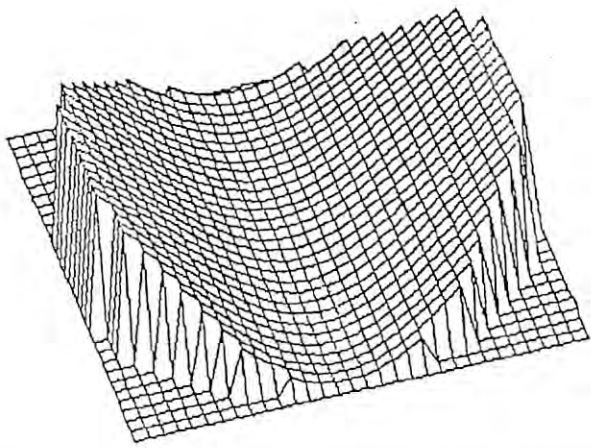

Fig. 34 Measured surface deformation of the Be-mirror under no SR irradiation. The side length of three-dimensional plot is 50 μm. The maximum deformation was 2.36 μm (peak to valley).

In our optical focusing system, the obtained beam image is blurred by a diffraction effect due to the finite aperture of an entrance pupil, and also by a deformation of the extraction mirror. Based on the wave optics, these effects can generally be treated using diffraction theory. If we know the point-spread function (PSF) of the focusing system, which describes the image from a point light source, we can restore (or deconvolute) the real beam image from the raw blurred image. This technique is widely used in modern astronomical observations. The PSF of our focusing system, which includes an effect of the deformation of the Be-mirror, was calculated using the computer code ZEMAX. The detail analysis is given in reference 2). A result of the PSF is shown in Fig. 35. The rms widths of the central peak of the PSF are 11 mm (in vertical) and 12.0 mm (in horizontal), respectively.

In order to demonstrate the capability of this monitor for measuring small beam sizes with sufficient accuracy, we measured the beam profile in the present PF storage ring operated at a beam energy of 1 GeV. With this energy, the estimated natural emittance is 20.7 nm·rad, which is almost the same emittance as that in the high-brilliance configuration. To avoid any further deformation of the mirror due to the irradiation of SR, the measurement was carried out at a stored current of 1 mA. A result of the raw image of the beam profile is shown in Fig. 36. The rms beam sizes from this image are 96.5 μm (in vertical) and 280 μm (in horizontal), respectively. This raw image was blurred by the diffraction effect (including the mirror deformation).

To obtain the original beam profile, the raw image was deconvoluted using the computer code Hidden Image, where the maximum entropy deconvolution

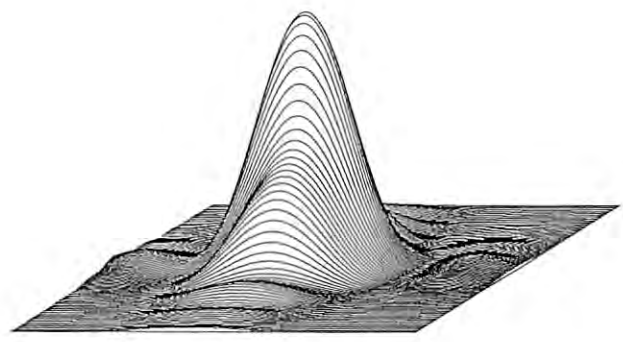

Fig. 35 Point spread function (PSF) of our focusing system at a balanced astigmatism point. The side length of the three-dimensional plots is 108 μm.

method was applied. In the deconvolution process, the previously obtained PSF was used. A result of the deconvolution is shown in Fig. 37. From this image, rms beam sizes of 49.2 μm (in vertical) and 206 μm (in horizontal) were obtained. Using the vertical and horizontal β functions at the source point, the beam emittances were estimated to be 0.13 nm·rad (vertical) and 22 nm ·rad (horizontal) at a beam energy of 1 GeV.

Fig. 36 Raw beam-image of the Photon Factory. The beam energy was 1 GeV, and the beam current was 1 mA.

Fig. 37 Beam image after the deconvolution process. The scale is the same as in Fig. 36.

References

1) T. Mitsuhashi, Proc. of the 10th Symposium on Accelerator Science and Technology, Hitachinaka, Japan, 1995, p.275.
2) T. Mitsuhashi and M. Katoh, to be presented in the EPAC96.

4. STORAGE RING SPECIFICATIONS

This section contains major specifications of the 2.5-GeV PF ring to provide quick and handy information for users and machine physicists.

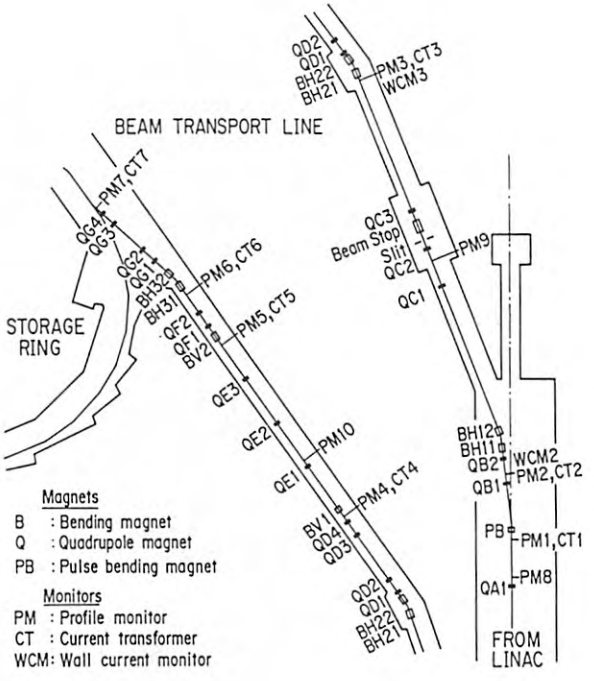

Fig. 38 Beam transport line.

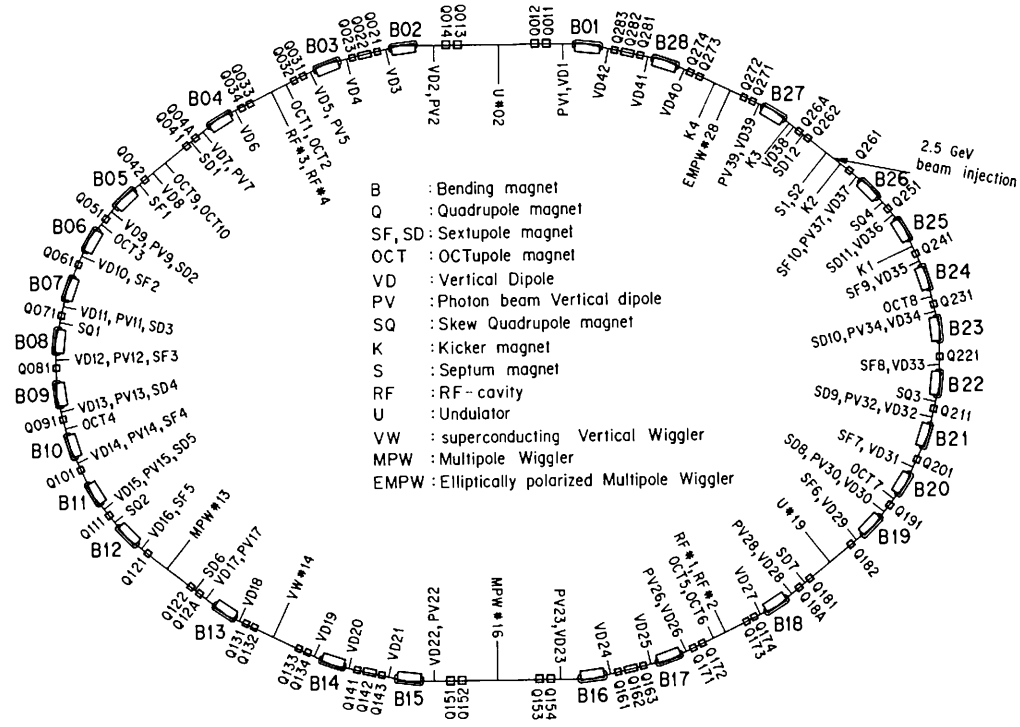

Fig. 39 Ring lattice components.

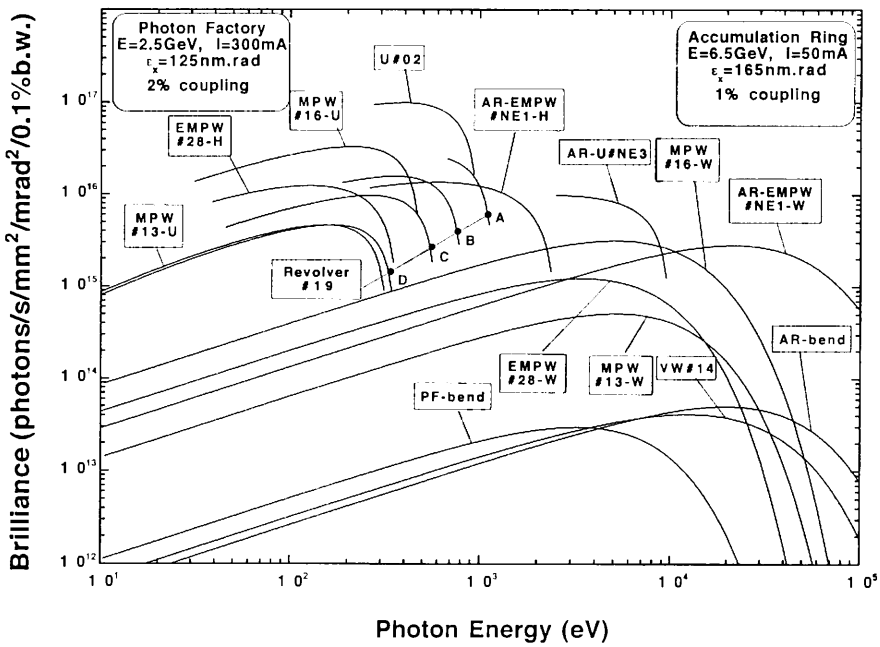

Fig. 40 Synchrotron radiation spectra.
Brilliance of radiation vs. photon energy for the insertion devices (U # 02, MPW # 13, VW # 14, MPW # 16, Revolver # 19 and EMPW # 28) and the bending magnet (bend) of the PF, and for the insertion device (EMPW # NE1) of the AR. The name of each source is assigned in Table 10. Several insertion devices have both undulator and wiggler modes, which are denoted by U or W, respectively. The spectral curve of each undulator (or undulator mode of multipole wiggler) is a locus of the peak of the first harmonic within the allowable range of K-parameter. Spectra of Revolver # 19 are shown for four kinds of period lengths.

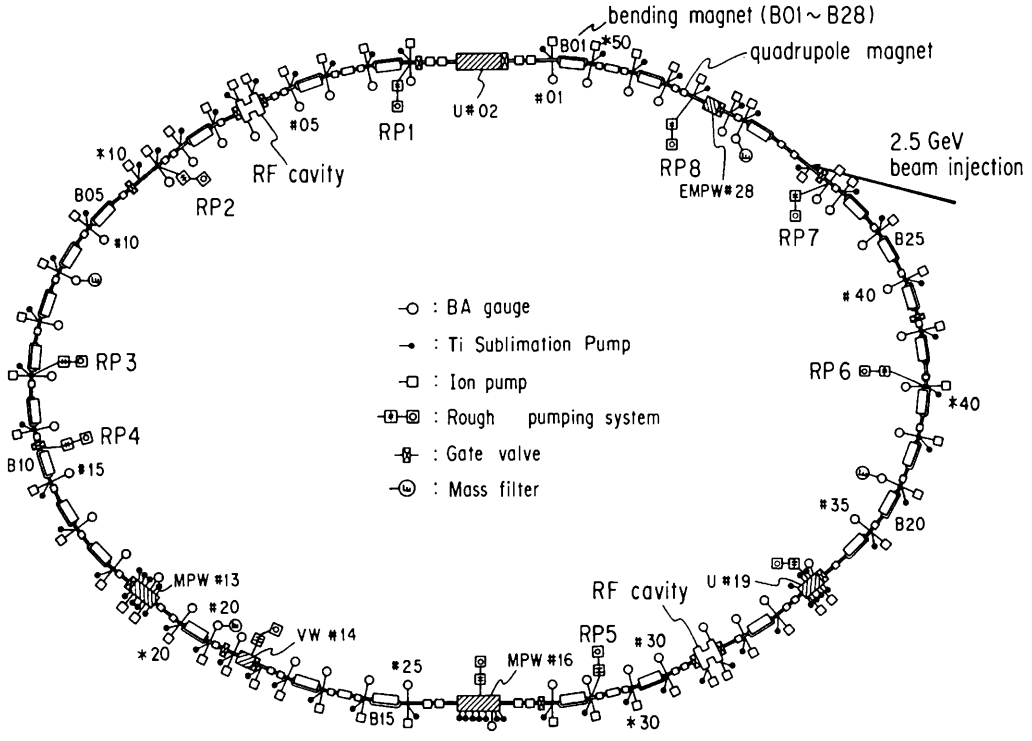

Fig. 41 Vacuum system components.

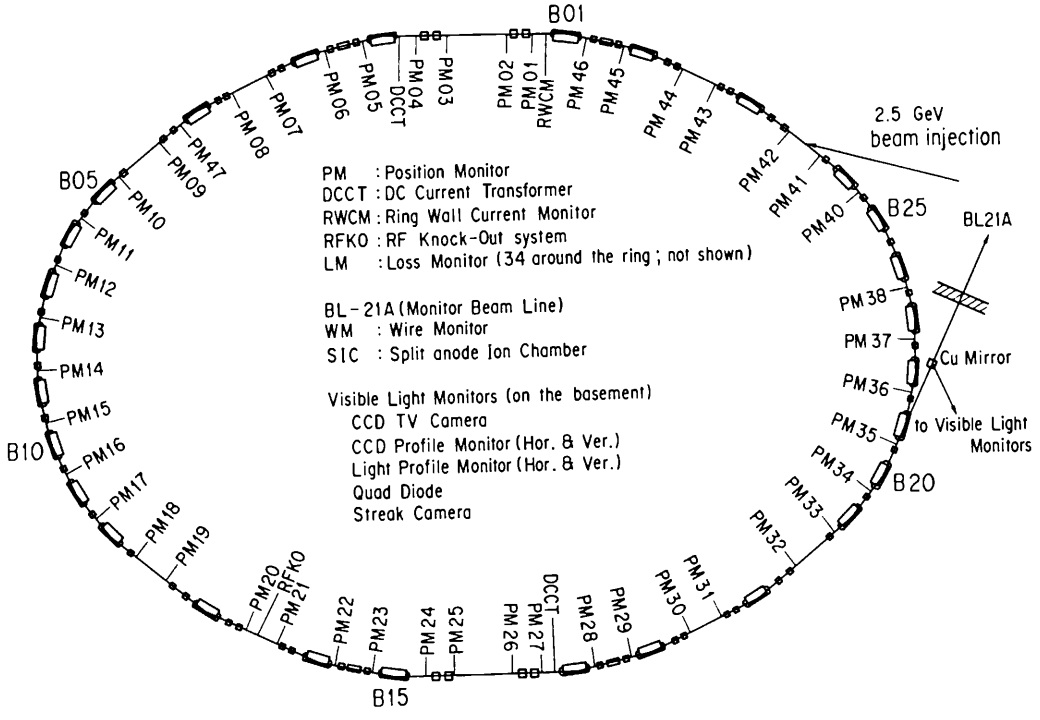

Fig. 42 Beam monitors.

Table 10 Insertion devices.

Calculated spectral performances of the bend source and 6 insertion devices at the Photon Factory. E/I: beam energy and current, λ_u: period length, N: number of periods, L: length of undulator or wiggler, $G_v(G_x)$: minimum vertical (horizontal) gap height, $B_v(B_x)$: maximum vertical (horizontal) magnetic field, P: pure configuration, H: hybrid configuration, S.C.: superconducting magnet, $\sigma_{x,y}$: horizontal or vertical beam size, $\sigma_{x',y'}$: horizontal or vertical beam divergence, $K_h(K_v)$; horizontal (vertical) deflection parameter, $\varepsilon_1/\varepsilon_c$: photon energy of the first harmonic (critical energy in the case of bend source or wiggler), $\Delta\varepsilon/\varepsilon$: relative bandwidth, Pc: degree of circular polarization, $\mathcal{D}$: photon flux in unit solid angle (photons/s·mrad^2·1%b.w.), $\mathcal{B}$: brilliance (photons/s·mm^2·mrad^2·0.1%b.w.), P_T: total radiated power, $dP/d\Omega$: power in unit solid angle. Different operating modes of undulator and wiggler are denoted by-U and-W, respectively.

Name	E/I GeV/mA	λ_u cm	N	L m	$G_v(G_x)$ cm	$B_v(B_x)$ T	Type of magnet	σ_x mm	σ_y mm	$\sigma_{x'}$ mrad	$\sigma_{y'}$ mrad	$K_h(K_v)$	$\varepsilon_1/\varepsilon_c$ keV	$\Delta\varepsilon/\varepsilon$	$\mathcal{D}$	$\mathcal{B}$	P_T kW	$dP/d\Omega$ kW/mrad^2
Bend	2.5/300							0.74	0.26	0.38	0.037		4.0		3.5E13	2.9E13		0.060
U#02		6.0	60	3.6	2.8	0.4	H(NdFeB)	0.78	0.11	0.16	0.022	2.25	0.28	0.029	5.2E16	9.7E16	0.68	2.7
MPW#13-W -U		18.0	13	2.5	2.7	1.5	H(NdFeB)	1.66	0.17	0.15	0.019	25.0 2.0	6.2 0.108	0.086	9.7E14 5.7E15	4.9E14 3.2E15	6.7 .042	2.6 0.19
VW#14					5.0	5.0	S.C.	1.05	.096	0.16	0.025		20.8		2.2E13	3.4E13		0.18
MPW#16-W -U		12.0	26	3.1	1.9	1.5	H(NdFeB)	0.78	0.11	0.16	0.022	16.8 2.0	6.2 0.162	0.050	1.8E15 1.6E16	3.1E15 2.8E16	8.3 0.12	4.9 0.52
Revolver #19		5.0 7.2 10.0 16.4	46 32 23 14	2.3	3.0	0.28 0.41 0.53 0.62	H(NdFeB) H(NdFeB) H(NdFeB) P(NdFeB)	1.66	0.17	0.15	0.019	1.3 2.7 5.0 9.5	0.637 0.176 0.0436 0.0078	0.021 0.039 0.047 0.066	4.1E16 2.1E16 6.9E15 1.2E15	2.3E16 1.2E16 3.8E15 6.3E14	0.21 0.44 0.78 1.05	1.27 1.54 1.53 1.09
EMPW#28 -W -U		16.0	12	1.9	3(11)	1(0.2)	P(NdFeB)	1.05	.096	0.16	0.025	15(1) 1(1)	4.2(Pc=89%) .18(Pc=99%)	0.11	2.5E14 6.3E15	3.4E14 9.8E15	2.3 0.02	0.38 0.058

Table 11 General parameters of the storage ring.

Energy	2.5 GeV	(0.75 GeV to 3 GeV)
Initial stored current (multi-bunch)	350 mA	(max 500 mA)
(single bunch)	40 mA	(max 104 mA)
Emittance	130 nm·rad(horizontal) ~2 nm·rad(vertical)	
Circumference	187 m	(bending radius=8.66m)
RF frequency	500.1 MHz	(harmonic number=312)
Injection	2.5-GeV Linac	(positron/electron)
Beam lifetime	60 h (at 300 mA)	$I\cdot\tau \geq 18$ A·h (at ~250 mA ~ 350 mA)
Vacuum pressure	$\leq 3\times10^{-10}$ Torr (at 300mA) P/I ~ 8×10^{-10} Torr/A (at ~250 mA ~ 350 mA) ~ 3×10^{-11} Torr (at 0 mA)	
Insertion devices	Superconducting vertical wiggler 5T 60 period undulator K=1.78~0.1 26 period multipole wiggler/undulator 1.5T~0.04T Four way revolver type undulator 14 period multipole wiggler Elliptically polarized multipole wiggler	
SR channels	SR experiment 22 Beam diagnosis 3	

Table 12 Beam parameters.

Horizontal tune ν_x	8.45
Vertical tune ν_y	3.30
Momentum compaction factor α	0.015
Natural chromaticity ξ_x	-15.8
ξ_y	-8.6
Bunch length σ_z	1.5 cm
Transverse damping time	7.8 msec
Longitudinal damping time	3.9 msec
Energy spread	7.3×10^{-4}
Radiation loss	400 keV

Table 13 Principal parameters of the accelerator system.

Magnet system	number of magnets	number of power supplies
Bending	28	1
Quadrupole	58	12
Sextupole	22	2
Octupole	11	10
Skew quadrupole	4	4
Dodecapole	6	6
Vertical steering	42	42
Photon beam steering	20	20
Others		
Backleg winding of bending magnet	28	
Electric shunt for tune compensation	12	

RF system

Number of RF stations	4
Number of klystrons	4 (180kW/klystron)
Number of RF cavities	4 (single cell cavity)
Shunt impedance	32MΩ (four cavities)
Unloaded Q	39000
Total power dissipated in cavity wall	89kW
Total cavity gap voltage	1.7MV
Synchrotron frequency	37kHz

Vacuum system

Main pumping system		
pump	pumping speed	number
SIP (Sputter Ion Pump)	128 l/sec	54
DIP (Distributed Ion Pump)	150 l/sec	26
Ti sublimation	----------	71
NEG (Non-Evaporable Getter)	----------	2
total effective pumping speed = 2×10^4 l/sec (for CO)		
Rough pumping system	pumping speed	number
TMP (Turbo Molecular Pump)	300 l/sec	12
Measurement	number	
B-A gauge	48	
mass filter	4	
cold cathode gauge	16 (for baking)	
Sector gate valve	number	
all metal with RF shield	5	
all metal without RF shield	1	
viton seal with RF shield	10	

Injection system

Septum magnet		
name	Septum I (S1)	Septum II (S2)
core material	laminated silicon steel (passive type)	
length [mm]	1500	1000
maximum current [A]	6000	6000
deflection angle [degree]	7.0	5.0
pulse width [msec]	88	60
Kicker magnet		
name	K1, K2, K3, K4	
core material	ferrite (window frame type)	
core length [mm]	300	
maximum current [A]	3500	
maximum deflection angle [mrad]	4.4	
pulse width [msec]	5	

Superconducting vertical wiggler

Maximum field strength on the beam orbit	5 Tesla
Magnet gap	66 mm
Magnet pole size (widthxhight)	40 mm x 260 mm
Number of magnetic poles	5 poles arranged every 200 mm
Rated exciting current	220 A at 5 Tesla
Superconducting wire	NbTi : Cu 1 : 1 size 1.70 x 0.85 mm^2
Cross section of coils	65 mm x 70 mm
Number of turn	2520
Liquid helium consumption in the permanent current mode	0.1 L/h
Damping rate of the permanent current	1.4×10^{-5}/h
Inductance	1.31 H/coil

FEL oscillator

1. General	
target wavelength	213 nm (177 nm)
FEL gain	13% (11.5%)
cavity loss	4% (8%)
net FEL gain	9% (3.5%)
2. Storage ring	
beam energy	0.75 GeV
number of bunches	4
bunch length (2σ)	60 psec
peak current	20 A
beam emittance	15 nm·rad
energy spread	3.8×10^{-4}
accelerating frequency	500.1 MHz
3. Optical klystron	
periodic length	9 cm
number of periods	19 + 19
max. magnetic field	0.7 tesla
max. deflection parameter	5.9
optimum N_d	169 (183)
FEL gain	0.6 %/amp
4. Optical cavity	
type	Fabry Perot
cavity length	23.38 m
mirror 1 (UHV Al)	R=92%
mirror 2 (MgF_2 multilayer)	R=96%
cavity loss at 177 nm	12%
5. Laser system	
mode-lock YAG laser	
mode-lock frequency	83.35 MHz (= f_{rf} /6)
regenerative YAG amplifier	
repetition rate	50 Hz
pulse energy at 532 nm	30 mJ
pulse duration	80 psec
harmonic generation	
harmonic material	KPT, BBO and KB5
max. pulse power	500 kW (100 kW)

Monitor system

I. Orbiting Beam Monitors

PM (Position Monitor)	46
DCCT (Direct Current Current Transformer)	2
RFKO (Radio Frequency Knock-Out system)	1
WCM (Wall Current Monitor)	1
LS (Loss monitor)	20
Visible Light Monitor	
CCD TV camera	1
CCD profile monitor (H & V)	1
light profile monitor (H & V)	1
four-element photo diodes (for oscillation detection)	1
streak camera	1
photon counting system	1

II. Photon beam position monitors installed in beamlines

Beamline	Source	Upstream	Downstream	Ver./Hor.
BL 2	U	DSPM	DSPM	V, H
BL 3A	B	SPM		V
BL 3C	B	SPM	SPM	V
BL 4C	B	SPM	SPM	V
BL 6B	B	SLIT		V
BL 6C	B	SLIT		V
BL 6C	B	SPM	SPM	V
BL 7C	B	SLIT	SPM	V
BL 10A	B	SIC		V
BL 10B	B	SLIT		V
BL 12A	B	WM	WM	V
BL 14C	SVW	SPM	SPM	H
BL 15A	B	SPM		V
BL 16	MPW	DSPM		V, H
BL 21	B	WM		V
BL 27	B	SPM		
BL 28	EMPW	Under constr.		

Note:
SPM : Split Photoemission Monitor
SIC : Split Ion Chamber
WM: Wire Monitor
DSPM: Dual SPM for insertion device line
B: Bending magnet
U: Undulator
SVW: Superconducting Vertical Wiggler
MPW: Multipole Wiggler
EMPW: Elliptical MPW

Control system

		number	memory
Control computers	FACOM S-3500	4	16 Mbyte
Library computer	FACOM M-780/10R	1	32 Mbyte
Computer network (type : optical token ring) number of nodes = 5 (max. 256)			

Table 14 Beam size and divergence at source point.

location	σ_x [mm]	σ_y [mm]	σ'_x [mrad]	σ'_y [mrad]
B15&B01	0.34	0.16	0.41	0.033
B02&B16	0.60	0.13	0.38	0.033
B03&B17	0.43	0.22	0.32	0.018
B04&B18	0.52	0.18	0.29	0.045
B05&B19	1.26	0.21	0.39	0.037
B06&B20	0.85	0.25	0.38	0.037
B07&B21	1.26	0.21	0.39	0.037
B08&B22	0.85	0.25	0.38	0.037
B09&B23	1.26	0.21	0.39	0.037
B10&B24	0.85	0.25	0.38	0.037
B11&B25	1.26	0.21	0.39	0.037
B12&B26	0.85	0.25	0.38	0.037
B13&B27	0.44	0.23	0.31	0.045
B14&B28	0.50	0.20	0.30	0.018

Table 15 Summary of Beamline Front Ends in FY 1995.

Beamline	Affiliation	Source	Spectral range	Status
BL-1	NTT	Bending magnet (B1)	VUV and soft X-ray	in operation
BL-2	KEK-PF	60-period undulator	soft-X-ray	in operation
BL-3	KEK-PF	Bending magnet (B2 & B3)	VUV and soft X-ray	in operation
BL-4	KEK-PF	Bending magnet (B4)	X-ray	in operation
BL-5	KEK-PF	Multipole wiggler/undulator	-	under installation
BL-6	KEK-PF	Bending magnet (B6)	X-ray	in operation
BL-7	University of Tokyo	Bending magnet (B7)	VUV and X-ray	in operation
BL-8	Hitachi Ltd.	Bending magnet (B8)	VUV and X-ray	in operation
BL-9	Nippon Electrical Co. (NEC)	Bending magnet (B9)	VUV and X-ray	in operation
BL-10	KEK-PF	Bending magnet (B10)	X-ray	in operation
BL-11	KEK-PF	Bending magnet (B11)	VUV and soft X-ray	in operation
BL-12	KEK-PF	Bending magnet (B12)	VUV	in operation
BL-13	KEK-PF	27-pole wiggler/undulator	Soft and hard X-ray	in operation
BL-14	KEK-PF	Superconducting vertical wiggler	hard X-ray	in operation
BL-15	KEK-PF	Bending magnet (B15)	X-ray	in operation
BL-16	KEK-PF	53-pole wiggler/undulator	Soft and hard X-ray	in operation
BL-17	Fujitsu Ltd.	Bending magnet (B16 & B17)	VUV and X-ray	in operation
BL-18	ISSP and KEK-PF	Bending magnet (B18)	VUV and X-ray	in operation
BL-19	ISSP and KEK-PF	Multi-undulator	VUV	in operation
BL-20	KEK-PF	Bending magnet (B20)	VUV and X-ray	in operation
BL-21	KEK-PF	Bending magnet (B21)	Beam diagnosis	in operation
BL-27	KEK-PF	Bending magnet (B27)	Soft X-ray and X-ray	in operation
BL-28	KEK-PF	25-pole wiggler/undulator	Circularly polarized VUV and soft X-ray	in operation

C. TRISTAN AR

The TRISTAN accumulation ring (AR) is a storage accelerator for accelerating electrons or positrons from 2.5 GeV to 8 GeV, and transferring them to the TRISTAN main colliding ring (MR). During the intervals of MR-injection the AR is operated with an electron beam of 6.5 GeV as a synchrotron-radiation source. Typically, it takes one hour for MR-injection. The following two hours are used for SR experiments. At present the AR has four beam lines (BL-NE1, -NE3, -NE5 and -NE9). BL-NE1 accepts SR from an ellipsoidal multipole wiggler and BL-NE3 from an X-ray undulator. The remaining two beam lines transport SR from the bending magnets in the normal cells. Table 14 shows the machine parameters of the AR.

Table 15 summarizes the operation statistics of the AR this year. Failures which took more than a day to be fixed were a leak in a crotch absorber and a water-leak in a power converter of the quadrupoles.

Dust-trapping experiments were performed at the AR[1]. An experimental system was developed to control the generation of dust. It consists of a micro-particle launcher and collector, a vacuum system and four lead-glass counters (two for observing Bremsstrahlung and two as beam-loss monitors). The launcher has eight small holders of micro particles, and drops micro particles onto the beam. The typical size of micro particles is about 0.1 μm to 45 μm, depending on the species. It was found that although no trapping of metallic micro particles (Al, Ti, Cu, CuO) was observed, the trapping of ceramic micro particles (TiO_2, Zr-V-Fe) and diamond micro particles was observed for several tens of minutes. According to preliminary calculations, diamond micro particles (melting point: 4000 K) have a lifetime of a few minutes, while Cu micro particles (melting point: 1360 K) melt away in a time of less then 1 ms due to heating by the beam. This result does not contradict the observation, and gives a qualitative explanation that micro particles of a material which has a high melting point would easily be trapped.

Reference

1) Proceedings of the 10th Symposium on Accelerators Science and Technology, Oct. 25-27, 1995, Hitachinaka, Japan, JAERI.

Table 16 Machine parameters of TRISTAN AR.

Energy	6.5 GeV
Natural emittance	293 nm rad
Circumference	377 m
RF frequency	508.6 MHz
Bending radius	23.2 m
Energy loss per turn	6.66 MeV
Damping time	
horizontal	2.5 ms
vertical	2.5 ms
longitudinal	1.2 ms
Natural bunch length	18.6 mm
Momentum compaction factor	0.0129
Natural chromaticity	
horizontal	-14.3
vertical	-13.1
Stored current	40 mA
The number of bunches	1
Beam lifetime	240 min.

Table 17 Operation statistics of TRISTAN AR. (From Oct. 1994 to Sep. 1995).

	Time(hr)
SR experiment and MR injection for physics experiment	3301.5
MR injection for machine study and beam tuning	597.5
Machine study and beam tuning of AR	676.0
Failure	151.5
Others	192.5
Total	4919.0

Collaborations

You can jump to the article by clicking its title.

CONTENTS

A. THE TSUKUBA ADVANCED RESEARCH ALLIANCE (TARA) SAKABE RESEARCH PROJECT

1. HISTORY AND PURPOSE OF THIS PROJECT

The Tsukuba Advanced Research Alliance (TARA) Sakabe Research Project is a cooperative project involving the industries, government and universities to pursue the understanding of the maintenance of life and the perpetuation of species from the functional viewpoint. Advanced technologies are developed to study three dimensional structures of biologically important matters by x-ray crystallography. The structures thus determined form the basis of research in biological control mechanisms. Furthermore, utilization of computer graphic techniques for molecular structure designing shall be pursued.

To achieve the above mentioned goals, an organization and a financial base must be established. The utilization of synchrotron radiation is fundamentally important for the X-ray crystal analysis of protein. Fortunately, Tsukuba University is very close to the Photon Factory. Since this project has a strong appeal to the industries, it should make a good case to conduct cooperative research including industries, the government, and universities. One year was spent to draw the plans for the proposal. The sub-projects (hereafter referred to as "groups") shown in Table 1 were set up during this period. Prior to the official approval of this project. Prof. Sakabe negotiated for collaborative research between Tsukuba University and the Photon Factory. This led to the possibility of building an experimental station for TARA. Simultaneously, he solicited participation from the industries, government labs, and universities. This process was difficult since efforts depended on the provisional assumption that the "TARA Sakabe Research Project" would be approved. We received a lot of cooperation and, despite the difficult situation, managed to set the startup date in 1995.

Table 1 List of Sub-Groups

1. Construction of the TARA Experimental Station and the development of various devices to be used in the station.
2. Setting up the analyzing devices and software.
3. Ultra-precise analyses of protein crystals, such as insulin.
4. Research of membrane proteins, especially in the bioenergy conversion system.
5. Research of ultra-macromolecules, such as viruses, and their application.
6. Structural analyses of enzymes and research on their functions, properties, and reaction mechanisms based on the structure.
7. Dynamic structure analysis of a protein molecules by the time-resolved Laue method.
8. Crystal structure analysis of a nuclear acid-related protein and research on their function and applications.
9. Research on proteins of medical importance and their applications.

2. ORGANIZATION AND FINANCIAL BASE OF THIS PROJECT

The organization of this project is shown in Table 2. Currently, 39 groups and 136 members are involved.

The budget consists of donations from companies, the official funds for TARA, and other subsidies from the public, such as Monbusho research funds. As shown on Table 2, 19 companies are currently participating; 12 of them have offered donations.

The budget for 1995:

Donation from the industries: ¥340,000,000

Official budget for TARA: ¥2,000,000

For 1996, we plan to finance the project through the official TARA budget, donations from the remaining companies (3.5 companies, ¥140,000,000), annual donations of ¥4,000,000 from the 12 companies. Among them, donations from five companies will be allocated for use by the Photon Factory to improve the cooperative study.

3. ACTIVITIES OF GROUP 1

An urgent task for Group 1 was to build and tune up the experimental station for TARA, and enable it to start experiments in May 1996. Dr. Nobuhisa Watanabe, Dr. Mamoru Suzuki, and the staff members of the Photon Factory have worked on the beam line and hutch. Many other tasks, such as interlocks, have been carried out in cooperation with staff members of the facility.

1) Location of the experimental station

The most important task was to build the experimental station for TARA at the Photon Factory and make it available by May 1996. An agreement was signed between the University of Tsukuba and the National Laboratory for High Energy Physics (KEK) to build the TARA

Table 2 Group and members participating in this project as of March 31, 1996

University	No. of people	Research Institute	No. of people	Company (Those who have decided to donate to this project are written in bold)	No. of people
Univ. of Tsukuba	8	PF	2	**Mitsubishi Chem. Corp.**	10
Osaka Univ.	6	RIKEN	2	**Biomol. Engineer Res. Inst.**	8
Kyoto Univ.	6	FAIS	1	**Japan Tabacco**	8
The Univ. of Tokyo	5	Natio. Inst. of Genetics	1	**Kirin Brewery Co., Ltd.**	7
Nagaoka Univ.	4	Max Plank Inst.	2	**Yamanouchi Pharm. Co., Ltd.**	6
Himeji Inst. of Tech.	3			**Eisai Co., Ltd.**	5
Tokyo Inst. of Tech.	2			**Banyu Pharm. Co., Ltd.**	5
Hokkaido Univ.	2			The Green Gross Corp.	5
Nagoya Univ. of Tech.	2			**Chugai Pharm. Co., Ltd.**	4
Ochanomizu Univ.	1			**Fijisawa Pharm. Co., Ltd.**	4
Univ. of Osaka Pref.	1			Tanabe Seiyaku Co., Ltd.	4
Osaka City Univ.	1			**Sankyo Co., Ltd.**	3
Nara Inst. of Sci. & Tech.	1			**Daiichi Pharm. Co., Ltd.**	3
Kitasato Univ.	1			Mochida Pharm. Co., Ltd.	1
Univ. of Oxford	2			Kyowa Hakko Kogyo Co., Ltd.	1
				Nippon Roche Res. Center	2
				Takeda Chem. Industries Ltd.	1
				Shionogi & Co., Ltd.	1
				Rigaku Corp.	1
total 15 Universities	45	5 Institutes	8	19 Companies	83

experimental station at BL6B of the Photon Factory. The cooperation of the KEK management division has been instrumental in accomplishing this. The experimental stations currently used for protein crystallography at the Photon Factory are BL6A and BL18B. The reason we requested BL6B was because it stands close to BL6A and cooperation between them would be possible. Furthermore, BL6B will become a convenient station if we can get permission to utilize BL5 as a beam line for the crystal analysis of protein.

BL6B was originally built as a multi-purpose station for XAFS or high-pressure diffraction, and therefore impossible to use as an experimental station for TARA unless it was remodeled. Therefore, our first action was to remove the multi-purpose station and investigate which devices to install.

2) Specifications of the diffraction device and optical system

A device to integrate diffraction data was specifically designed for this project. The design was based on the Weissenberg-Camera[1),2),3)] for macromolecular crystallography which was developed by the author and co-workers. Many improvements have been made to this camera and it now has a very high reputation world-wide. The device includes two large size imaging-plates (400-by-800 mm IP) as a detector and a cylindrical cassette. Considering both area resolution of the diffraction spots on the IP and resolution of the crystal structure analysis, we have chosen the cassette with camera radius of 573 mm. The relationships between the wavelength, resolution, cell dimensions, etc. are shown in Table 3.

3) The IP Reader

A high-sensitivity detector was developed by Fuji Film Inc. with outstanding characteristics; its sensitivity is at least 30 times higher than a high-sensitivity X-ray photo film and its dynamic range (linear domain of recording volume against exposure) is fifty to sixty thousand times greater. Furthermore, it can be reset by irradiating visible light and may be reused, as long as the protecting film is clean and not damaged by scratches. Two types of IP, 200 by 250 mm and 200 by 400 mm, are manufactured by Fuji Film Inc. for physical and chemical use, and the BAS2000 is compatible to the IP reader. The size of the camera to be built for collecting diffraction data is 800 × 800 mm, so it is

Table 3 Specifications at 573 mm radius

Two 800-by-400 sized IP, X-ray wavelength:1.0Å

Cassette radius (mm)	IP position	Range of photography in θ direction			Range of photography in horizontal direction		
		mm	θ deg.	Å	mm	β deg.	Å
573.0	upper IP	400	20.00	1.46	395	34.58	1.76
573.0	lower IP	390	19.50	1.50	395	34.58	1.76

X-ray wavelength λ (Å)	0.9	1.00	1.10	1.20	1.40	1.60	1.80
resolution: (vertical direction) (Å)	1.31	1.46	1.61	1.75	2.04	2.34	2.63
resolution: (horizontal direction) (Å)	1.58	1.76	1.94	2.11	2.29	2.82	3.17
layer line interval 3 mm [a] (Å)	172	191	210	229	267	306	344

a) When the layer line interval was 3 mm and the coupling constant was 2 degree/mm, one plate could record 6 degrees. These numbers indicate the cell dimension along the oscillation axis, which allow 6 degree oscillation.

best to order an 800 mm IP and to produce the reader according to this size. However, we decided to use two 400 mm × 800 mm size IPs since the 800 × 800 mm size IP is difficult both to manufacture and to handle. Two IPR4080s (the IP reader that we developed for large format IP 400 mm × 800 mm) are installed. Along with the IPR4080 s, one BAS2000 is installed so that the ordinary IP could also be used.

4) Other equipment
Other equipments installed at BL6B include an IP Eraser, an IP storage box to protect recorded data on the IP from cosmic rays, three computers, an cryo-device to cool samples down to -180 degrees Celsius, two microscopes, a filing cabinet, and a sofa.

5) BL6B Hatch
A hutch sized 2945 × 3150 × 2900 mm was built. The hutch is air-conditioned to keep the inside temperature down to 4 degrees Celsius. The space is still not large enough, so we made the second floor into a wide deck which includes area for BL6A.

4. ACTIVITIES OF GROUP 2

Analysis of protein crystallography data for three dimensional structure determination involves calculations based on ten thousand to several million pieces of diffraction data. A computer and appropriate software are therefore essential for this analysis. Many computers will be installed in 1996. The power supply line of the computer room at the Univ. of Tsukuba was increased by 100A and an air conditioner was installed. A provisional computer system was acquitted prior to setting up the main computer system. The members of TARA could also access these computers by Ethernet. The computers installed so far are the Mac 9500/120, Mac 7100/80AV, S-4/5 model 110, Alpha Station 600 5/266, and Power Indigo2 (High IMPACT). Installed software is WEIS, CCP4, PROTEIN, XTALVIEW, XPLOR, and AUTOMR. Software to be installed in the near future are DENZO, O, TURBO-FRODO, MOLSCRIPT, QUANTA, CHARM, Insight II, and Xsight.

5. SUPPORT TO THE ACTIVITIES OF GROUP 3-9

These groups cannot carry out structure analysis as members of TARA until the experimental station for TARA is built. However, many project members, who are also PF users, have been carrying out researches using BL6A and BL18B and have obtained successful results. There is an intimate relationship between TARA and PF and so, to make the experiments using PF easy for TARA members, we supported them with Polaroid film, magnetic tape, and travel expenses. Furthermore, the beamline assistant system was established to reduce the work of the PF staff since they

are busy constructing the experimental station for TARA. This system also helped members to obtain successful results. The part-time assistants are recruited from postgraduate students associated with our members. They first study the beam line design and later support the experiments of the co-users. This system has received favorable reviews and we are assuming that it will continue after the construction of the TARA Experimental Station has been completed. In addition to what is listed above, a DNA sequential analyzer was purchased to support the studies of members who specify biochemistry as their research area.

6. SCIENTIFIC OUTPUT

Dr. S. Iwata, Dr. H. Michel, and their coworkers sent a report to Nature about the molecular structure and function of a respiratory chain enzyme. The investigation was done by analyzing the structure of a citchrome-C oxidized enzyme (Fig. 1), and they reported this as members of TARA. Similar research was carried out by Prof. Tomitake Tsukihara (Protein Research Institute, Osaka University) who is a guest researcher of this project, and his group. Both projects received frequent press coverage. Under the support of TARA, Tsukuba University succeeded in crystallizing a certain protein for the first time. Moreover, many crystals have been improved in quality during the research.

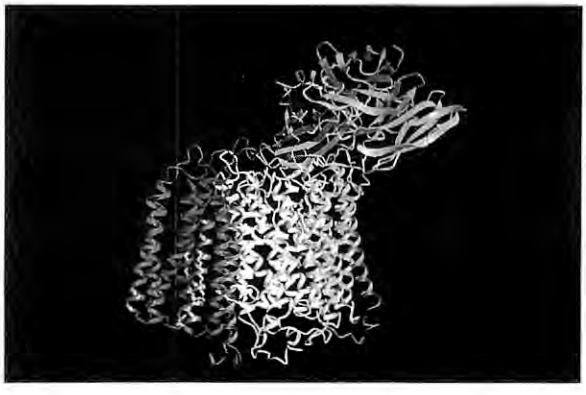

Fig. 1 Complete figure of citchrome-C oxidized enzyme single antibody FV fragment complex seen from the direction parallel to the membrane (offered by Dr. S. Iwata).

References

1) N. Sakabe, A focusing Weissenberg camera with multi-layer-line screen for macromolecular crystallography. J. Appl. Crystallogr. 16, 542-547, (1983).
2) N. Sakabe, X-ray diffraction data collection system for modern protein crystallography with Weissenberg camera and an imaging plate using synchrotron radiation. Nucl. Instrum. and Methods A 303, 448-463, (1991).
3) N. Sakabe, S. Ikemizu, K. Sakabe, T. Higashi, A. Nakagawa, N. Watanabe, S. Adati and K. Sasaki, Rev. Sci. Instrum. 66 (2), 1276-1281, (1995).

B. SYNCHROTRON RADIATION LABORATORY, INSTITUTE FOR SOLID STATE PHYSICS, UNIVERSITY OF TOKYO

The Synchrotron Radiation Laboratory of the Institute for Solid State Physics, University of Tokyo, has constructed the Revolver undulator and three beamlines, BL18A, BL19A and BL19B, in the Photon Factory and opened them to general users in collaboration with the Photon Factory. In the following we describe a brief introduction of these beamlines and report a few of the recent scientific activities which were performed during fiscal 1995.

1. BL18A

This beamline has been constructed to be dedicated to photoemission experiments investigating the electronic structures of solids, solid surfaces and adsorbates. Since the beamline was opened to users in 1991, many active users have used it to investigate the electronic structures of various materials. The beamline is equipped with a grazing incidence monochromator which covers an output photon energy from 15 to 150 eV and an angle-resolved photoelectron (ARPES) spectrometer (VG-ADES 500). An energy resolution of 50 meV is achieved at the Fermi edge of Au at a photon energy of 15 eV at room temperature, and the angle resolution was found to be 0.5°. With the sample holder, which could be cooled down to 30K, an energy resolution of 65 meV is achieved at an excitation energy around 120 eV. Recent works performed in this beamline are ARPES experiments of metal and

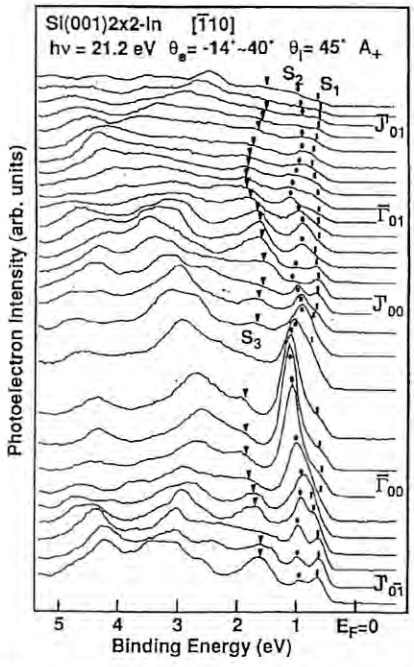

Fig. 2 ARPES spectra for a single-domain Si(001)2×2-In surface taken along [110].

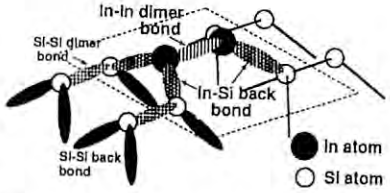

Fig. 3 Schematic illustration for structure model of Si(001) 2×2-In.

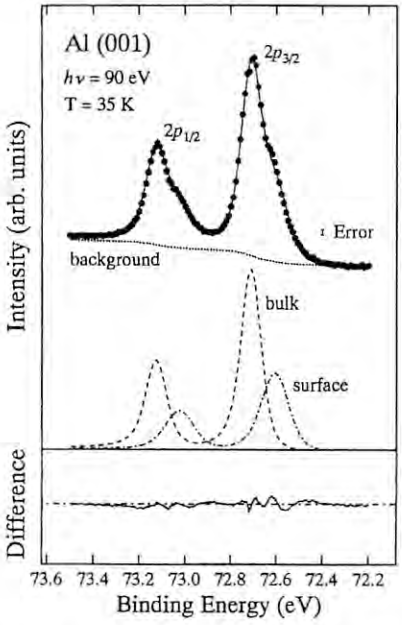

Fig. 4 High resolution Al 2*p* core level spectrum.

semiconductor surfaces, metal overlayers on Si single crystal surfaces, and high-resolution photoemission experiments of simple metals.

Figure 2 shows the ARPES spectra of Si(001) 2 × 2-In surface [1]. Three of five surface state bands, denoted S1, S2 and S3, are resolved within the bulk band gap between 0.6 and 2.2 eV in binding energy. The dispersions of these surface states enables us to determine the atomic structure of Si(001) 2 × 2-In which is illustrated in Fig. 3.

Figure 4 shows Al 2*p* core level spectrum with an energy resolution of 112meV [2]. From the line shape analysis, a singularity index 0.058 was obtained, which is a considerably smaller value than those reported previously. This implies that the screening of the Al 2*p* core hole is not only due to Al 3*s* electrons, and that the theoretical calculation including the structure of the core hole potential and the phase shifts with large angular momenta of scattered electrons is needed to evaluate the singularity indices.

2. BL19A AND 19B

The beamline is specially designed to accept radiation from the Revolver undulator and is divided into two branch beamlines, BL19A and BL19B, by means of a reflecting mirror system. They have been constructed to be dedicated to the solid state spectroscopies which need a high intensity of light from the undulator. BL19A is equipped with a grazing incidence monochromator and covers the output photon energy of from 20 to 250 eV. It is dedicated to spin- and angle-resolved photoemission (SARPES) experiments with a 100 keV Mott detector for electron spin analysis. BL19B has a plane grating monochromator with varied-space plane gratings (VSPG), which cover the photon energy range from 10 to 1000 eV [3]. BL19B was originally considered to be dedicated to the photoelectron spectroscopic studies of solids at various temperatures. It is equipped with a hemispherical electron energy analyzer with a spin-polarized low energy electron diffraction (SPLEED) detector for electron spin analysis and experimental apparatuses for soft X-ray emission spectroscopy.

Figure 5 shows SARPES spectra of the Ni 3*p* core-level measured at an excitation energy of 175 eV [4]. The difference spectrum between the spin up and down spectra (open circles) and the calculated spin polarization spectrum (broken curve) which are shown

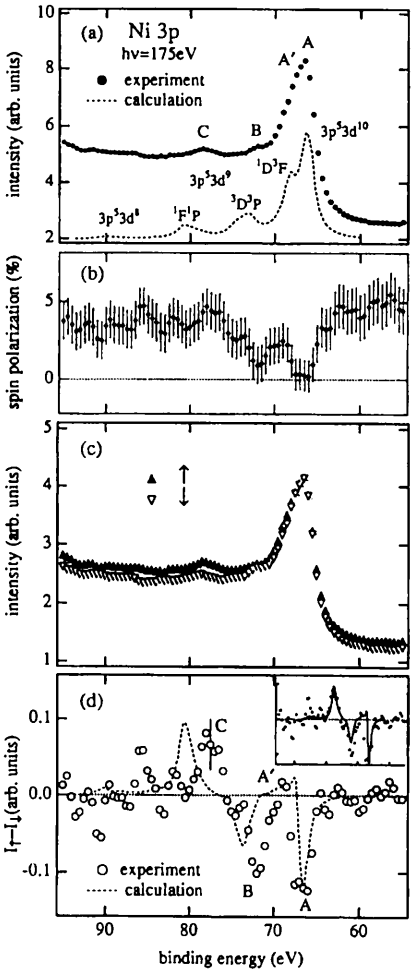

Fig. 5 SARPES spectra of Ni 3*p* core-level measured by means of SPLEED.

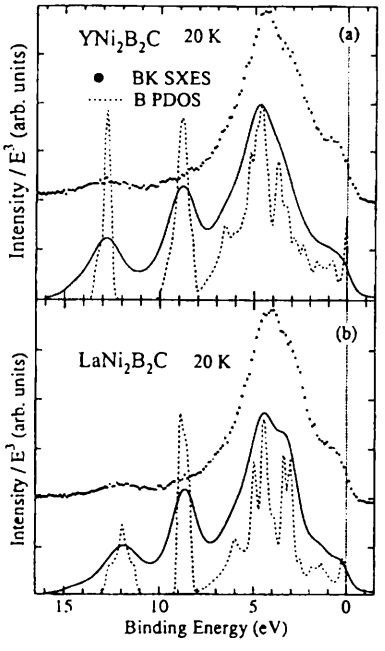

Fig. 6 B *K* SXES spectra of YNi_2B_2C (a) and $LaNi_2B_2C$ (b) compared with calculated B 2*p* density of states.

in Fig. 5 (d) qualitatively agree with each other but the 3*p*-3*d* interaction in the calculation [5] was found to have been overestimated. The inset shows the comparison where the energy scale of the calculated spectrum is reduced by 20 %.

In fiscal 1995, soft X-ray emission spectroscopy (SXES) experiments were successfully achieved at BL-19B [6]. Figure 6 shows the B *K* SXES spectra of YNi_2B_2C and $LaNi_2B_2C$. The spectra are reproduced well by the calculated B 2*p* partial density of states, which reveals that the SXES spectra provide important information concerning the initial state of photoexcitation, whereas PES spectra correspond to the photoexcited final states.

A.Kakizaki, Institute for Solid State Physics, University of Tokyo

References

1) H. W. Yeom et al. : Phys. Rev. B **53**, 1948 (1996).
2) M. Watanabe et al. : J. Phys. Soc. Jpn. **65**, 1730 (1996).
3) M. Fujisawa et al. : Rev. Sci. Instrum. **66**, 1584 (1995).
4) Y. Saitoh et al. : Phys. Rev. **B52**, R11549 (1995).
5) G. van der Laan et al. : Phys. Rev. **B46**, 9336 (1992).
6) S. Shin et al. : Phys. Rev. **B52**, 15082 (1995).

C. OTHER MINISTRIES

Using the multipole wiggler/undulator beamline BL13, a variety of advanced materials have been studied as collaborative projects between four national institutes in Tsukuba and the Photon Factory. Participating institutes are: *National Institute of Research for Inorganic Materials (NIRIM)*, Science and Technology Agency (STA), *National Institute of Materials and Chemical Research (NIMCR)*, Agency of Industrial Science and Technology (AIST)/Ministry of International Trade and Industry (MITI)), *Electrotechnical Laboratory (ETL)*, AIST/MITI and *National Research Laboratory of Metrology (NRLM)*, AIST/MITI. The multipole wiggler beamline has been designed and built by the four national institutes (NIRIM, NIMCR, ETL, NRLM) and *The Institute of Physical and Chemical Research (RIKEN)* of STA.

The 27-pole wiggler/undulator provides an intense

photon beam covering the hard X-ray (4-29 keV) and the soft X-ray (200-2,000 eV) regions. Efforts have been made to characterize a number of advanced materials, in particular in situ structural studies, using various techniques ranging from photoemission to X-ray scattering since the beamline came into operation. Independent tuning of the insertion device allowed tuning to a particular species of atom in an undulator mode by varying the deflection parameter (K-value). Hard X-ray branches (BL13A, BL13B) and a soft X-ray branch (BL13C) are in operation.

At BL13A studies on the precise measurement of lattice constant have been conducted by NRLM. A part of the wiggler radiation is diffracted in a horizontal plane by an asymmetric (422) diffraction of silicon for BL13A. Two asymmetric crystals are arranged in a double crystal parallel setting with fixed exit geometry. X-rays with energy up to 60 keV are available. A monolithic monochromator with successive (331-331) diffraction provides an X-ray with a 57 pm wavelength. The short wavelength X-ray is conveniently used for Laue case diffraction where the refraction effect is reduced, improving the accuracy in the Bragg angle measurement to an angular resolution of 0.07". Outer l mrad in horizontal divergene of X-ray radiation is stably introduced to BL13A without disturbing down-stream experiments. A precision goniometer with an angular setting accuracy of 0.1" for full circle rotation is installed. Preparation of lattice paramenter measurement is under way. The absolute lattice parameter measured at NRLM will be used to calibrate X-ray wavelength.

Efficiency in fluorescence excitation and detection at BL13B has been greatly improved by combinding the use of wiggler and dense-packed solid-state detector arrays, thereby allowing us to probe the *dynamic* aspects of electron states of solids. The advantage of X-ray absorption fine structure (XAFS) is that the local atomic arrangements for dilute atoms (10^{19}/cm^3 or 10^{14}/cm^2) can be probed with a time scale of 10^{-16} sec. These features make this technique attractive for various dynamic processes such as local lattice anomaly in high T_C superconductors. At BL13B1, a compact Huber goniometer equipped with a closed cycle helium refrigerator and a 19-element pure germanium detector are in operation for polarized fluorescence-detected XAFS. Figure 7 shows the experimental setup arrangement for the goniometer. A collaborative research team of ETL and the University of Rome have

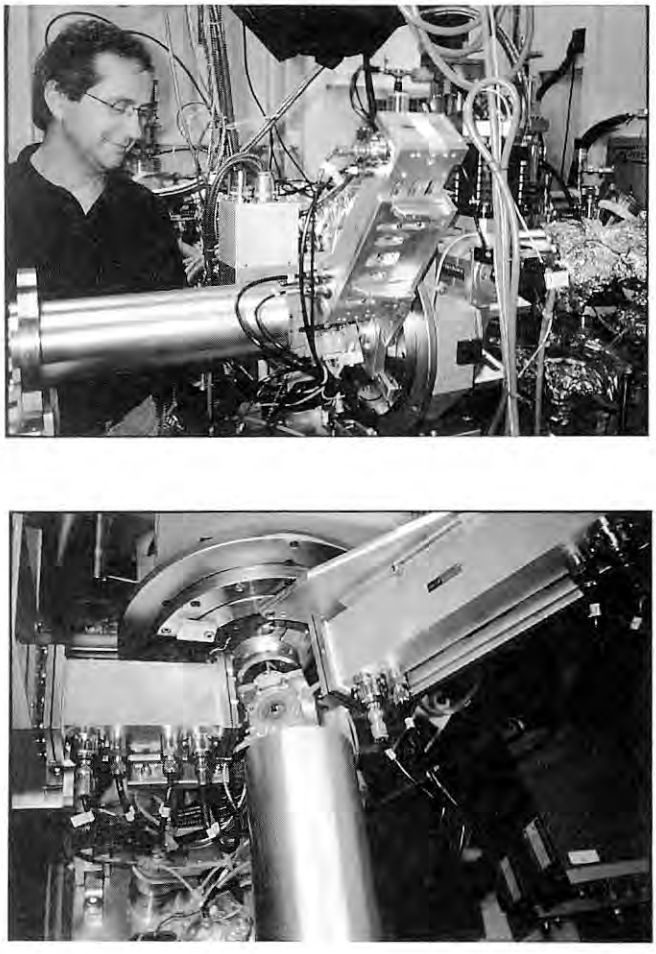

Fig. 7 Layout of the apparatus for surface-sensitive X-ray absorption fine structure (XAFS) experiments. The intense monochromatized X-ray beam from the 27-pole wiggler at the Photon Factory irradiates a sample mounted on a helium closed cycle refrigerator installed within a Huber 420 goniometer. The 19-element solid state detector array records the fluorescence yield as a function of the energy of the incident beam.

performed a series of studies on the temperature dependence of the local structures for $Bi_2Sr_2CaCu_2O_{8+y}$ (Bi2212), $YBa_2Cu_3O_7$ and $La_{1.85}Sr_{0.15}CuO_4$.

In Bi2212, two distinct regions with different conformations characterized by two Cu-O (apical) bond lengths separated by 0.17 A were found below 1.4 T_C~120 K. Together with the modulation period obtained by electron diffraction, this indicates that stripes of distorted lattice with polaronic nature are formed. In $YBa_2Cu_3O_{7-\delta}$, it was found that the local lattice anomalies occur not only at T_C but also well above T_C. Figure 8 shows the temperature dependences

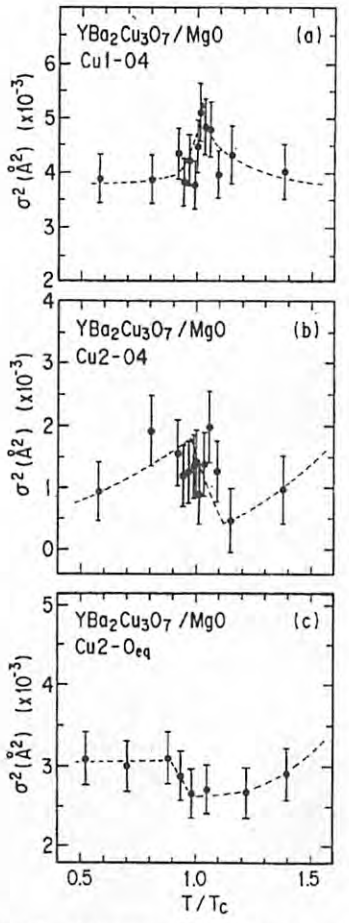

Fig. 8 Normalized temperature dependences of the mean square relative displacement σ^2 in $YBa_2Cu_3O_7$-δ for (a) Cu1-O4, (b) Cu2-O4 and (c) Cu2-Oeq bonds. Dashed lines are for eye-guide.

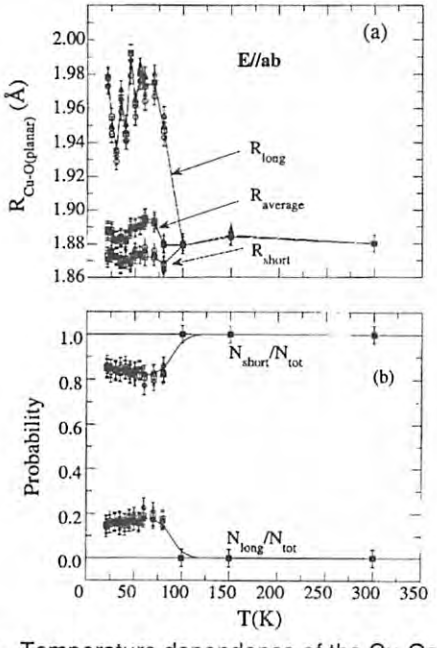

Fig. 9 Temperature dependence of the Cu-Oeq distance (a) and their relative probability (b) for La1.85Sr0.15CuO4.

of the mean square relative displacements σ^2 for three types of Cu-O bonds: Cu1-O4, Cu2-O4, Cu2-Oeq. The mean-square relative displacements for the two out-of-plane Cu-O bonds (Cu1-O4, Cu2-O4) simultaneously increased at T_C while the in-plane Cu-O bonds showed an anomalous decrease below 120 K ~ 1.5 T_C followed by a sharp increase at T_C, consistent with other lattice anomalies or dynamic spin susceptibilities observed at ~1.5 T_C. In $La_{1.85}Sr_{0.15}CuO_4$, two conformations with different CuO_6 octahedra were confirmed below 120 K. In Fig. 9, temperature dependence of the Cu-Oeq distance (a) and their relative probability (b) is indicated. The results show that a single Cu-Oeq distance consistent with crystallographic data appears above 100 K. These results demonstrate that the local lattice anomalies occur well above T_C, which implies the active role of lattice instabilities in the mechanism of high T_C superconductivity.

At BL13C, several experiments were conducted based on accepted proposals: the analysis of unoccupied states using X-ray absorption spectroscopy (XAS) and valence states by X-ray photoemission spectroscopy (XPS). In both experiments, a high flux and high resolution photon beam from the undulator was essential to elucidate the surface properties of functional materials. NIMCR developed a non-destructive XPS depth profiling method taking advantage of the energy tunability of variable-gap undulator. Figure 10 shows a typical result on the depth profiling analysis for zeolite particles. Al/Si atomic ratios with different probe depths were obtained by measuring the Al 2*p* and Si 2*p* photoelectron peaks at various excitation energies. The profile obtained was then simulated on the model shown in the inset. The results demonstrated that the Al/Si ratio near the surface is obtained with sub-nanometer resolution. Researchers from universities collaborated with NIMCR in studies of the surface

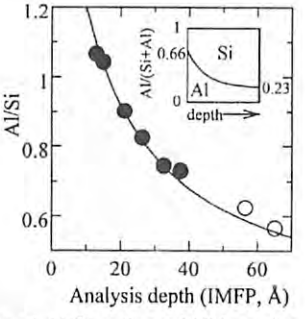

Fig. 10 Plots of Al/Si ratios of HY zeolite with different probing depths.

oxidation behavior of metal nitride films using the N K-edge XAS and the CaO/CaF_2 surfaces using the photodiffraction technique. In the single bunch operation mode, local photochemical decomposition of organic polymers was investigated.

H. Oyanagi, Electrotechnical Laboratory

D. INDUSTRY BEAMLINES

BL-1A is an NTT (Nippon Telegraph & Telephone Co.) beamline for semiconductor surface and interface analysis. Its optics consist of a grating/crystal monochromator (GCM) and a set of off-axis paraboloidal mirrors, which are located upstream and downstream of the GCM for collimating and focusing beams. During the shutdown of this year the Pt-coated off-axis paraboloidal mirrors, used since BL-1A was constructed in 1983, were replaced with Ni-coated ones. The aim of replacing the mirrors was to remove absorption structures at the Pt M-edges from the transmission function of BL-1A in the soft X-ray region for X-ray absorption fine structure(XAFS) and X-ray standing wave(XSW) measurements. Transmission functions with higher output in the region of 2000-3000 eV were obtained using the Ni-coated mirrors, because Ni has no absorption edges in this region. The transmission functions of BL-1A before and after the mirror replacement are reported in this volume.

At BL-1A, photoelectron, XSW and XAFS measurements on mainly GaAs surfaces were performed using VUV and soft X-rays monochromatized by the GCM. Surface chemical bonding during InAs nanocrystal formation on a Se-terminated GaAs and differences in surface chemical bonding structures between As-rich and Se-terminated GaAs were studied by photoelectron spectroscopy employing a VUV beam (100 eV). A new electron analyzer (SES200) installed in the *in situ* photoelectron spectroscopy system was utilized for these photoelectron experiments. Si-adsorbed and Sb-terminated GaAs(001) surface structures were determined by back-reflection XSW analysis using soft X-rays. The core-level photoelectron collection mode of the back- reflection soft X-ray standing-wave technique was used to investigate the latter surface structure. Si K-edge XAFS experiments were performed for the first time at BL-1A since the transmission function in the soft X-ray region was improved by replacing the mirrors. X-ray absorption near the edge structure (XANES) of organic silicon compounds at Si K-edge were measured to examine the correlation between XANES and X-ray emission spectra in order to clarify their electronic structures. These experimental results are reported in this volume.

BL-9, which is an NEC beamline, consists of three branch beamlines, BL-9A, 9B and 9C. At BL-9A, basic experiments on X-ray lithography have been carried out since 1986. Various experiments have been conducted such as optical/X-ray hybrid lithography for sub-half micrometer devices, resist-hardening by X-ray irradiation, and study of the mechanisms of high aspect ratio resist pattern collapse. However, in order to proceed to the next development stage, NEC decided to shift its major activity to out of the PF. BL-9A was returned to the PF, as a public beamline.

At BL-9B, photon energy dependence of the SR irradiation effect on Al-thermal-CVD was examined. A clear difference was observed between valence and core electron excitations. The core electron excitation was found to be effective in suppressing the CVD reaction, while the valence electron excitation was effective in initiating the reaction. The mechanism of this drastic energy dependence was cleared by the AES chemical shift analysis of surface layer, which was formed by SR photochemical reaction.

At BL-9C, which is an X-ray diffraction- and XAFS-beamline, several kinds of experiments were carried out as follows. Si surface imperfection was investigated using extremely asymmetric (311) reflection, in which the glancing angle of the incident X-rays was near the critical angle of total reflection. (published in Jpn. J. Appl. Phys. **32** (1993) L1581.) Thin films of tantalum oxide, one of the promising high-ε materials for device applications, were studied by XAFS measurements to clarify the relation between electronic properties and structure. It was found that the electronic properties were strongly dependent on oxygen deficiency but not on crystal structure (long range order), which was believed to be important. These results were published in Appl. Phys. Lett. **66** (1995) 2209. Another experiment of an energy-dispersive grazing incidence in-plane diffraction with white X-rays was carried out to study very thin poly-Si films.

At BL-17, which is a Fujitsu beamline, two

techniques of X-ray reflection and diffraction on the grazing incidence condition have been developed for investigation of thin films.

In a field of X-ray reflection, there are two improvements for precise measurements and analysis. The former is the method and instrument for precise parallel alignment between the incident X-ray and sample surface. The latter is the method for extracting the interference oscillation components. The typical accuracy of film thickness, density and roughness are 0.01 nm, 0.01 g/cm^3, and 0.02 nm, respectively. We can characterize very thin films up to ~1 nm with synchrotron radiation and these techniques, and report the results of thin oxide films of SiO_2 for LSI fabrication.

We have studied very thin SiO_2 gate oxide 7-4 nm in thickness and discovered the high density interface layer. The interface layer has always formed after thermal oxidation with wet, wet O_2, dry O_2, and dry O_3. Their densities were similar to each other, about 2.4 g/cm^3. But, thickness depended on the oxidation methods and growth temperature. They decrease in order of dry O_2, dry O_3, wet O_2 and they all decrease as temperature increases. This was published in JPN. J. Appl. Phys. vol35(1996) L67. Furthermore, we could precisely characterize the native oxides after chemical etching of Si wafers, too. Their thicknesses and densities depended on the etchants. (Published in JPN. J. Appl. Phys. vol34(1995) L1013.) The relation between these results and MOS-FET device characteristics has also been obtained.

The crystalline structure of titanium silicide films has been studied by grazing incidence X-ray diffraction. We can sensitively study the X-ray diffraction of thin films and orientation or epitaxial relation between a film and a substrate. There are two phases of titanium silicide, C49-$TiSi_2$ and C54-$TiSi_2$. The C49 phase is stable at low temperature and has high resistivity, and the C54 phase is stable at high temperature and has low resistivity. We have found epitaxial grain growth of the C49 phase to Si(001) substrate after low temperature annealing of deposited Ti films. Furthermore, it was obvious that these epitaxial grains were thermally stable and their phase transition rate to the C54 phase was small. These results were published in JPN. J. Appl. Phys. vol 34 (1995) L876, vol 35 (1996) 242.

S. Maeyama (NTT), H. Kimura (NEC) and S. Komiya (Fujitsu)

E THE AUSTRALIAN NATIONAL BEAMLINE FACILITY

1. INTRODUCTION

The Australian National Beamline Facility (ANBF) at BL-20B consists of a hard X-ray beamline capable of delivering white and monochromatic X-rays (4-21 keV), and a multipurpose experimental station equipped with a wide range of instrumentation for experiments in the fields of diffraction, spectroscopy and optics.

The main beamline instrument is a multi-configuration two-circle diffractometer and imaging plate camera optimised for high-resolution powder and triple-axis diffraction,[1,2] grazing-incidence surface diffraction[3] and small-angle scattering. A second experimental station located downstream from the diffractometer is equipped for transmission and fluorescence X-ray spectroscopy (XAFS). Detectors available for XAFS experiments include ion chambers (3) and a Lytle fluorescence detector. Available sample geometries include normal transmission configuration and normal- and grazing-incidence fluorescence configurations. The second experimental station may also be used as a general-purpose workspace for X-ray optics experiments.

2. NEW TECHNIQUES AND EQUIPMENT

2.1 Energy- and Temperature-Resolved Powder Diffraction

The potential of the main beamline instrument was further realised during 1995 with the running of the first energy and temperature-resolved powder diffraction experiments. In this configuration, a large circular Weissenberg screen is mounted inside the diffractometer leaving a gap of just 5 mm through which the powder diffraction pattern of the sample is recorded on the imaging plates. By horizontally translating the cassette in which the IPs are mounted behind the slit, 30 or more separate complete powder diffraction patterns can be collected on a single set of IPs as experimental conditions are varied. Figure 11 shows a schematic representation of the Weissenberg screen experimental configuration of the diffractometer. This mode of operation has been particularly useful in the study of phase transitions when the sample

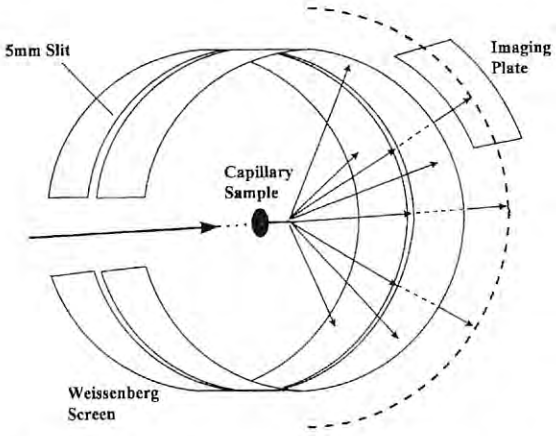

Fig. 11 Schematic representation of the Weissenberg slit configuration of the diffractometer at the ANBF

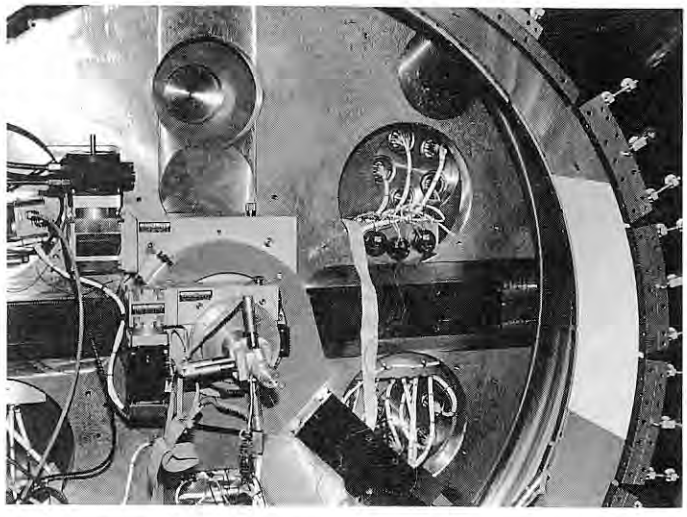

Fig. 12 Photograph of the inside of the ANBF diffractometer in single-IP GIXD mode. The X-ray beam enters horizontally from the left. The sample stage mounted on a motorised goniometer head is in the lower left and the IP mounted in the translating cassette is on the far right.

temperature is cycled, most recently in anomalous dispersion studies. In such studies, multiple diffraction patterns are collected as the incident beam energy is incremented through an absorption edge of one element in the sample. In this way, the effective scattering power of the absorbing atoms may be modified. This technique is useful for providing information on site occupancies of a particular component of a unit cell.

2.2 Grazing Incidence X-ray Diffraction and the IP Camera

Another technique which has been newly applied at the ANBF during 1995 is that of grazing-incidence X-ray diffraction (GIXD) from monolayers and multilayers on solid substrates. For the first time anywhere in the world, imaging plate detectors have been applied successfully to experiments of this type with excellent results[3]. For these experiments, the Phase II sagittally-focussing monochromator was employed, and the resulting increased flux, the sensitivity of the IPs and the ability to operate the diffractometer in a vacuum have all contributed to produce a leading instrument in the world for this type of measurement. Figure 12 is a photograph of the inside of the diffractometer in IP-GIXD mode showing the sample stage mounted on a motorised goniometer head at the centre of the instrument and a single IP mounted in the cassette to record diffraction due to periodic structure in the plane of the wafer/thin film sample.

The capability of the diffractometer for this and other experiments was further enhanced during 1995 by the design and implementation of a multiple imaging plate camera which mounts inside the diffractometer chamber and allows up to 13 IPs to be stored and exposed in succession, avoiding the need to break the instrument vacuum. This facility has proved to be invaluable for time-resolved GIXD experiments. In particular, the IP camera has been used to study temperature-induced phase transitions in Langmuir-Blodgett (LB) multilayers. Figure 13 shows a series of GIXD diffraction patterns collected using the IP camera as the temperature of a 31-layer cadmium arachidate LB film was increased. The change in film crystal structure that accompanies the phase transition that takes place at around 106 deg C has been clearly captured.

3. FUTURE DEVELOPMENTS

The next major addition to beamline capabilities scheduled for early 1996 is the acquisition and installation of a 10-element Ge solid state detector system. This state-of-the-art instrument will be used primarily for XAFS measurements on dilute and surface samples and single crystals though it may also find application in microbeam fluorescence experiments. The addition of this detector system along with the capacity for doing XAFS experiments at

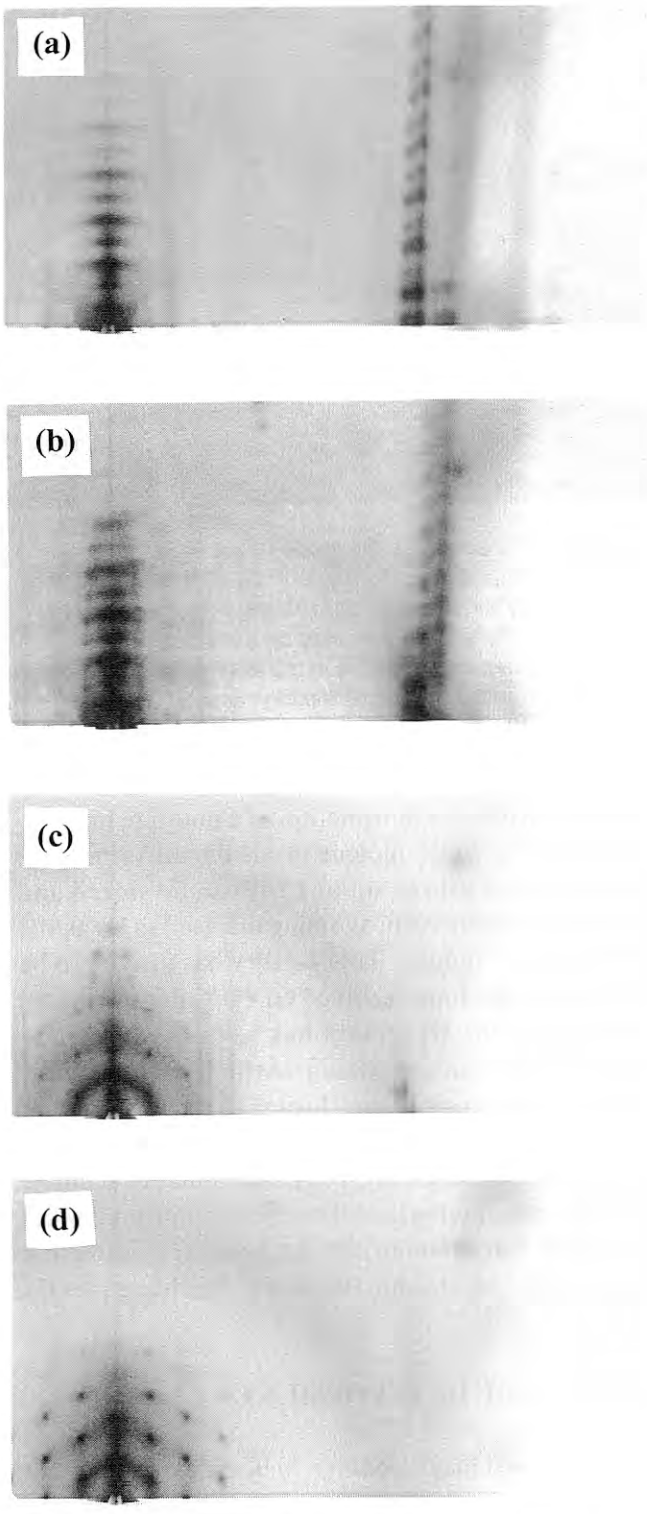

Fig. 13 A series of GIXD patterns taken from a 31-layer sample of Cd arachidate on a Si(111) wafer as the sample temperature is increased. (a) room temperature, (b) T = 105°C, (c) 110°C (d) 110°C (after 1 hour annealing). The conventional in-plane diffraction pattern shown in (a) is replaced by an hexagonal pattern characteristic of the temperature phase as the temperature is progressively increased through to 110°C and the film allowed to anneal at this temperature.

cryogenic temperatures which will follow, will bring the XAFS system at the ANBF up to world standard and provide access to the latest in XAFS instrumentation for our user community.

References

1) Garrett, R.F.; Cookson, D.J.; Foran, G.J.; Sabine, T.M.; Kennedy, B.J.; Wilkins, S.W. Rev. Sci. Instrum. **66**(2) (1995) 1351.
2) Nikulin, A. Yu.; Stevenson, A.W.; Hashizume, H.; Wilkins, S.W.; Cookson, D.J.; Foran, G.J.; Garrett, R.F. J. App. Cryst. **28** (1995) 57.
3) Foran, G. J.; Peng, J. B.; Steitz, R.; Barnes, G. T.; Gentle, I. R. Langmuir **12** (1996) 774.

Projects

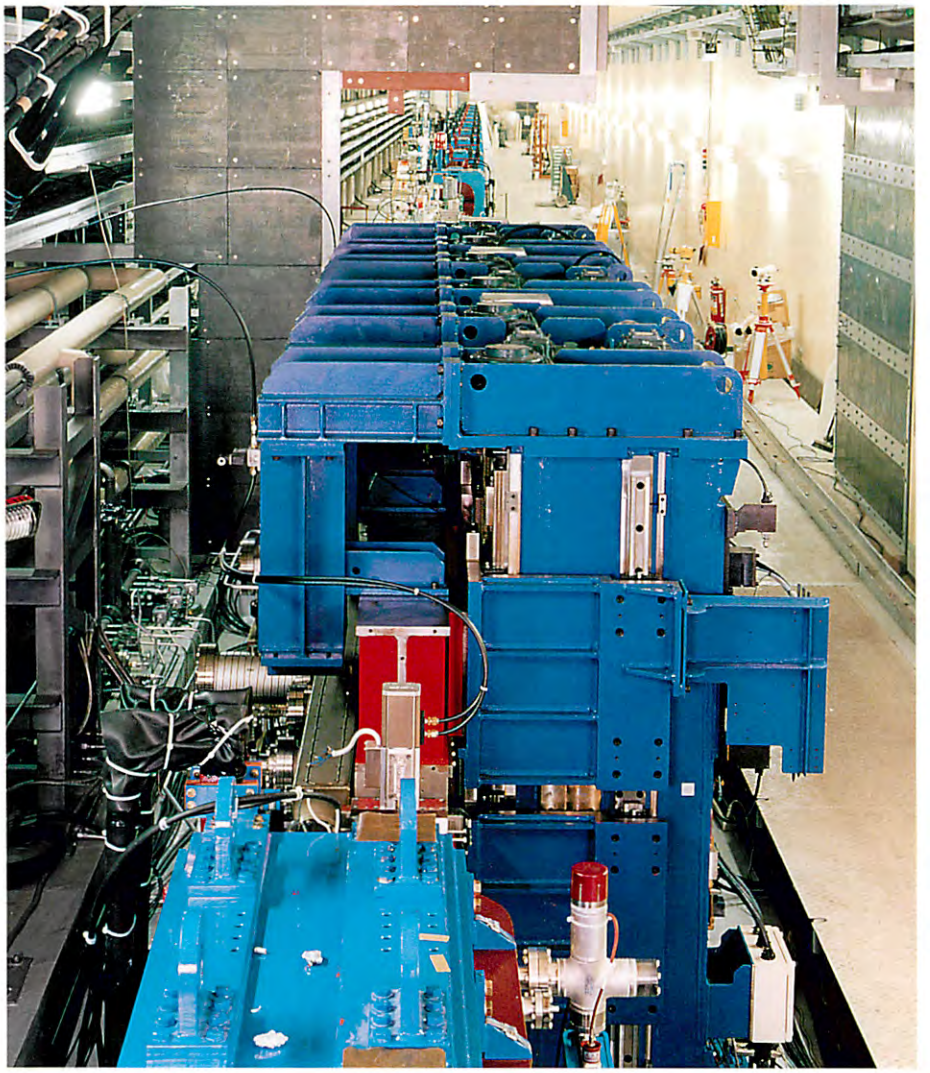

The undulator and the beamline installed at the Tristan Main Ring just before the super-brilliant SR experiments had started.

CONTENTS

A. THE TRISTAN SUPER LIGHT FACILITY

1. INTRODUCTION

During the period 1994.10.01-1995.09.30 all of the beamline components involving the use of super-brilliant synchrotron radiation from the Tristan Main Ring, including a monochromator, were designed, fabricated, and installed in the ring tunnel; even further their commissioning was started. The design and fabrication of a system for radiation safety was also completed. Prior to these activities we made a precision measurement of the coordinates of the quadrupole magnets along the 100-meter long straight section in order to observe any change incurred due to some sort of ground instability after the same measurement was made in August, 1994. It was almost sufficiently reliable to be able to align the beamline components.

Soon after completing the entire program of the Tristan High Energy Experiments and Accelerator Tests in mid June, 1995, we spent almost three months to install all of the beamline components, including the insertion device as a super-brilliant light source. However, a discrepancy in the order of microradians between the expected direction of the synchrotron radiation from the insertion device and the direction of the beamline was found when all of the components were properly aligned. This led to holding a meeting to solve this problem. We reached the most practical conclusion that the insertion device was realigned so that the optical axis available from the device would be in the same direction as that of the beamline; further, if we can not obtain synchrotron radiation in the proper direction at the machine-commissioning stage, the magnetic field of the bending magnets, which were newly made and installed upstream and downstream of the insertion device, must be adjusted so that the synchrotron radiation becomes available at the correct point of the downstream beamline.

Since the budget requirement for a new building as an experimental hall for this project has not been approved, we have tried to find an alternative space for the experiments; a semi-detached and shielded area was discovered one floor below the orbit. By that means, the first piece of the monochromator had to be located at the end of the beamline in a ring tunnel on the minus-third floor, while the second piece should be in the experimental space at the minus-fourth floor, so that the height difference between the two pieces of the monochromator is 4.5 meters. Due to such a big height difference, since a wide photon energy range covering more than 8 keV for this monochromator using the 220 and 400 series diffraction order of silicon, was required, a 2.7-meter long rail on which the second piece of the monochromator would be scanned was used.

The 9th MR Super Light Committee meeting, chaired by Seishi Kikuta, was held on November 4th, 1994, for choosing experimental subjects from among the presented proposals. Also, the 10th meeting was held on January 11th, 1995. These meetings were partly presided by Nobuhiro Shiotani when the committee evaluated a proposal presented by the chairman. The following items are the approved proposal numbers, the titles of the experiments and the persons in charge of each program.

MR95A: Production of Highly Brilliant Hard X-Ray Microbeam and Its Application; Yoshio Suzuki.

MR95B: X-Ray Excited Process of Semiconductors; Fumio Sato.

MR95C: Production of Submicron Beam Made by a Grazing Incidence Mirror; Sadao Aoki.

MR95D: High Speed Time-Resolved X-Ray Diffraction of Muscle Under Contraction Using a Single Fiber; Katsuzo Wakabayashi & Naoto Yagi.

MR95E: X-Ray Parametric Scattering Induced by Intense Laser Light; Kazumichi Namikawa.

MR95F: Precision Measurement of Emittance; Atsuo Ogata.

MR95G: Intensity Correlation of X-Ray Photons Using Nuclear Resonance Scattering; Seishi Kikuta.

MR95H: Growth Control of Atomic Scale Crystal by X-Ray Wave Field; Koichi Akimoto.

MR95I: Search by Means of Synchrotron Radiation for Neutral Undiscovered Bosons Interacting Very Weakly with Matter; Shuji Orito.

MR95J: A Study of Crystallinity in Nano-Crystalline Materials; Dudley Creagh.

MR95K: Development of Position Monitor Using a Diamond Plate; Hideo Kitamura.

MR95L: Development of Profile Monitor Using a Carbon Wire; Hideaki Shiwaku.

A workshop was held on February 16th and 17th, 1995, at KEK in order to inform the Tristan accelerator community about this activity. Speakers were those whose proposals were accepted.

On the occasion of the KEK Open House on September 10th, soon after installing the insertion device and beamline components, many people visited the ring tunnel. They have indicated their curiosity, and have asked many interesting questions concerning the structure and performance of the beamline and experiments using super-brilliant synchrotron radiation.

A part of this program has financially been supported by a grant-in-aid for scientific research provided by the Ministry of Education, Science and Culture.

Further, another Grant-in-Aid for Scientific Research was approved for the International Scientific Research Collaboration Program for the activities concerning the production and utilization of coherent X-radiation. An international conference is being planned.

M. Ando

2. ACCELERATOR

The TRISTAN MR was greatly modified during the summer shutdown of 1995 according to the accelerator plan1) for a light-source study scheduled in the autumn.

The lattice was changed so as to enable the installation of an undulator and to achieve a very low-emittance beam of up to 10GeV. A considerable number of accelerating cavities, namely all of the superconducting cavities and two-thirds of the normal conducting cavities, were removed from the MR in order to minimize the impedance of the higher order modes of the cavities, which may limit the beam current. To improve the vacuum condition in the location of the removed cavities, alkaline-cleaning was applied to the chamber surface. For the stability of the light beam, a local feedback system of the electron beam was installed into the MR. In preparing for measuring the beam emittance, a system to observe visible synchrotron light from a bending magnet was totally improved.

During preparatory operation of the MR in June, 1995, the head-tail damping rate was measured under various conditions in order to confirm the effectiveness of the highly positive chromaticity to suppress any coupled-bunch instabilities. To find the optimum working points in the tune diagram, tune-survey using the SAD code was conducted intensively, based on the estimated errors. This led to a final decision to adopt the non-interleaved sextupole arrangement for the light-source operation of the MR.

The following describes the systems newly installed, and the measurement result of head-tail damping. Also reported is the dynamic aperture measured during the early stage of the MR operation as a light-source in the autumn of 1995, together with the tracking result.

Table 1 summarizes the design parameters of the beam for the MR light-source operation.

Table 1. Design beam parameters

	Design
Beam energy (GeV)	10
Number of bunches	8
Beam current (mA)	10
Cell phase advance (hor.)	90°
(ver.)	90°
Momentum compaction	0.00073
Betatron tune (hor.)	48.20
(ver.)	41.15
Natural chromaticity (hor.)	-65
(ver.)	-57
RF voltage (MV)	90
Synchrotron tune	0.073
Damping wiggler field (T)	1.2
Radiation damping time (ms)	
(trans./long.)	30/15
Natural bunch length (mm)	5.3
Natural emittance (nm)	5.0
Orbit stability with feedback	
position (mm) (hor./ver.)	±1500/±50
angle (mrad) (hor./ver.)	±15/±5
Beam life time (min)	120

2.1 Orbit Feedback System

The requirements of the orbit stability at the source point are ±1500μm, ±50μm in the horizontal and vertical position, respectively, and ±15μrad and ±5μrad in the horizontal and vertical angle, respectively. The orbit movement (measured previously) shows that the fast movement of 3-100Hz is small enough, but that the slow movement needs to be stabilized by an orbit-feedback system.

The orbit-feedback system[2] is shown schematically in Fig. 1. The beam position and angle at

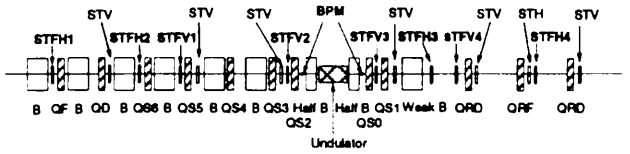

Fig. 1 Arrangement of the orbit feedback system

the center of the undulator are measured each turn using a pair of beam-position monitors (BPM). Four horizontal steering magnets (STFH) correct both the position and angle of the beam horizontally and four vertical one's (STFV) do the same vertically. The steering magnets are fabricated by laminated steel in order to obtain a fast response of the magnetic field and to reduce the hysterisis effect.

2.2 Emittance Measurement

Fig. 2 shows the experimental set up for an emittance measurement by observing visible light from a bending magnet. Visible light is extracted from a vacuum chamber by a Be mirror, defined by a horizontal slit and focused on a CCD camera by a lens having a focal length of 1000mm. A filter selects light having wavelength (λ) of 500±5nm. The intensity of light accepted by the CCD camera is adjusted by a circular linear wedge-type ND filter. All of the devices are located in the TRISTAN tunnel.

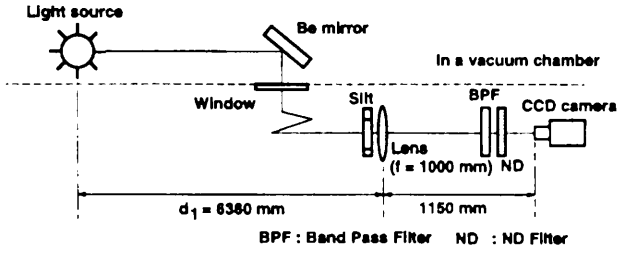

Fig. 2 Experimental setup of the emittance measurement.

The image is projected on to the horizontal and vertical axes and fitted to a Gaussian distribution with a linear background. The standard deviation of the distribution gives the beam size (σx,y(obs.)), which is expressed as

$$\sigma^2_{x,y}(obs.) = \sigma^2_{x,y} + \sigma^2_d + \sigma^2_f + \sigma^2_a + \sigma^2_\beta + \sigma^2_{CCD},$$

where sx,y is the horizontal and vertical beam size, expressed as $\sqrt{\varepsilon_{x,y}\beta_{x,y}}$, because the dispersion is negligibly small at the source point. σ_d is the broadening of the beam size by diffraction, and is determined vertically by the radiation angle of the synchrotron radiation (σ'r) and horizontally by the Fraunhofer diffraction by the slit. sf arises because the camera accepts the light emitted from a finite region (σl) along the orbit, which is unfocused on the camera. The error due to astigmatism by deformation of the Be mirror (σ_a) is estimated from the positions of horizontal and vertical focal points, which shift each other by 127mm(=Δf) when converted back to the source point. σ_β is caused by a change of the beta function ($\Delta\beta$x, y) in the region σl. σ_{ccd} is the digitizing error by the CCD camera. These errors are summarized in Table 2.

Table 2. Error sources in a beam size measurement

	Horizontal	Vertical
σ_d	0.380 λ d_1 /D	(λ /4π) / σ'r
σ_f	σs / d_1 σl	σ'r σl
σ_a	σs / d_1 Δf/2	σ'r Δf/2
σ_b	0.5($\Delta\beta/\beta$x) σ_x	0.5($\Delta\beta/\beta$y) σ_y
σ_{CCD}	17.6μm	17.6μm

$\sigma'r = 0.723/\gamma\,(\lambda / \lambda c)^{1/3}$,
$\sigma s = D/\sqrt{12}$, $\sigma l = \rho D/ d_1/\sqrt{12}$
λ_c: critical wave length, ρ: bending radius,
D: opening of the slit

2.3 Head-Tail Damping

When the current is high or the chromaticity is positive and large, head-tail damping occurs. The damping rate is proportional to the current and chromaticity. In Fig. 3, the measured damping rate of the vertical oscillation is plotted as a function of the product of the current and vertical chromaticity. The current of the data points ranges from 0.16 mA to 0.6 mA. The bunch length observed with a streak camera was almost the same for all cases, about 13 mm.

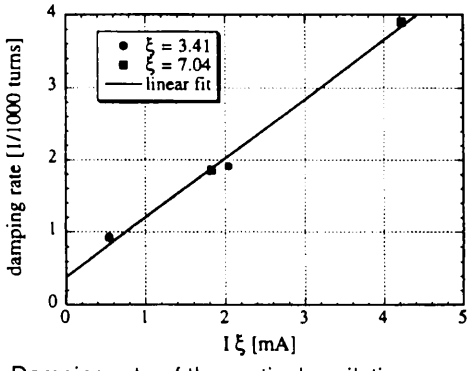

Fig. 3 Damping rate of the vertical oscilation as a function of the product of the current and chromaticity.

Based on this fact, the head-tail damping was intentionally enhanced by making the chromaticity high so as to suppress the coupled-bunch instability during the light-source operation of the TRISTAN MR.

2.4 Dynamic Aperture

The energy and transverse acceptance were measured and compared through a simulation using the computer code SAD (Fig. 4). The measurements are consistent with the simulation for the energy and horizontal acceptances. The vertical acceptance was measured to be one tenth of the simulation and can be explained by the physical aperture of the undulator vacuum chamber.

S. Kamada

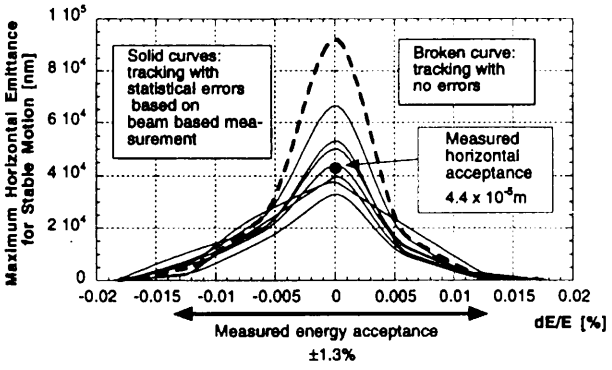

Fig.4 Comparison of the measured and the simulated dynamic aperture.

References

1) S. Kamada et al., Rev. Sci. Instrum. 66(2), 1913 (1995).
2) T. Mimashi et al., Int. Conf. on Acc. and Large Exp. Phys. Cont. Systems, Chicago, U.S.A. 1995.

3. UNDULATOR FOR THE TRISTAN SUPER LIGHT FACILITY

SR test experiments using the Tristan Main Ring had been planned[1] and were performed in the autumn of 1995. A prototype undulator[1] (named XU#MR0), which was originally fabricated for development of a construction method for the very long undulators required in the full version of the TSLF plan,[1] was used for these experiments as a super-brilliant X-ray source.

XU#MR0 comprises three precise standardized-unit undulators.[2,3] Each standardized-unit (1.8m long) is placed very precisely on a rigid common frame so as to form a 5.4-m undulator. We adopted a pure-Halbach-type configuration of NdFeB magnets (remanent field, Br=12.8kG; coercivity, iHc=17 kOe). The selection of the period (λ_u=4.5 cm) was made so that a Mössbauer energy of ^{57}Fe (=14.4 keV) could be obtained at the first harmonic under 10-GeV operation of the MR. The support structure of the XU#MR0 is shaped like the letter "C", so that it can be installed without breaking the vacuum of the MR.

Although the MR was not completely converted, compared to the full version of the TSLF plan, we aimed to obtain a natural beam emittance of 5nm·rad and an emittance coupling of 2% at the MR's operation energy of 10GeV, owing to an adequate and minimum modification of the MR lattice. The spectrum corresponding to this case is reproduced from the previous issue of this report in Fig. 5. A calculation shows that the XU#MR0 is able to produce quasi-monochromatic X rays as the first harmonic with a brilliance of 3.0×10^{18} [photons/s/mm^2/mrad^2/0.1% bandwidth] in the case of K=0.97 at 14.4 keV when the MR is operated at 10 GeV and 10 mA with the above-mentioned beam quality. By combing 8- and 10-GeV operation, a photon energy from 8.4 to 21 keV can be covered by the first harmonic, and that from 25 to 60 keV can be covered by the 3rd harmonic.

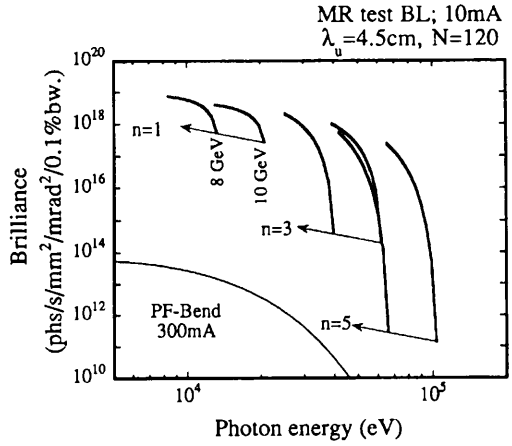

Fig.5 Brilliance of radiation from the XU#MR0 in the cases of 8- and 10-GeV operation of the MR with a beam current of 10mA. Each curve shows the locus of the peak position of the n-th harmonic when K decreases from its maximum.

In order to install the XU#MR0 into the MR for the test experiments, some modification of the common frame of the XU#MR0 was required, since the beam-

path height of the installation point (located at the arc section of the MR) available in the present conversion of the MR is shorter by 600mm than that (located at the long straight section) planned in an original TSLF. In order to resolve this problem, we reconstructed the common frame of the XU#MR0 to a slim version with a height of 100 mm (the original had a height of 500 mm), and also lowered the floor level of the installation point by making a pit 200 mm deep (Fig. 6). The effects of reassembling the whole system of the XU#MR0 using this new common frame (for a magnetic field of the XU#MR0) are negligibly small, if reconnection of each unit undulator is made carefully with the accuracy of ±10 mm.[2,3]

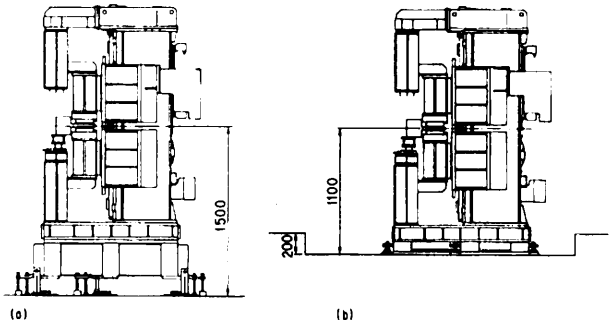

Fig.6 Installation of the XU#MR0 and the difference in the floor level in the MR tunnel: (a) installation in the long straight section, and (b) installation in the arc section.

The arrangement of the XU#MR0 and magnets adjacent to it is shown in Fig. 7. In the present case, we must place the XU#MR0 between the short bending magnets, which were newly fabricated and placed so as to create a free space for installing the XU#MR0. Figure 8 shows photographs of the XU#MR0 after the installation: (a) the view from inside of the MR, and (b) the view from upstream along the photon beam axis. For aligning the undulator and beamline system, we adopted the following procedure: (1) the undulator XU#MR0 was aligned using the nearest quadrupole magnets (between which the XU#MR0 and the short bending magnets exist (Fig. 7)) by taking the bending angle due to these bending magnets into account; (2) the beamline was independently aligned using the quadrupole magnets in the long straight section of the MR as targets, where the relationship between the beamline and the long-straight quadrupole magnets was determined on the basis of the designed value of the bending angle between the undulator axis and the long straight section. However, we found that the undulator axis was inclined by as large as 0.5 mrad in the horizontal plane with respect to the beamline axis, and that this was due to a misalignment between the arc section and the long straight section in the MR. Fortunately, in this case, since the beamline was only one in the MR, we realigned the XU#MR0 directly along the beamline in turn, and decided that the bending angle should be adjusted during the operation of the MR.

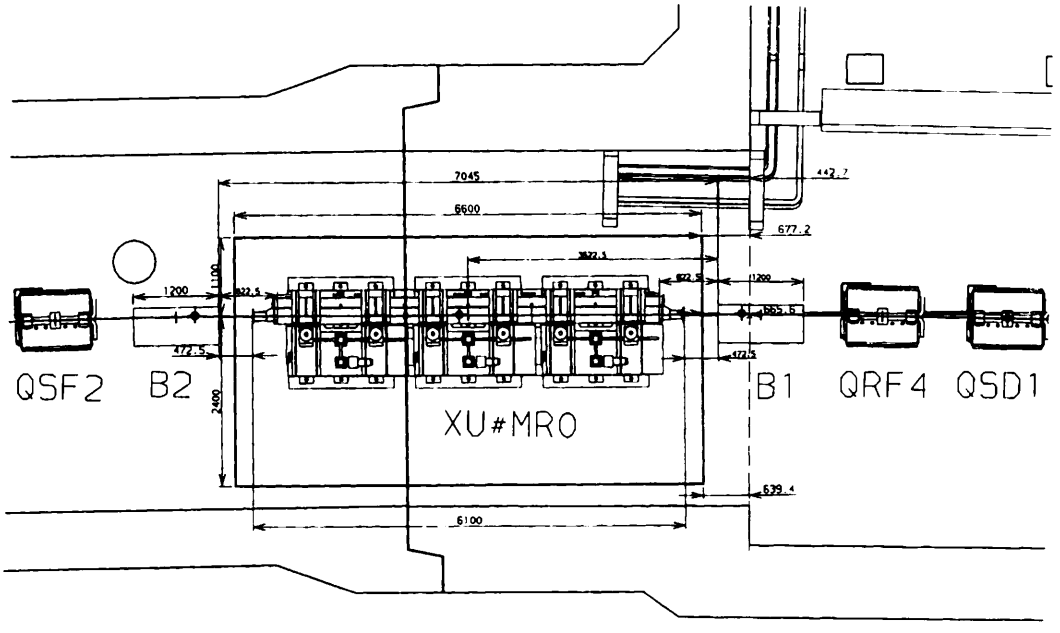

Fig.7 Arrangement of the XU#MR0 and the magnets adjacent to it.

(a)

(b)

Fig.8 Photograph of the XU#MR0 after the installation: (a) view from inside of the MR, and (b) view from upstream along the photon beam axis.

The Operation of the MR for the test experiment was started on Sept. 18, 1996, and the electron beam was stored as early as on Sept. 20. Immediately after the commissioning of the beamline, X-rays from the XU#MR0 were successfully introduced to the first crystal piece of the double-crystal monochromater of the beamline. The XU#MR0 provided X-rays very stably for commissioning of the double-crystal monochromater and for various utilizations until the end of the test experiments on Dec. 27, 1995.[4]

Table 3 Parameters of the XU#MR0.

Magnetic structure	Pure configuration
Magnetic material	NdFeB (B_r=12.8kG, iH_C=17kOe)
Period length	λ_U=4.5cm
Number of periods	120 [=3×40/unit undulator]
Magnet length	5.4m [=3×1.8m/unit undulator]
Maximum peak field	B=2.64kG
Maximum K	K=1.11
Range of magnet gap	3~50cm
Aperture	2.4cm

S. Yamamoto

References

1) The Tristan Super Light Facility; Conceptual Design Report 1992, KEK Progress Report No. 92-1 (1993).
2) S. Yamamoto et al., Rev. Scientific Instrum., **66**, 1996 (1995).
3) S. Yamamoto, PF Activity Report #12, P-5 (1994).
4) Chapter "Project", Section A-4 and A-5, this report.

4. BEAMLINE ISSUES

4.1 Installation and Commissioning of the Beamline MR-BW-TL

The beamline MR-BW-TL with a monochromator was installed in the MR tunnel and the commissioning was started.

The beamline components had been tentatively assembled at other locations to test connections and their performance concerning the vacuum, accuracy and motion. We also tried to the examine alignment of the beamline at that time. However, the monochromator was independently tested concerning its performance at another location, because it occupied 2 stories of the structure.[1] Since the beamline is about 70 m long, the tentative place was not sufficiently large. We thus assembled the beamline by bending into three parts.

We started to install the beamline into the MR tunnel in June, 1995, since TRISTAN physics experiments were executed until then. We had only 3 months to install the beamline. Since remodeling of the accelerator also had to be done during the same period, we had no reference line for the alignment around the undulator. The base lines for the alignment were drawn in July, 1994, by referring to the quadrupole magnets in the long straight section beforehand, because these magnets were intact during the remodeling of the accelerator, and were located within 2 m from the SR axis. We ascertained in August, 1993, that these magnets were aligned within ±0.8 mm accuracy.

We used special tools to locate the beamline components. The special tool comprised a frame, a water level and a plumb bob. The tool was attached to a pipe or a cylindrical part of the beamline, and made horizontal by the water level. The plumb bob and mark on the frame indicated the center of the pipe to within ±0.3 mm accuracy in the horizontal and vertical plane, respectively. We adjusted the beamline components to

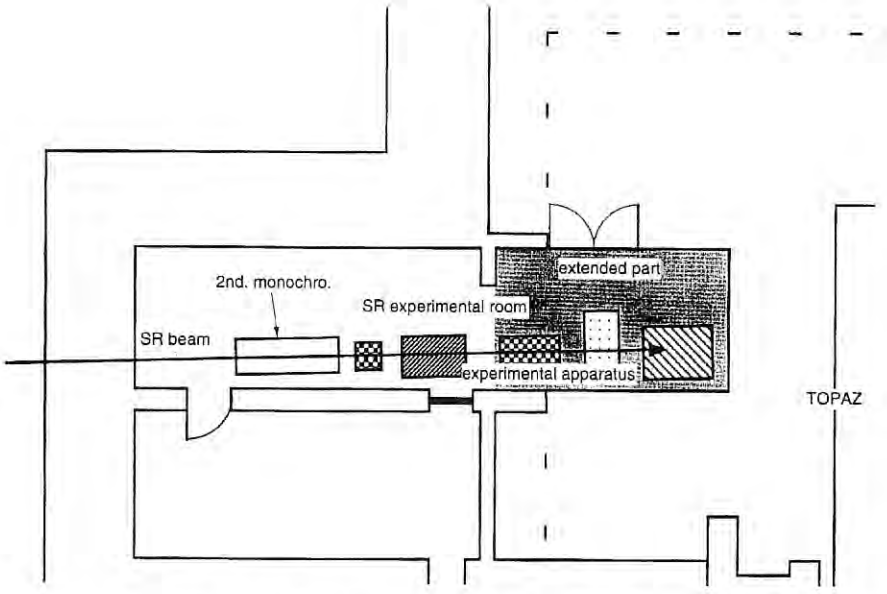

Fig.9 SR experimental room with the extended part on the -4th floor of the Tristan Tsukuba experimental hall. Several pieces of the SR experimental apparatus were set in tandem in the SR experimental room.

the base line in the horizontal direction and the center of the quadrupole magnets in the vertical direction while referring to the plumb bob and the mark on the frame, respectively.

We have confidence that the beamline components were aligned within ±2 mm accuracy throughout. In fact, the differences in the SR axes estimated by any two sets of horizontal/vertical beam-position monitors (BPMs) [2] were less than 1mm. The horizontal/vertical BPMs used were a graphite-wire type, three sets were installed at 16/17, 48/49 and 83/84 m from the source point.

The SR experimental room[1,3] was extended by 6.7 m downstream, as shown in Fig. 9. The hole for leading SR into this room was bored in January, 1995. The extended part was built of steel (7.7 mm thick) and lead (5 mm thick) plates, like the experimental hutches at the PF. Several pieces of the SR experimental apparatus can be set in tandem in this room by this extension. We can avoid replacing the apparatus by setting them in tandem, since we have only 3 months for SR experiments. The SR experimental room has the role to protect from both outgoing radiation to the outside and incoming radiation from the accelerator. This room is used like the experimental hutch at the PF. We can access this room as long as the monochromatic X-ray shutter, like the DSS at the PF, is closed, even though the SR shutter, like the MBS, is opened and the accelerator is under operation.

The vacuum of the beamline was on the order of 10^{-9} torr at the upstream part, and 10^{-5} torr at the downstream part from the Be windows. Leakage of the mechanically fixed Be window[4] was about 1×10^{-5} torr·litter/sec. This type of Be window was able to maintain a pressure on the order of 10^{-5} torr against the air pressure, and to maintain a pressure on the order of 10^{-9} torr against a pressure on the order of 10^{-5} torr.

The radiation-safety system of the beamline passed an inspection on September 28, 1995, and has worked well.

H. Sugiyama

References

1) H. Sugiyama and Y. Higashi, PF Activity Report #12, P-9 (1994).
2) H. Shiwaku, Chapter "Project", Section A-4, this report.
3) H. Sugiyama, PF Activity Report #11, S-9 (1993).
4) H. Sugiyama, PF Activity Report #12, P-8 (1994).

4.2 The Diamond Beam Position Monitor

4.2.1 Introduction

For third-generation synchrotron facilities, the photon beam-position monitor with a high position sensitivity of less than a few microns and stability under a high heat load is required. For example, the

maximum total power and density of undulator radiation of SPring-8 will reach about 11 kW and 470 kW/mrad^2, respectively. As a candidate to satisfy these requirements, a beam-position monitor using a diamond foil as a position-sensitive device, operated in a photoconductive mode, has been developed. As a collaborative effort between KEK and SPring-8, the prototype monitor will be tested on the TSLF beamline. The monitor was installed on the beamline 20 m from the insertion device, and an operation test has been made. The design of the monitor is discussed below.

4.2.2 Diamond Monitor

A schematic view of the diamond monitor is shown in Fig. 10. A synthetic polycrystalline diamond film is made through a chemical vapor deposition process (CVD), and is used as an active element.[1] There are electrodes on both sides of the diamond, and an external voltage is applied between these electrodes in order to produce an electric field in the diamond. When a photon beam irradiates the diamond, free carriers (electrons and holes) are created due to the interaction of photons with the diamond. These carriers drift along the electric field and generate a current in the external circuit.[2] The electrodes of the monitor are segmented into four parts so as to obtain information concerning the two-dimensional beam position. With the currents from each electrode, the beam centroid can be found using the following formulae :

$$X = A_x \times \frac{(I_{U\text{-}R} + I_{D\text{-}R}) - (I_{U\text{-}L} + I_{D\text{-}L})}{I_{U\text{-}R} + I_{D\text{-}R} + I_{U\text{-}L} + I_{D\text{-}L}} \quad (1)$$

$$Y = A_y \times \frac{(I_{U\text{-}R} + I_{U\text{-}L}) - (I_{D\text{-}R} + I_{D\text{-}L})}{I_{U\text{-}R} + I_{U\text{-}L} + I_{D\text{-}R} + I_{D\text{-}L}} \quad (2)$$

where IU-R, IU-L, ID-R, ID-L (U : upper, D : down, R : right, L : Left) are the currents from each electrode and Ax, Ay are calibration factors.

The superior thermophysical properties of diamonds, such as a high thermal conductivity, low thermal expansion, high mechanical stiffness and radiation hardness, make it usable in a harsh environment on the front ends of beamlines, where other semiconductor-like detectors can not be used.

Since the photoconductive current of the monitor is proportional to the radiation power absorbed in the diamond, the sensitivity to hard X rays radiated near to the axis is emphasized compared with that of a photoelectron-emission type monitor having a high sensitivity to UV and soft X rays. Therefore, the contamination with soft X rays from the bending magnets is expected to be reduced.

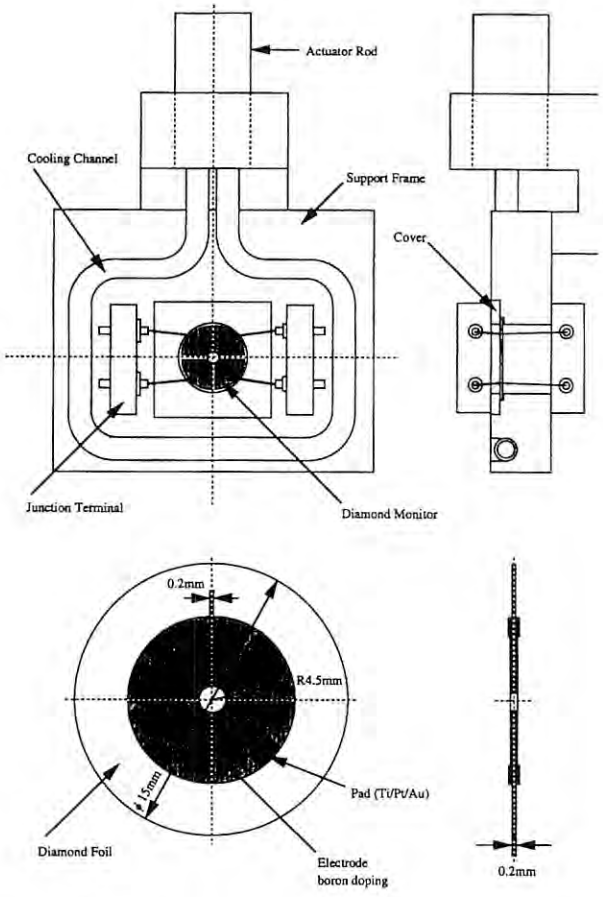

Fig.10 Schematic view of the diamond monitor.

H. Sakae and H. Aoyagi, RIKEN

References

1) The diamond foil was manufactured by Sumitomo Electric Industries.
2) Y. Sugimoto, High Energy Quarterly, 10, 59 (1993).

4.3 Wire-type beam monitor at the TSLF

The development of a wire scanning-type beam-position monitor has been studied. As a result of a previous investigation at the TRISTAN AR-NE3,[1,2] it was found that the wire scanning-type beam position monitor (BPM) is very effective for undulator X rays. Thus, wire scanning-type BPMs were installed at the TSLF, and a beam-monitoring system is being constructed.

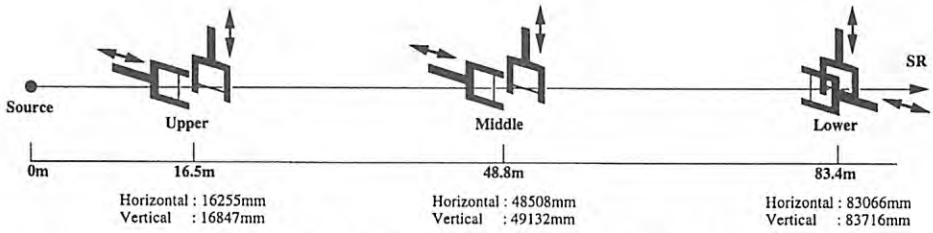

Fig.11 Layout and positions of the beam monitors.

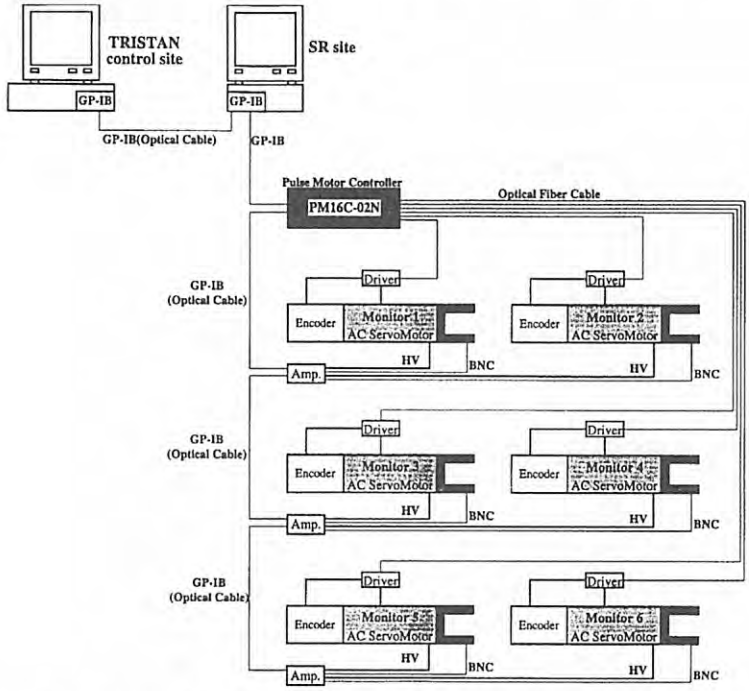

Fig.12 Schematic diagram of the control and data-acquisition system of the beam monitors.

Three pairs of beam monitors, which comprise horizontal and vertical monitors, were located in the TSLF beamline at 16.5 m for the upper position, 48.8 m for the middle position and 83.4 m for the lower position from the emission point, respectively. These positions correspond to position in front of a water-cooled mask, a center position of the beamline, and a position in front of a water-cooled X-Y slit, respectively. Figure 11 shows an outline of the positions of the beam monitors. Especially, the upper monitors are located in front of the other front-end instruments, since it is available to measure the beam position at all times, even if a beam shutter (water-cooled shutter) is closed. Furthermore, this situation allows measurements of non-transmitted X rays from the undulator, since there is no X ray shielding material (for example, carbon filters and/or beryllium windows).

Figure 12 shows a scheme of the control and data-acquisition system. Optical fiber cables including the GP-IB extender are employed for control and data taking. The main control unit is located at the -4th floor of the TSUKUBA experimental area at TRISTAN; a sub-control unit will be located at the TRISTAN control site. The principles of beam-position measurement and instrumentation of the beam monitor were described in detail elsewhere.[1,2] A carbon wire (0.3mm width), cut from a carbon sheet (0.1mm thick) was used as a monitor probe for the TSLF beamline. Two modes are available for measuring: a) the wire-scanning mode, which measures the X-ray beam profile, and b) the wire stay mode, which measures the intensity variation. The fundamental control system has already been constructed.

H. Shiwaku, JAERI

References

1) Rev. Sci. Instrum., **66**, 1990 (1995).
2) PF Activity Report #11, S-13 (1993).

5. PREPARATIONS FOR THE SR EXPERIMENTS

5.1 X-ray Microbeam with Grazing-Incidence Mirrors

X-ray microprobes have been developed for various spectroscopic and structural studies concerning matters with spatial resolution. Detectable signals are fluorescent X rays, photoelectrons, micro-X-ray diffraction, EXAFS and so on.

There are several approaches to produce an X-ray microprobe. Among the various optical elements, grazing-incidence mirrors are very convenient focusing elements, because they can be used for a wide spectral range. Due to the large optical aberrations inherent to a single grazing incidence mirror, it was difficult to produce a small X-ray spot less than one micron. In order to produce a much smaller microbeam, these aberrations must be reduced.

A Wolter type-I mirror is one of the best grazing-incidence mirrors which can reduce aberrations considerably. For a highly collimated beam a telescopic mirror system can be applied. The Wolter mirror comprises a paraboloidal mirror and a hyperboloidal mirror, which compensate each other's aberrations. For the optical system in the limited distance between the X-ray source and the mirror, an ellipsoidal mirror is used instead of a paraboloidal one. Figure 13 gives the parameters of a Wolter type-I mirror which is being developed for X rays from an undulator. The average grazing angle(θ) is about 7mrad and the mirror surface is coated with platinum. X rays of energy less than 12keV can be reflected. Since the inner diameter of the mirror is not large enough to be polished directly, it is fabricated by a vacuum-replication method. First, the master mandrel

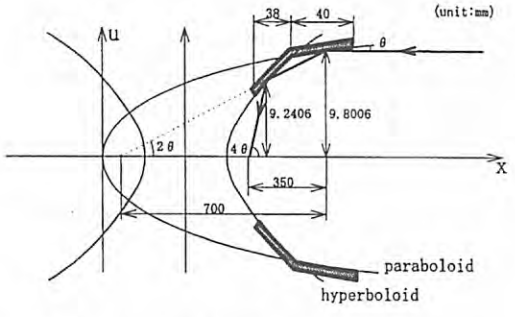

Fig.13 Parameters of a Wolter mirror.

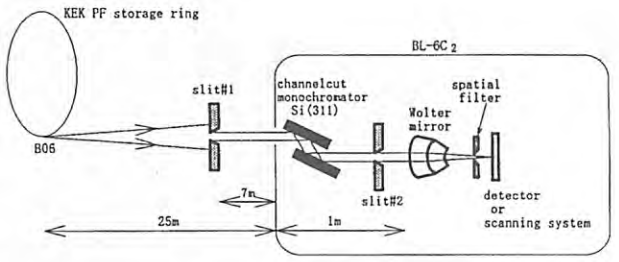

Fig.14 X-ray microbeam optics.

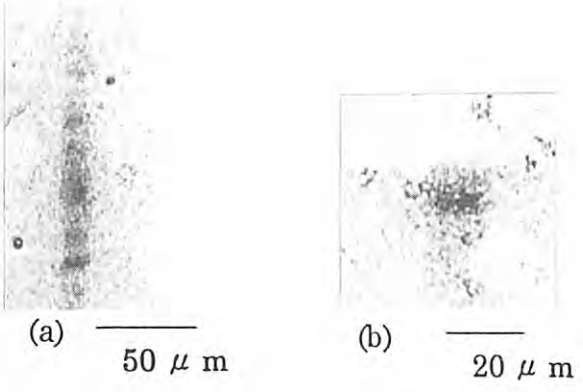

Fig.15 9keV X-ray microspots (a) and the selected one spot by the spatial filter (b).

(tungsten carbide) is polished, and its replica is made with Pyrex glass. Then, the inner surface is coated with platinum in order to enhance the reflectivity of shorter wavelengths. The total reflectivity of the mirror was calculated to be about 67% at 9keV.

The performance of the Wolter mirror was examined at BL-6C2 of the PF. A schematic diagram of the microbeam optics is shown in Fig. 14. A collimated 9keV X-ray beam, whose horizontal divergence was about 30 μrad and vertical one was about 20 μrad, was obtained by combining a Si(311) channel-cut monochromator and two slits (#1, and #2). The surface undulation of the mirror produced separate micro-spots in the focal plane (Fig. 15(a)). One microspot was selected by using a spatial filter near to focal plane (Fig. 15(b)). The size of the microbeam obtained was about 9 μm × 12 μm.

A smaller spot is expected to be obtained by using a highly collimated beam from an undulator at the MR. A high collimation better than 10 μrad will make the spot size sub-micron or so.

S. Aoki, University of Tsukuba

5.2 Hard X-ray Microprobe with Sputtered-sliced Fresnel Zone Plate

The X-ray microbeam is considered to be one of the key-technologies for a third-generation high-brilliance SR source. Achieving an X-ray microprobe with a sub-micrometer spot size is expected to add a new dimension to various X-ray analysis methods, such as scanning microscopy, micro-diffraction, absorption spectroscopy and fluorescent X-ray analysis. We are planning to carry out a hard X-ray microprobe experiment at the TRISTAN-MR test beamline. Three kinds of optical systems (total-reflection mirror optics, multilayer mirror optics and Fresnel zone-plate optics) are being developed for a microbeam experiment; a spatial resolution of about 1 μm has been achieved.[1-3] However, the alignment and tuning of the mirror optics within the limited machine time are considered to be very difficult. Therefore, we have chosen Fresnel zone-plate optics.

A sputtered-sliced FZP, fabricated by Kamijo and Tamura[2,3] at the Osaka National Institute, has been tested at BL-8C2 of the Photon Factory 2.5-GeV storage ring; a focused beam size of 0.9 μm has been achieved at an X-ray energy of 8keV. However, the FZP is not a practical device at the bending-magnet beamlines because of its low efficiency (about 4%) and small numerical aperture. The total photon flux available at the normal bending-magnet station of the PF 2.5-GeV ring is much less than 10^3 photons/s for a focused beam size of 1 μm. However, a beam intensity of higher than 10^6 cps is expected at the TSLF. The design parameters of the FZP microprobe optics for the TSLF are listed in Table 4.

The sputtered-sliced FZP is fabricated by the following method: Alternate multilayer zones are constructed by magnetron sputtering. The Ag/C concentric multilayers (50 layers) are deposited onto a Au wire substrate (47μm in diameter). The film thickness (zone width) of the first inner layer is 0.4μm, and 0.25μm for the outermost layer. The diameter of the FZP is 80μm. After deposition, the wire sample is sliced into a plate normal to the wire axis. Finally, the FZP is mechanically polished until it has appropriate thickness.

Recently, we tested new zone plates at BL-8C2. The improvements to the FZP are as follows:

1) Use of a graphite substrate; thin sliced FZP was bonded onto a 1-mm thick PMMA plate. The substrate is now being replaced by graphite plate of 1mm thick for a possible high heat load at the TRISTAN-MR beamline.
2) Testing of the phase-modulation zone plate; the previously tested FZP had a thickness of about 50μm. The thick FZP is an amplitude-modulated FZP, and the theoretical limit of the first-order diffraction is about 10%. A thin (less than 10μm) FZP is considered to be a phase-modulated FZP; thus the theoretical limit of the first-order diffraction efficiency increases up to 40%.

Table 4 Design value of the X-ray microprobe (Fresnel zone plate optics)

Optics	single stage Fresnel Zone Plate
Monochromator	Si(220) double crystal $\delta\lambda/\lambda = 5 \times 10^{-5}$
X-ray wavelength	1.54 Å
Source size (assumed)	0.3 mm × 0.05 mm
Distance between source and focal point	100 m
Divergence of radiation accepted by mirrors	0.4 μrad × 0.4 μrad (half angle)
Focal length	140 mm at 1.54Å
Diameter of FZP	80 μm
Nominal demagnification	1.3×10^{-3}
NA	3×10^{-4}
Calculated spot size (by geometrical optics)	0.42 μm × 0.07 μm
Diffraction limit	0.31 μm
Photon flux at sample point (Efficiency of 5% is assumed) (B = 2×10^{18} photons/s/mm²/mrad²/0.1%bandwidth is assumed)	about 3×10^7 photons/s

The X-ray focusing properties were evaluated by the conventional knife-edge scan at a wavelength of 1.54Å. The results of a focusing test for the newly developed FZP are shown in Fig. 16. The focused beam size, defined by the 25%-75% criterion, is about 0.9μm. The diffraction efficiency for the first-order focus is 10%, and by considering apodization by the center beam stop (47μm diameter gold), the pure diffraction efficiency is estimated to be 16%.

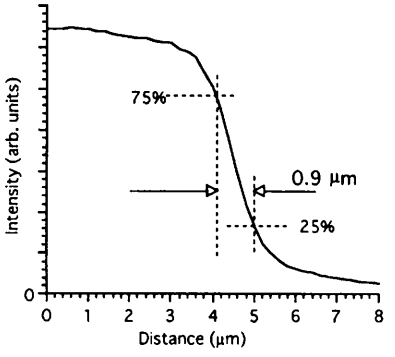

Fig.16 Focusing Test Results for the Newly Developed FZP

The undulator used at the TRISTAN-MR light source has a length of about 6m. Therefore, the tolerance on the focal depth should be carefully examined. The depth of focus (δ) can be written using the well-known formula,

$$\delta = 0.61\lambda /2/(NA)^2$$

Here, λ is the X-ray wavelength, and *NA* is the numerical aperture of the focusing lens. When the distance between the source and the FZP is *a*, and the distance between the FZP and the focal point is *b*, the focusing condition is also expressed by the well-known equation.

$$1/a + 1/b = 1/f .$$

Here, *f* is the focal length of the FZP. When the source has a depth of Δa, the difference in the focal point (Δb) can be approximately expressed by

$$\Delta b = -\Delta a\,(f/a)^2 .$$

Here, we assumed $f << a$ and $\Delta a << a$. Therefore, the tolerance on the source depth is written as

$$\Delta b < \delta .$$

When we use the optical system listed in Table 4, and the parameters a = 100 m, f = 140 mm, $NA = 3 \times 10^{-4}$, λ = 1.54Å, and Δa = 6 m, we have $\delta = 5.2 \times 10^{-4}$ (m), $\Delta b = 1.2 \times 10^{-5}$(m). Therefore, a light-source depth of 6 m is negligibly small in this optical system.

Y. Suzuki, Advanced Research Lab., Hitachi, Ltd. and N. Kamijo, Osaka National Institute

References

1) Y. Suzuki and F. Uchida, Rev. Sci. Instr., **63**, 578 (1992).
2) N. Kamijo, S. Tamura, Y. Suzuki, and H. Kihara, Rev. Sci. Instr., **66**, 2132 (1995).
3) N. Kamijo, S. Tamura, Y. Suzuki, and H. Kihara, PF Activity Report #12, 165 (1994).

5.3 Mechano-chemical X-ray Diffraction on Single Muscle Fibers

5.3.1 Design of a small-angle camera

An ideal small-angle X-ray diffraction camera for an undulator beamline would be rather complicated and expensive. Considering the limited time available to set up such a camera for the Tristan MR beam line, it is necessary to design a simple small-angle camera that can fulfill the requirements of the proposed experiments.

The design shown below is simple and sufficient for our purpose (Fig. 17). Since the specimen is a horizontally laid muscle fiber, a single X-ray mirror (Pt-coated) reflecting in the vertical direction may suffice. The horizontal beam width can be decreased using slits.

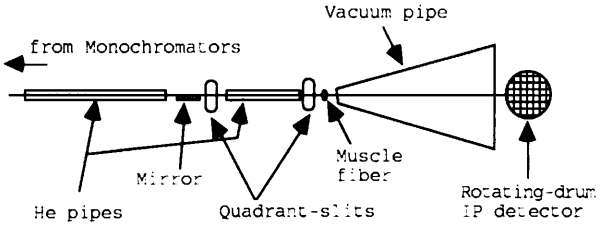

Fig.17 Design of a small-angle X-ray diffraction camera for the MR experiments.

We are currently looking for a mirror and a bender for this purpose. If they are not available, it is planned to carry out an experiment without using a mirror. Even in this case, a calculation shows that the low emittance electron beam in the MR produces such a small photon beam that we can still obtain a flux about one-order higher than that of the Photon Factory.

5.3.2 Proposed experiments

We are currently planning to carry out two experiments:

1) An oscillation experiment using a rotating-drum imaging-plate detector. For this experiment, a single skinned muscle fiber is activated and its length is sinusoidally changed by a linear motor at 0.5-1kHz with an amplitude of about 0.5%. The intensity distribution along the meridian (that is, in the direction along the fiber axis) is recorded on a rotating imaging-plate with a time resolution of 0.1-0.2 msec. The streak diffraction image is read out in the detector and transferred to a UNIX workstation through ethernet.
   A preparatory experiment was performed at beam line 15A of the Photon Factory in June, 1995. The specimen control system and the detector worked as expected. Programs necessary for data reduction have been written. The exposure required to record a myosin meridional reflection (at 1/14.5 nm^{-1}) was about 10 min. We did not observe an intensity change that could be associated with sinusoidal oscillation, which was probably because the long exposure and the large size of the specimen (a bundle of fibers, 0.8 mm in diameter) caused a depletion of ATP. A higher flux from the MR undulator will make it possible to shorten the exposure and to use a smaller specimen.
2) A caged-ATP experiment using an X-ray TV detector. In this experiment, a single skinned fiber in a rigor solution containing caged-ATP is illuminated by a strong UV flash. The two-dimensional diffraction pattern is recorded by an X-ray TV detector consisting of an X-ray image intensifier, a lens coupling, a CCD video camera, and a 12-bit image analyzer. The intensity of the equatorial reflections, actin layer-lines, and myosin meridional reflections will be measured. The time-resolution is limited to 17 msec because of the scanning rate of the video camera.
   A preparatory experiment was performed at beam line 15A of the Photon Factory in April, 1995, using a 0.5-mm bundle of muscle fibers as a specimen. The specimen control system and the detector system worked fine, and changes in the intensity of the (1,0) and (1,1) equatorial reflections were observed. All of the programs necessary for the data analysis have been prepared. The specimen control system will be improved for the Tristan MR experiment so that the experiment can be performed in a hutch, which will make access for the researcher more difficult.

N. Yagi, Tohoku University and
K. Wakabayashi, Osaka University

5.4 Preparation for an Experiment of the Two-Photon Correlations in SR X Rays

In 1956 R. Hanbury-Brown and R.Q. Twiss had observed that photons in a monochromatic light beam from a thermal source did not arrive completely at random, but arrived in bunches. In their experiment, a light beam from a mercury arclamp after passing through a filter and a pinhole was divided by a semi-transparent mirror, and then impinged on two detectors. The correlation between the instantaneous intensity fluctuations in the detectors was observed as a function of the degree of coherence of the light at the detectors by traversing one detector. This technique was applied to an optical steller intensity interferometer, and the angular diameters of visible stars were measured. We plan to extend the experiment made by Hanbury-Brown and Twiss to shorter wavelengths beyond visible wavelengths and observe the bunching effect of X-ray photons. We can expect that this experiment may be promising by using highly brilliant SR from the MR. Further, it may be possible to use this technique for the characterization of an SR source, such as the source size and the bunch length.

5.4.1 Precision Goniometer System

For this experiment we designed and constructed special equipment. Figure 18 is a front view of a precision goniometer system comprising four goniometers, two of which are high-precision goniometers and two of which are θ-2θ goniometers. They were designed so as to be used for the horizontal

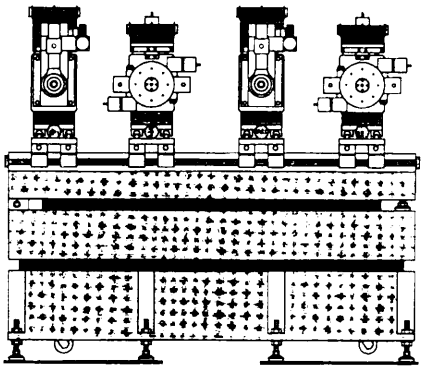

Fig.18 Front view of a precision goniometer system.

axis. In the precision goniometer, the θ axis is driven by a tangential bar mechanism with a precision micrometer head. The finest step of rotation is 0.005 arcsec. In the θ-2θ goniometer the θ and 2θ axes are driven independently by stepping motors. The finest step of rotation is 0.0001. For adjusting the goniometers during their installation along the expected beam path, each goniometer is mounted on a vertical translation table supported by a coil spring. This stage is in turn mounted on a horizontal stage attached to a cast-iron base.

5.4.2 Spatial Coherence

High degrees of spatial and temporal coherence of the X-ray beam are necessary for observing two-photon correlations. A high spatial coherence can be obtained by limiting the beam cross section with a precision slit, which is located about 100m apart from the SR source point, since the source size of MR is very small. The typical slit size is 20 μm × 40 μm. Figure 19 is a front view of a precision slit comprising a horizontal and a vertical slit. The blades of the slits made of tantalum metal are driven by stepping motors, and their positions are read by linear encoders. The slit width is set to an accuracy of 1 μm.

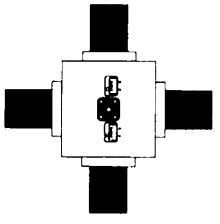

Fig.19 Front view of a precision slit.

5.4.3 Temporal Coherence

Concerning temporal coherence, the most favorable condition is that the X-ray beam be monochromatized to a bandwidth of about 10 μeV, which corresponds to the pulse width of the SR (60 ps). One choice for monochromatization is to use a nuclear monochromator based on nuclear resonant scattering. The (777) nuclear reflection from an ^{57}Fe-enriched α-$^{57}Fe_2O_3$ hematite crystal provides an ultra-monochromatic beam with a bandwidth of less than 1μeV at a resonance energy of 14.4 keV. The other choice is to use an electronic monochromator based on the usual Thomson scattering. A monochromator giving a bandwidth of 6 meV is available, which was used for experiments of nuclear resonant scattering. It comprises two channel-cut Si crystals with asymmetric 422 reflections and symmetric 12 2 2 reflections. We are now developing a new type of Si monochromator with a bandwidth of sub-meV. In this monochromator asymmetric 844 reflection with grazing incidence is made two times successively. Two of these assemblies are arranged in the (+, +) setting.

S. Kikuta, University of Tokyo

5.5 MBE apparatus for the growth control of thin films by X-ray standing-wave fields and measurements of the semiconductor surface stress

A molecular beam epitaxy (MBE) apparatus, furnished with E-gun evaporators and Knudsen Cells and RHEED, was built by reorganizing the apparatus for in-situ grazing incidence X-ray diffraction.[1] The first purpose of the apparatus is the growth control of thin films by irradiating intense X-ray standing fields using synchrotron radiation from the Tristan AR and MR. The second purpose of the apparatus is to measure the stress or minute strain fields of a semiconductor surface induced by surface reconstruction using extremely asymmetric bulk X-ray diffraction.[2]

The pumping system is a 50 *l*/s turbomolecular pump and a 140 *l*/s ion pump with a titanium sublimation pump (TSP). The base pressure in the MBE chamber is 2×10^{-10} Torr. The E-gun evaporators and Knudsen cells and the TSP are surrounded by liquid N_2 shrouds.

The apparatus has a high-precision manipulator

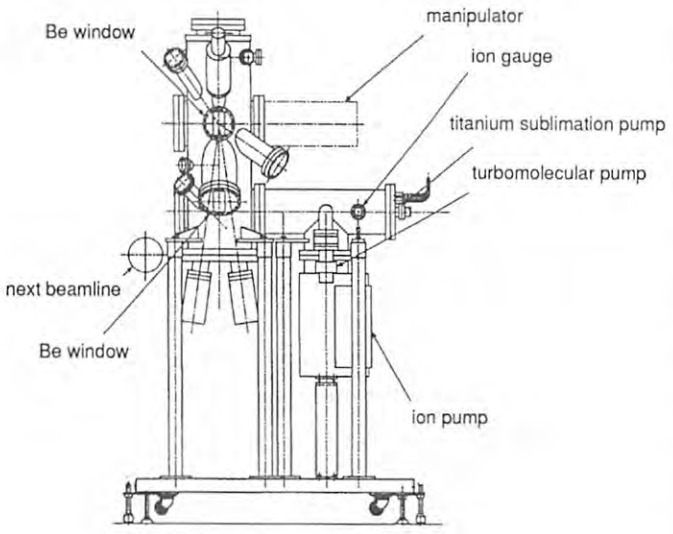

Fig.20 Overview of the MBE apparatus.

for X-ray diffraction. The precision of the manipulator for sample rotation is 0.0036 degree/pulse, which is sufficient for extremely asymmetric bulk X-ray diffraction conditions. For the growth control of thin films by X-ray standing-wave fields, the incident angle is set to a fixed angle and the angle of monochromator is varied for changing the diffraction condition.

K. Akimoto, Nagoya University and
A. Tanikawa, Microelectronics Research Labs., NEC

References

1) K. Akimoto, J. Mizuki, I. Hirosawa, and J. Matsui, Rev. Sci. Instr., **60**, 2362-2364 (1989).
2) E. Hasegawa, A. Ishitani, K. Akimoto, M. Tsukiji, and N. Ohta, J. Electrochemical Society, **142**, 273-282 (1995).

5.6 First Light from the Undulator on the MR

We observed for the first time the SR beam from the undulator on the MR on September 29, 1995 by using the most-upstream beam-position monitor (BPM), which was of the graphite wire scanning type. The beam profile by the BPM changed while varying the gap of the undulator. This fact confirmed that the observed beam by the BPM was the SR beam from the undulator. On the next day (September 30) the SR beam reached the BPM furthest downstream which was located 84 m from the source point.

H. Sugiyama

B. VUV-FEL

FEL-research in the UV/VUV-region is under way at BL-2 using an optical klystron. We set an FEL-gain measurement of 213/177-nm as our first goal using the 5th/6th-harmonics of a Nd-YAG laser as external coherent light. An optical beamline to transport the 213-nm coherent light from the laser source to the optical klystron was constructed during 1995. The optical pass creates a 213-nm beam envelope of light having a waist of 270 μm at the center of the optical klystron. Figure 21 shows the laser beam sizes in the beamline. The solid curve is the calculated beam size and the circles are the measured size. The measured waist size was 265 ± 10 μm at the center of the optical klystron.

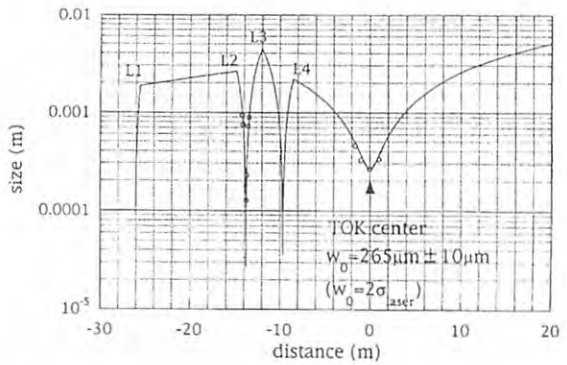

Fig. 21 Laser beam size in the FEL beamline.

A precise match between the incident laser-beam and the electron beam is required for both their positions and timing at the center of the optical klystron. We have established a method to control the positions of both the electron and laser beams within an accuracy of 50 μm. The position of the laser beam is adjusted using two SiO_2 parallel plates. The positions and angles of the electron beams at the optical klystron were obtained by measuring the positions of the spontaneous emission at two locations 7 m a part in the beamline.

A system is under development which can control the timing of the electron bunch and the laser pulse using a streak camera. Figure 22 shows a block diagram of the timing system.

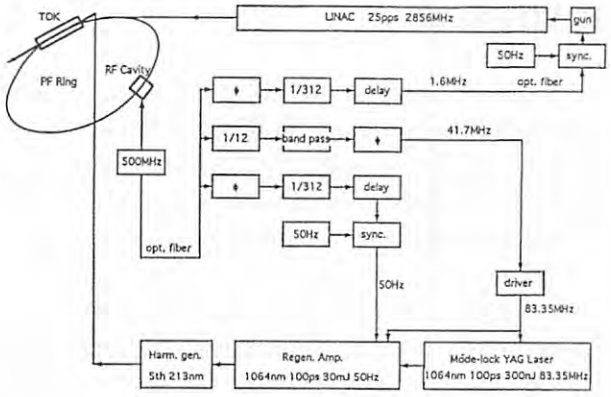

Fig. 22 Block diagram of the timing system.

C. KEKB

1. PROGRESSIVE STATUS

The KEKB, an asymmetric, double-ring electron-positron collider, requires an upgrade of the Injector Linac in order to increase the energy of the electron and positron beams to 8 and 3.5 GeV, respectively. Formerly it was 2.5 GeV.

Reconstruction of the KEKB injector's PF 2.5-GeV linac was started in FY1994 as a five-year program. From the autumn of 1994, high-current acceleration tests of single-bunch electron beams, which are necessary for producing intense positron beams, were carried out while gradually increasing the charge per bunch up to 6 nC. Regarding high-current tests, the linac was realigned using an improved laser alignment system. During the winter shutdown (1994-1995), three rf-compression systems (SLEDs) were installed in the 4-7, 4-8, and 5-6 accelerator units. In FY 1995, new accelerator-unit components (including accelerator guides) were ordered, and fabrication was started. During the summer shutdown of 1995, extensive reconstruction of the linac was carried out in which the positron generator linac was completely dismantled and removed according to the new linac layout for KEKB (see Photon Factory Act. Rep., 1994). The layout of the second sector of the PF linac was changed for the production and acceleration of positron beams. Part of the positron generator was moved there.

The eleven 30-MW klystrons in the gallery were replaced by seven 40-MW and four 50-MW klystrons. An upgrading of the klystron modulator was completed in 21 of 57 sockets, doubling the average power of the existing ones.

2. CONTROL SYSTEM

The linac control system has been operating well since being upgraded in October 1993, with an availability rate of more than 99%. However, we should even further increase its reliability in order to make the system usable in the KEKB project. It was improved in several ways this year, especially in areas concerning base services for control processing and communication:

1) Because of cost constraints, only one computer was being used for central control processing. A new central UNIX computer (DEC3000/Alpha) was introduced to share the controlling functions with the original computer.
2) The communication network was replaced with fiber-optic Ethernet and an FDDI network. A star topology was employed for its performance and maintainability.
3) The basic control communication protocol was switched from TCP to UDP for better failure recovery in real time.
4) A disk-less boot-up procedure was developed in order to eliminate hard disks in the field VME computers. Since hard disks are mechanical devices, their failure rates are high.
5) Because of technical difficulties, MS-Windows based RS232C serial lines are being used for communication between the UNIX servers and the operator's console systems. While employing new software, these are gradually being replaced by a TCP connection over FDDI and Ethernet.

These improvements provide basic functions for the KEKB linac operation along with higher reliability.

3. SUB-BOOSTER KLYSTRON

The KEKB-project requires an energy upgrade of the PF linac from 2.5 GeV to 8.0 GeV. New 50-MW klystrons have already been developed, requiring 60-kW (2856 MHz, pulsed) sub-booster klystrons (SBK) to feed the drive power to these 8 tubes, which are operated with SLED cavities. Since there are no commercial tubes available which satisfy our specifications, a new tube has been designed at KEK

and manufactured through a collaboration between KEK and MHI (Mitsubishi Heavy Industries Co.). The specifications for the sub-booster klystron are given in Table 5.

We have been using two 10-kW tubes of Thomson CSF (TH2436) in each sector. The differences regarding the TH2436 and the new SBK-tubes are as follows:

1) Electromagnet focusing has been adopted instead of a permanent magnet.
2) The frequencies for each klystron cavity need not be tunable since the role of this tube is limited. The new tube has 6 cavities, while the old tube has 4. These modifications enable us to obtain a high gain.
3) The new tube has an ion pump.
4) Water cooling has been adopted in order to stabilize the operation performance.
5) The input power feeder has been set vertically to reduce the inside bore diameter of the magnet (Fig. 23).
6) The output waveguide is a coaxial 39D type and the flange of the output waveguide is a BFX-39D standard, which is popular in Japan. (The old type was EIA-39D standard.)

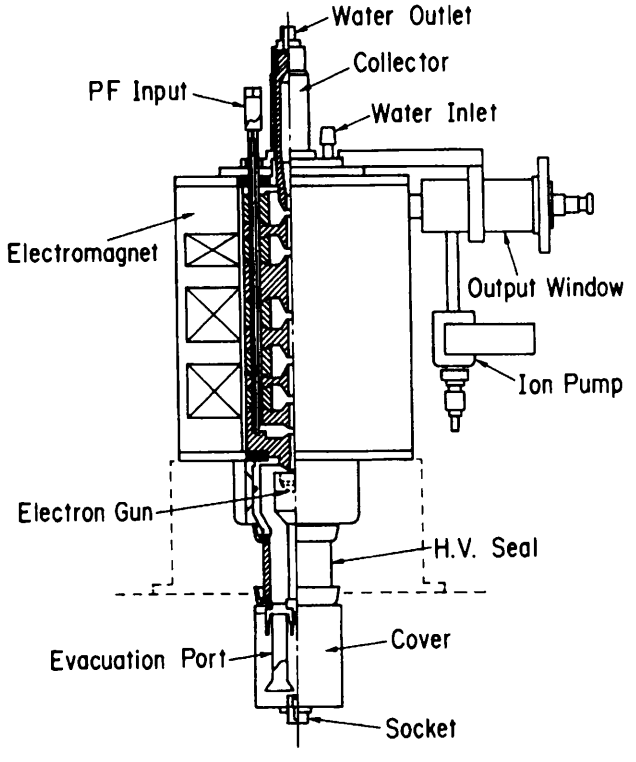

Fig. 23 Cross-section of the 60 kW sub-booster klystron.

7) An Ir-coated dispenser cathode 25.4 mm in diameter has been adopted instead of the oxide cathode in consideration of its operating life.
8) Our tube configuration has some similarities to the design of the SLAC sub-booster klystron.

The basic design of the tube has been fulfilled at KEK, and some manufacturing processes, such as cathode processing, tube baking and pinching off, were also demonstrated at KEK. A prototype tube manufactured in FY1994 was tested in FY1995 where 60 kW output power was obtained at a beam voltage of 25 kV. The beam voltage was supplied by the newly developed SBK-modulator using a semiconductor switching device.

Three tubes were ordered in FY1995 and two were tested. These tubes were installed at the klystron gallery in order to evaluate the SLED operation, which has been satisfactory.

We plan to manufacture 6 tubes or more for the KEKB project. Up to now, we have achieved an output power of 60 kW, while the efficiency is around 30%. It is neccesary to check the magnetic field near the electron gun in order to increase the efficiency.

Table 5 Specifications of SBK.

Item	Unit	Specification
Peak pulse voltage	kV	25.0
Peak pulse current	A	7.91
Microperv	mA/V3/2	2.0
Pulse width (rf)	msec	4.0
Pulse width (beam)	msec	>6.0
Repetition	pps	50
Peak RF power	kW	>60
Average RF power	W	12
Efficiency	%	>30
Gain	dB	57
Input power	mW	120
Total length	mm	690
Electric gun		BI Cathode
Focusing		Electromagnet
Cooling		Water cooling
Vacuum pump		1 l/s ion pump
Number of cavities		6
Output Waveguide		39D Coax. Waveguide
Output Flange		BFX-39D standard

4. SLED-SYSTEM OPERATION

4.1 RF Conditioning

Conditioning procedure and history

Since the maximum RF power fed into an

accelerator guide was about 8 MW before the upgrade, multiplied microwaves greater than 70 MW, which are required for KEKB operation, cannot be fed in the short term. It is necessary to increase the RF power gradually so that a drastic outgassing from the surface of the RF components will not cause a discharge. If the vacuum pressure in the waveguides or the accelerator guides exceeds the alarm level during conditioning, a control system will immediately cut off the RF pulses so as to prevent any serious damage due to discharging.

When the SLED system is being set up, the first conditioning of the high-power RF system is carried out according to the following steps:

1) The SLED cavities are detuned and RF pulses are fed into the accelerator guide while gradually increasing its power from 0 to 30 or 40 MW.
2) The SLED is turned on. The operating klystron output power is from 0 to 10 MW, mainly for conditioning the SLED cavities. This normally takes 4 or 5 days.
3) The klystron output power is from 10 to 40 MW or more, mainly for conditioning the accelerator guides. The length of this stage strongly depends on the accelerator guide, but is more than two weeks.

Although the above processes are presently carried out by manually operating a local controller while monitoring the vacuum, it will be automated this summer. Figure 24 represents the conditioning history of unit 4-7 as an example. In this case, the processes were completed within a relatively short time.

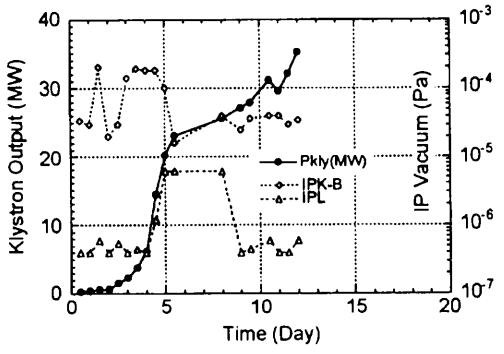

Fig. 24 Conditioning history of unit 4-7. The plotted symbols of IPK-B and IPL represent the pressures in the waveguide and the accelerator guide, respectively.

RF pulse reflection caused by discharge

The RF pulse reflected in the accelerator guide is observed with a long delay time (0 ~ 1 μs) since the group velocity of the microwaves in the accelerator guide is very slow and the filling time of the guide is about 0.5 μs in our case. That is, the delay time can determine the discharge position in the accelerator guide.

Here, we focus on the multiplied part (width w = 0.6~1 μs) of a SLED RF pulse, and assume the following for the analysis: an RF pulse traveling in an accelerator guide causes a discharge at some position in the guide because of its high field strength. A part of the traveling RF pulse, filling the accelerator guide from the upper stream to the discharge position, is then reflected backward, and the other downstream part of it moves forward.

When a reflected RF pulse with a width of t_2 is observed (Fig. 25), the pulse appears with a delay time of t_1, which is equal to the traveling time of the RF pulse to and from the discharge position (L). We can then arrive at the following equations, which give the discharge timing (T) of an RF pulse and the normalized position (L) in an accelerator guide:

$$T = w - t_2$$

and

$$L = \frac{1}{g}\left[1 - \exp\left(\frac{t_1 - T}{2T_f}\ln(1 - g)\right)\right],$$

where T_f is the filling time of the accelerator guide and g is defined as $1 - \exp^{-2\tau}$ (τ is the attenuation parameter for a constant-gradient structure). The positions L = 0, 1 correspond to the input and the output couplers, respectively.

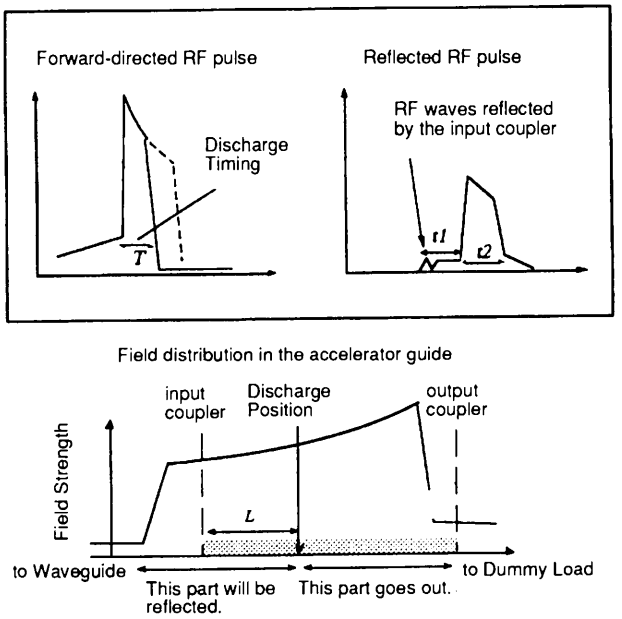

Fig. 25 Schematic diagram of rf pulse reflection.

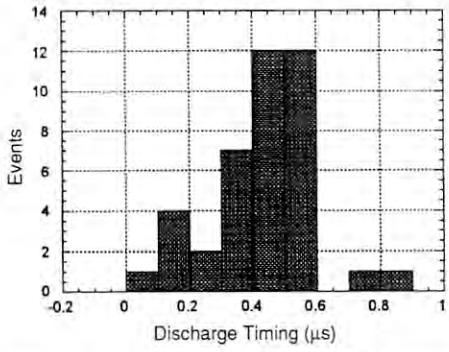

Fig. 26 Discharge-timing distribution of RF pulses for accelerator guide 4-7.

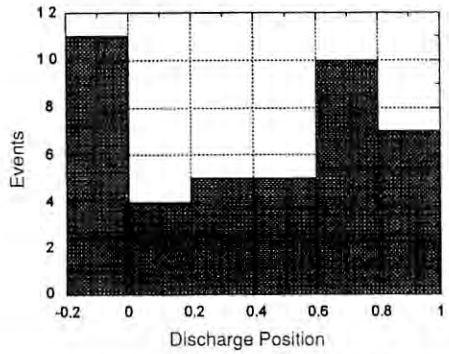

Fig. 27 Discharge-position distribution of RF pulses for accelerator guide 4-7. The negative positions were caused by errors in reading t_1 or t_2.

In reality, the shapes of the reflected pulses were not as ideal as that assumed above, and it was not easy to determine T and L. However, the analysis was performed according to the equations. Figures 26 and 27 are examples of the T and L distributions of the discharges which occurred in accelerator guide 4-7. Figure 26 illustrates how the growth of a discharge takes time. Figure 27 shows that discharges around the input or output couplers are remarkable. This result is consistent with the fact that a reflection from both couplers has been clearly observed. It should be noted that the events around the input coupler may contain discharges in the waveguide.

4.2 Acceleration Test

Beam-acceleration tests were perfomed in order to obtain the energy gain of the acceleration units and the energy multiplication factors of the installed SLED. Table 6 shows the distribution of the obtained values

Table 6 Energy gains and multiplication factors in several acceleration units with SLEDs in operation.

Klys. No.	Klys. power [MW]	Energy gain [MeV / unit]	Energy mltp'n factor
4-1	32	152.5	1.92
4-2	30	164.5	2.12
4-3	43	164.0	1.78
4-4	32	148.5	1.87
4-5	38	165.0	1.90
4-6	48	179.0	1.85
4-7	35	170.0	2.06

for a SLED cavity charging time of 3 μs. (The distribution depends on the tuning condition of each SLED system.) It shows that the energy gains are around a specified value of 160 MeV; the average is 163 MeV/unit (21.6 MeV/m). The multiplication factor is 1.93 on average, which is very close to the computed value of 1.96.

The shape of the RF pulse emitted by the SLED does not have any flat section; the pulse width must be compressed as much as possible in order to obtain a high multiplication factor. The RF timing regarding the beam pulse is thus important. We experimentally and theoretically examined the decrease in the energy gain caused by the timing shift, as shown in Fig. 28. We fitted a quadratic curve onto the experimental results, and according to the obtained function, accomplishing a beam-energy jitter of less than 0.1% would require timing jitters of less than 7 ns. A new trigger system having RF-synchronized timing circuits will be adopted so that the timing jitters will be much smaller.

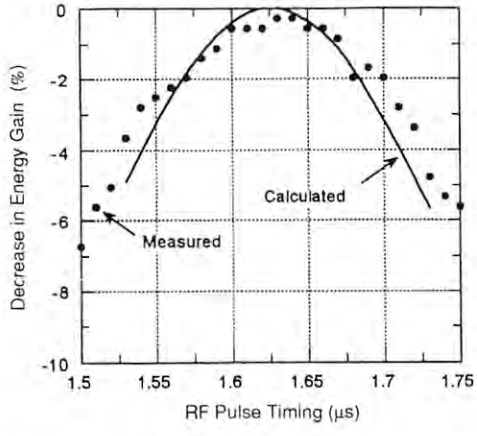

Fig. 28 Decrease in energy gain as a function of RF pulse timing. The SLED cavity charging time was 3.3 μs. The width of the multiplied pulse was 0.7 μs.

4.3 RF Measurement System

RF Monitor station

For a good understanding of the condition of the linac, it is very important to quickly detect any symptom regarding RF system problems, such as a defect in the RF-waveform or a rise in vacuum pressure in the waveguides. A signal-analyzing system will be newly installed which will continuously feed monitoring signals from the modulator and SLED into its computer. This system will also automatically execute RF conditioning of the high-power RF units, including the accelerator guides.

A prototype system based on a VXI system has been undergoing development since the spring, 1995 (Fig. 29). It comprises a controller, a waveform digitizer, an ADC and a digital I/O. Also, along with the RF measurement equipment (a peak power meter, a phase detector, etc.), an RF monitor station for observing two high-power RF units has been developed. All of the monitoring stations will be networked, and a few servers will manage the VXI controllers and databases. Measured and analyzed data or waveforms can be monitored on a remote X terminal anywhere. The waveform of a SLED RF pulse is displayed and is renewed more than 30 times per second.

In the practical operation of all monitor stations, it can be expected that the poor reliability of the hard disks of each VXI system may spoil the performance of the total system. A complex system comprising a server and a couple of diskless VXI systems will undergo test operation in 1996.

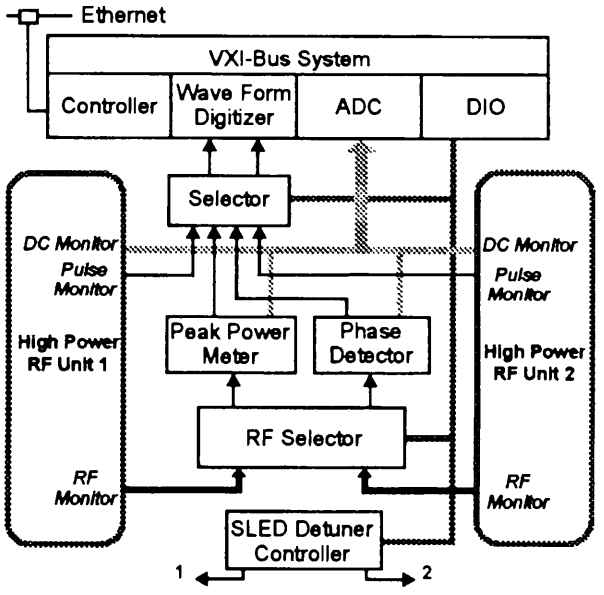

Fig. 29 Block diagram of the prototype RF monitor station.

Bethe-hole coupler

When the first prototype SLED was installed, conventional Bethe-hole directional couplers (coupling ratio: 70 dB, Fig. 30 (a)) were mounted on the waveguide in order to monitor the RF pulses from the SLED. However, a ceramic disk inside which separated the vacuum from the air was damaged during SLED operation. From the electric-field calculations, the conventional type of couplers, except for the 80-dB type, may be damaged under SLED operation with a 50-MW klystron.

There are two solutions to this problem:

1) Make the disk-hole distance longer in order to reduce the field strength in the disk.
2) Adopt vacuum coaxial feedthroughs for microwave use, and design a new simple coupler without a ceramic disk.

The first method was tried in several of the present couplers which cannot be replaced by new ones.

The second one was chosen for manufacturing the Bethe-hole couplers for new waveguides. Prototype couplers with a vacuum feedthrough were produced (Fig. 30 (b)), and their performance was examined with a resonant ring. 70-dB couplers passed a 400-MW test

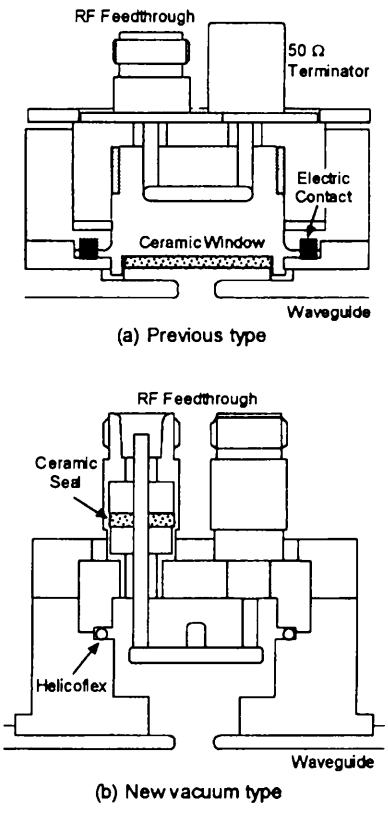

Fig. 30 Cross-section of the Bethe-hole coupler with vacuum coaxial feedthroughs.

for a few days. Fourteen directional couplers of this type were mounted early in the spring of 1996.

5. DESIGN OF INPUT AND OUTPUT COUPLERS FOR ACCELERATOR GUIDES

It is necessary that no asymmetries exist in the amplitude or phase of the electromagnetic fields in the accelerator guides input and output couplers. Although the design of the present couplers satisfies this requirement, there is a deficiency concerning its RF breakdown strength. New input and output couplers for 2m-long S-band linear accelerator guides for the KEKB linac upgrade have been designed and tested (Figs. 31and 32). The dimensions of the coupler cavities were estimated by a variation of the Kyhl method using the MAFIA code, and determined by low-power tests using the Kyhl method. It was shown that the coupler dimensions can be predicted with a precision of less than 0.5 mm. The asymmetry of the electromagnetic field (amplitude and phase) in the coupler cavities was corrected by making a crescent-shaped cut on the opposite side of the iris.

The effect of this correction is shown in Fig. 33. The VSWR and the standard deviation of the phase distribution for the accelerator guides with the new couplers measured by a nodal-shift technique were 1.06 and 1.1 degrees, respectively.

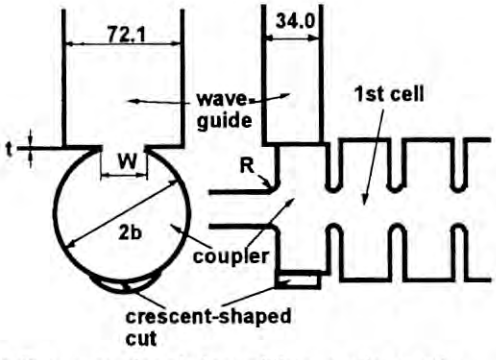

Fig. 31 Cross-sectional view of the coupler cavity.

Fig. 32 Photograph of the coupler cavity.

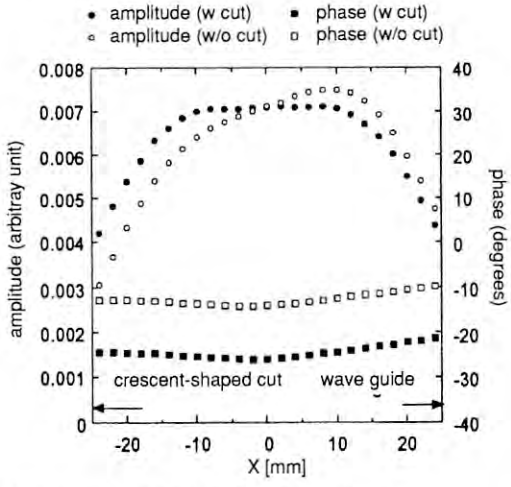

Fig. 33 Effect of a crescent-shaped cut on electromagnetic-field asymmetry. The field distribution (amplitude and phase) was measured by a bead-pull method based on non-resonant perturbation theory.

6. HIGH-CURRENT ACCELERATION TEST OF SINGLE-BUNCH ELECTRON BEAMS

The KEKB injector linac requires that a single-bunch electron beam containing a 10 nC charge be stably accelerated up to a positron production target to produce a sufficient number of positrons. Precise alignment of the accelerator is one of the key issues concerning the prevention of wake-field instability. We realigned the linac along a standard line from the pre-injector to the end of the 3rd sector within an accuacy of $\pm$ 0.1 mm. After the realignment, an attempt was made to accelerate a high-current single-bunch beam to the target, which is scheduled to be installed at the top of the second sector. The observed transmission rates were higher than 80% before the target position. This is consistent with the design of the bunching system of the linac.

The bunch shapes were measured at a point of

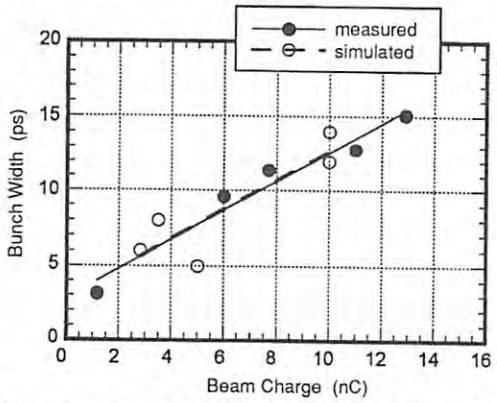

Fig. 34 Charge dependence of the bunch length. Closed circles are values measured utilizing a streak camera. Open circles are predictions simulated using PARMELA.

about 45 MeV utilizing a streak camera, the time resolution of which was 2 ps. It was observed that the shapes of the bunches became wider as the beam charge increased. The charge dependence is consistent with predictions calculated using the PARMELA numerical code (Fig. 34). The typical bunch length (FWHM) was 13 ps for the 11-nC beam, which is nearly equal to the design value, and meets the specifications at present. This result indicates, however, that an adequate modification may be necessary in the bunching system when a single-bunch beam containing more than 10 nC is required.

D. SLOW-POSITRON SOURCE

A slow-positron flux of 1×10^8 e^+/s was successfully achieved with a 2.0-GeV, 2-kW primary electron beam. This was owing to an improvement in the positron yield by annealing of the moderator assembly (tungsten foils) at 2270 K for 10 minutes under ultra-high-vacuum conditions. The achieved conversion efficiency has almost reached our design goal; we can therefore expect a slow-positron flux in the order of 10^9 e^+/s with a maximum primary beam power of 30 kW in the near future.

The energy of the positron beam was successfully varied from 400 eV to 40 keV by applying a voltage to a high-voltage station at the initial part of the slow-positron beam-transport line. This enables us to measure the depth-profile, which is very useful for locating any defects in the materials.

A slow-positron beam switch system, which comprises a pair of beam deflecting coils and two pairs

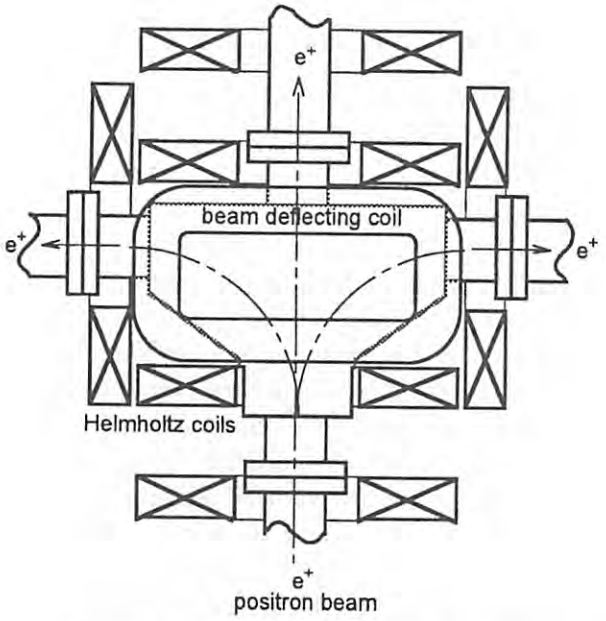

Fig. 35 Schematic view of the slow-positron beam switch system.

of Helmholz coils with magnetic-field directions crossing each other (see Fig. 35), was tested. A slow-positron beam with a beam energy of 800 eV was successfully switched from one direction to another, enabling us to direct slow-positron beams to several experimental stations at a time without breaking the vacuum.

Energy-distribution measurements of the positronium (Ps) emitted from a single-crystal sample of insulators are in progress. Ps is known to form in the interior of many insulators with a wide band-gap energy. The energy loss and slowing-down process of positrons in matter is becoming better understood. For positrons with energies less than the band gap, the production of Ps and phonon excitation become the dominant energy-loss mechanism. To date, very little has been studied about the kinetics of the formation and diffusion of Ps, which is the state immediately after production and before delocalization.

We will obtain the energy distribution of Ps by adopting the time-of-flight (TOF) method for emitted Ps. The TOF will be determined by measuring the time interval between the arrival time of a pulsed positron and the detection of radiated γ rays from annihilated Ps. Since the lifetime of Ps is well known, we can easily deduce the energy distribution of Ps from the TOF spectra, which are measured by changing the distance

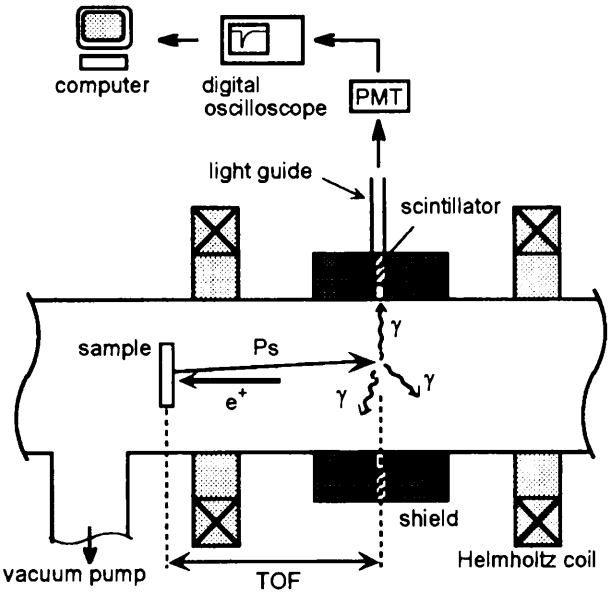

Fig. 36 Schematic drawing of the Ps detector for the Ps TOF experiments.

between the sample surface and the annihilation γ-ray detector, only if the pulse width of the injected positron beam is much shorter than the lifetime of the Ps. Figure 36 is a schematic drawing of the Ps detector for the Ps TOF experiments which will be attached down stream of the slow-positron beamline (B-1-E).

ISSN 0912-1803

PHOTON FACTORY
ACTIVITY REPORT
1995
#13

PHOTON FACTORY ACTIVITY REPORT 1995

#13